CHARACTERIZATION OF HORIZONTALLY-ISSUING REACTING BUOYANT JETS

THESIS

Joshua J. Heffernen, Second Lieutenant, USAF

AFIT/GAE/ENY/11-M12

DEPARTMENT OF THE AIR FORCE
AIR UNIVERSITY

AIR FORCE INSTITUTE OF TECHNOLOGY

Wright-Patterson Air Force Base, Ohio

AFIT/GAE/ENY/11-M12

CHARACTERIZATION OF HORIZONTALLY-ISSUING REACTING BUOYANT JETS

THESIS

Presented to the Faculty

Department of Aeronautics and Astronautics

Graduate School of Engineering and Management

Air Force Institute of Technology

Air University

Air Education and Training Command

In Partial Fulfillment of the Requirements for the

Degree of Master of Science in Aeronautical Engineering

Joshua J. Heffernen, BS

Second Lieutenant, USAF

March 2011

AFIT/GAE/ENY/11-M12

CHARACTERIZATION OF HORIZONTALLY-ISSUING REACTING BUOYANT JETS

Joshua J Heffernen, BS

Second Lieutenant, USAF

Approved:

_____//signed//_____	18 March 2011
Carl R. Hartsfield, Lt. Col., USAF (Chairman)	Date
_____//signed//_____	18 March 2011
Marc D. Polanka, PhD (Member)	Date
_____//signed//_____	18 March 2011
Mark F. Reeder, PhD (Member)	Date

AFIT/GAE/ENY/11-M12

Abstract

This research studied the mixing and combustion behavior of low Reynolds number, horizontally-issuing gaseous fuel jets with ambient air. The study focused on the mixing characteristics of propane and ethylene. These fuels are, respectively, heavy and neutral with respect to air, and were tested at various Froude numbers and laminar tube Reynolds numbers. Using low Froude and Reynolds number flows allowed for isolation of the buoyant jet effects. The process was characterized through the use of a non-invasive, OH Planar Laser-Induced Fluorescence (PLIF) technique, and supplemented with filtered (CH*) and unfiltered high speed imaging. The resulting cross sectional PLIF images were used to produce a three-dimensional mapping of the jet spreading, jet path, and combustion progress through OH concentrations up to $x/D = 9$, for both fuels. Combustion locations were further visualized and confirmed through CH* high speed imaging.

Acknowledgements

Table of Contents

List of Figures

List of Tables

List of Abbreviations and Symbols

μ .... *Viscosity in kg/m-s*
AFIT .... *Air Force Institute of Technology*
C_2H_4 .... *Ethylene*
C_3H_8 .... *Propane*
CCD .... *Charged-Coupled Device*
COAL .... *Combustion Optimization and Analysis Laser*
D .... *Diameter*
D_m .... *Mass Diffusivity in m^2/s*
DoD .... *Department of Defenese*
F_B .... *Buoyant Force*
fps .... *Frames Per Second*
FWHM .... *Full-Width, Half-Maximum*
g .... *Acceleration due to Gravity*
Hz .... *Hertz*
ICCD .... *Intensified Charged-Coupled Device*
ID .... *Inner Diameter*
Img .... *Images*
ITB .... *Inter-stage Turbine Burner*
kg .... *Kilograms*
L_f .... *Flame Length*
LIF .... *Laser Induced Fluorescence*
LPM .... *Liters Per Minute*
m .... *Meters*
m/s .... *Meters/Second*
ms .... *Millisecond*
N_2 .... *Nitrogen, Nitrogen*
NDrive .... *Network Digital Drive*
nm .... *Nanometer*
NO_x .... *Nitrous-Oxides*
ns .... *Nanosecond*
OD .... *Outer Diameter*
OH .... *Hydroxyl Radical*
PAHs .... *Polycyclic Aromatic Hydrocarbons*
Q .... *Volumetric Flow Rate in m^3/s*
r .... *Radius*
R .... *Universal Gas Constant*
$r_{1/2}$ .... *Jet Half Width*
ROI .... *Region of Interest*
s .... *Seconds*
SCF .... *Scaled Correction Factor*
SLPM .... *Standard Liter Per Minute*
T .... *Absolute Temperature*
T_∞ .... *Ambient Temperature*
T_s .... *Surface Temperature*

CHARACTERIZATION OF HORIZONTALLY-ISSUING REACTING BUOYANT JETS

I. Introduction

I.1. Motivation

The world's demand for energy has reached an all time high. For example, in 2008 the world's energy consumption grew by 1.4%. Although this number may seem small, and is the smallest since 2001, it still represents a constant growth trend spanning well over three decades. The Asia-Pacific region accounted for 87% of the world's energy consumption growth, with China leading the way at 7.2% increase and accounting for nearly three quarters of the global growth (1). As nations continue to develop, populations grow, and individual consumption rises, the demand for energy will undoubtedly increase as well.

Not following suit for 2008, the United States (US) had a decrease in energy consumption of 2.8%, representing the largest decline since 1982. This was due almost entirely to the decline of oil consumption by 6% (1). Reduction in oil consumption could be the result of a degrading economy or could be the first signs that America's push towards a "greener" future is working. Regardless of the reason, it should not be assumed the US will be unaffected by the reduction in natural resources worldwide. The US still accounted for 20.4% of worldwide energy consumption, which is nearly as much as all of Europe and Asia combined, ultimately making the US the number one worldwide consumer of energy. Additionally, in terms of oil consumption alone, the US still accounted for over 22.5% of world usage (again making the US number one), despite its considerable reduction in consumption from 2007 (1).

Although the US saw a decrease in energy consumption, it is apparent that the world's demand for energy is rising, and will continue to rise in the future. As the Earth's resources are slowly drained, competition for the remaining resources will inevitably arise. This competition over remaining resources will greatly affect the United States Department of Defense (DoD) which is already the world's largest individual consumer of energy. With the Air Force accounting for over half of this consumption and Jet fuel accounting for more than 50% of all DoD energy consumption, there is a real cause for concern about the future state of fossil fuels (2). Thankfully, this issue has not gone unnoticed; efforts have been made towards decreasing the energy dependence of the DoD. However, even though nearly three quarters of DoD energy is consumed for mobility purposes, most current conservation efforts are focused on reducing the energy consumption of standard buildings, which account for less than 25% of all DoD energy consumed (2).

Energy conservation efforts alone will not be sufficient to solve the growing energy crisis; in order to combat this growing need the US military is also constantly searching for alternative, renewable energy sources. For example, the Navy is studying alternative propulsion options as well as creating proposals for an all nuclear navy. The Navy also operates the world's largest wind and diesel hybrid power plant in Guam. The Air Force is the country's largest purchaser of renewable energy and third largest in the world. Additionally, the Air Force already has four bases which operate entirely on renewable energy sources. The US Military has clearly taken its first steps towards energy independence with 9% of its energy coming from renewable sources, and plans to increase this to 25% by the year 2025 (2).

Although efforts are being made towards a fossil fuel free military through conservation and an increase in alternative energy sources, the Air Force's reliance on fossil fuels still seems unavoidable, at least for the next few decades. Even if not just the DoD, but rather, the entire US could decrease energy consumption 25% by 2025, the US would still be the world's second largest consumer of energy, second only to China, assuming current and projected trends are accurate (1). Therefore, it becomes apparent action must be taken in order to ensure availability of these natural resources. It is imperative future research and development focus on ways to improve efficiency in engines. More specific to the Air Force, future gas turbine engine development must focus on creating engines with higher thrust to weight ratios, higher efficiencies, and lower thrust specific fuel consumptions (TSFC) in order to reduce the Air Force's reliance on fossil fuels, ultimately ensuring continued domination of air and space.

I.2.   Application

Despite an apparent need for more advanced gas turbine engine technologies, current funding initiatives for advancing propulsion technology has recently declined. One program created to combat this decline is the Versatile Affordable Advanced Turbine Engines (VAATE) initiative. The VAATE initiative was created with hopes of obtaining gas turbine engine advancements such as a two-fold increase in engine thrust to weight ratio, a 60% decrease in engine development, procurement, and life cycle maintenance cost, as well as a 25% reduction in fuel consumption (3). In order to meet these developing needs, many partial solutions have been proposed.

One advanced engine component design currently being considered is the Ultra-Compact Combustor (UCC). The UCC will significantly reduce the axial length required

for combustion by making alterations to the airflow direction and fuel mixing within the combustor of a gas turbine engine. These changes allow the UCC to offer three unique advantages over conventional combustors. First, shortening the combustor and placing it circumferentially over the turbine, instead of immediately in front of it, greatly increases the engines thrust to weight ratio, by providing more efficient combustion, and thus more thrust. More importantly, however, it provides the option to designers to implement an inter-stage turbine burner (ITB). The ITB effectively acts as a second combustor located between the high and low pressure turbine stage which thermodynamically re-energizes the flow after it leaves the high pressure turbine and before it enters the low pressure turbine, resulting in improved thermodynamic cycle efficiencies. The second distinct advantage provided by the UCC arises when it is used simply in place of a conventional combustor, without an ITB. This configuration offers a considerable decrease in weight and length of the overall engine, which result in better overall performance of the aircraft and a reduction in fuel consumption. The third advantage offered is a result of the circumferential design of the UCC. As a result of the circumferential design and shortened length, the UCC must have trapped vortex combustion (TVC). The TVC allows for increased airflow and fuel mixing capabilities which results in increased combustion efficiency (4) (5).

Although the UCC will offer a good step in the direction towards energy independence, the mechanics and feasibility behind its implementation are still not fully understood. The implementation of the UCC into current and future gas turbine engine designs is complex and brings about many issues yet to be researched and analyzed. One of the most complex and interesting aspects of the UCC is the mixing of air and fuel. In a

conventional design there is sufficient length for the fuel and air to be mixed, ignited, and sent through the turbine. Implementing the UCC, on the other hand, provides the unique challenge of completing these tasks, within a shorter distance. When this task is accomplished within the UCC, the performance is dominated by body forces due to the high circumferential loading. In conventional combustors these forces are present, but are often disregarded because they are much lower and generally unimportant to the overall performance. Within the UCC, these body forces cannot be ignored. Therefore, it becomes critical to gain a better understanding of the interactions occurring within the UCC in order to help advance and predict performance of future designs. Unfortunately the classification of flow inside an UCC is outside the realm of this paper; however, through the investigation of reactive buoyant jets (a UCC in its simplest form) the author hopes to gain an understanding of how body forces influence the interactions of fuel and air when they are combined, mixed, and combusted. Although this research will address the laminar mixing situation and is not representative of the turbulent mixing occurring within the UCC, the goal is to gain knowledge of the laminar condition which will provide insight into the mechanisms present in the turbulent condition. This research will provide a baseline for future UCC research as well as offer a stepping stone towards investigations of other horizontally issuing buoyant jet applications.

In addition to the UCC, the combining, mixing, and combustion of fluids with different densities is a situation which also has many other relevant applications. However, by comparison to other research paths, this area has not received as much attention from the academic or research realms. In 2009, Xiao, Travis, and Breitung noted, "The horizontal buoyant jets with large density variations, for instance hydrogen

5

or helium injecting into air, have not received sufficient research before, and almost no experimental data could be found in the open literature (6)." This deficiency was partially addressed in this research; in order to gain an enhanced understanding of this situation, because understanding the effects of buoyancy, even in applications with simple geometries, is a crucial step for engineering advancements in the future.

I.3.   Objectives

The purpose of this study was to analyze the behavior of low Reynolds number, horizontally-issuing gaseous fuel jets as they mix and combust with ambient air. More specifically, the study focused on the mixing characteristics of two different fuels: propane and ethylene. These fuels, which are considered heavy and neutral, respectively, were tested at various Froude and Reynolds numbers. Using low Froude and Reynolds number flows kept the tube flow laminar, and allowed for the isolation of the buoyant jet effects. The process was characterized through the use of a non-invasive, OH Planar Laser-Induced Fluorescence (PLIF) technique, and supplemented with filtered (CH*) and unfiltered high speed imaging. The resulting cross sectional PLIF images were used to produce a three-dimensional mapping of the jet spreading, jet path, and combustion progress through OH concentrations for all three fuels. Combustion locations were further studied through CH* high speed imaging.

One project goal was to gather critical information about the near field mixing characteristics. A second goal was to determine how the buoyant fuel jet and its reaction with air influence the trajectory. Another critical objective was to characterize the propane fuel because it was the most applicable to the Ultra Compact Combustor.

II.   Theory and Background

II.1.   Traditional Gas Turbine Combustor

In a traditional gas turbine engine there are five main components: inlet, compressor, combustor, turbine, and nozzle. The compressor, combustor, and turbine are often referred to as the gas generator of the engine and are found on a variety of different engines to include: turbofan, turbojet, turboprop, and turboshaft engines. As seen in Figure 1, the combustor comprises a significant portion of the overall engine size. Therefore, reducing its overall size and increasing its performance are critical to overall engine performance. While its primary goal is to provide gas of high temperature and pressure to the turbine, the following properties are also preferred: total combustion, pressure losses held to a minimum, combustion stability, uniform temperature distribution, short length, small cross section, reduced chance of flameout, relight ability, and operation over a broad range of mass flow rates, pressures, and temperatures.
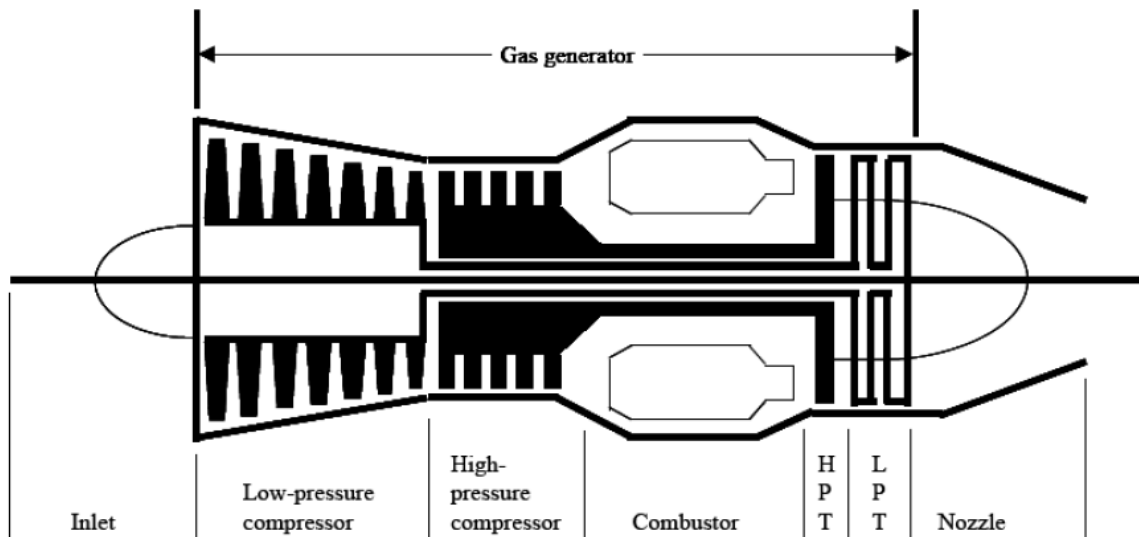
Figure 1. Typical Jet Engine Schematic (7)

The combustor, commonly known as the burner, is the gas turbine engine component responsible for taking the high pressure air from the compressor and combining, mixing, and combusting it before expelling the hot gas to the turbine. Traditionally, combustors followed three basic configurations: annular, can, and can-annular. The annular burner resembles a donut-shaped, single, continuous chamber which encompasses the turbine. Due to the smaller amount of surface area in this design, less cooling air is needed. This configuration also provides a better flow inlet into the turbine as well as simple cross-ignition capabilities during engine startup. The largest disadvantage to this design is the difficulty associated with acoustic control due to flame instability at ultra-low emission levels. The can-annular design is comprised of multiple, single burner "cans" spaced evenly around the center shaft. This type of design allows for individual cans to be removed from the engine without the removal of the entire burner assembly. Cans are one or more combustion chambers placed external to the gas turbine body (8).

In all three traditional gas turbine combustor configurations, high pressure air enters into the combustor from the compressor and the fuel is injected axially into the flow. Due to the axial injection of fuel, the resulting combustion occurs in two zones. In the first zone, or primary zone, fuel and air are mixed slightly fuel rich, and combustion begins as the air flows around the fuel injectors. The air flow around the fuel injectors causes a region of recirculation which allows the combustor to remain lit. These areas of recirculation effectively act as flame holders, much like the pilot light on a furnace. After the primary zone, more air is added, allowing for the combustion of any remaining hydrocarbons in the secondary or dilution zone. Additional air also helps prevent damage

to the high pressure turbine by lowering the temperature of the gas (7). Because combustion occurs in the axial direction of a limited space, complete combustion is not achieved; in other words, there is insufficient time for all of the fuel to mix with the air and totally combust. This incomplete combustion in traditional burner designs result in lower efficiencies.

II.2. Ultra Compact Combustor

The UCC was developed by the Propulsion Directorate, US Air Force Research Laboratory, at Wright-Patterson Air Force Base in Dayton, Ohio. Unlike traditional gas turbine engine combustors, the UCC uses the circumference of the engine to combust the air and fuel mixture, resulting in a significant reduction in length. The UCC also utilizes the acceleration due to swirl to further enhance the combustion process resulting in even more reduction in length (4). If traditional combustors were made as short as the UCC, the residence time would be insufficient and complete combustion could not occur before the flow entered the turbine section. Not allowing for complete combustion would severely degrade the life of the turbine blades and create significant reductions in efficiency (9). In order to resolve these issues, the UCC achieves complete combustion through enhanced, high g-loading swirl mixing. This high g-loading swirl mixing allows for sufficient residence time and reduced chemical time, resulting in complete combustion in a shortened area. Additionally, g-loading uses the different density of the reactants and combustion products to improve efficiencies.

II.2.1. Trapped Vortex Combustion

One of the enabling technologies or ideas required for the UCC to be successful was advancing the concept of TVC. This enabling concept is essentially a vortex created by axial flow passing over a recessed cavity, as seen in Figure 3. When air and fuel are combined in the direction of the flow, the vortex created in the cavity is strengthened. Upon ignition, the vortex stabilizes the flame causing the cavity to act like a flame holder. In addition to flow in the recessed cavity, air is also traveling in the axial direction. When the axial flow interacts with the vortices produced in the cavity, increased mixing occurs, allowing for more complete combustion in a relatively shorter distance. As a result of increased mixing, low lean-blow-out equivalence ratios are observed as well as an improved combustion efficiency of approximately 99% (10). ⁻ Additionally, the TVC offers larger operating ranges, higher altitude relight capabilities, and reduced nitrous-oxide (NO_x) emissions, compared to traditional combustors (11).
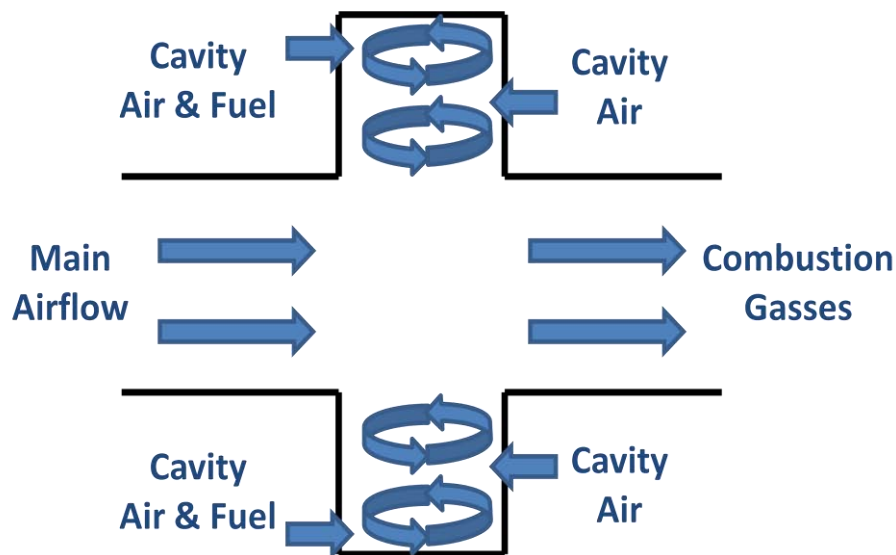
Figure 2. Trapped Vortex Combustion (12)

II.2.2. Centrifugally Enhanced Combustion

In addition to using TVC for improved mixing and flame stabilization, the UCC also utilizes centrifugally loaded swirling. Centrifugally enhanced combustion allows for greater residence time as the air and fuel mixture navigate circumferentially around the engine. When fuel and air are injected into the UCC, a swirling motion is created in the cavity surrounding the main air flow. Upon entering the cavity, this highly accelerated flow experiences substantial centripetal acceleration. This acceleration causes the more dense and colder air and fuel droplets to be forced to the outer edge of the cavity while the hotter, less massive products are brought to the center of the cavity, much like a centrifuge (9).

According to Lewis, centripetal acceleration and the resulting centrifugal forces felt by the air and fuel mixture produce increased mixing and flame propagation speeds (13). These increases are the result of buoyancy effects. As the flow is accelerated, flame speed is also increased as a result of the increased mixing. Additionally, the buoyancy forces imparted on the flow field cause the flame to travel into areas of lower density, ultimately maximizing the combustion process (5). The buoyant force, per unit volume, imparted onto a particle can be calculated using the following equation (14):

$$F_B = \rho_a g \left[1 - \frac{\rho_f}{\rho_a} \right] \tag{1}$$

where F_B is the buoyant force, g, is the acceleration, and ρ_a and ρ_f represent the air and fuel densities, respectively. In traditional gas turbine combustors the buoyant force is extremely small. As a result it is often neglected because the laminar and turbulent flame speeds are the dominant factors in flame spreading. In the UCC, however, combustion is

occurring under high centrifugal loads. This causes the magnitude of gravitational acceleration, g, from the above equation to significantly increase, resulting in a large buoyant force being imparted. As larger g-loads are experienced, the buoyancy force becomes dominant, causing the flame to spread much quicker than it would due to laminar and turbulent flame speeds (12).

In order to achieve increased flame speed, substantial centripetal acceleration, or g-loading, needs to occur. According to Lewis, g-loading below 200g is insufficient to achieve increased flame propagation. An area of transition occurs between 200g to 500g, and up to 3500g, the buoyant flame speed increases as the acceleration increases. As the centripetal acceleration was increased (up to 3500g), the buoyant flame speeds became larger than the laminar and turbulent flame speeds. In areas experiencing accelerations greater than 3500g, the flame speed quickly decreased, often causing flame extinction (13).

Because the UCC incorporates both trapped vortex and centrifugally enhanced combustion it is able to outperform all three traditional combustor designs. The TVC increases mixing and stabilizes the flame while the centrifugal loading yields higher flame speeds (13). The result is more efficient combustion occurring in a smaller axial length, ultimately increasing efficiencies while decreasing overall engine size.

II.3. Laminar and Turbulent Flow

Laminar flow, often referred to as streamlined flow, is when a fluid flows in approximately parallel streamlines, without disruption or flow between the layers. At some point, however, laminar flows will become turbulent. Reynolds number, pressure distribution, smoothness of a surface, and external disturbances are all factors which will

12

combine and eventually cause a laminar flow to become unstable and change to a turbulent flow. The process of changing from laminar to turbulent flow is known as transition (15).

With respect to fluid dynamics, laminar flows define the regime which contains high momentum diffusion and low momentum convection. This is fundamentally the opposite of what occurs in a turbulent flow. Turbulent flows are characterized by chaotic and stochastic property changes, which include low momentum diffusion and high momentum convection. Simply put, laminar flow is smooth and clean while turbulent flow is rough and chaotic. Turbulent flows also contain rapid variations of pressure and velocity as they progress through time and space. These fluctuations in velocity can be on the order of a tenth of the mean velocity, and as a result, they can cause the characteristics of the turbulent boundary layer to be profoundly different than those observed within laminar boundary layer. For example, they create enhanced mixing, while the consequent rates of momentum diffusion, vorticity, and heat are significantly larger than the analogous rates due to only molecular interceptions in laminar flows. More specifically, the turbulent fluctuations in the presence of mean velocity gradients create eddies, which subsequently increase mixing (15).

Although the fuels in this experiment were delivered via laminar tube flows, it is important to at least understand turbulent flows and the connections between the two. More importantly, however, is the application of this research towards the UCC which undoubtedly contains turbulent flows and turbulent mixing. In the current research different fuels were expelled through a pipe in a laminar fashion. In order to ensure flows retain laminar characteristics, Reynolds numbers were kept low. While Reynolds number

is not directly related to laminar and turbulent flows, parallels can be drawn between the two. Generally speaking, pipe flows characterized by Reynolds numbers greater than 4000 correspond to turbulent flows while flows with Reynolds numbers less than 2300 are laminar. Flows with Reynolds numbers between these two values are referred to as transition flows and represent the region where the flow is changing from laminar to turbulent.

In these experiments all flames were classified based on the Reynolds and Froude numbers present in the tubes, before combustion occurs, because densities and velocities within the reacting jet are constantly changing and can only be assumed. Although the tube flows contained Reynolds numbers suggestive of laminar flows, the actual reacting jets were not laminar. With the introduction of combustion and buoyancy, all jets quickly became unsteady and displayed turbulent behaviors.

II.4. Buoyant Flow

In physics, buoyancy is defined as an upward acting force resulting from fluid pressure which reduces an objects weight. There are two ways an object can remain afloat. Either the object is less dense than its surroundings or is shaped appropriately (like a boat). The former case is the one of interest for this research. Specifically, the trajectories of the different fuels varied, as a direct result of their density, as they were ejected into air. As expected, the lighter (less dense) non-reacting fuels curved upwards while the heavier non-reacting fuels followed a downward trajectory.

For the purposes of this research it was pertinent to define the expressions for "positive buoyancy" and "negative buoyancy." Positive buoyancy was used to represent situations where the ambient fluid was denser than the jet while the term negative

buoyancy represents the case in which the jet was the more dense fluid. Simply put, a positively buoyant jet will tend to curve upwards while the negatively buoyant jet will follow a downwards trajectory for horizontally issuing jets, as seen in Figure 3.
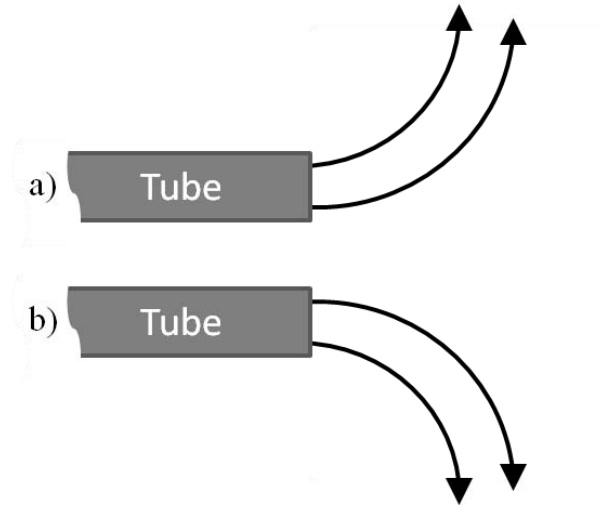
Figure 3. Sketch of Horizontal Jets with (a) Positive and (b) Negative Buoyancy (16)

II.4.1. Buoyant Jets

A buoyant jet in the simplest terms consists of a jet of gas or liquid flowing into another gas or liquid containing a different density; even in these terms, predicting the behavior of the flow becomes a complex fluid dynamics problem. Consider, for example, the case where a jet of hydrogen (low density) is ejecting horizontally into a room containing air (higher density). Due to the buoyant effects and body forces acting on the hydrogen, the jet would be predicted to follow an upward trajectory, where its curvature and rate of ascent would be dependent upon the inertia contained within the jet. Conversely, it can also be predicted that the path of the trajectory would decrease when the hydrogen and air begin to mix because the body force resulting from buoyancy is dependent upon local density. Therefore, hypothesizing the true trajectory of the

15

hydrogen becomes a daunting task. Buoyant jets, although seemingly simple, are in reality exceedingly complex. Thus, the characterization of buoyant jets and their flows entails a rigorous analysis of the jet inertia, body forces resulting from buoyancy, mixing through molecular diffusion, mixing resulting from jet instabilities dependent upon transition and turbulence (16).

II.4.2. Classifications

In order to aid in the analysis and account for the interplay of physical parameters many characterization numbers are associated with experiments involving jets. Specifically, Reynolds, Froude, Schmidt, Richardson, and Grashof numbers are the most commonly used in defining the characteristics of a jet flow.

II.4.2.1. Reynolds Number

The Reynolds number is a dimensionless number which represents a flows ratio of inertial forces to viscous forces. Reynolds number is frequently used in fluid mechanics when performing dimensional analysis. More importantly, however, it is also used to characterize flow regimes into laminar or turbulent flow. At low Reynolds numbers, the viscous forces are dominant. As a result, the flow is laminar, characterized by smooth constant motions. Conversely, at high Reynolds numbers, inertial or momentum forces dominate, resulting in turbulent flows which produce seemingly random vortices and flow instabilities. Reynolds number has numerous definitions depending on the application. While there are many definitions, each generally contains: the density and viscosity of the fluid, a velocity, and a characteristic length or dimension. Since this research involves flow within a pipe, the characteristic dimension is D, the

inner diameter of the pipe in meters, m, and the following equation for Reynolds number

is used:

$$Re = \frac{4\rho_j Q}{\pi D \mu} \tag{2}$$

where the, Q is the volumetric flow rate in m³/s, μ is the viscosity in kg/m-s and ρ_j is the

density of the fluid being ejected from the tube.

II.4.2.2. Froude Number

The Froude number is a relationship originally created to classify objects moving

in open flow channels (i.e. boats in water). Since its publication by William Froude in

1868, the Froude number has expanded to define the resistance of an object moving

through a fluid. Specific to this research, the Froude number is a ratio of inertia to

gravitational forces observed by the fluid particles of the jet as they are ejected into the

surrounding air and is represented as follows:

$$Fr = \frac{4Q}{\pi D^2 \left[gD \left| \frac{\rho_a - \rho_j}{\rho_j} \right| \right]^{1/2}} \tag{3}$$

where, Q, D, and ρ_j represent the same values as in the Reynolds number equation, ρ_a is

the density of the ambient air, and g is the gravitational constant.

II.4.2.3. Grashof Number

The Grashof number is another dimensionless number, often used in fluid

dynamics and heat transfer, which represents the ratio of buoyancy forces to viscous

forces acting on a fluid. In many situations the Grashof number is used in place of the

Froude number to account for molecular as well as thermal diffusivity in situations where the buoyancy force is driven by thermal gradients. The Grashof number for pipes is:

$$Gr = \frac{g\beta(T_s - T_\infty)D^3}{v^2} \qquad (4)$$

where, g is the gravitational constant, β is the volumetric thermal expansion coefficient (approximately equal to $1/T$ where T is the absolute temperature), T_s is the surface temperature, T_∞ is the ambient temperature, D is the pipe diameter, and v is the kinematic viscosity. For natural convection from vertical flat plates turbulent flows are often observed for Grashof numbers ranging from 10^8 and 10^9, while lower numbers most often represent laminar flows.

II.4.2.4. Schmidt Number

The Schmidt number is a dimensionless number which is used to characterize fluid flows in which simultaneous momentum and mass diffusion processes are occurring. It is defined as the ratio of momentum diffusivity to mass diffusivity. In other words, the Schmidt number is the ratio of the viscous diffusion rate to the molecular diffusion rate. It is a physical representation of the relative thickness of the hydrodynamic layer and the mass transfer boundary layer and is represented as follows:

$$Sc = \frac{v}{D_m} = \frac{\mu}{\rho D_m} \qquad (5)$$

where, v is the kinematic viscosity in m^2/s, μ is the dynamic viscosity, ρ is the density, and D_m is the mass diffusivity in m^2/s.

II.4.2.5. Richardson Number

The Richardson number is often used in place of the Froude number. It is a dimensionless number representing the ratio of potential and kinetic energy. It is most often used to characterize atmospheric and oceanic flows in which buoyant flows may be an issue. In flows characterized by Richardson numbers less than unity, buoyancy becomes an insignificant factor in the flow. However, if it is considerably larger than unity, buoyancy forces dominate within the flow. In situations where the Richardson number is on the order of unity, then the flow will most likely by affected by buoyancy forces. Interestingly, the Richardson number can be expressed as a combination of the Grashof and Reynolds numbers as follows:

$$Ri = \frac{Gr}{Re^2} \qquad (6)$$

It is imperative to understand all of these classifications relating to jet flows because they help to clarify past research as well as to characterize the current study. Although they are all significant, it is important to note that only the Reynolds number and Froude number were used to classify flows in this project.

II.4.3. Past and Present Research on Buoyant Jets

Buoyant jets occur in, and are relevant too, many natural phenomena and engineering processes across the world. As such, many studies were and still are being conducted in order to understand the complex interaction of variable density flows. While the majority of past research has focused on vertically issuing jets, there was also some analysis done on horizontally issuing jets.

II.4.3.1. Vertically Issuing Buoyant Jets

Much of the past research focused upon buoyant jets with turbulent flow, most likely because they have more applications than laminar jets. As such, there is an abundance of information based on extensive research which classifies the effect of density gradient on turbulent mixing in jets where the buoyant force is a driving factor. For example, in 1992, Batchelor, Canuto, and Chasnov successfully developed a set of governing equation, and solutions, for a turbulent flow using a Boussinesq approximation stating minute changes in density alter the flow only through the buoyant force (17). More recently, in 2008, Livescu and Ristorcelli were able to illustrate considerable differences in the mixing process occurred when the Boussinesq approximation was not applied (18). In many applications, the driving force behind the jet is momentum, while the buoyant force is generally insignificant. However, in situations where the buoyant force is dominant, interesting phenomena begin to occur. For example, in 1989 Papantoniou and List analyzed jets in which the buoyant force was the dominating mechanism and observed an increase in entrainment rate, accredited to the buoyant force (19). This simply means, the more buoyant jets, spread faster and pulled more air into their core, resulting in quicker mixing.

The majority of the inquisitions into buoyant jets are conducted upon jets oriented such that the jet or plume is being expelled in a direction parallel to the forces due to gravity. Simply put, most research on buoyant jets has focused on vertically issuing jets. In 1991, Monkewitz and Pfizenamier became some of the first to identify and classify "side jets" they observed on vertically issuing buoyant jets. The side jets were attributed to the streamwise vortices which were present in the braid region of the jet, between the

vortex rings and the Widnall instability of the rings (20). A year later, Subbarao and Cantwell classified the mixing characteristics of a vertically issuing helium jet through the implementation of stroboscopic Schlieren imaging and Doppler velocimetry. One of their interesting findings they remarked upon was the peculiar transition to turbulence which appeared to depend upon the Richardson number and Reynolds number (21).

II.4.3.2. Horizontally Issuing Buoyant Jets

Although the majority of research relating to buoyant jets relates to vertically issuing jets, the studies focused on horizontal jets are more applicable to the current research efforts investigated in this paper. One interesting study conducted by Jirka in 2004 actually compared a vertical and horizontal jet. In the study, Jerka defines an integral model, which considered the buoyant force and its effects, applicable to numerous naturally occurring environmental turbulent flows, including aqueous jets. Jirka classified the vertically issuing buoyant jet as an advected line thermal, which in his integral model can be defined by an asymptotic solution. The horizontally issuing buoyant jet, on the other hand, fell outside the limits of an asymptotic solution. Jerka remarked, "General buoyant jet flows, often with complex three-dimensional trajectories, with variable ambient stratification and/or with cross flows, are in a non-equilibrium state lacking local self-similarity (22)."

When considering the general nature of horizontal buoyant jets, it is remarkable how few studies have been conducted on them when compared against vertical jets and jets in a cross flow. While research seems minimal, the subsequent literature defining and characterizing buoyant jets is even scarcer, and when considering the addition of laminar jets and combustion effects, there is even less documentation. The difficulty associated

21

with gathering measurements, complexity in the flow, and possibly the lack of abundant practical applications are all potential indicators towards the scarcity of ample studies conducted upon horizontally issuing buoyant jets.

Before the introduction of the ultra compact combustion and the need to further understand buoyant effects in horizontally issuing jets, the most practical applications for research were with aquatic discharges. Research into aquatic discharges has been conducted for decades. In 1982, Satyanarayana and Jaluria arranged a set of experiments to gather pointwise temperature measurements on the vertical axis of hot water jets. The jets were injected at angles of inclination, including zero degrees or horizontal, and results were compiled for jets characterized by Reynolds numbers ranging from 500 to 2000. The researchers concluded that the jet trajectories were best modeled by the Froude number, as opposed to Reynolds or Grashof numbers alone. Additionally, with flows containing Reynolds numbers or approximately 600, they observed higher mixing rates on the upper portions of the jets than on the bottom, especially in regions where the ratio of length to diameter was less than ten, $x/D < 10$ (23).

Another important reference point is the study conducted in 2000 by Arakeri, Das, and Srinivasan which investigated laminar, horizontally issuing buoyant jets ejecting mixtures of aqueous salt solutions. The study showed that given the appropriate Reynolds and Froude numbers, the jet would actually bifurcate into a "main jet and a plume region." The results found related to Reynolds numbers ranging from 40 to 1800 and Froude numbers on the order of 0.4 to 30, while the Schmidt number was on the order of 10^3. The term bifurcation does not define two equal axis-symmetric distributions of fluid that may be observed in a vertical jet; rather, it was used by the authors to classify what

they identified as two distinct regions within the jet. In order to illustrate their findings the bifurcation was observed through the use of laser induced fluorescence (LIF) technique which mapped the concentration of the core fluid as a function of position. They noted the lower density fluid in the core region resembled the shape of a teardrop while the upper portion of the downstream jet separated from the main jet and took on the characteristics indicative of a plume. Through the use of LIF they illustrated the main core region of the jet was composed of the inner portion of the jet, as expected. More interestingly, however, they illustrated how the surrounding fluid contained within the boundary layer of the fluid at the nozzle exit is essentially grabbed and taken into the plume, initiating from the top center of the jet cross section (24).

In general, the observations and consequent conclusions drawn by Arakeri, Das, and Srinivasan are consistent with expected results for flows in which the buoyant forces are more influential than the inertial forces. However, there was one exception. In flows containing Reynolds numbers less than 100 and Froude numbers on the order of 1 to 5, bifurcation was not observed. The reasoning provided by the authors was, "the jet turns vertically too quickly to permit bifurcation (24)." In other words, the buoyant forces are overwhelming to the point where the inertial forces become insignificant. Without, the presence of inertial forces, the jet maintains no forward (horizontal direction) momentum. Thus, it rapidly turns vertical, does not bifurcate, and assumes the characteristics indicative of a vertical jet.

In 2005, Querzoli and Cenedes conducted yet another study on aqueous jets. This time, however, the study focused on characterizing jets with negative buoyancy using particle tracking velocimetry and LIF. They collected data for flows with Reynolds

numbers between 900 and 3850, Froude numbers ranging from 3.0 to 17.6, and Richardson numbers from 0.05 to 0.31. Their results revealed negatively buoyant jets also experience bifurcation. Similar to results found by Arakeri, Das and Srinivasan, the jet bifurcated into a plume and a core region; however, due to the change in buoyancy, the plume was observed on the lower or under side of the jet. Their analysis of flows with Froude numbers of 4.3 revealed a single plume ejecting from the bottom of the jet, while the corresponding velocimetry data for flows with the lowest Froude numbers revealed significant jet core curvature. The authors also noted an increase in mixing rate when the buoyancy forces were increased due to the excitement of the Kelvin-Helmholtz structures by the buoyant forces (25).

In most studies relating to horizontally issuing buoyant jets the flows are characterized by the trajectory of the peak concentration of core fluid. There is much less experimental data focused on classifying the specific shape of the jet cross sections in terms of concentration of the core fluid. The current research focused on developing more inclusive views of the jet cross section as the mixing and combustion progressed, as a function of streamwise position, in addition to trajectory plots.

II.4.3.3. Alternating Buoyancy

For the most part, past studies have focused on either positively or negatively buoyant jets. Minimal studies have investigated the effects of both positive and negative buoyancies. It may be natural to assume that the two buoyancies would simply be mirror images of each other, as they are in vertically issuing jets. However, when considering horizontally issuing buoyant jets, it is important to entertain the idea of differences in jet configuration due to the dissimilar density gradients in the flow field and centripetal

effects. Identifying and classifying these distinctions is yet another goal of the current research.

One recent study conducted by the Air Force Institute of Technology (AFIT) analyzed the near field mixing characteristics of both positively and negatively buoyant, horizontally issuing jets. The first tests conducted used a non-intrusive filtered Rayleigh scattering technique to determine the cross-sectional mass fraction of a horizontal helium buoyant jet flowing into ambient air. The first tests operated with Reynolds numbers on the order of 50 to 1200 and Froude numbers as low as 0.71 with Schmidt numbers on the order of unity for all tests. Numerous subsequent tests were also conducted using carbon dioxide rather than helium in order to determine if the direction of the buoyancy (positive or negative) created any significant changes to the characteristic shape of the jet cross section (16).

Although some of the results of this testing were consistent with the hypothesized outcomes, many of the tests indicated conclusions inconsistent with previous predictions. When tests were conducted with jet Froude numbers between 1.5 and 3, the resulting shape of the jet plume cross section was consistent with those found in a single plume of fluid ejecting vertically from the center of a jet. However, for tests conducted at Froude numbers less than unity, the jet distortion was significantly different. Instead of a single plume, two plumes seemed to emanate from both sides of the jet, eventually joining above it while suppressing flow from the center. This tendency was observed in both the positive and negative buoyant jet cross sections. Because it is observed in both buoyancies, the study suggests "the mechanism which determines the cross-sectional shape of the jet core is only mildly influenced by centripetal effects

brought about by streamline curvature (16)." The researchers go on to hypothesize for buoyant jets experiencing "sufficiently low" Froude numbers, the buoyant jet will significantly influence the upstream velocity field to the point that streamwise vorticity will begin upstream of the tube exit, which in due course effectively alters the form of the jet cross-section (16).

Although many studies and research efforts have focused on buoyant jets and their applications, none have characterized the combustion of horizontally issuing, laminar, buoyant jets. The investigation conducted by AFIT into the mixing of gas-phase horizontal laminar jets with positive and negative buoyancy using the filtered Rayleigh scattering, is perhaps the most relevant to this research. It provided a stepping stone of sorts, offering insights into the mixing characteristics of the different fluids. However, that particular investigation only focused on mixing and its properties of 'cold' gasses. The issue of combustion was not tested nor hypothesized about. Therefore, this research sought to answer those questions; what happens with 'hot' gasses and buoyant jets? This research effectively characterized the effects of introducing combustion into horizontally issuing, laminar, buoyant jets.

II.5. Combustion

Webster defines combustion as "rapid oxidation generating heat, or both light and heat; also, slow oxidation accompanied by relatively little heat and no light." For the purposes of this research the terms combustion and burning refer to the former part of the definition (rapid oxidation generating both heat and light). Combustion in its simplest form is a means for transforming energy stored in chemical bonds to a usable source of energy such as heat (26).

II.5.1. Flame Types

Combustion generally occurs in two forms, flame or nonflame mode, and can be further classified as premixed and nonpremixed (diffusion) flames. The differences between these two types of flames can be illustrated by the process occurring within a knocking spark-ignition engine as seen in Figure 4 (26).
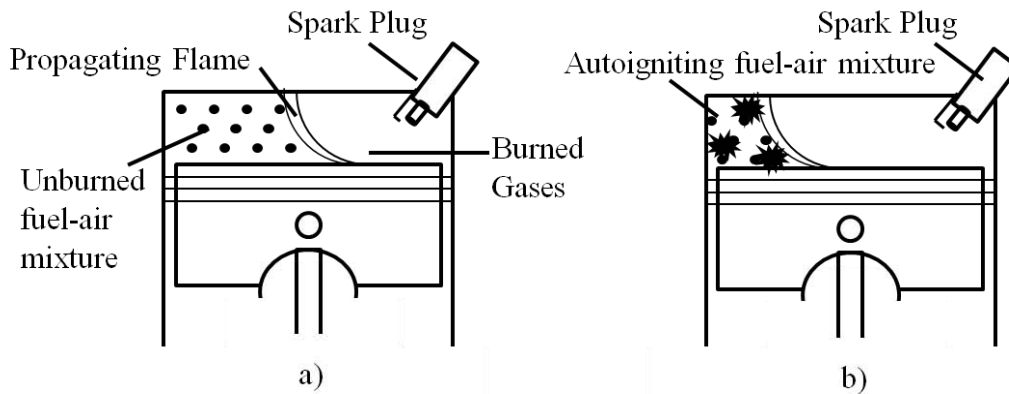

Figure 4. (a) Flame and (b) Nonflame Combustion in a Spark-Ignition Engine (26)

Figure 4a illustrates a narrow zone of severe chemical reactions as it propagates across the unburned fuel-air mixture. This narrow zone, or reaction zone, is generally referred to as the flame. As the flame propagates it leaves a wake of hot combustion products and causes the temperature and pressure of the unburned fuel-air mixture to rise. Under some conditions, like those seen in Figure 4b oxidation may occur rapidly at numerous locations within the unburned fuel-air mixture resulting in rapid combustion throughout the volume. This rapid combustion of fuel occurring before the propagation flame results in volumetric heat release known as autoignition, and the dramatic pressure rise causing the sound of engine knock. The presence of knocking in an engine is undesirable; in an ideal engine, the flame would propagate across the unburned fuel-air mixture and achieve

complete combustion before an autoignition occurs (26). In this research, all of the flames were flames, instead of nonflames.

As their names imply, the two classification of flames, premixed and nonpremixed (diffusion), refer to the state of the reactants; specifically, how mixed they are. Flames that are mixed at the molecular level prior to any significant chemical reaction are known as premixed flames. An example of a premixed flame is the flame found in the cylinder of an internal combustion gasoline engine, common to most cars. Diffusion flames, on the other hand, result from flames in which the fuel and the oxidizer are initially separated, and the significant chemical reactions are only occurring at the interface between the two. With a diffusion flame the mixing and the reacting are occurring at the same location – the interface between oxidizer and fuel. A simple example of a diffusion flame is a candle. It is important to note that the term diffusion refers specifically to the molecular diffusion of the chemical species; fuel molecules will diffuse towards the flame from one direction while the oxidizer molecules will approach from a different one (26). In this research, all flames were diffusion flames.

II.5.2. Regions of the Flame

There are many potential configurations capable of producing laminar diffusion flames; however, this research focused on the case of a laminar jet of fluid (fuel) being ejected horizontally into an infinite reservoir of quiescent fluid (oxidizer). In order to better understand what the flame will look like, it is important to develop the state of the system prior to ignition as seen in Figure 5. Additionally, the following analysis is applicable to horizontal issuing jets where the densities of the fluids are approximately

28

the same (such as an ethylene jet ejecting into air) as well as vertical jets in which density of the fluids is a less significant factor.
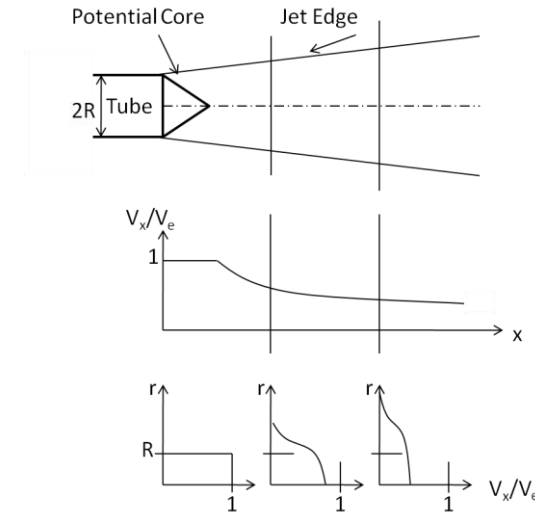

Figure 5. Laminar Fuel Jet Issuing into an Infinite Reservoir of Quiescent Air (26)

In order to ease analysis, it is assumed that the velocity profile at the exit of the tube is uniform. Immediately following the exit is the potential core region of the jet. In this region, viscous shear and diffusion effects are not felt; therefore, velocity and nozzle fluid mass fraction will remain unchanged (26).

In the region between the potential core and the outer edge of the jet both the velocity and fuel concentration decrease to zero at the edge of the jet. In the subsequent regions of the jet, those beyond the potential core, the effects of viscous shear and mass diffusion are felt. Even though viscous shear effects are not observed within the potential core of the jet, jet momentum is conserved throughout the entire flow field. As the jet of fuel is ejected into the surrounding oxidizer, the fuel captures and entrains the surrounding oxidizer and transfers some of its momentum. This transfer of momentum causes the jet to lose energy and decrease in velocity, while more and more oxidizer is

29

entrained into the jet as it proceeds downstream. The central graph of Figure 5 depicts this degradation of centerline velocity with distance while the bottom figures depicts the radial velocity decay from its maximum state at the centerline to zero at the edge of the jet (26).

The velocity field of the jet is controlled by the convection and diffusion of momentum while the fuel concentration is governed by the convection and diffusion of mass. Therefore, it is expected that fuel mass fraction is consistent with the dimensionless velocity distribution. As the jet progresses downstream the fuel molecules will diffuse radially outward as a result of the high concentration of fuel in the jet core. Additionally, transgressing downstream effectively allows more time for diffusion to occur. Thus, the width of the jet grows with axial distance while the centerline fuel concentration continually decays. Because the jet grows as it slow, the mass of the fluid issuing from the nozzle is conserved (26).

II.5.3. Laminar Diffusion Flames

Now that the isothermal fuel jet composition is understood, it will be much easier to understand what happens when the fuel is ignited. Figure 6 depicts the general composition of a laminar diffusion flame structure for a vertically issuing jet. Although the focus of this research is on horizontally issuing jets, it is important to first understand the simpler vertically issuing jet and its properties.
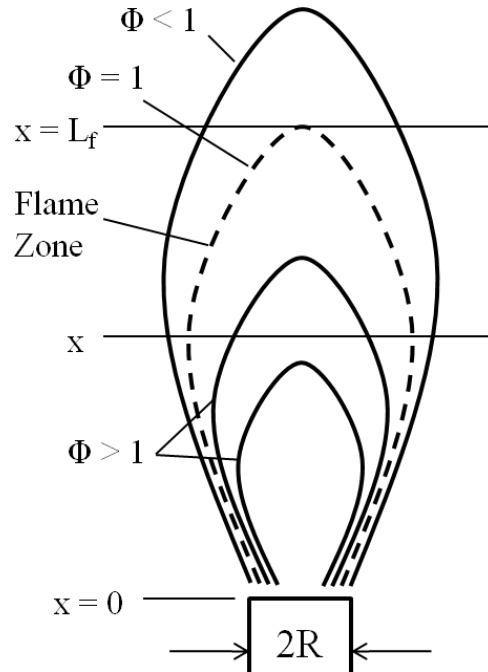
Figure 6. Laminar Diffusion Flame Structure (26)

Similar to the un-ignited fuel jet, the burning fuel jet will diffuse radially outward as it travels axially while the oxidizer will diffuse radially inward. The region where the diffusing fuel and oxidizer combine in stoichiometric proportions is nominally defined as the flame surface. The flame surface is also often referred to as the area experiencing an equivalence ratio of unity. The flame surface is the region of the jet where combustion is taking place. As it combusts the fuel and oxidizer combine to form new products (often referred to as products of combustion) which will diffuse radially both inward and outward. For flames existing in areas where there is significantly more oxygen present than necessary for combustion to occur continuously, such as this research, the flame length L_f can be determined by finding the axial region of the flame where the equivalence ratio, Φ, is equal to one and the flame radius, r, is equal to zero (26).

With respect to the general appearance of the flame, the actual region where chemical reactions are occurring is rather narrow. Typically, the high temperature reaction zones will resemble an annular shape up to the flame tip. With respect to a vertically issuing flame, the upper regions contain significant amounts of hot gasses, such that buoyant forces become a factor. These buoyancy forces will cause the flow to accelerate and thus form a narrower flame as a result of the conservation of mass which requires the streamlines of the nozzle or cone to compress or become closer together when the velocity increases. Conversely, however, as the flame accelerates and narrows the fuel concentration gradients will increase leading to an increase in diffusion. Generally, both of these phenomena are present in flames issuing vertically from a circular port. Since their effects counteract each other, most theories are able to neglect buoyancy while still accurately predicting flame characteristics. In this research, however, the buoyancy forces could not be neglected due to the low Reynolds and Froude number tests being conducted. In fact, understanding the impacts of the buoyancy forces will be the key for effectively predicting and characterizing these flows. It is also important to note that even though laminar jets were produced, the addition of combustion causes the jet to become turbulent at some point simply due to the large density changes resulting from combustion (26).

II.5.4. Flame Characterization

Flames can be characterized in large number of ways ranging from temperature to density gradients to mean centerline trajectory. Unfortunately, the flames tested in this research cannot be characterized in all possible ways due to equipment and time restraints. Therefore, this research focused on defining the flames with three measures:

spreading or growth rate, trajectory, and concentration gradients. Because
characterizations such concentration gradients will change with different axial positions
of the flame, measurements will be taken at numerous different axially locations.

II.5.4.1. Spreading Rate/Spreading Angle

A primary parameter used frequently to characterize jets is the spreading rate.
Often associated with the spreading rate is the jet spreading angle, α. In order to define
and understand both of these parameters it is first necessary to introduce the idea of jet
half-width, $r_{1/2}$. Jet half-width is defined as the radius of the jet corresponding to the
radial location where the jet velocity has decreased to half of its centerline value as seen
in Figure 7 which depicts definitions of both spreading angle and jet half width.
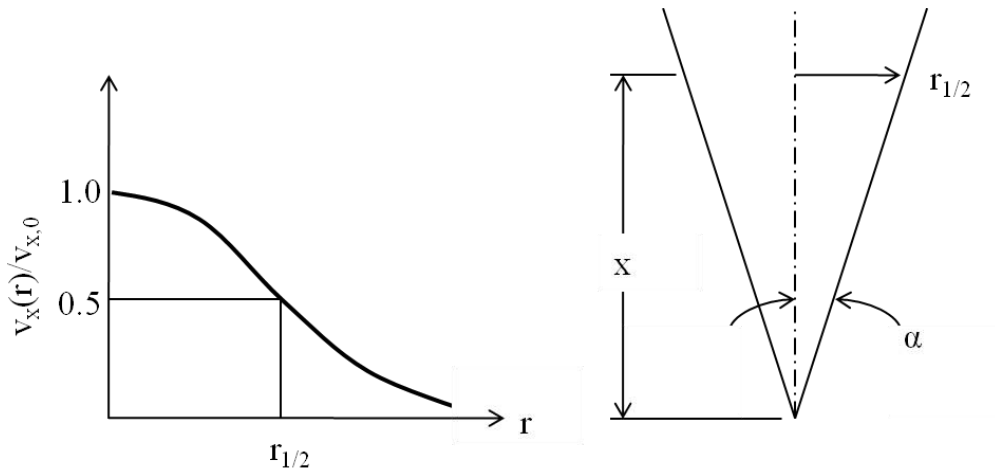
Figure 7. Definitions of Jet Half-Width, $r_{1/2}$, and Jet Spreading Angle, α (26)

The jet spreading rate is defined as the ratio of jet half-width to the axial distance x, while
the spreading angle is the angle whose tangent is the spreading rate. Both of these
physical parameters are defined as follows (26):

$$r_{1/2}/x = 2.97 \left(\frac{\mu}{\rho v_e R}\right) = 2.97 Re_j^{-1} \tag{7}$$

$$\alpha = tan^{-1}\left(r_{1/2}/x\right) \tag{8}$$

where v_e is the jet exit velocity and R is the universal gas constant. Evaluation of the two previous equations shows that jets characterized by high Reynolds numbers are narrow, while jets resulting from low Reynolds number flow diffuse radially quicker and thus are wider (26).

II.5.4.2. Trajectory

As the name implies, the trajectory of the jet is simply the path which it takes after leaving the nozzle of the tube. In this research the bottom edge trajectory was tracked in three different ways. Because the presence of combustion, in jets that would otherwise be laminar, causes turbulence in this experiment, numerous jet trajectories were found and then averaged to find the normal behavior of the jet. It is also important to note the jet trajectories were all normalized based on the exit diameter of the tube used in the respective test case.

II.5.4.3. Concentration Gradients

In this research OH concentrations were tracked using PLIF techniques. Tracking where the OH appears and in what quantity provides insights into where the chemical reactions are occurring. The OH concentration gradients can help show how the jets are diffusing and where the air is being entrained.

II.5.5. Research Related to Buoyancy and Flames

When it comes to research related to buoyant jets, there is no shortage. However, studies focused on horizontally issuing buoyant jets are somewhat rare, and studies which deal with reacting horizontally issuing buoyant jets are even less prevalent.

II.5.5.1. Vertically Issuing Buoyant Jet Flames

One study conducted by Kolhe and Agrawal in 2007 investigated the effects of buoyancy on instabilities and structure of transitional gas jet diffusion flames. Although this study was focused on the effects in the transitional flame region, parallels can be and were drawn to the effects present in the laminar region and the turbulent region because transitional jet diffusion flame dynamics identify the link between laminar and turbulent flames. While focusing on isolating the buoyancy effects of the flame, instabilities and their influence on the flow structure was examined. The flames being tested were hydrogen flames with Reynolds numbers of up to 2200 and an average jet velocity of 54 m/s. Transitional flow was achieved by taking advantage of the hydrodynamic instabilities in the shear layer of the jet fuel. In essence, the laminar flow present at the nozzle of the jet quickly transfers into the transitional regime as a result of shear forces acting on the flow. In order to capture and visualize the flow instabilities, a rainbow schlieren deflectometry technique was implemented in conjunction with a high speed imaging system. Ultimately, the flame structure and instabilities are identified, explained, and compared against those present in the laminar and turbulent flames (27).

From their experiment, Kohle and Agrawal drew five main conclusions. First, they observed large scale, vortical structures on the outer surface of the flame with features similar to those known to be present in flickering laminar flames. These vortices

were the result of buoyancy induced instability between the surface of the flame and the surrounding air. The outer vortices also appeared to "squeeze" then expand the flame surface in a cyclical fashion. As the Reynolds number increased, the flame oscillation amplitude observed decreased (27).

Second, a small scale instability was observed in the shear layer between the outer vortices and the flame surface. This instability was created by variable Coriolis forces in the stratified region of the flame experiencing local acceleration along a curved path. This instability, more appropriately named the baroclinic instability, resulted in "small-scale roll-up" vortices. Again these features of the transitional flame remarkably resemble those observed in flickering laminar jet diffusion flames (27).

Third, in addition to the instabilities present in the shear layer, the fuel jet also oscillated. Kohle and Agrawal observed low frequency periodic oscillations in the fuel jet which were in phase with the periodic squeezing and expanding of the flame surface by the larger, outer vortices (27).

Fourth, they concluded the intermittency observed in the breakdown point of the flame was the direct result of the periodic squeezing and relaxing of the flame surface. Interestingly, they found flames with higher Reynolds numbers breakdown at approximately the same fixed axially location. They concluded this was the result of a reduction in oscillation amplitude of the flame surface due to the higher momentum flow (27).

Finally, in the turbulent region of the flame (downstream of the transition region), the outermost vortices are stretched, but maintain their coherence for "some distance." More interesting, however, was the fact that the turbulent flame and fuel jet both

continued to experience periodic oscillations at a frequency consistent with that of the stretched outer vortices (27).

Although these results are applicable to the transition region of a vertically issuing buoyant flame, many parallels were found to the laminar and turbulent regions of the flame. Kohle and Agrawal's research is similar to this research, in which a laminar horizontally issuing buoyant jet was studied to gain insight into the turbulent region (most prevalent type of flame in the UCC).

II.5.5.2. Horizontally Issuing Buoyant Jet Flames

Similar to buoyant flows not involving combustion, most research involving combustion and buoyant jets is related to vertically issuing buoyant jets and their applications. However, some studies were conducted on horizontally issuing jets. One such study, conducted by Escudier, observed and analyzed inclined turbulent flame plumes. The study analyzed jets expelling plumes at angles ranging from, and including, vertical to horizontal. More specifically, a quasi one-dimensional analysis based upon the entrainment concept was first conducted and the results were then compared against those inferred from shadow and direct photographs of ethane flame plumes. The focus of the research was to gain understanding of the aerodynamics of turbulent jets composed of pure gaseous fuel and burning in stagnant air (28).

Using the quasi-one-dimensional approach the researchers were able to calculate the turbulent shear flows. By using the Emmons and Ying model these calculations were used to further calculate and predict plume parameters such as trajectory, local bulk properties, velocity, density, fuel concentrations, and plume radius. After the predictions were made burning ethane diffusion flames were created at room conditions. Shadow

photographs were then taken of numerous plumes with varying nozzle sizes, angles of inclination, and jet velocities (28).

Finally, the researchers took multiple sets of plume boundaries and trajectories created through the Emmons and Ying model and overlaid plots of points which represented the mean plume boundaries found in the shadow photographs. Surprisingly, they found a high level of agreement between the two methods for a large range of flow conditions. Therefore, they concluded the physics of turbulent flame plume dynamics is captured within the Emmons and Ying model. This experiment acted as a stepping stone which illustrated the fact that even something as seemingly random as a flame can be predicted and visualized through the use of sophisticated analysis tools (28).

II.6. Laser Diagnostic System and Techniques

Traditionally, combustion diagnostics is performed in two ways – sampling or probing. The most common method used is sampling. This method entails gathering a sample of the combustible gas and performing an analysis upon it. Although it is the most common method, it also has shortfalls. Mainly, it is difficult to achieve time accurate results because the combustion process continues to occur even after the sample is removed. The molecules will continue to interact with each other through a series of chemical reactions causing the composition of the sample to change between the time it is removed from the sample and the time it is analyzed. Additionally, in order to achieve accurate, reliable, and repeatable results, the sample requires precise temperature controls which are often hard to achieve. Ultimately, this method was not used.

The second method often used is probing. Probing entails placing probe, physical or not, into the flame in order to characterize it. Often a thermocouple or other physical

temperature measuring device is used with this diagnostic system. The biggest problem with this method is that when the physical probe is placed into the flame, it acts as an intrusion. When any intrusion (in this case the probe) is placed into the path of the flame, the flame becomes disrupted, changing the dynamics of combustion. This ultimately results in gathering inaccurate data about the true nature of the flame, which defeats the purpose of using a probe in the first place, with respect to this research.

A third, less traditional, method is laser based diagnostics. Due to their non-intrusive nature, laser diagnostic systems can be used to capture the events occurring within a combustion field. Often, in cases where high temperatures will melt or disable a traditional probe or thermocouple, or the flame dynamics of interest are at risk of being altered and disrupted by the analysis method, optical analysis is used (5). Accurate combustion diagnostics is achievable through the use of laser spectroscopic methods. Laser spectroscopic techniques are capable of providing real time information about the flame as well as the combustion process. It offers a non-intrusive method, resulting in more accurate flame data. Finally, it also has higher resolution capabilities (29). For this research, laser based diagnostic techniques were used because of all the advantages aforementioned. Although there are many different types, this research will focus on the Planar Laser-Induced Florescence, or PLIF.

II.6.1. Planar Laser-Induced Florescence (PLIF)

PLIF, sometimes referred to as Laser-Induced Fluorescence (LIF), is a particular laser based diagnostic method which uses a two-dimensional imaging technique for combustion diagnostics. PLIF works by using a laser travelling through a region of interest (ROI) to introduce a plane of light. It functionally operates on the principles of

molecular absorption and energy emission in the form of light at high energy levels. Specifically, as a molecule absorbs a photon, its electrons become excited causing it to move to a state of higher energy. Almost immediately following this excitation, the molecule will release energy in the form of photons because the molecule always wants to be at its ground or stable state configuration. This photon release is referred to as fluorescence. Fluorescent absorption is the concept that when light of a specific wavelength is introduced and interacts with a molecule, the resulting fluorescence will occur at a different wavelength. These basic principles form the foundation for PLIF. With relation to combustion, PLIF is most often used for calculating the concentrations of different species present as well as the temperature gradients through the flame(5).

II.6.1.1. Mechanics of PLIF

Conservation of energy is the driving concept behind the mechanics of fluorescence. Simply put, it is the light emission resulting from energy absorption (30). With relation to PLIF, a laser is used in order to excite a molecule to a state of higher energy. As previously mentioned, molecules do not like to remain at excited energy levels; therefore, in order to return to a state of lower energy, it relaxes and emits some sort of energy. Most often, this energy emitted is in the form of light. The light emitted from the molecule, or fluorescence, creates a unique fluorescent signal which is detected by a camera and used to produce an image of the ROI. How strong the fluorescent signal is, is directly related to the concentration of the emitting species (30). A stronger fluorescent signal means a larger concentration of the emitting species. The fluorescence phenomenon can be seen in Figure 8a where the photon being absorbed is depicted by an arrow pointing upwards to represent the energy being absorbed and moving to state of

higher energy, and then a subsequent arrow pointing downwards representing the release of energy (in the form of light) and a return to a state of lower energy. With PLIF, absorption occurs at distinct wavelengths while the emissions occur span a multitude of wavelengths, as depicted in Figure 8b.
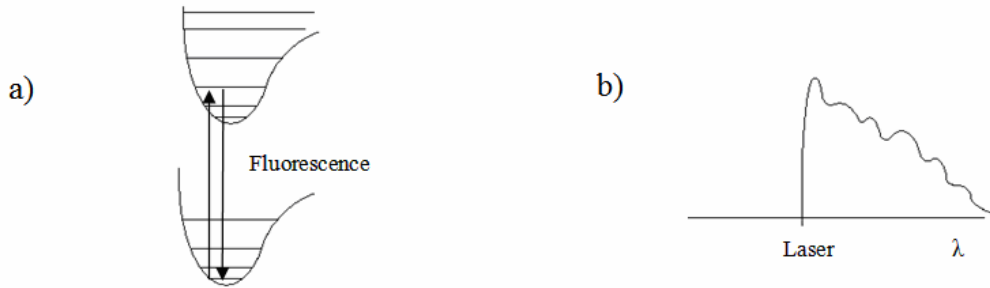
Figure 8. a) Fluorescent absorption and emission b) Emission spectra (30)

PLIF is capable of detecting concentrations for numerous different molecules within the combustion region. In the combustion region, almost all electron energy radiation occurs in the visible light spectral range. Additionally, nearly all important molecules and radicals in a combustion region containing H, O, C, N and S are detectable through PLIF techniques (30). Each molecule contains its own discrete band of spectral absorption; therefore, each molecule will only absorb photons of a specific wavelength. Table 1 provides a list of the species commonly detected by PLIF techniques and the range of electronic transitions that correlates to each molecule. Generally, the fluorescence wavelength resulting from an incident excitation is longer than the excitation wavelength (29).

Table 1. Range of Electronic Transition for Selected Molecules (30)

Molecule	Electronic Transition (nm)
C_2	400-600
	230-330
CH Radical	500-430
	450-360
CO	200-250
	120-240
N_2	100-500
	Vac u.v.
NO	195-340
	200-500
O_2	500-900
	170-220
OH Radical	240-400
CH_4	145-500
C_2H_2	210-237
CO_2	140-170
H_2O	145-186

It is important to note electron transition is not occurring over the entire region listed in the above table; rather, transition occurs at a few discrete wavelengths within the range provided. Therefore, it is important to know the discrete absorption wavelengths for the molecule of interest in any PLIF experiment. In this research LIFBASE was used in order to determine these values. LIFBASE is a free, and readily available, database system which is used to simulate the electronic transitions for diatomic and other molecules. It has the capacity to simulate absorption and emission, as well as calculating the collisional and Doppler broadening correction factors (31). The collisional correction factor is needed to correct for pressure effects while the Doppler broadening factor corrects for temperature effects (5). For the purposes of this experiment, these errors were considered to be insignificant, and consequently, not corrected for.

II.6.2. Detection of the OH Radical

In combustion related research, the molecule most commonly detected by PLIF techniques is the hydroxyl (OH) radical. The OH radical is a good candidate for detection because it is a radical produced during the intermediate reactions of combustion, but destroyed by the completion of the combustion process. Therefore, the OH radical is found in high concentrations within most flames, but not often in the surrounding environment, which helps to avoid clutter and can increase resolution. Because the OH radical is most often measured it has undergone extensive research and, subsequently, its spectroscopy is well documented (30). Additionally, the OH molecule is an excellent indicator towards the true behavior of the flame and can help reveal and provide critical information on flame mixing, propagation, ignition, structure, and local extinction (30). OH PLIF offers a vast range of implementations and utilizations such as acting as a flame marker for flame location studies, flame temperature gradient measurements, and determining the OH species concentration (31).

Detection of OH can also be used for determining the flame temperature. Fluorescent intensity of a species' photon emissions can be approximated with a linear relationship to its concentration. More specifically, areas which contain higher concentrations of OH, consequently, maintain higher temperatures. The fluorescence signal, or light intensity, within the ROI can be determined through the implementation of cameras specifically designed and spectrally filtered to detect OH emissions. Ultimately, the vast abundance of OH molecules present in combustion processes coupled with its relatively long fluorescence time, between 10^{-5} and 10^{-10} seconds, make OH the best option for PLIF studies related to high temperature combustion (30).

II.6.2.1. OH PLIF Thermometry

When evaluating combustion dynamics, OH PLIF thermometry is used to offer

insight in regions containing unburned areas, or pockets, of gas and to indicate or

determine the temperature gradient through the ROI (32). OH PLIF is able to provide this

information through the use of the OH (A-X) electronic transition system. As seen in

Figure 9, the (A-X) term is used to designate the energy states manipulated by the

incident laser sheet.
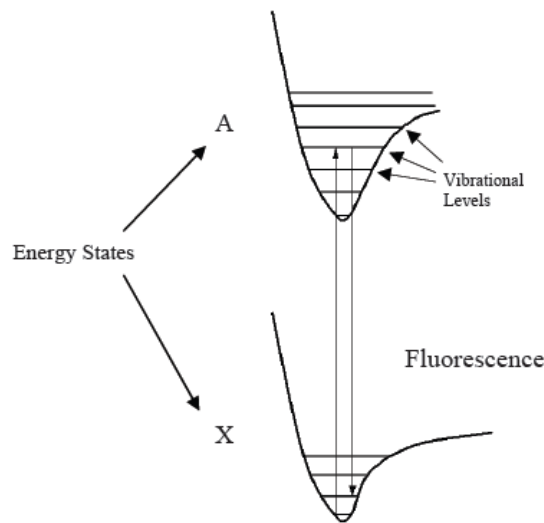
Figure 9. The X and A Energy States (29)

This figure depicts the X energy state as OH molecule electrons in their ground

state configuration, while the vertical arrow pointing upwards corresponds to their

excitation to a state of higher energy. One interesting concept not conveyed in Figure 9

are the rotational states occurring within each vibrational level (29). These rotational

states are used to further identify the electrons condition. More importantly, these states

correspond to the level at which the PLIF system excites the subject (OH) molecules.

Figure 10 provides a better representation of the numerous rotational states occurring at

each vibrational level, including the multiple variations of rotation within the states.

Rotational states are depicted by a letter and number combination followed by a specific variation in parentheses, such as $P_1(7)$. Each of these states can be excited through the use of unique wavelengths of incident light, and are most often referred hereafter to as "lines" (29). For the purposes of this research, the $Q_1(6)$ rotational state was excited, which corresponds to an excitement wavelength of 282.9 nm.
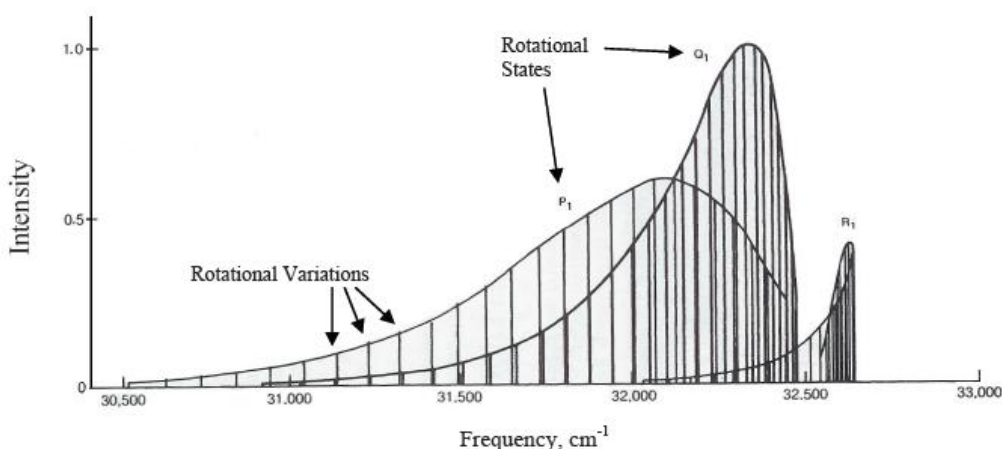
Figure 10. An Example of the Rotational Structure of a Vibrational Level (29)

In order to determine flame temperatures, two methods are most often used. The first method requires the examination of fluorescent intensity ratios resulting from excitation produced from two different wavelengths of light. The two wavelengths chosen are generally referred to as "line pairs," and are specifically chosen based on their sensitivity to temperature and wavelength proximities. When choosing a line pair, it is important to choose one line which is relatively insensitive to temperature and another which varies significantly with temperature. In order to determine temperature, the resulting fluorescent intensities can be correlated and compared with theoretical data available in LIFBASE (31). Several studies conducted produced temperature

45

measurement errors as low as 7%, which is considered good in areas of high temperature combustion, for this technique (31).

The second option for this research is called an excitation scan. The first step in this method is to choose a line of interest from LIFBASE. Once the line is chosen, the incident laser must progress in small increments through a range of wavelengths from just below and above the peak (31). The resulting fluorescent intensities reveal the "shape" of the line which plotted against wavelength. Because line shape is also a function of temperature, LIFBASE can again be used to correlate and compare the findings in order to determine the flame temperature (31).

Although this method is capable of determining flame temperatures with simply one laser, three correction factors must be implemented in order to achieve accurate results. The first error which needs correction is the result of laser, or line broadening. When a laser is tuned to a specific wavelength, it is actually emitting a minute range of wavelengths know as the "line width," despite the fact that a single number is displayed (29). As a result, the resolution and consequently the accuracy with which the OH line shape can be determined is limited.

The second correct factor which must be accounted for is the result of Doppler broadening. Doppler broadening, a function of temperature, is the result of the fluorescent emitting molecules moving about. According to the Doppler principles, when a molecule is traveling towards the collection device, a camera in this case, the molecule will seem to emit at a higher frequency, while the molecules traveling away from the device will yield appear to emit at a lower frequency (29). This result is similar to the sound received by an ear as an ambulance, with its siren on, passes from one side to

another. As a result of Doppler shift, the range of frequencies captured is generally wider than what is actually being emitted.

The third type of error is the result of collisional or pressure broadening. Collisional broadening is the result of molecules colliding with each other as they are acted upon by the incident laser. Collisions often interact with both the absorption and the fluorescent emission processes, resulting in errors (29). Correction for all three of these errors is necessary for more accurate temperature calculations. Fortunately, line broadening can be measured experimentally and, through the use of LIFBASE, Doppler broadening can be calculated based upon the anticipated temperatures. Finally, the collision broadening can be empirically determined. However, due to their minimal errors, corrections were not performed in this study.

With the excitation thermometry technique, the ultimate goal is to produce an accurate line shape which can be compared to information in the LIFBASE database in order to determine flame temperature. Most previous studies implementing this technique have used the full-width, half-maximum (FWHM) values of recorded line shape to determine a temperature. The FWHM is the width of the line (in wavelength) at half of its peak intensity value. Figure 11, generated in LIFBASE provides a representation for the physical meaning of this value.
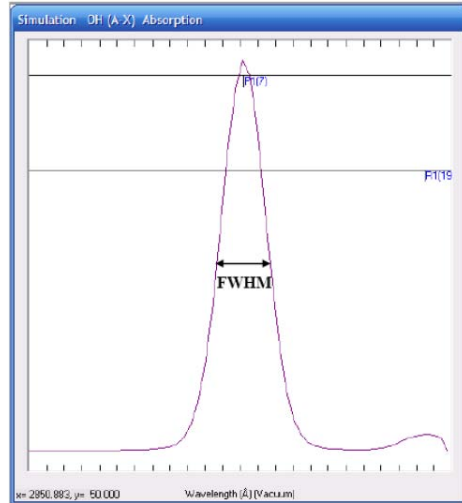
Figure 11. Illustration of the FWHM Method for Excitation Scan Analysis (31)

The FWHM provides a relatively simple way to consistently characterize the line width. Since this value is temperature dependent, it can be compared against the LIFBASE database to accurately determine temperature.

Both of these two methods, ratio of intensity and line scan, have been successfully implemented in AFIT's Combustion Optimization and Analysis Laser (COAL) lab. Unfortunately, however, the ratio of intensity thermometry method implements a two line system, which essentially requires the use of two lasers in situations where the flame is not steady. Therefore, this method cannot be used due to the limitations of one laser within the lab and the expected unsteady flame resulting from the buoyant mixing and combustion. Originally, an excitation scan was intended; however, due equipment malfunction, this was not achieved.

II.6.3. Quenching

While trying to calculate flame temperatures and concentrations from a fluorescent signal, the most important quantity is fluorescent quantum yield (30).

Unfortunately, the fluorescent signal strength, or yield, is most often adversely affected by quenching. Quenching is when the molecule of interest, OH in this research, fails to emit a fluorescent signal when it moves from a state of higher to lower energy. More specifically, quenching is when the molecule of interest is depopulated from its excited energy state without a fluorescent emission. Generally speaking, quenching prevents the release of a fluorescent signal in one of three different ways. When quenching occurs, molecules excited to a higher energy state release their energy through either dissociation, transfer of energy internally or externally to another molecule, or through general chemical reactions (31). In order to account for these three factors, analytical models, like the one published in Tamura et. al (33), must be used to incorporate quenching effects into the PLIF system results. Quenching, however, was not corrected for in this experiment.

III.   Test Setup

In order to accurately measure the OH concentration, with the goal of successfully discerning the behavior of reacting buoyant jets, a complex experimental setup with many diverse components was required. The arrangement consisted of a buoyant jet apparatus, a laser diagnostic system, and a camera system. These three systems working in conjunction allowed for the accurate measurement of OH concentrations within various buoyant jets. In order to ensure experimental consistency, the entire system was mounted on stationary optical tables within the AFIT COAL laboratory. Figure 12 provides an overall schematic of the test setup and the following sections will discuss in detail each of the main components.
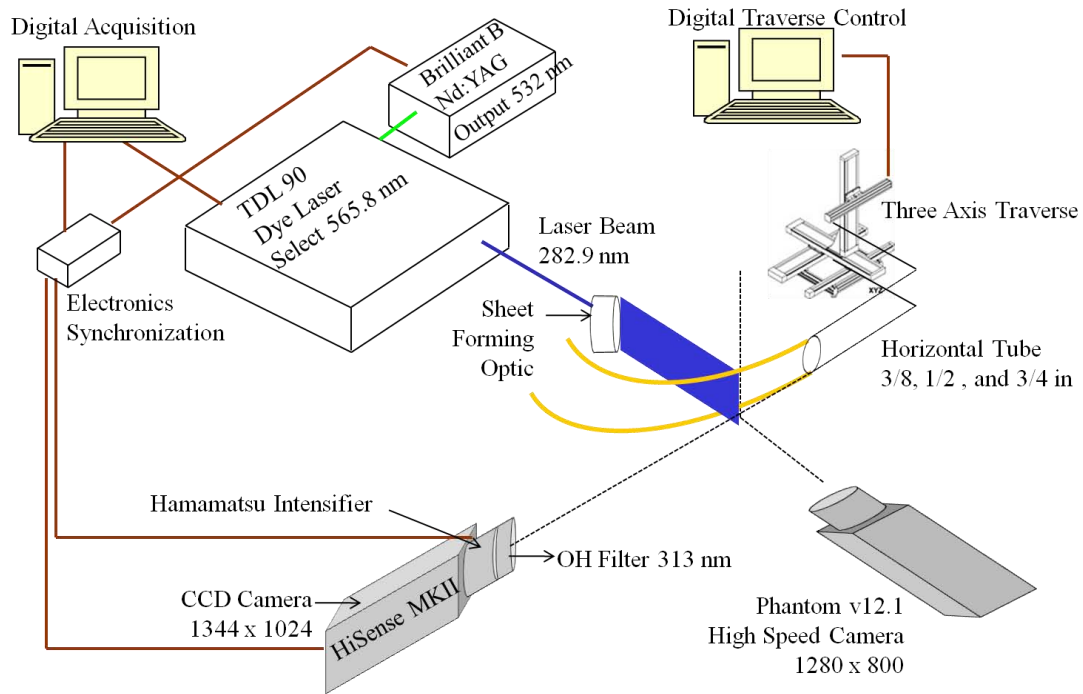
Figure 12. Test Setup Schematic

III.1. Laser Diagnostic System

Perhaps the most tedious part of the experimental setup was the alignment and setup of the laser system. In order to conduct PLIF research in combustion applications, it was necessary to have a laser producing a beam capable of exciting the molecule of interest, for the current research, this was the OH radical.

III.1.1. Nd:YAG Laser

The heart of the laser system was the Brilliant B pulsed neodymium-doped yttrium aluminum garnet (Nd:YAG) laser made by Quantel, and can be seen in Figure 13. This laser operates at 10 Hz, emitting a pulse every 100 ms. Figure 14 shows the power supply and cooling group cabinet required to operate the Brilliant B. The power supply, in addition to energizing the optical head, also provides all the logical functions necessary to operate the laser, and the cooling capability to dissipate the heat generated in the optical head by the operation of the flashlamp.

Figure 13. Brilliant B Laser and TDL 90 Dye Laser

The Brilliant B acts as a pump to provide an initial infrared beam to the rest of the laser system. Using a flashlamp, it was able to excite triply ionized neodymium doped garnet rods, which in turn release photons at 1064 nm. These photons are then amplified by forcing them to pass through the same medium several times. The optical cavity was composed of the medium and two mirrors on either end such that amplification will occur after the photons pass through the medium numerous times. After sufficient amplification, the laser emission was retrieved from the output of the cavity (resonator) by a mechanism known as Q-Switching. When the YAG pump laser was operated in a Q-Switched fashion, the laser emission was obtained by preventing light from continuing to pass through the cavity while suddenly enabling emission by altering the internal configuration (34). This control actuation was autonomous and controlled internally.

Figure 14. Power Supply and Cooling Group Unit

By implementing a Q-Switched YAG (pulsed) beam, the laser system was capable of producing a peak laser pulse power approximately 30,000 times greater than a free running laser, because the Q-Switched pulse duration was approximately 30,000 times shorter than free run mode (34). Having more peak power in the pulse becomes important when conducting combustion diagnostics, because it requires a relatively large amount of power to excite the OH radical.

III.1.1.1. Nd:YAG Laser Emission Characteristics

The Brilliant family of lasers are able to emit at 1064, 532, 355, 266, and 213 nm; however, for the purposes of this experiment, 532 nm emissions were used. When operating in Q-Switched mode, the Brilliant family of lasers emits laser pulses of approximately 4-6 ns. As a direct result of the short pulse time, the energy per pulse was on the order of 450 mJ per pulse, at 532 nm. The average laser power is the product of the energy per pulse and the repetition rate; therefore, at 10 Hz the Brilliant B average power was 4.5 W (34).

Figure 15 is a simplified illustration of the Nd:YAG type Q-Switched laser used in the current experiment. The cavity consisted of a cavity rear mirror with maximum reflectivity and the partially reflecting output mirror. The active medium was the aforementioned Nd:YAG rod optically pulse-pumped by a flashlamp. The other three main components; polarizer, quarter wave plate, and the electro-optical modulator, are all used to block and Q-Switch the laser emission. Once the laser emission was released from the cavity, it continues on to a tunable dye laser where it was further manipulated.
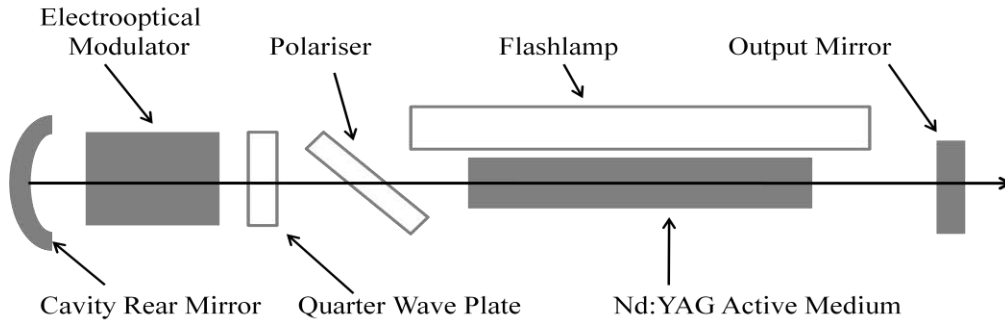
Figure 15. Simplified Diagram of a Nd:YAG Q-Switched Laser (34)

III.1.2. Tunable Dye Laser

After leaving the pump laser the pulses entered the main cavity of Quantel's Tunable Dye Laser (TDL) 90, which was comprised of numerous lenses, splitters, prisms, and three dye cells: one oscillator, and two amplifiers. Figure 16 provides an illustration of the optical layout in the main cavity of the TDL 90.
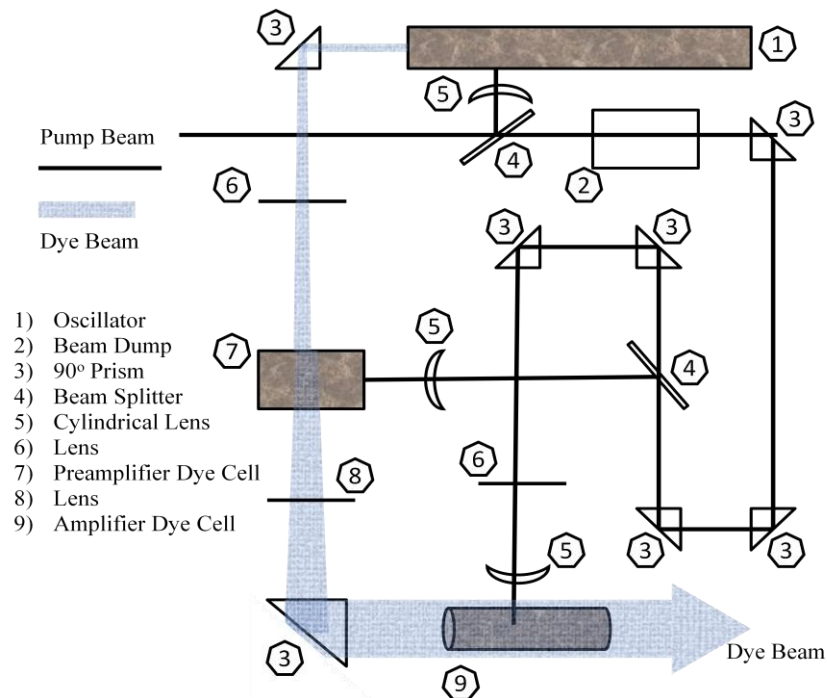
Figure 16. TDL 90 Optical Layout (35)

Perhaps the most important components of the TDL 90 are the oscillator and two amplifiers responsible for grating and amplifying, respectively. The Quantel design uses a high resolution grating in grazing incidence to tune over a wide range of wavelengths with a narrow line width. Simply put, the oscillator was used to select the specific wavelength of interest from the incoming laser pulse. For these experiments the wavelength of interest was 565.80590 nm, which corresponds to the $Q_1(6)$ rotation vibration transition. The dye cells located within the oscillator, as well as the preamplifier, are rectangular, while the dye cell in the main amplifier was a capillary cell; all cells were transversely pumped, meaning the dye was pumped transverse to the beam path.   By implementing both an amplifier and a pre-amplifier, the operator was able to optimize the amplification while still maintaining beam quality. The power from the incoming beam was split between these three main components. 10% of the total power was diverted to the oscillator, while 20% was diverted to the pre-amplifier, and 70% was used to pump the main amplifier.

The next mechanism the beam encountered before leaving the TDL 90 was a frequency doubling crystal, which effectively halves the wavelength to 282.90295 nm (visual to the operator as a blue hue when observed on a white business card). The frequency doubling crystal was located within a UVT-1 automatic tracking unit, through which both the residual dye beam and the generated UV beam exit. The UVT-1 doubling crystal assembly was mounted on a gear and was controlled by a computer capable of adjusting the prism to optimize the output power. After exiting the doubling crystal, the beam encountered a Pellin-Broca prism before finally exiting the TDL 90. Due to its unique shape, the prism acts as a sort of beam splitter by dispersing different wavelengths

in different directions, one of which was 90 degrees (perpendicular) to the incoming beam. By rotating the prism, the operator was capable of selecting and directing the wavelength of interest, which for this experiment was 282.9 nm.

III.1.3. Dye Pumps

Perhaps the most important parts of the dye laser, are the two dye pumps, shown in Figure 17. The oscillator and amplifiers depend on the dye being pumped transversely through the cells to perform their respective functions. The dye being used was a combination of methanol and Rhodamine 590 in an aqueous solution. By manipulating the concentration of the Rhodamine 590 and methanol solution being pumped into the oscillator and amplifier cells, the dye system allowed for the fine tuning of the output frequency for the entire system.
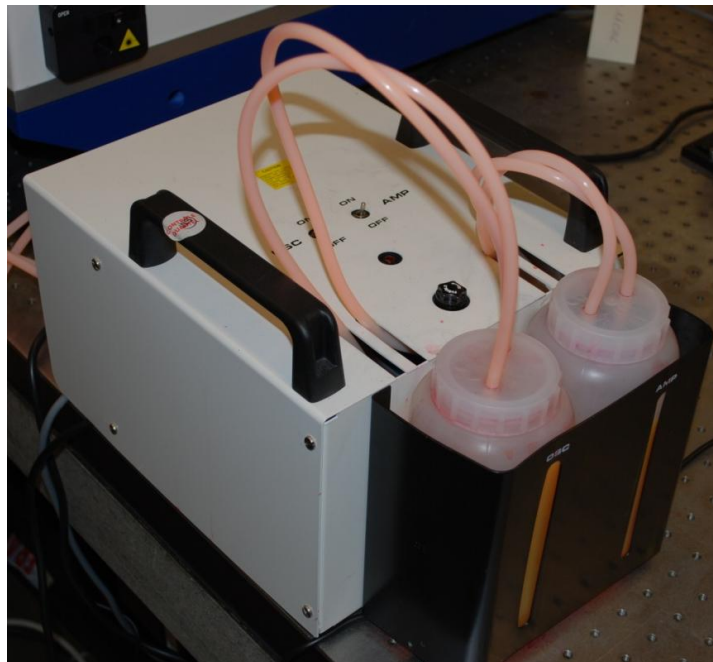
Figure 17. TDL 90 Dye Pumps

III.1.4. Sheet Forming Optical Assembly

Up to this point, the beam has been circular in cross section. However, since one of the goals of the experiment was to gather cross-sectional data of a reacting buoyant jet, it was necessary to change the cylindrical beam into a flat sheet. A sheet forming optical assembly was used to convert the beam exiting the TDL 90 to a 2 inch tall flat sheet, approximately 1 mm wide, and observed as a vertical blue line when a business card was placed perpendicular to the direction of travel of the beam. The sheet forming optical assembly can, seen in Figure 18, was produced by Dantec Dynamics. It works by using an internal series of lenses, both cylindrical and spherical to manipulate the beam.
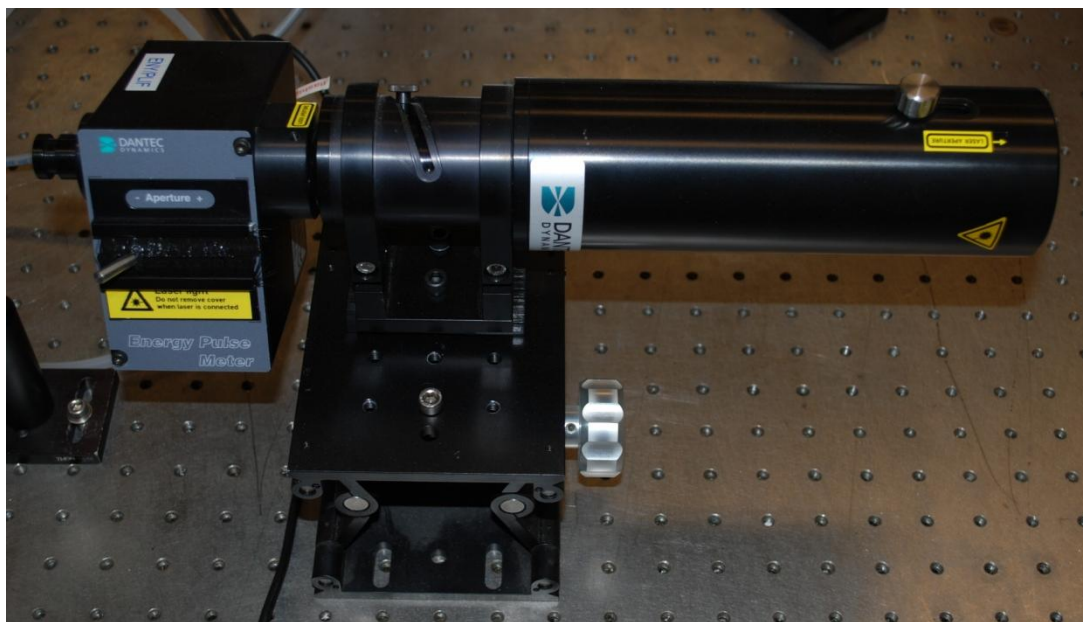
Figure 18. Laser Sheet Optic

III.2. Camera System

The three main components of the camera system are a camera, an intensifier, and a filter. All three components operate in conjunction with each other in order to capture the OH radical fluorescence event. In order to ensure the camera and intensifier are firing,

or opening their apertures, at the appropriate time, a timer box and pulse generator are also being used.

III.2.1. Camera

The most important aspect of this experiment was actually being able to capture the OH fluorescence. In order to achieve this, a HiSense MkII camera was used, as seen in Figure 19. This camera was an optimal choice for the experiment due to its high quantum efficiency, 72% at 532 nm, and relatively low background noise. The HiSense MkII camera uses a progressive scan interline charged-coupled device (CCD) chip, which includes an array of 1344 by 1024 light sensitive cells and an equal number of storage cells.
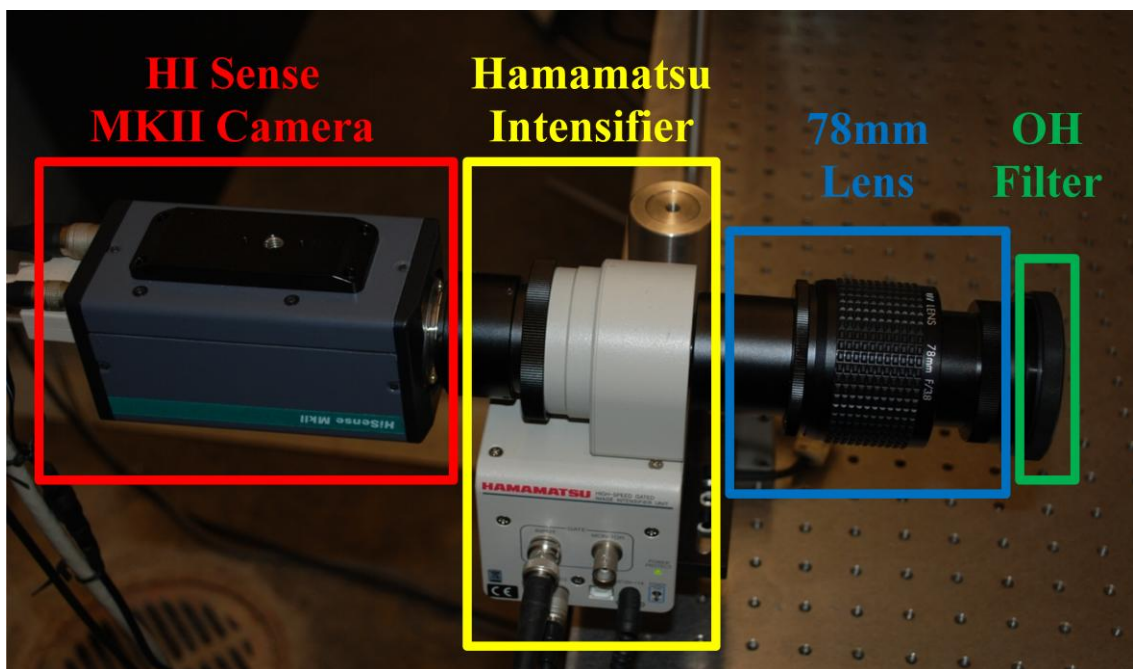
Figure 19. Camera and Intensifier Setup

The camera was operated in a cross-correlation mode, such that the first laser pulse exposes the CCD, and the impending charge was transferred immediately to the

storage cells. When the laser was fired a second time, the second frame was captured in the light sensitive cells. The first two frames were now captured in the storage cells and the light sensitive cells, respectively. Subsequent laser firing cause these two frames to be sequentially transferred to the camera's digital outputs for acquisition and processing.

III.2.2. Intensifier

With the exception of the camera, the intensifier was the most important component of the intensified CCD camera. In this setup, the intensifier was located directly in front of the camera, as seen in Figure 19. As the name implies, the purpose of an intensifier was the multiplication of the incoming light photons. By acting as an amplifier for the camera, the intensifier allowed for an optimum adaptation of the ICCD camera to any specific application. In the current combustion experiment the camera was operated at relatively low frame rates. Although the frame rates were slow (10 Hz), the image quality was still reduced due to extremely low light conditions resulting from low intensity fluorescence events. Therefore, for the purposes of this experiment, a Hamamatsu Intensifier was used in order to amplify the OH emissions before they reach the camera.

III.2.3. Filter

In addition to the camera and intensifier, a filter was also used. It was important to use a filter when using an intensified camera to capture the OH fluorescence. The purpose of the filter was to block out unwanted intensities and background noise present in combustion diagnostics. Implementation of a band pass filter centered with a peak transmission of 59% at 313 nm, and a FWHM of the peak transmission of 25 nm. The

filter being used was mounted in a circular mount which was capable of screwing directly into the front of the intensifier.

III.2.4. Timing

One OH fluorescence event occurs on the order of nanoseconds. Therefore, it was crucial that the camera and intensifier timing was set up appropriately to capture the fluorescence. To assist with the intensifier timing, a Quantum Composers, model 9514, delay pulse generator was used, as seen in Figure 20. In its current configuration, the delay generator takes an incoming signal from the Quantel laser, temporarily pauses for 300 ns, and then sends a 300 ns pulse width trigger signal to the intensifier.

Figure 20. Quantum Composers 4 Channel Pulse Generator

By using a delay generator, the operator was capable of adjusting when the camera fires in relation to the laser pulse arriving at the area of interest. The width of the signal or pulse sent to the intensifier was also adjustable. This allows for manipulation of the intensifiers gating. With the 300 ns delay and pulse width, the intensifier was receiving an input signal approximately 125 ns before the incident laser sheet arrived. This allowed

for sufficient time for the intensifier to heat up, which takes approximately 100 ns. The gate then remained open for 175 ns after the laser sheet arrived.

III.3. Combustion Setup

In addition to the laser setup, there was also a combustion setup responsible for creating and maintaining the reacting buoyant jets. The combustion setup was comprised of four main components, the fuel, flow control, the tubing, and the traverse. The fuel flow control and tubing are used to manipulate jet parameters such as flow rate and exit velocity, which in turn determine important jet characteristics such as Reynolds number and Froude number. The traverse, on the other hand, was used merely to control the location of the jet with respect to the laser diagnostic system.

III.3.1. Fuels

For the purposes of this experiment both fuels were stored externally to AFIT's COAL lab. The ethylene (C_2H_4) was stored in gaseous form, while the propane (C_3H_8) was stored in liquid form. The propane, therefore, must be vaporized before being used for experimental purposes. In order to vaporize the propane Zimmer vaporizer made by Algas was used. Both fuels were at or above 99.9% purity and are fed into the COAL lab through copper tubing before being converted to polyethylene tubing. Implementation of the polyethylene tubing offers more options for lab layout and experimental setup due to its higher flexibility than its copper counterpart.

III.3.2. Flow Control

The fuel flow being used in all experiments was controlled by a MKS, model 247D, four channel readout control panel and a corresponding MKS thermal mass flow

controller. The MKS mass flow controller was capable of flowing 20 standard liters per minute (SLPM) of Nitrogen (N_2) gas. Before entering the flow controller, the fuel was sent through an inline filter to remove any remaining impurities down to 0.5 microns. Both the mass flow controller and the inline filter can be seen in Figure 21. The mass flow controller was connected to, and controlled by, the MKS control panel via a serial cable.
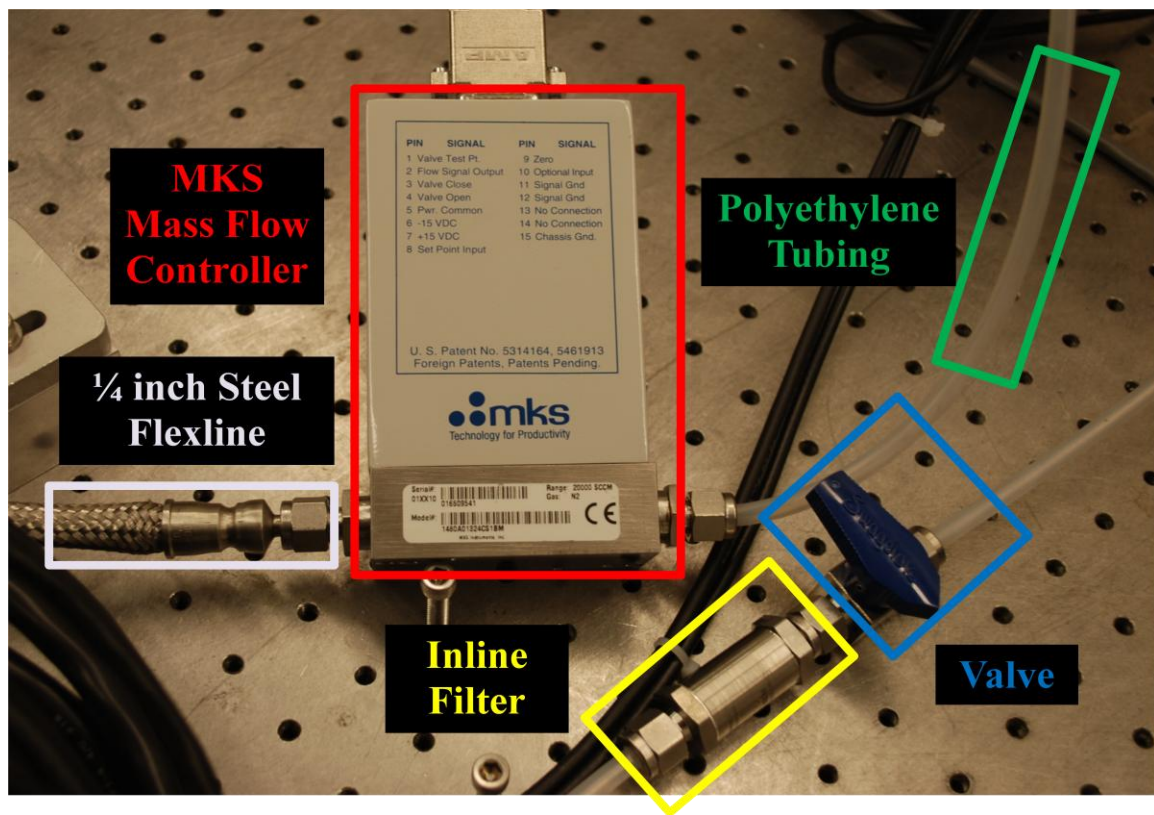
Figure 21. MKS Mass Flow Controller and Inline Filter

The MKS control panel, seen in Figure 22a, was capable of controlling up to four mass flow controllers at once; however, for the purposes of this experiment only one controller was being used for both fuels. Although only one mass flow controller was used, the channel to which it was connected was varied depending on the type of fuel being used. Because the mass flow controller was calibrated with Nitrogen, a scaled

correction factor (SCF) must be input into the MKS control panel for each fuel being

tested, as seen in Figure 22b. In order to ensure experimental repeatability, each of the

channels was assigned a different fuel and the corresponding SCF was locked in place.

Therefore, changing the fuel being used required simply connecting the mass flow

controller to a different channel.

a) Front   b) Back

Figure 22. MKS Flow Control Panel

The scaled correction factors being used for propane and ethylene were 72 and

146, respectively. Because both fuels used had different properties, inputting the scaled

correction factor ensured the digital read out on the front of the control panel was

accurate for the specific fuel being used. Additionally, the maximum flow capacity was

also different for every fuel. The maximum flow capacities for propane and ethylene

were 7.2 and 14.6 SLPM, respectively.

III.3.3. Tube Sizing

After leaving the mass flow controller, the fuel traveled through a ¼ inch (inner

diameter) steel flex-line hose. The flex-line was attached to a bulkhead, which was bolted

to an angle bracket, as depicted in Figure 23. By mounting the fuel line to a bulkhead,

quick changes in experimental setup were made simply by attaching a different tube to

the bulkhead. This also means that only one fuel line was required to both fuels.

Although only one fuel line was used, it is important to note that the fuel line was purged

with Nitrogen (N_2) when switching between fuel types.
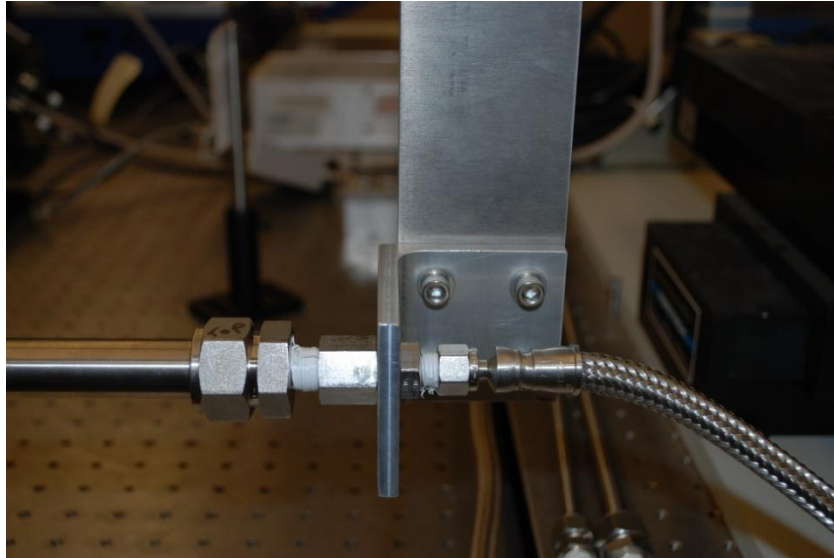
Figure 23. Bulkhead Assembly

Three different sizes of tubes were utilized during testing, with each tube

approximately 16 inches long, and attached to an adapter which allowed it to mount

directly to the bulkhead. The outer diameter (OD), inner diameter (ID), and length

normalized by the inner diameter for each of the three tubes can be seen in Table 2.

Having a tube length more than 25 times greater, than the inner diameter allowed for the

flow to straighten, become fully developed, and remain laminar before exiting the tube

into the combusting regime. This was important for experimental repeatability; although

exactly the same flame was never created, by holding the exit conditions constant a

baseline for comparison was achieved.

Table 2. Tube Sizes

Nominal Tube OD	Tube ID mm	Normalized Length
3/8 inch	7.75	52.4
1/2 inch	10.92	37.2
3/4 inch	15.75	25.8

Implementing three different tube diameters drastically increased the range of Froude and Reynolds numbers achievable per fuel, as well as simplifying the ability to compare different fuels. Using all three tubes (instead of just the 3/4 inch tube) increased the maximum Reynolds number achievable for propane from 2000 to 4000, as well as increasing the maximum Froude number from 2.5 to 14, while still maintaining laminar tube Reynolds and Froude numbers. Using three tubes also allowed for isolating one of the two jet characteristics being studied. Either Reynolds number could be held constant while Froude number was varied, or vice versa, for a given fuel.

III.3.4. Three Axis Traverse

The bulkhead assembly, angle bracket, and fuel lines are all mounted on a traverse as seen in Figure 24. Mounting the bulkhead on the traverse allowed for simplified and accurate manipulation of the jet. In order to maximize range of motion, minimize location error, and simplify experimental adjustments an Aerotech Automation 3200, three axis traverse was used. Each of the three axis was independently driven by Aerotech's Network Digital Drives(NDrive), as seen in Figure 24. All three drives are connected via IEEE-1394 (FireWire®).
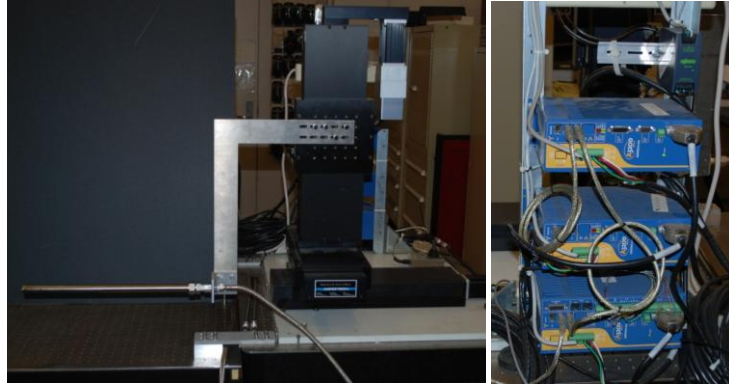
Figure 24. Three Axis Traverse Assembly and NDrive Motors

This allows for communication between drives and enables the drives to act independently or in unison. From the center position, the Aerotech traverse was capable of translating 150 mm in any direction. Manipulation of traverse location can be done in one of two ways, either via a joystick or through computer inputs. For the purposes of this experiment, the joystick was not used due to its lack of precision control. Through computer controls; however, the traverse was capable of precision on the order of micrometers (µm). Figure 25 depicts the traverse control interface.
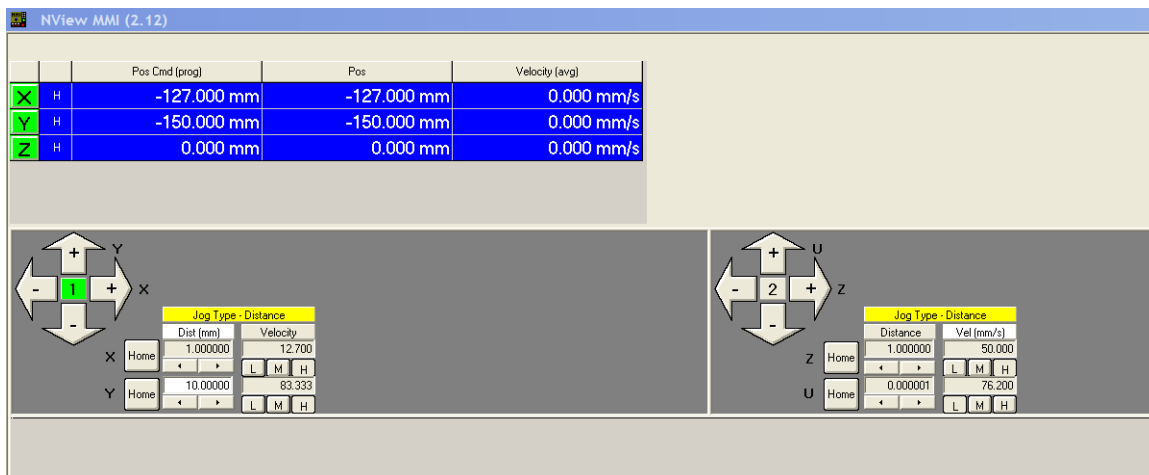
Figure 25. Traverse Control Interface

III.4. Data Acquisition

In order to accurately collect data all of the main components must work in unison. Therefore all of the main components of the system were interlinked to the main computer for control and synchronization, with the exception of the traverse, which has an independent control computer.

The first step of the data acquisition process was to place the tube in a predetermined location. For all the jets, the first data point was taken at the exit of the tube. This was achieved by placing the jet such that the laser sheet intersects the jet path just after the tube. Once the desired location was achieved, the fuel jet was ignited and acquisition was able to commence. Subsequent downstream data points were taken by simply moving the traverse aft.

Acquisition of data was managed via Dantec Dynamics Dynamic Studio software loaded on the main computer. Through this software, the computer was able to act as the master clock for the entire system by connecting all the components to a timing box. The timing box, seen in Figure 26, received timing signals from the computer, and sent consequent signals to the flashlamp, Q-switch, camera, and delay generator inputs. Successful implementation of the timing box was vital to the success of capturing the nanosecond OH fluorescence events. Figure 27 shows Dynamic Studio's user interface.

Figure 26. Dantec Dynamics Timing Box

67

Upon pressing acquire (highlighted in Figure 27) the system was setup to capture 200

images at the desired cross sectional location. Because the system was operating at 10

Hz, data was gathered at each location for 20 seconds. After the 200 images were

captured the system automatically stopped gathering data, and the traverse was moved to

the next location. This process was repeated approximately 10 times per flame, to

accurately capture the stream-wise variation within the flame. Figure 28provides a

sample image captured at the exit of the tube, where the yellow represents OH

fluorescence and the red indicates a lack of OH fluorescence. In order to gain an

understanding of the average location and behavior of the flame, the 200 images per test

location were averaged together. Figure 29 shows the mean image of a raw data set.
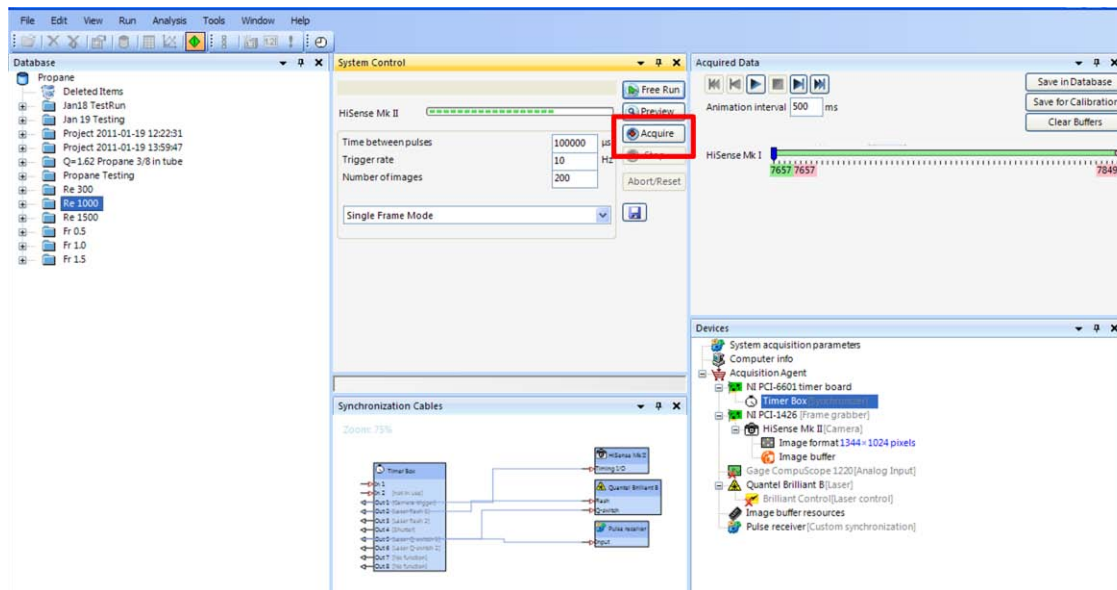
Figure 27. Dynamic Studio Interface
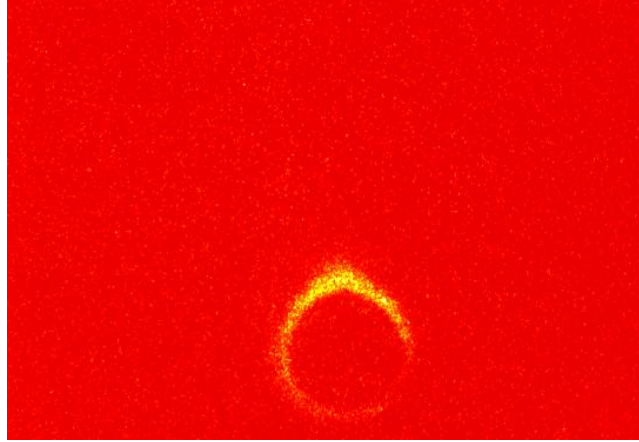
Figure 28. Sample Raw Image, Re = 1000, Propane, ½ inch Tube
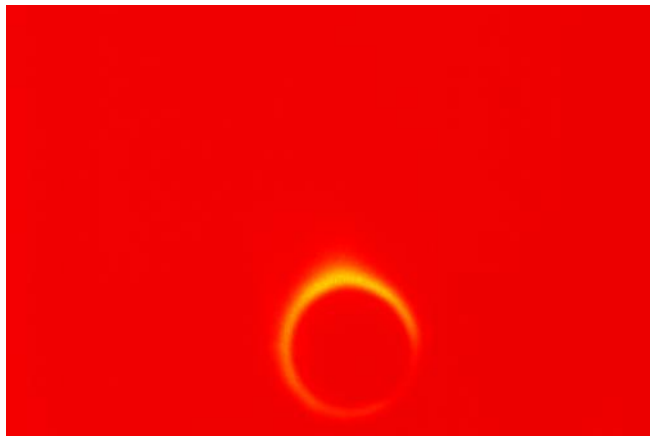
Figure 29. 200 Averaged Raw Images, Re = 1000, Propane, ½ inch Tube

In order to help eliminate the effects of background noise, 200 images were also taken without a combusting jet. These 200 images were averaged, and then subtracted from the averaged raw data. Figure 30 provides a visual representation of the resulting image. This image and the following downstream images were further manipulated to produce a three-dimensional mapping of the jet spreading, path and combustion, as seen in Figure 31.

Figure 30. Averaged Image with Background Noise Removed
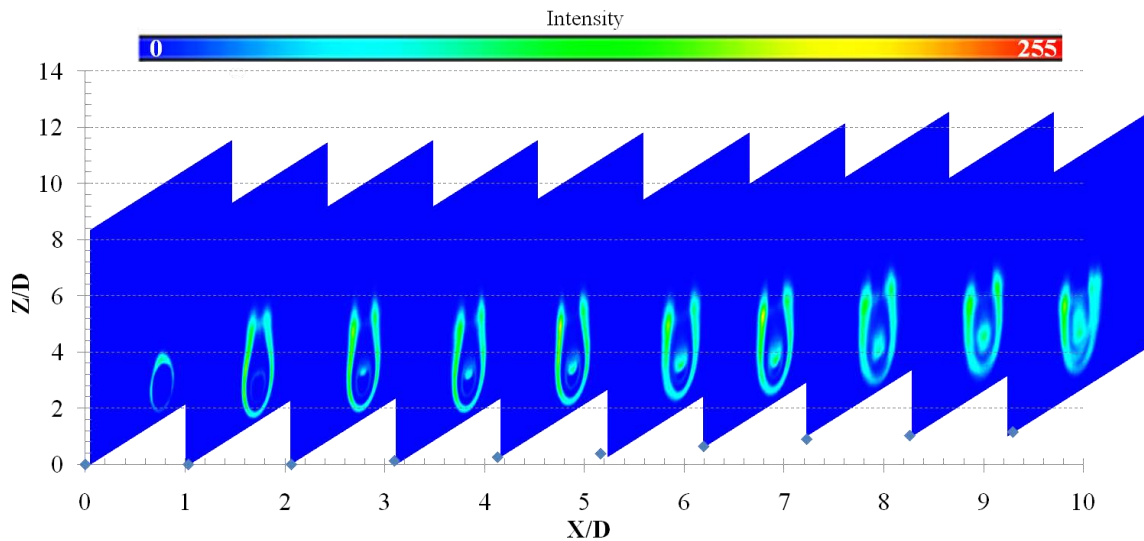
Figure 31. Three Dimensional Mapping of a Flame

III.4.1. High Speed Camera Images of Propane and Ethylene

In order to supplement and validate the PLIF data two types of high speed images were captured with a Vision Research high-speed Phantom v12.1 high speed camera. For both types of imaging the camera was placed perpendicular to the reacting jet, approximately 4 ft away. The Phantom camera was used in conjunction with a Micro-

70

Nikkor 105mm f/2.8 fully adjustable lens. Figure 32 shows the camera setup. This camera has the capability to capture images up to 1,000,000 frames per second (fps) at 8 x 128 pixels or up to 6200 fps at full resolution of 1280 x 800 pixels. For the purposes of this research, the full resolution was used; therefore, no images were gathered at rates above 6200 fps.

Figure 32. Phantom v12.1 High Speed Camera

The first set of images taken were simply unfiltered raw, color, images of the flame. These images provided a baseline for determining general flame length and behavior. For all of these experiments 2000 images were collected at maximum frame rate, 6200 fps. Capturing at such high frame rates allowed for capturing and tracking the turbulent structure of the reacting jets. Figure 33 shows an example series of frames collected.

| Image 1 | Image 400 | Image 800 |

| Image 1200 | Image 1600 | Image 2000 |
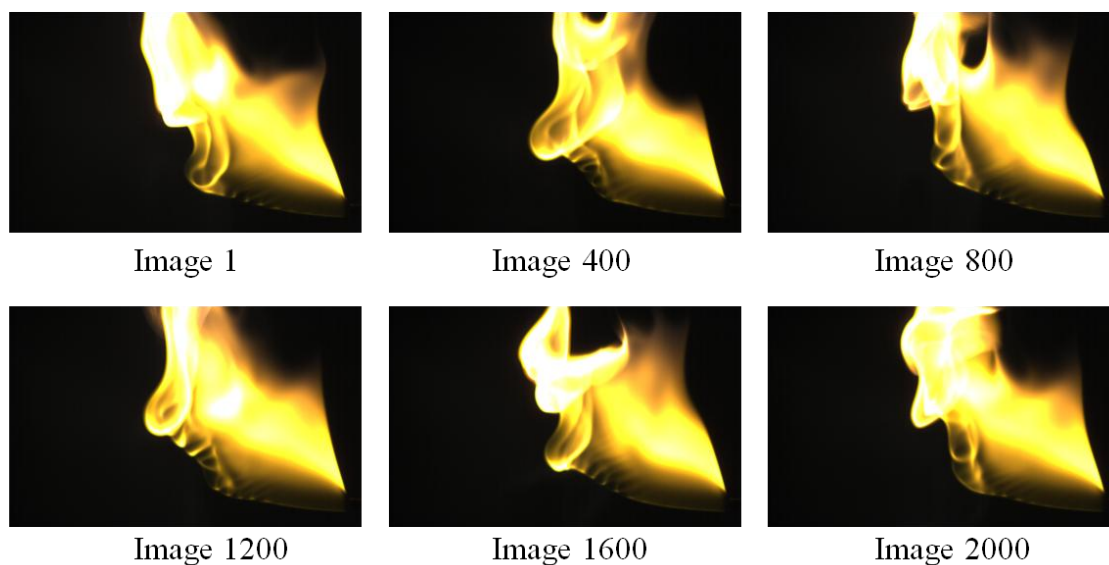
Figure 33. Series of High Speed Images for an Unfiltered Ethylene Flame

It is important to note the yellow and orange hues observed are a result of soot production and black body emissions, and stronger intensities do not necessarily represent higher OH production regions. In order to better track the trajectory of the flame all of the images were also averaged together, as seen in Figure 34, which represents 600 unfiltered images averaged together and depicted with an intensity scale.
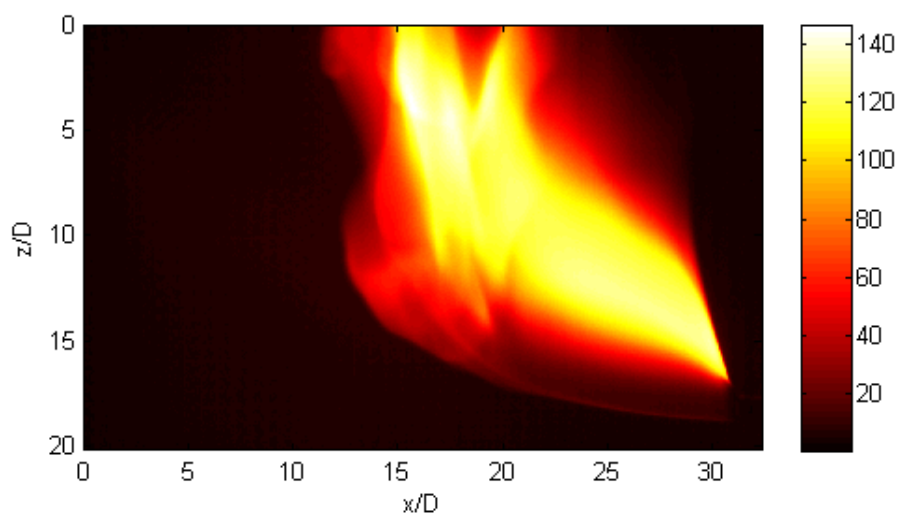
Figure 34. Averaged Unfiltered Ethylene Flame

Furthermore, the ethylene flames produced significantly larger amounts of soot as a result of the higher carbon to hydrogen ratio in its chemical equation. Therefore, the signal intensities captured by the Phantom were also different between fuels. Initial runs of ethylene were attempted at the same test conditions as the propane; however, the signal strength was so strong it saturated the camera. As a result, a lower exposure time was used with ethylene while maintaining the same frame rate. The exposure times were 160 μs and 40 μs for propane and ethylene, respectively.

In an attempt to isolate the reaction location, the second types of images gathered with the Phantom camera were filtered. For these experiments a 2 inch diameter band pass filter, with a 10 nm band, centered at 430 nm, was attached to the front of the camera lens. This was done in order to isolate the CH* chemiluminescense, which emits at approximately 431 nm, appearing blue to the observer. Tracking the CH* allowed for determining where the reaction was actually occurring, because it was an interim product of combustion. Due to low flow rates it was expected the CH* and OH radical should both exist at approximately the same location in time and space; therefore, tracking both provides two independent methods for flame characterization.

Figure 35 represents a series of CH* filtered images captured in these experiments and Figure 36 depicts the averaged results used to track trajectories. All of the filtered images were captured at 100 fps, with an exposure time of 9999 μs. Unfortunately it was not possible to capture the filtered images at the same 6200 fps. Due to the lack of signal strength emitted by the CH*, longer exposure times were required, which in turn reduced the maximum frame rate. However, to remain consistent with the PLIF testing, data was gathered for 20 seconds; therefore, 2000 images were captured for each test case.

73

Image 1   Image 400   Image 800

Image 1200   Image 1600   Image 2000
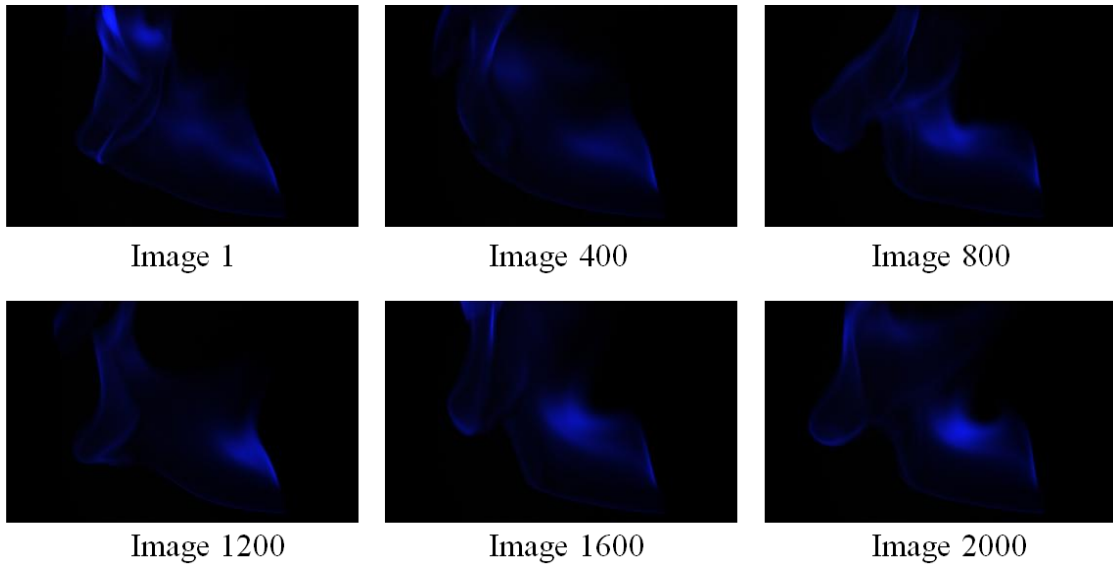
Figure 35. Series of High Speed Images for a CH* Filtered Ethylene Flame
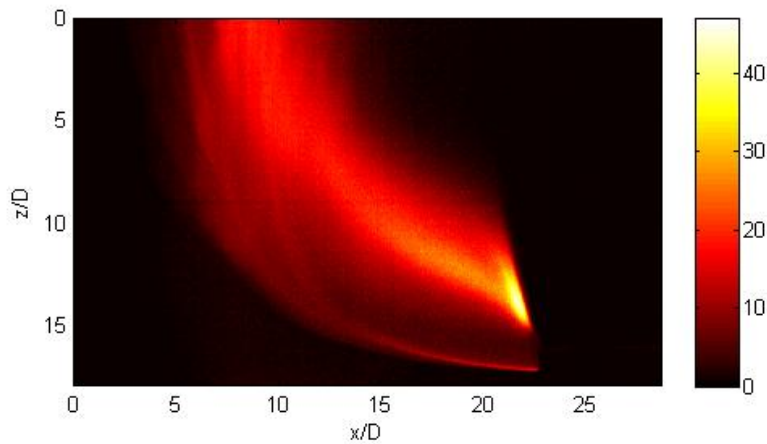
Figure 36. Sample Averaged CH* Filtered Image

III.5. Error Analysis

As with any experiment, no measurement taken can be proven to be exactly true.

However, gaining insights into the errors present allowed for predictions of accuracy.

Therefore, this section focused on defining the errors present in this experiment. The

main output or response variable of these experiments was the intensity of the flame, to

include the OH and CH* concentrations. Its measurement was influenced by many inputs

or variables as well as other factors, some of which were controllable, while others were

uncontrollable.

The main error associated with the inputs was due to deviations in mass flow rates

through the mass flow controllers. A fluctuation in flow rate changes the inherent

properties of the flame such as Reynolds and Froude number. This source of error affects

all three types of experiments conducted. On numerous runs these fluctuations were

measured with a Bios International Definer 220 flow meter and found to be within 0.5%

of the set point. Due to the range of flow rates used, this was determined to be an

acceptable and rather insignificant error.

The second type of input error, which only affected the PLIF results, was

associated with location of the combusting jet. The location of the jet was controlled by

the traverse capable of μm adjustments; however, like any mechanical system, there were

errors associated with it. In order to minimize the location error, the traverse was bolted

to the stationary optics table. This solved the problem of accidental bumps knocking it

out of place. Furthermore, because the laser sheet width was approximately 1 mm, the

traverse was limited to 1/10 mm adjustments. Therefore, any errors in location less than 1

mm, were negated by the width of the laser sheet.

The main source of uncontrollable outside error was due to room currents.

Because the flow rates and velocities were both low, outside air currents were able to

drastically affect the flame stability. Many of the test cases produced flames similar to a

candle. Therefore, it was important to control the surrounding environment as much as

possible. In an attempt to eliminate the wind current effects, testing was conducted with

only one person in the lab (the test conductor), all ventilation ducts were shut, the heating

and cooling was turned off, and movement in the lab was reduced to the minimal amount

required for operation. Furthermore, for both the filtered high speed images and the PLIF

data, the results were averaged over a twenty second period of time. Averaging over an

extended period of time helps to eliminate errors due to outside perturbations in wind

currents.

The second type of uncontrollable error was the shot to shot variance of laser

power. Having a different amount of power from shot to shot changes the intensity of the

OH concentrations within the PLIF data. In order to determine the magnitude of this

error, a power meter was used to determine the variation from shot to shot. The results

showed that the average laser sheet contained 3mJ of energy, with a variation of

approximately 5%. This variation was determined to not be a significant factor in flame

characterization because the data was averaged over a 20 second period of time and the

overall shape and reaction of the jet was not changed.

Several other known but uncontrollable sources of error were also present such as

beam intensity and quality within the sheet, shot to shot variations in wavelength, and the

effects of absorption as the laser sheet transits through the flame. However, since the

purpose of the research was to gain a global understanding of how the flame was

changing, these errors are minimal, and do not significantly influence the overall results.

Although quantifiable errors were not a significant factor for determining the

overall shape of the jets, there were errors associated with the trajectory plots. As

previously mentioned, trajectory plots were created based on all three acquisition types,

PLIF, unfiltered, and filtered. Because the PLIF images spanned the largest amount of

time, 20 seconds per test point, its resulting trajectories were believed to be the most accurate. However, they still contained errors simply based on the way the bottom edge was defined. The range for max intensity across different frames and cases was 120 to 260, and because the background noise was subtracted out, the intensity in the free stream was zero. Therefore, the bottom could have been defined anywhere between an intensity of 2 and 40. For the purposes of this experiment, however, the bottom edge was defined as the lowest point containing a pixel intensity of 20. Figure 37 illustrates how changing this definition would have altered where the bottom edge appeared to be. Figure 37a shows where the bottom edge would be if the threshold intensity was 2, while b and c correspond to threshold intensities of 20 and 40, respectively.
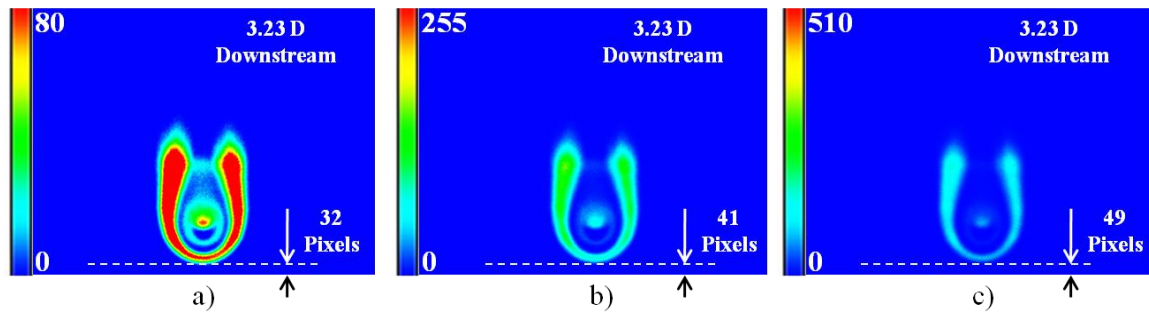
Figure 37. Different Bottom Edge Definitions

In addition to the definition error, there was also spatial resolution and human error associated with all three acquisition types. In the PLIF images, 16 pixels represented 1 mm, while the unfiltered and filtered had 5.1 and 5.8 pixels/mm, respectively. Although the spatial resolution of these images was good, there was still human error in the data reduction. In the worst case scenarios, values pulled from the PLIF and high speed images were off by 5 pixels. Table 3 shows the magnitude of which these errors could affect the results, in terms of diameters.

Table 3. Spatial Resolution and Human Error, Represented in Diameters

	$^3/_8$ in Tube	½ in Tube	¾ in Tube
PLIF	0.040 D	0.029 D	0.020 D
Unfiltered	0.127 D	0.090 D	0.062 D
Filtered	0.111 D	0.079 D	0.055 D

Table 3 also shows these errors were nearly 3 times greater for the unfiltered results when compared to the PLIF results. This was due to the higher spatial resolution of the PLIF images. Additionally, these errors were larger in tubes with smaller diameters. Figure 38 shows a sample trajectory plot with the associated error bars. The error bars represented the spatial resolution and human error for all three acquisition types. The PLIF error bars also incorporated error associated with the bottom edge definition, representing a range of intensities from 2 to 40, with 20 being the actual data point used.
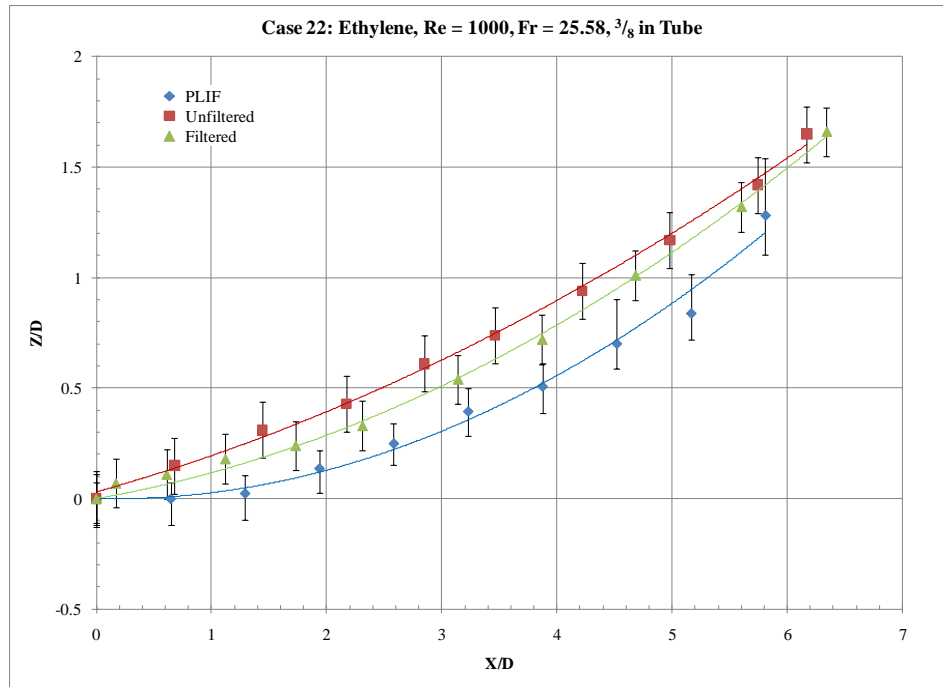
Figure 38. Sample of Error Associated With Trajectory Results

In general Figure 38 shows the filtered and PLIF error bars overlapping, while the unfiltered and PLIF error bars are close to overlapping. These findings showed the trajectory results were consistent across different acquisition types. Additionally, these findings were expected to be consistent across all test cases, because Figure 38 shows the trajectories associated with case 22, an average case with respect to flow rate and variability between acquisition types. Some of the cases showed much better correlation, while others were worse. All of the trajectory data can be found in Appendix D.

IV.   Results and Discussion

IV.1. Test Matrix

The test matrices were produced prior to testing in order to ensure data was collected efficiently and at significant locations, while optimizing key flow parameters. For this experiment it was important to ensure data points were tested below, at, and above Froude numbers of 1.0. A range of laminar tube, or Poiseuille, Reynolds numbers was also required. In order to satisfy these requirements the test matrices were customized to each fuel as well as manipulated such that comparisons could still be drawn between the two fuels in addition to evaluations within the same fuel type.

IV.1.1. Propane

For propane, 18 different test cases were evaluated. Data from the ensuing flames was collected in three different ways for each case: high speed unfiltered images, high speed filtered images, and PLIF images. Within the 18 test cases, 9 were considered constant Reynolds number, while 9 were considered constant Froude number. This allowed for the isolation of one variable. Within the 9 constant Reynolds number cases, 3 different Reynolds numbers were chose and evaluated for each of the three different tube sizes. The three constant Reynolds numbers were 300, 1000, and 1500. A similar setup was used with the constant Froude number cases. The three constant Froude numbers were 0.5, 1.0, and 1.5. Table 4 provides the details for each of the propane test cases.

Table 4. Propane Test Matrix

Case Number	Reynolds Number	Froude Number	Tube OD	Flow Rate (SLPM)
1	300	1.06	3/8 in	0.49
2	300	0.63	1/2 in	0.69
3	300	0.36	3/4 in	0.99
4	1000	3.49	3/8 in	1.62
5	1000	2.09	1/2 in	2.29
6	1000	1.19	3/4 in	3.30
7	1500	5.26	3/8 in	2.44
8	1500	3.13	1/2 in	3.43
9	1500	1.78	3/4 in	4.95
10	142	0.5	3/8 in	0.23
11	240	0.5	1/2 in	0.55
12	412	0.5	3/4 in	1.37
13	283	1.0	3/8 in	0.46
14	476	1.0	1/2 in	1.09
15	840	1.0	3/4 in	2.79
16	425	1.5	3/8 in	0.69
17	716	1.5	1/2 in	1.64
18	1234	1.5	3/4 in	4.10

IV.1.2. Ethylene

For ethylene, only 9 test cases were evaluated because constant Froude number cases were neither achievable nor insightful due the insignificant flame propagation outside of the tube. Therefore, the 9 tests conducted were on constant Reynolds number cases. Similar to propane, three Reynolds numbers were chosen and evaluated for each of the three tube sizes. The three Reynolds numbers chosen were again 300, 1000, and 1500 because they provide a good range of laminar tube flow conditions. Additionally, using the same Reynolds numbers in both propane and ethylene allowed for comparisons to be drawn between the two fuels. Table 5 provides the details for each of the ethylene test cases.

Table 5. Ethylene Test Matrix

Case Number	Reynolds Number	Froude Number	Tube OD	Flow Rate (SLPM)
19	300	7.67	3/8 in	0.98
20	300	4.57	1/2 in	1.38
21	300	2.63	3/4 in	2.01
22	1000	25.58	3/8 in	3.27
23	1000	15.31	1/2 in	4.62
24	1000	8.75	3/4 in	6.70
25	1500	38.41	3/8 in	4.91
26	1500	22.97	1/2 in	6.93
27	1500	13.13	3/4 in	10.05

IV.2. PLIF Results

The main purpose of this research was to characterize various low Froude and Reynolds number flows through the use of PLIF. In total, 27 different flow conditions, or cases, were examined. Within each flow condition, approximately 10 streamwise planar interrogation regions were investigated, and within each location 200 images (representing 20 seconds) were captured. Theses 200 images were used to create a time-averaged image at each location. The resulting cross sectional PLIF images were then used to create a three-dimensional mapping of the jet spreading, jet path, and combustion progress through OH concentration tracking.

Due to equipment constraints, specifically the 40mm laser sheet height, the entire cross section of the jet could not be observed. Fortunately, however, the majority of the inner combustion region was captured in most interrogation regions. Since combusting, horizontally issuing buoyant jet cross sections are yet to be classified in current literature, the following sections will focus on describing the behaviors observed within the inner combusting regions as well as the surrounding regions.

IV.2.1. Three-Dimensional Mapping

Each image within the three-dimensional figure shows the scalar image intensities. These intensities are a direct result of OH emissions; therefore, regions depicting higher intensity values correlate to regions of higher OH concentrations. Additionally, each image was plotted with the same intensity scale. Figure 40 shows the three-dimensional image map produced for case 1. While only the most interesting and representative cases are shown here, all 27 three-dimensional image maps can be found in Appendix A.

It is important to first note that the laser sheet produced did not cross the entire screen. Therefore, often it appears the image was truncated; however, in reality the laser sheet was only 40 mm tall, and thus can only excite the OH in a limited spatial regime. Figure 39 depicts the incident laser sheet as observed on a business card (averaged over 200 shots).
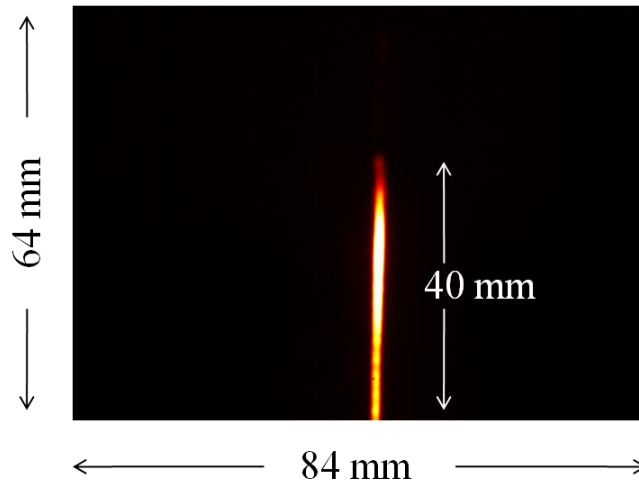
Figure 39. Incident Laser Sheet Height
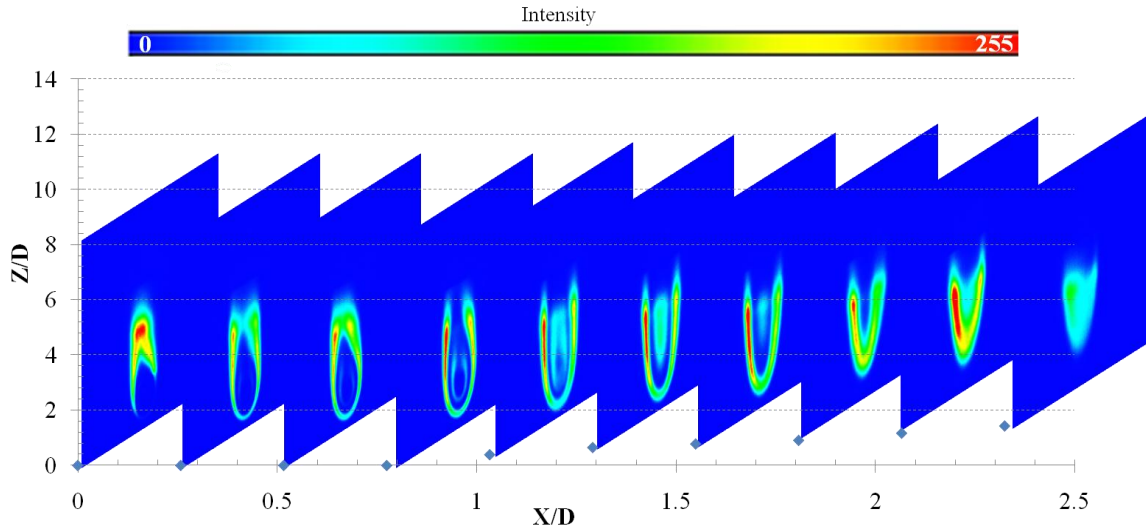
Figure 40. Case 1: Propane, Re = 300, Fr = 1.06, $^3/_8$ in Tube

One general trend observed in all cases was the propensity for the jet to turn, or move, in the vertical direction as it got further from the tube exit. This vertical movement was the result of combustion. If this experiment had been conducted on a non-reacting jet, such as those investigated by Reeder, et al., different phenomena would have been observed. Propane would be defined as heavy with respect to air, while ethylene would be neutral. Therefore, the propane would have curved downward, while ethylene would likely have taken a flatter trajectory (16). With the addition of combustion, however, both fuels moved in the vertical direction. As combustion processes break down the fuel molecules, smaller and lighter particles are produced, temperatures rise, and the overall density of the jet is reduced. Most of these products are lighter than air; therefore, as interrogation planes further from the tube exit were examined, the jet was found to shift, or curve, vertically as depicted in Figure 3a and Figure 40. In these 27 cases, the introduction of combustion effectively caused potential negatively and neutrally buoyant cold flow jets to become positively buoyant. This implies the overall average density

84

within the jet was significantly less than the density of air. Additionally, the jets produced

in all cases were clearly buoyancy dominated, which resultantly implies the reacting

Froude numbers was less than 5, which is defined as the median between momentum

dominated jets and buoyancy dominated jets (26). The actual density within the jet can

only be speculated, because the jet density is constantly changing as it progresses

downstream. At the exit of the tube, most of the fuel is unreacted; however, as the jet

progresses downstream the density decreases as the core combusts and warms up.

IV.2.2. Laser Energy Absorption

Another trend observed in nearly all of the interrogation planes was the tendency

for the maximum intensity to decrease from one side of the flame to the other. In other

words, the jet cross sections were not necessarily symmetrical in shape and intensity. In

most cases, the shapes were symmetrical about a vertical axis; however, the intensities

observed within the general shape were not. In nearly all cases, higher intensities were

observed on the left side of the image, as seen in Figure 41. These variations in intensity

were the result of absorption. As the laser sheet propagates through the ROI, it loses

energy due to absorption. Therefore, the molecules on the right side are not illuminated

with equal beam intensity, and consequently do not emit with equal strength when

compared to those on left side. Even though the intensity on the right side is not of the

same magnitude as the left side, the general trends are still the same because the physics

are the same. Those areas with higher OH concentrations will still be observed as areas

with higher intensities. The intensities are relative, and not necessarily absolute

indications of OH concentrations.
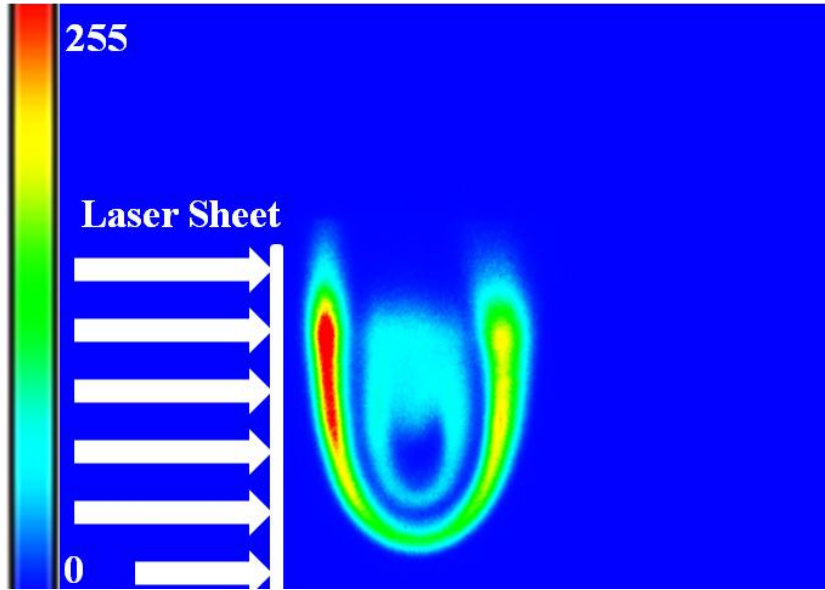
Figure 41. Energy Absorption Affects on PLIF Images, Case 16

IV.2.3. Regions of the Flame

Variations in intensity or OH concentration were also used to determine different types or regions of combustion within the flame. As with any diffusion flame, combustion occurred within a range of equivalence ratios. Therefore, differences in intensity strength were used to indicate different combustion regimes within the flame. Figure 42 provides a plot of OH mole fraction versus equivalence ratio for a premixed propane and ethylene reacting with air (21% oxygen and 79% nitrogen), which was created using data from GasEq, an open source program for calculating gas equilibrium. This plot shows the highest concentrations of OH are produced in areas experiencing lean combustion, $\phi < 1.0$, for both propane and ethylene.
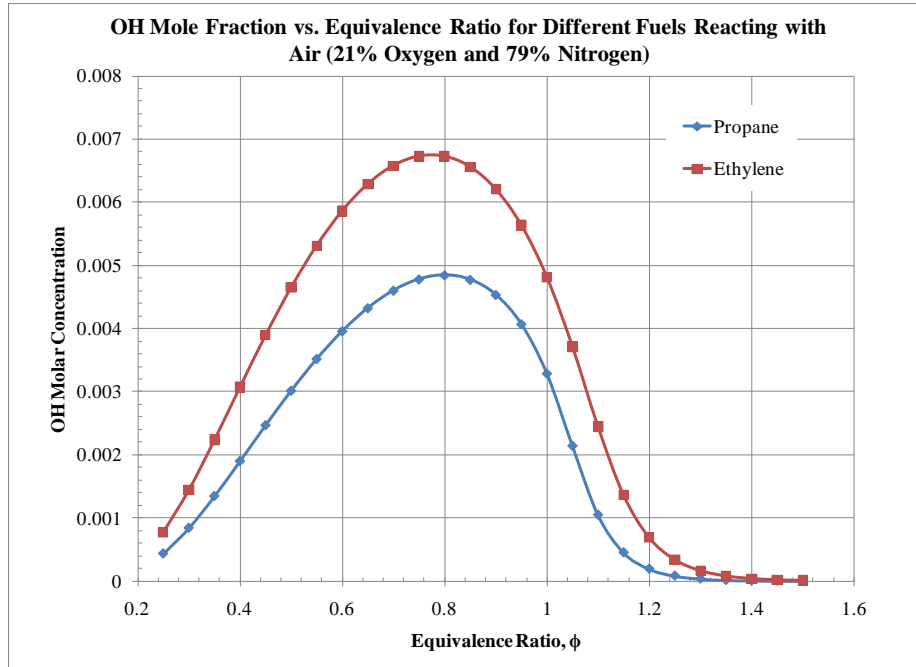
Figure 42. Predicted OH Mole Fraction vs. Equivalence Ratio

Figure 42 also shows ethylene produces more OH for all combustion regimes when compared with propane. Within a diffusion flame a wide range of equivalence ratios is expected as the solid fuel core diffuses into an infinite reservoir of ambient air. In both fuels, however, minimal OH is produced for extreme lean and rich conditions. Therefore regions observed with weaker intensities are either rich or very lean combustion. With respect to the jets produced in these experiments, weak intensity areas were observed at the outer edges (extremely lean, $\phi < 0.5$) and near the core (rich, $1.0 < \phi < 1.3$). The area in the middle of these regions was observed to have the strongest intensities; therefore, it was concluded to contain lean combustion, $0.5 < \phi < 1.0$. Different combustion regimes of the flame can be seen in Figure 43. Additionally, intensities are also a function of temperature. Therefore, locations with higher temperatures, closer to stoichiometric, also contained larger amounts of OH production.
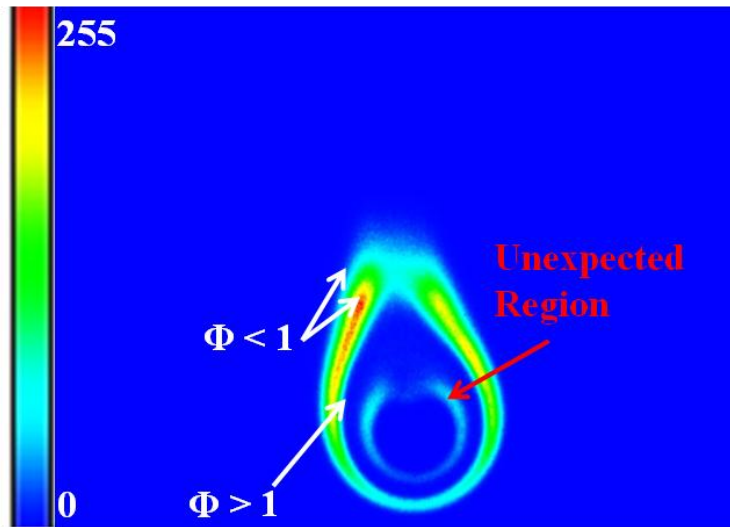
Figure 43. Different Expected Equivalence Ratios Within the Flame, Case 8

The presence of two distinct regions within the flame structure, as seen in Figure 43, was an unexpected result. The presence of both lean and rich combustion was expected; however, the area between these two regions was not expected to contain minimal OH production. Figure 43 clearly depicts what appeared to be a rich area of combustion surrounding the core and an area of lean combustion near the outer edges of the flame, separated by an area with minimal to no OH production. A continuous range of equivalence ratios was expected to be present from rich near the core to lean near the edges. Similarly, all of these regions were expected to produce OH as predicted by Figure 42. The lack of a continuous range of OH production from the core to the edges suggested some other phenomenon was occurring. Initially, this region was hypothesized to be comprised of the air being entrained from the top of the jet, or possibly the byproducts of rich combustion occurring at the edges of the inner core, or some combination of the two scenarios. However, further analysis revealed this region which appeared to be low OH production was actually another product of combustion called

polycyclic aromatic hydrocarbons (PAHs). In order to confirm this region did not

represent OH production a frequency sweep was conducted with the laser. Because OH

requires a specific wavelength in order to become excited, changing this wavelength to an

off condition should eliminate the ability of the camera to capture OH fluorescence

events. If both regions were representative of OH production, moving to a different an off

condition wavelength should eliminate both regions. However, when this test was

conducted, the stronger outer region disappeared while the weaker inner region remained,

as seen in Figure 44. This test was conducted on Case 4 at an axial location of 3

diameters downstream. This test condition was chosen because it clearly depicted both

inner and outer regions. All of the images captured in the frequency sweep can be seen in

Appendix F.

| 282.89662 nm | 282.90295 nm | 282.90916 nm | 282.91301 nm | 282.91723 nm |
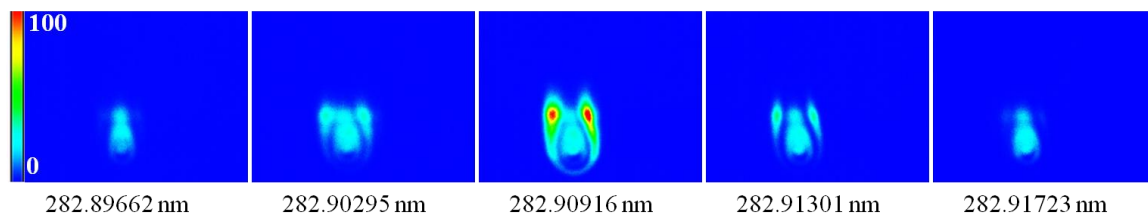
Figure 44. Frequency Sweep Revealing Non-OH Inner Core

This finding confirmed the inner core region was not actually OH production.

Rather, it was postulated this area was actually PAHs, which are a known byproduct of

hydrocarbon combustion. Although the initial intention was to capture only OH

fluorescence, conclusions could also be drawn from the PAHs. Tracking both the OH

production in the outer region as well as the PAHs in the inner core allowed for a more

complete analysis. The OH production in the outer region showed where the flame was

and where the reactions were occurring while the PAHs in the inner core provided insights into the mixing characteristics in this region.

IV.2.4. Inner Core

An inner region of PAHs was observed in all cases, regardless of fuel and tube size, as seen in Figure 45, where a, b, and c, represent 3/8, 1/2, and 3/4 inch tubes, respectively. Henceforth, this inner region shall be referred to as the inner core.
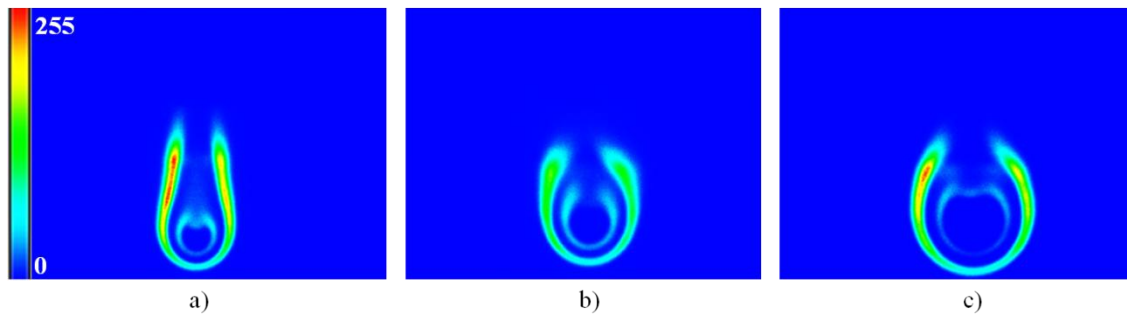
Figure 45. Presence of Inner Core: a) $^3/_8$ in Tube, b) ½ in Tube, c) ¾ in Tube

Even though all of the jets contained an inner core, they did not all behave in the same manner. While many of the attributes associated with the different cores were similar, there were also subtle differences. All inner cores experienced some sort of elongation as well as breakdown.

IV.2.4.1. Elongation

As the jet moved further from the tube exit, it entrained more air, reacted more, and consequently, grew, or elongated, in size, as seen in Figure 46. In many cases the inner core grew to the point where it was no longer possible to capture in its entirety. It is interesting to note, rather than dissipating, the inner core actually grew with the flame. At the tube exit, the inner core is approximately the same height as the tube exit. Subsequent

downstream interrogation regions revealed the core was actually elongating as it progressed. As such, the core appeared to grow with the flame. Figure 47, provides an example as to how much the core grew.
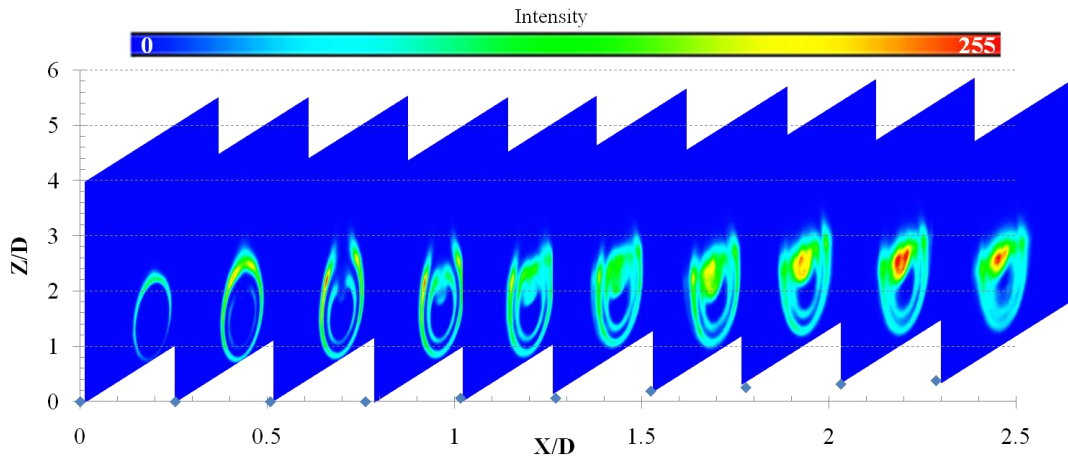
Figure 46. Case 18: Propane, Re = 1234, Fr = 1.5, ¾ in Tube
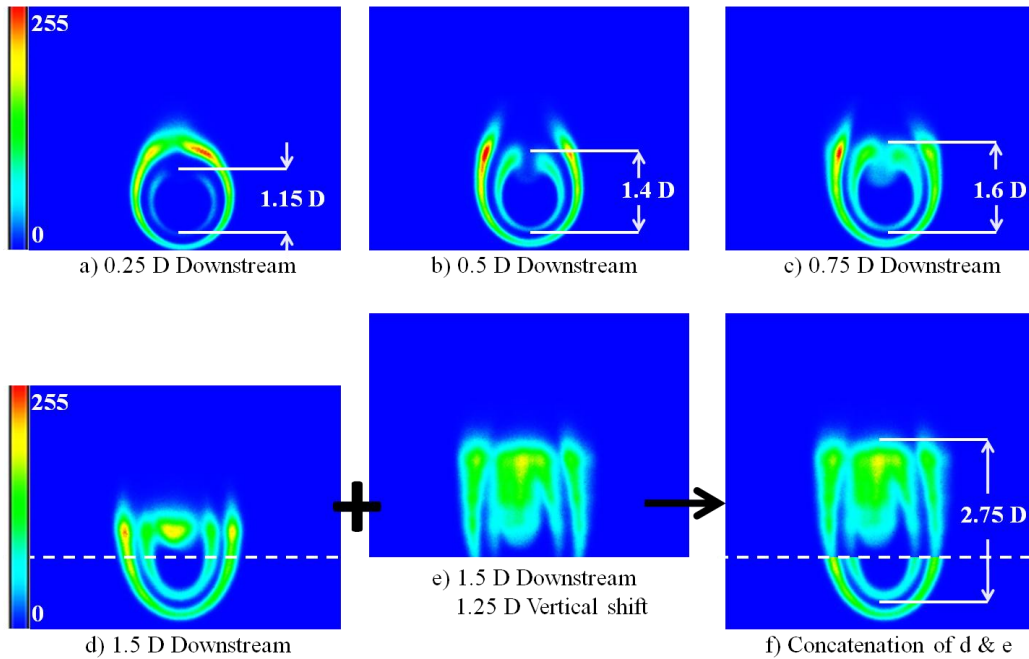
Figure 47. Case 6, Core Elongation

Figure 47f, also shows a composite image comprised of Figure 47d and Figure

47e. Both of these images were captured at the same axial location; the difference was a

20mm shift from image d to e. These two images were superimposed to illustrate how the

core continues to elongate even in regions beyond the constraint of laser sheet size. It is

interesting to note, even in areas where the core grew to nearly three times its original

height, the width of the core stayed relatively constant. Simply put, the core appears to

stretch vertically as it moved downstream. Again, this was most likely the result of the

buoyancy forces acting upon the inner core. As the core progressed downstream, its cross

sectional area became larger due to elongation. As the core elongated, the momentum at

any given location reduced. Reducing the momentum, in turn caused the flame to more

rapidly turn vertical, in an exponential manner. This empirically supports the visual

observation of the jets being buoyancy dominated.

IV.2.4.2. Breakdown

Another phenomena observed in all cases was the breakdown of the inner core.

Whether it was rapid or slow, all of the inner cores eventually broke down. Figure 48 and

Figure 49 provide distinct examples of inner core breakdown. Case 7 and case 10

represent the two extremes of what was observed in core breakdown for propane within

the 3/8 inch tube. These results are consistent with those found in all tubes, regardless of

fuel. In case 7, breakdown was slow with respect to axial distance, while case 10 depicted

almost immediate breakdown of the inner core. The differences observed were most

likely due to the initial velocities of the jets. Jets with relatively higher exit velocities

(higher Reynolds numbers) were found to maintain inner core structure for longer and

appeared to breakdown in a methodical way. Jets with relatively lower exit velocities (lower Reynolds numbers) seemed to experience a more rapid inner core breakdown.
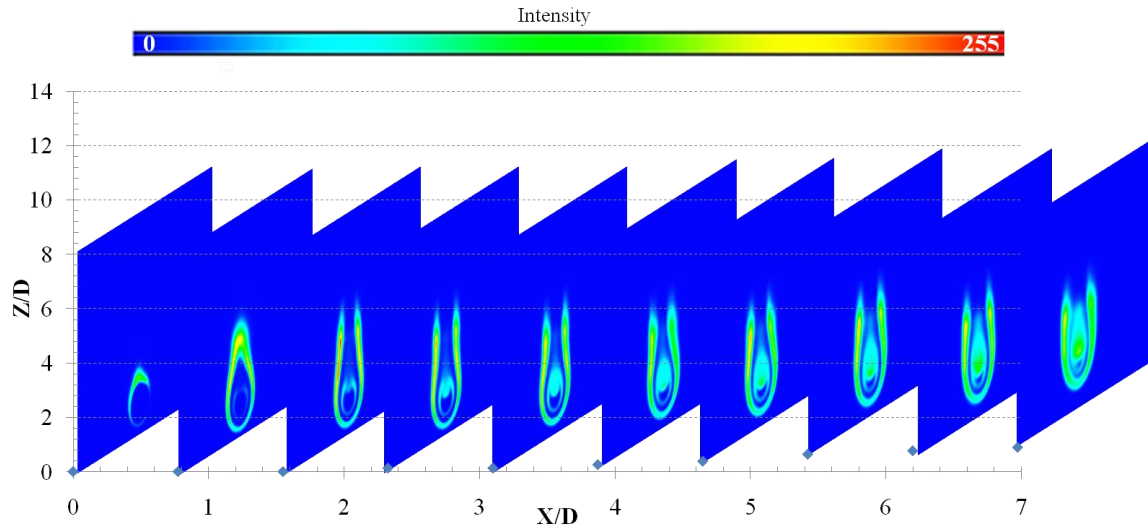
Figure 48. Case 7: Propane, Re = 1500, Fr = 5.26, $^{3}/_{8}$ in Tube
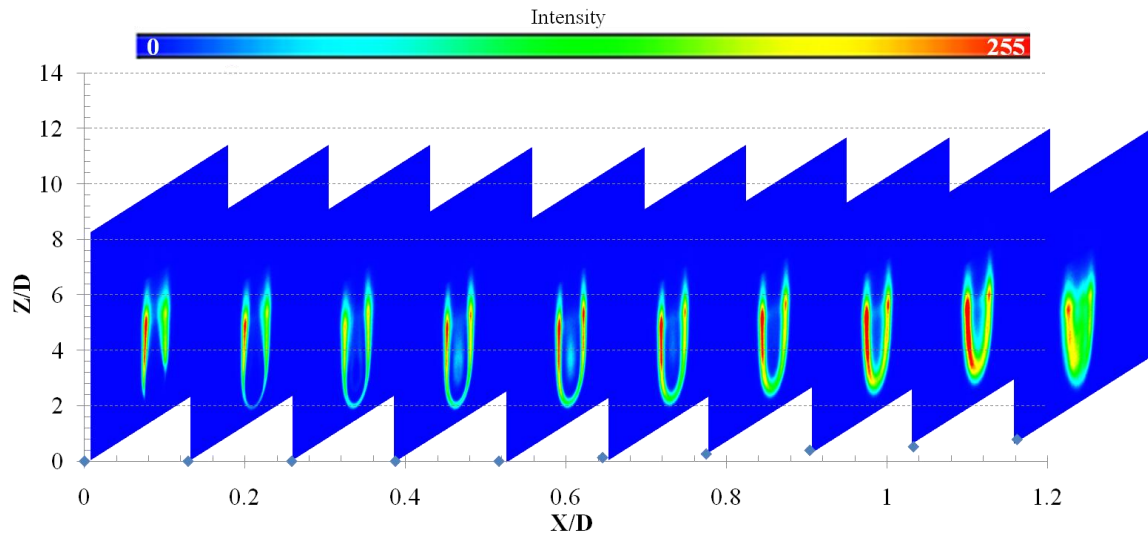
Figure 49. Case 10: Propane, Re = 142, Fr = 0.5, $^{3}/_{8}$ in Tube

Figure 50 shows how the jet cross sections from case 7 changed with axial location. Near the exit of the tube, the inner core was nearly a perfect circle. As the core

93

progressed downstream it appeared to entrain more air from the top of the jet. As the air encountered the fuel core, increased mixing began to occur at the top of the inner core. The once nearly perfect circle then began to react on the top side. The amount of reaction, or breakdown, of the inner core increased with axial position. Figure 50 also shows the progression of inner core PAH production as the core reacts from top to bottom.
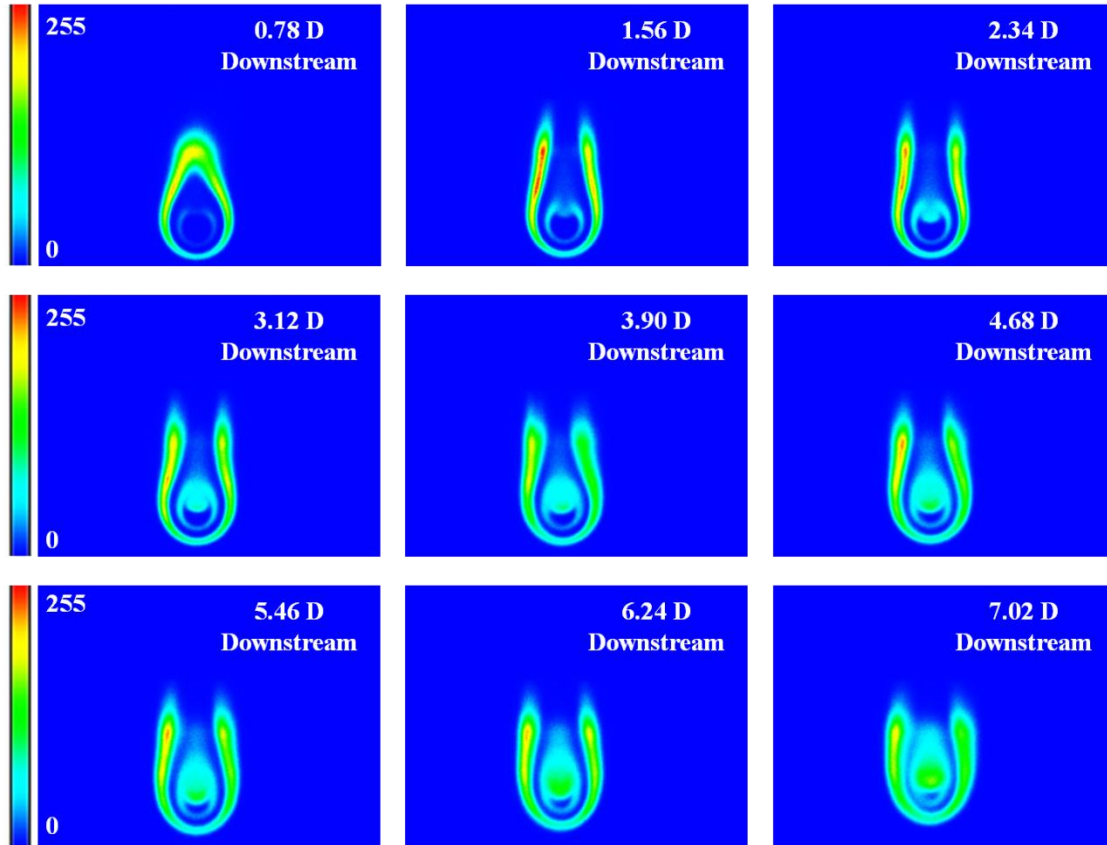
Figure 50. Case 7, Inner Core Breakdown

Slow and methodical breakdown of the core was not observed in all of the test cases. Generally, the cases with lower flow rates looked similar to case 10. Although different behaviors were observed in the inner core, the same inner core behavior was expected in all jets. These variations were attributed to the axial scale at which the images were collected as well as the range of exit velocities present. It was hypothesized all jet

inner cores experience the same type of breakdown; however, the scale and speed at which this occurred was a direct result of jet momentum. Figure 51 depicts the rapid core breakdown for case 10. Because this jet had the lowest Reynolds number of any case, it transitions from an elongated circular state, at 0.26 D downstream, to a completely reacting inner core by 0.52 D downstream. With minimal amounts of momentum, this case appeared extremely buoyancy dominated and the inner core quickly turned vertical, resulting in quick mixing, and rapid breakdown.
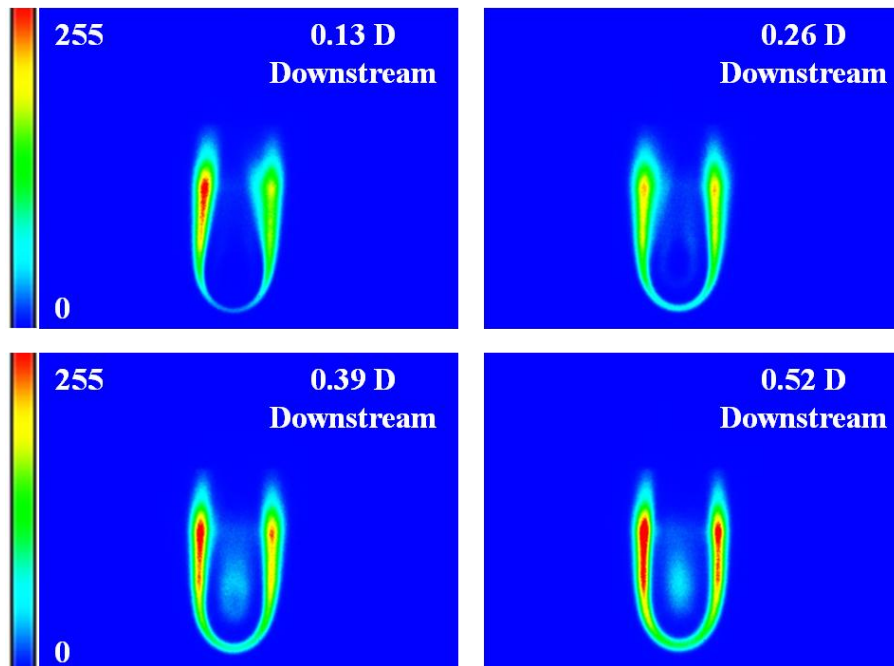
Figure 51. Case 10, Rapid Core Breakdown

Inner core structure and breakdown were also found to be remarkably consistent across fuels. Figure 52 shows some of the interrogation plane data collected from cases 5 and 23. In both of these cases the Reynolds number was 1000 and images were gathered at increments of 0.65 tube diameters downstream. When overlaid on each other, these two sets of images had striking similarities. At each axial location the inner core was

behaving in a similar fashion. Furthermore, the amount of core breakdown was approximately the same. These findings implied inner core breakdown was not necessarily fuel dependent; rather, it was concluded the driving factor in the progression of inner core breakdown was the jet's momentum.
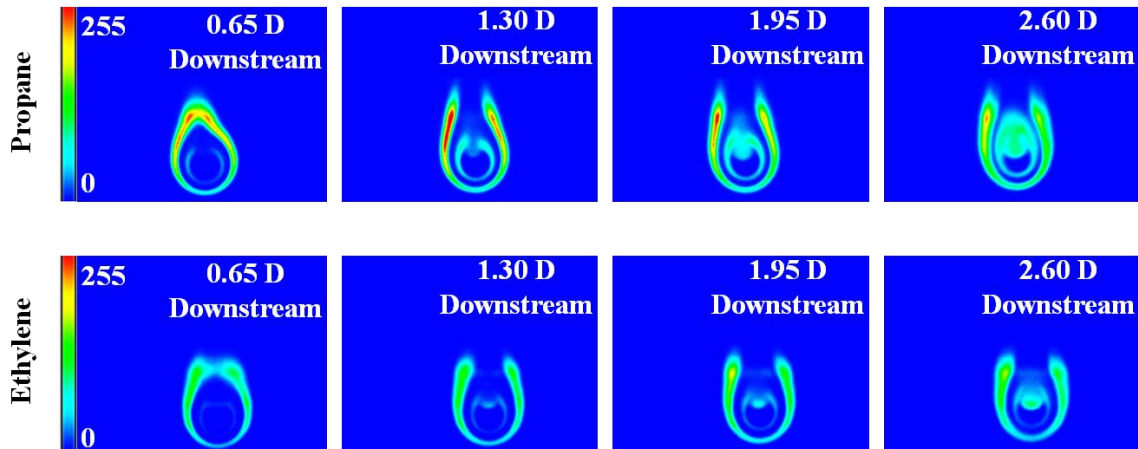
Figure 52. Similar Breakdown, Re = 1000; Case 5 (Propane) and 23 (Ethylene)

IV.2.5. Entrainment

Entrainment was observed both in the outer combustion region as well as the inner core. Figure 53 provides a good representation of how the inner core entrained air. Close to the tube exit this process was mild; however, as the jet progressed, the inner core entrained more air, resulting in increased mixing and ultimately more PAH production.
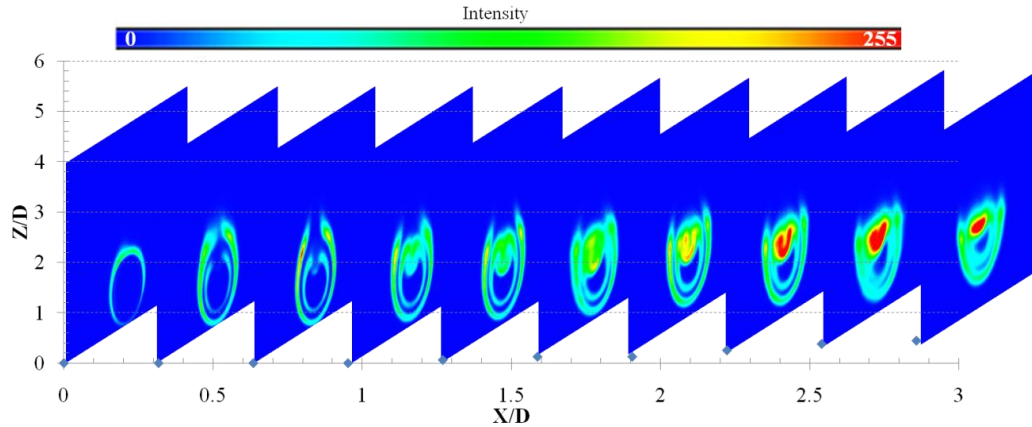
Figure 53. Case 9: Propane, Re = 1500, Fr = 1.78, ¾ in Tube

Within the inner core, entrainment was the result of two competing buoyant forces. The cold heavier propane in the inner core had the natural tendency to want to move downwards. As the edges warmed, smaller, less dense products were produced. These products had a natural tendency to move in the upwards vertical direction. As a result of these two competing forces, increased mixing was observed along the boundary of the inner core. Images gathered from interrogation planes further downstream, revealed the presence of what appeared to be vortices at the top of the inner core, as seen in Figure 54.

a) 0.63 D downstream   b) 0.95 D downstream   c) 1.27 D downstream
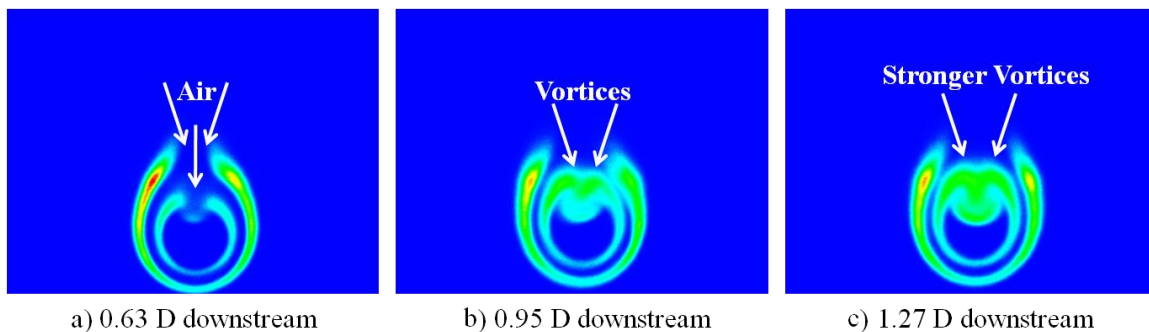
Figure 54. Case 9, Hypothesized Vortices are Displayed

97

Figure 54a shows how the outer region of combustion also entrained air. Entrainment in the outer region occurred in a similar fashion to the inner core. The hot, low density, products of combustion appeared to wrap upwards around the core of the jet. As the products encompassed the core, they inherently trapped, or entrained some of the surrounding air. The two sets of combustion products (PAHs from the top of the inner core and OH from the outer region) appeared to merge together near the top of the jet to form a teardrop shape with a sharp point, as seen in Figure 55. As with inner core elongation, the teardrop shape was assumed to likewise elongate.
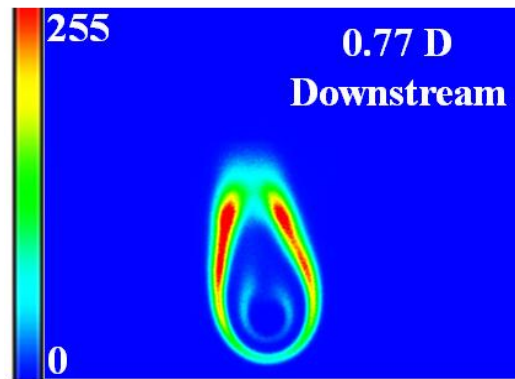
Figure 55. Case 16, Teardrop Shape

IV.2.6. Unsteady Flames

One of the major issues observed during testing was the effects of turbulence and unsteady flames. As stated in the test setup chapter, attempts were made to control outside factors like room currents. However, completely eliminating these effects was not possible. Therefore, some of the composite images (200 image averages) appeared to have less well defined combustion regions. Therefore, it is important to understand that the averaged images observed in the three-dimensional imaging maps are not necessarily representative of the actual flame thickness. Averaging the images alone would have

98

caused the images to smear and widen the apparent flame thickness, even without the presence of room currents. However, these effects were increased when room currents were present.

Figure 56 provides an example of how the individual images gathered at 10 Hz appeared good; however, when averaged, the clarity was reduced. In addition to uncontrollable room currents, many of the jets also appeared to shed vortices along the bottom edge of the flame at regular intervals. These vortices had an effect similar to wind currents, especially on interrogation planes further from the exit of tube. Although these vortices were not visible in the PLIF data, they were observed in the high speed images and will be discussed in a latter section.
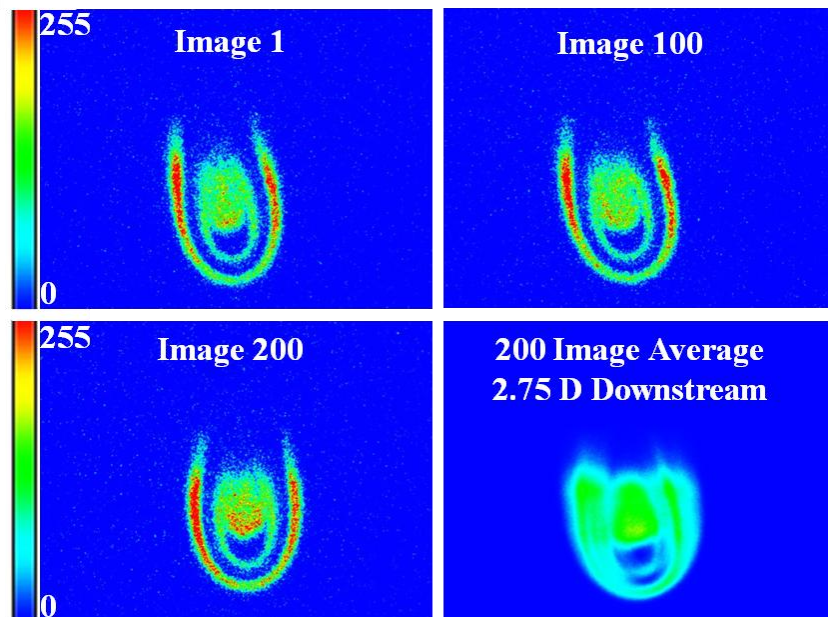
Figure 56. Case 5, Turbulence Example

IV.2.7. PLIF Trajectory Results

In addition to cross sectional data, the bottom edge trajectories for all of the cases were also produced from the PLIF data. Unfortunately, it was not possible to view the entire cross section of the jet at one time. Therefore, producing center of mass trajectories was not possible. However, by tracking the bottom edge trajectories, insights into the turning rates of the jets and the factors that were most influential were gained.

From the PLIF data, several plots were produced to compare the trajectories of the 27 different jets. Figure 57, compared 6 different jets all with a Reynolds number of 300. The data points were fit with a second order polynomial curve fit to provide a baseline for comparison between test cases. Within each fuel type, the plots were consistent with the expected results. Those cases with higher tube Froude numbers experienced lower turning rates, and thus had flatter trajectories.
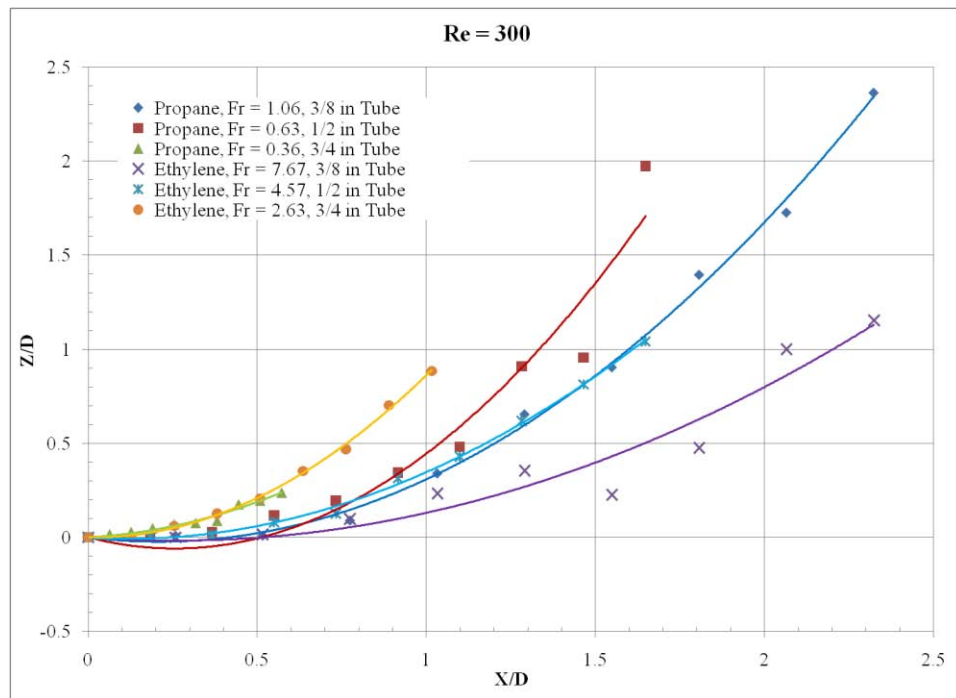
Figure 57. Re = 300, Bottom Edge Trajectories, PLIF Data

Figure 58 also compared 6 different jets. These jets contained a constant Reynolds number of 1000. Similar to the Reynolds number of 300 cases, within each fuel type, those jets with higher Froude numbers were flatter, while the lower Froude number jets had a higher turning rate. However, the 6 jets also seemed to break into 3 pairs. Jets with similar tube sizes and Reynolds numbers behaved remarkably similar, despite having vastly different Froude numbers. It is important to remember the tube flow Froude numbers were used when comparing the jets, because the actual Froude numbers were unknown. Therefore, these results implied the tube Froude numbers were not a significant factor for determining the shape of the jet trajectory. Rather the major factors influencing the jet trajectory were determined to be the exit velocities and the associated momentum.
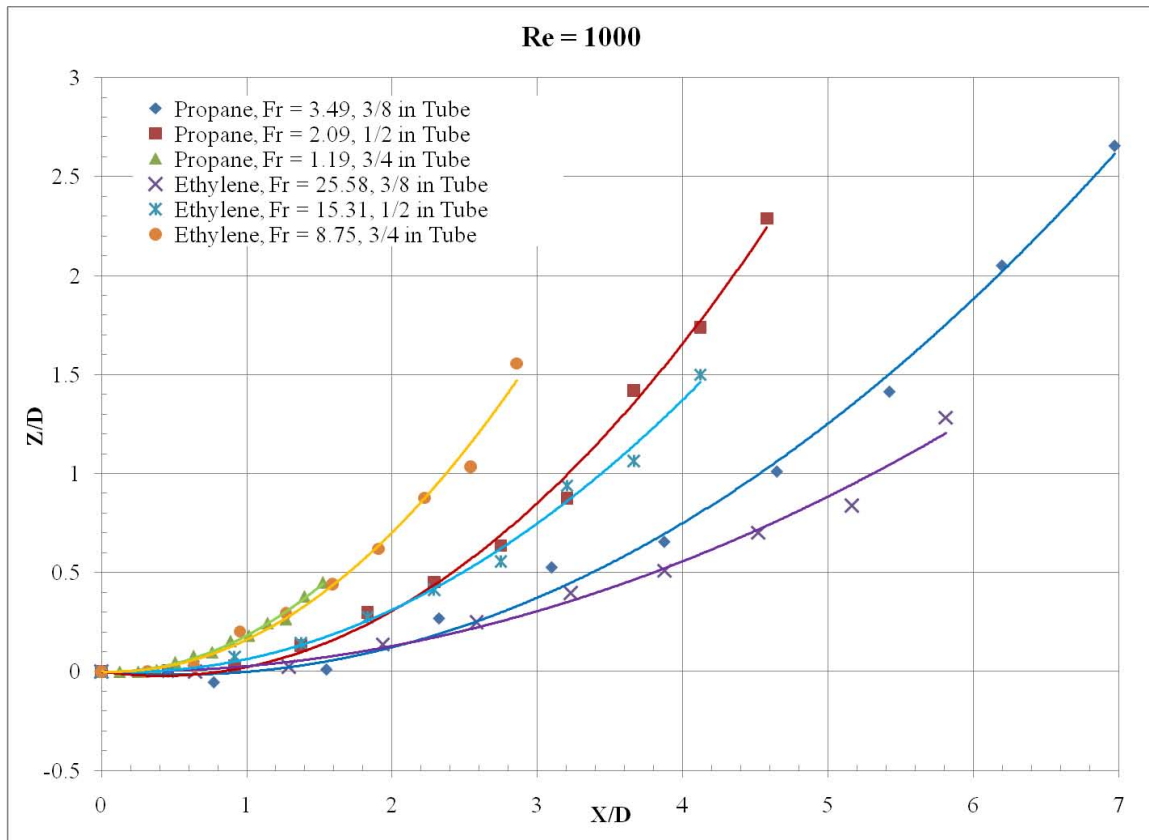
Figure 58. Re = 1000, Bottom Edge Trajectories, PLIF Data

Figure 59 compares the constant Reynolds number of 1500 cases. These jets displayed the same tendencies as those in the Reynolds of 1000 cases. The obvious difference was the flatter curves, or slower turning rates observed in the higher Reynolds number cases. Higher Reynolds number jets, by definition have more momentum; therefore, it took longer for the buoyant forces to take over.

In both Figure 59 and Figure 58 there are some negative jet locations with respect to the exit of the tube. It was expected these were the result of jet growth, as well as a propensity for the heavier fuel to move downward in the earlier stages of the jet, before it was sufficiently heated to the point where buoyant forces overcame the momentum forces.
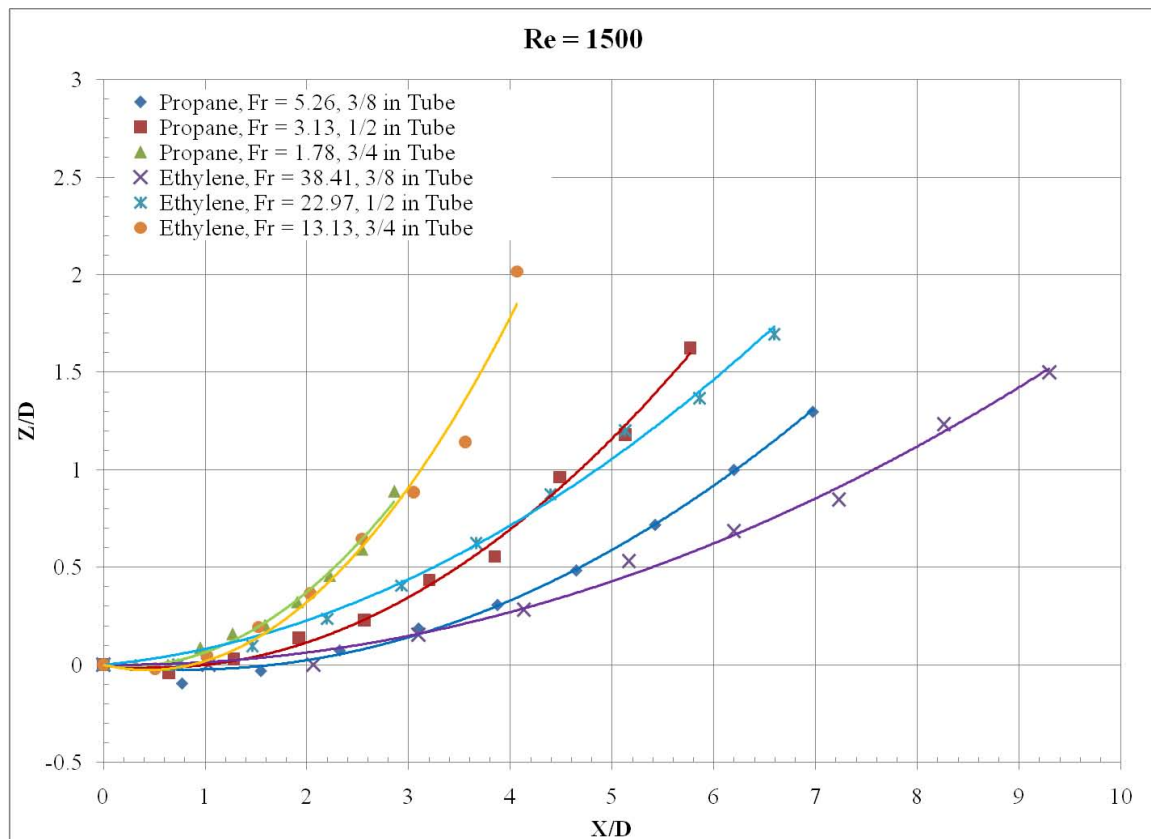
Figure 59. Re = 1500, Bottom Edge Trajectories, PLIF Data

Another interesting observation was the tendency for the trajectories of jets similar in Reynolds number and tube size to cross over each other, as seen in Figure 59 for the 1/2 and 3/8 inch tube cases. In these cases the propane jets started out with flatter trajectories, and then hit a point where they began to turn faster than the corresponding ethylene jets. These findings were attributed to the variations in density and velocities. At locations close to the exit of the tube it was predicted the propane core had not been heated to the point where its density was less than that of air. Therefore, the negative buoyancy of the heavier propane dominated. Eventually the jets both reached a point where they had approximately the same temperature and density. After this was achieved, it was expected the driving force for trajectory was the momentum. Because the ethylene jets required higher initial exit velocities in order to match tube Froude numbers, they have a lower turning rate after the point where the two jets appear to have the same density.

Prior to testing it was hypothesized the ethylene jets would turn vertical more rapidly due to their lower density with respect to air. However, testing revealed this was not the case. In all of the Reynolds number of 1000 and 1500 cases, the ethylene jets had an overall slower turning rate than the corresponding propane jets. Therefore, since the reacting Froude numbers were speculatively the same, as deduced from Figure 57's findings, the differences in the jets were attributed to different reacting Reynolds numbers. It was predicted the reacting Reynolds number for propane cases was lower than the corresponding ethylene cases.

The final three plots created represent constant tube Froude numbers for propane only. Figure 60 shows the bottom edge trajectories for three tube flows with Froude

numbers equal to 0.5. With such low flow rates, all three of these jets were extremely

susceptible to outside perturbations such as air currents. As such, the bottom edge

trajectory plots were inconclusive. Clearly, all three of these jets were buoyancy

dominated. With tube Froude numbers equal already less than unity, it was predicted the

reacting Froude numbers would have been even lower. As the fuel reacts and heats up,

the density will decrease, and the buoyant force will get stronger. Furthermore, as the jet

reacts and expands, momentum will be lost, further lowering the Froude number.
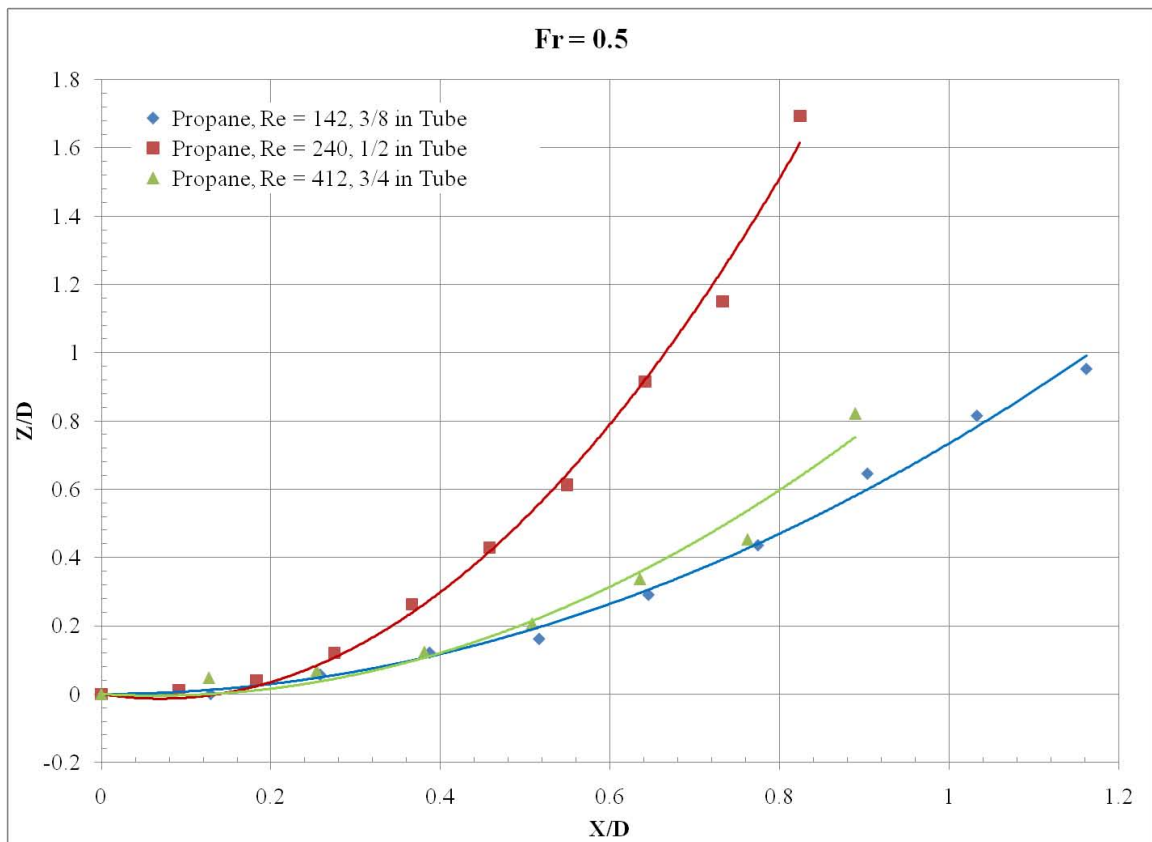
Figure 60. Fr = 0.5, Bottom Edge Trajectories, PLIF Data

Figure 61 represents the propane jets with tube Froude numbers equal to 1.0, or

unity. In these jets the momentum force was equal to the buoyant force at the exit of the

tube. Therefore, regions further downstream appeared to have Froude numbers less than

1.0. One interesting observation made was the bottom edge trajectories for these three jets were very close to each other, regardless of their different Reynolds numbers, as seen in Figure 61. Although the curve fits do not perfectly align, the data points up to 1.0 D downstream were all nearly on top of each other and the curves are generally in good agreement.
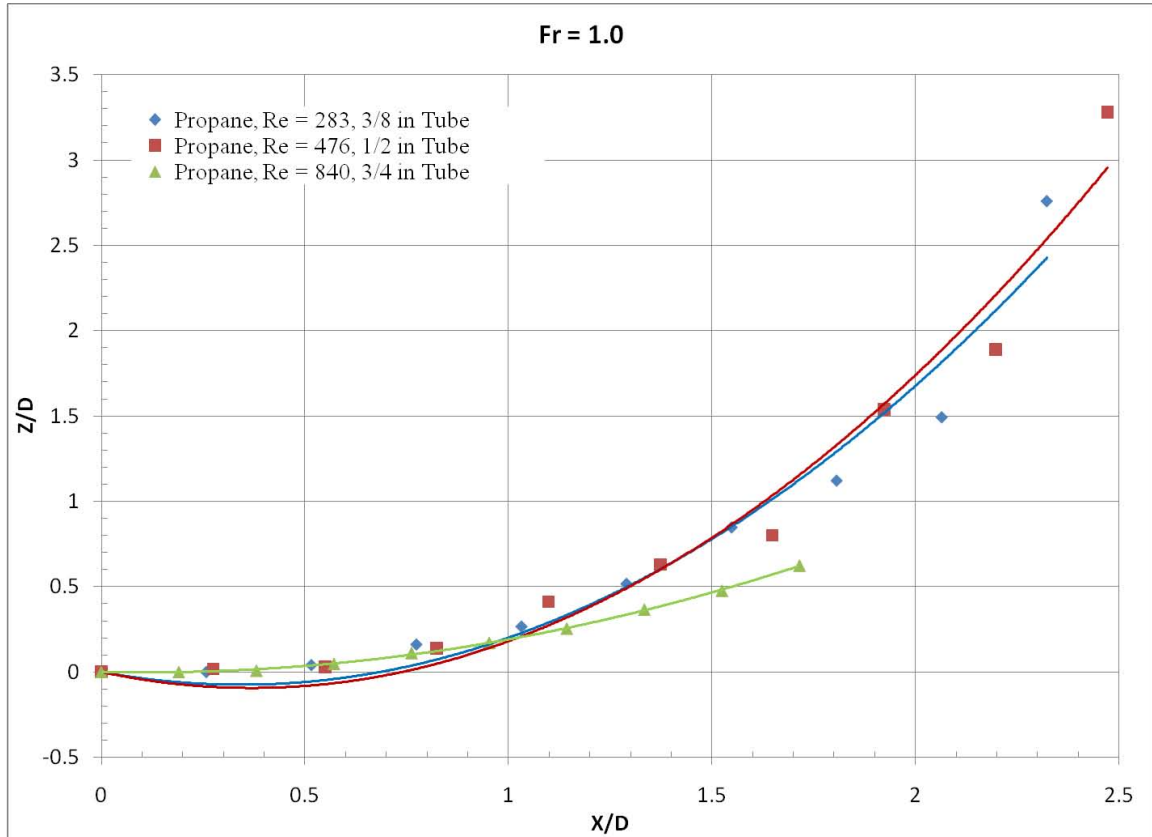
Figure 61. Fr = 1.0, Bottom Edge Trajectories, PLIF Data

Figure 62 created from the PLIF data represent propane jets with tube Froude numbers equal to 1.5. In these jets, the flow rates were 1.5 times larger than those jets observed in Figure 61. In these three jets the jets with the higher Reynolds numbers had lower turning rates. This is what was expected of all the constant Froude number cases; however, these were the only jets to behave as expected. Therefore, it was concluded jets

105

defined by tube Froude numbers greater than one were most heavily influenced by the

momentum or exit velocity of the jet, while the dominating factors in jets with tube

Froude numbers less than 1.0 were dominated by buoyancy.
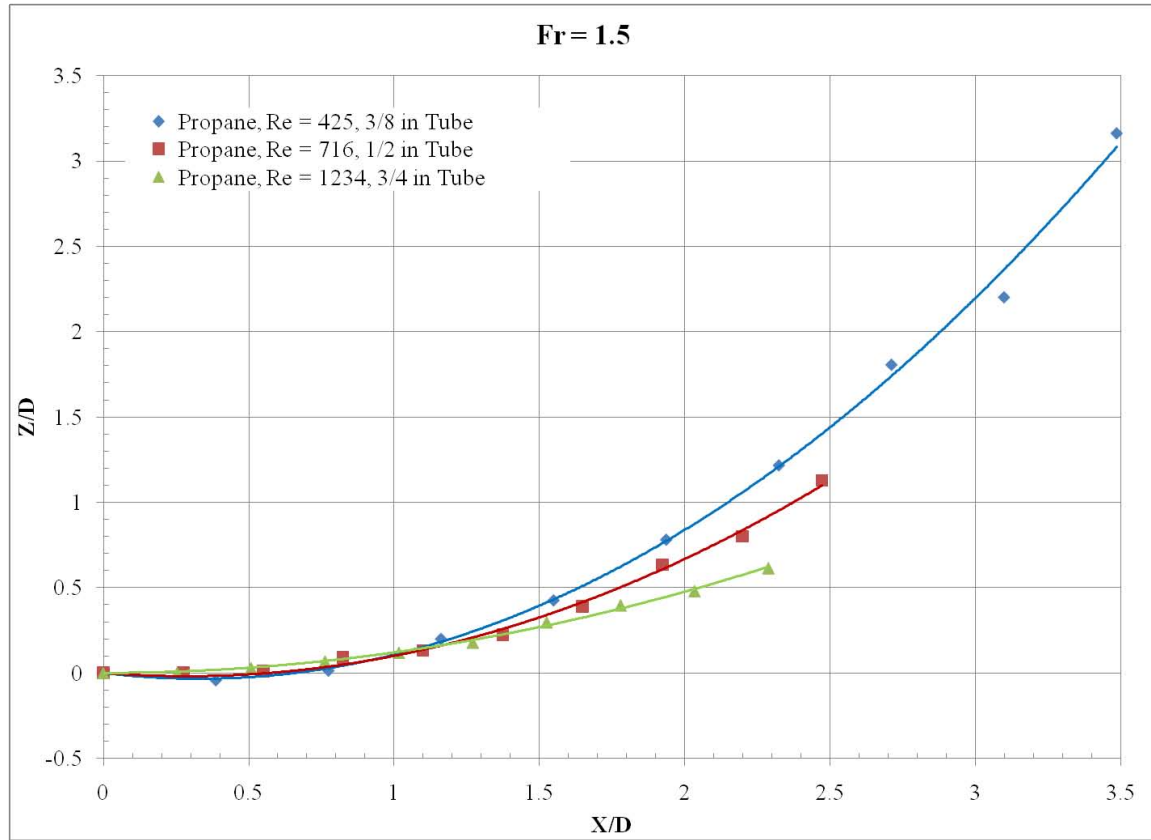
Figure 62. Fr = 1.5, Bottom Edge Trajectories, PLIF Data

IV.2.8. Comparison with Non-Reacting Jets

Overall, the PLIF data showed a remarkable similarity to some of the cold flow

data collected by Reeder, et al, seen in Figure 63 and Figure 65. That study focused on

classifying the effects of positively and negatively buoyant, non-reacting, jets. Helium

and CO_2 jets were produced; however, it was the lighter, more buoyant, helium jets that

were more comparable to the PLIF data (16). Although propane and ethylene were on the

order of, and heavier than air, respectively, both portrayed lighter than air properties due to the temperature effects on density.
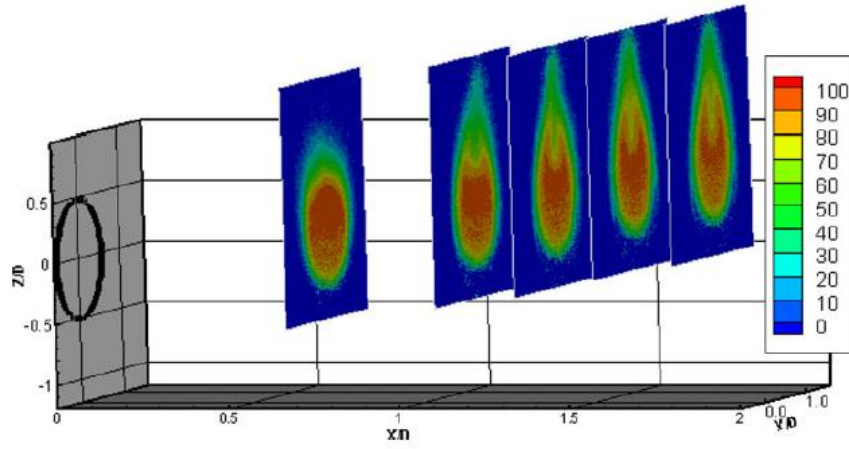
Figure 63. Helium Jet Cross-Sections, Re = 161, Fr = 1.14, 16.7 LPM (16)

Figure 64 provides an example of similar trends observed between the cold flow data and the reacting jet data. From the cold flow data, two overall similarities were observed. First, the overall cross sectional shape of the flame, as well as the non-reacting jet, was teardrop in nature. In both cases, the jets started off in a rather uniform circular shape. As planar interrogation regions further downstream were investigated, it was discovered that the jets started to grow vertically, almost as if a knife edge was extending from the center of the jet and creating a nearly axis-symmetric teardrop shape.
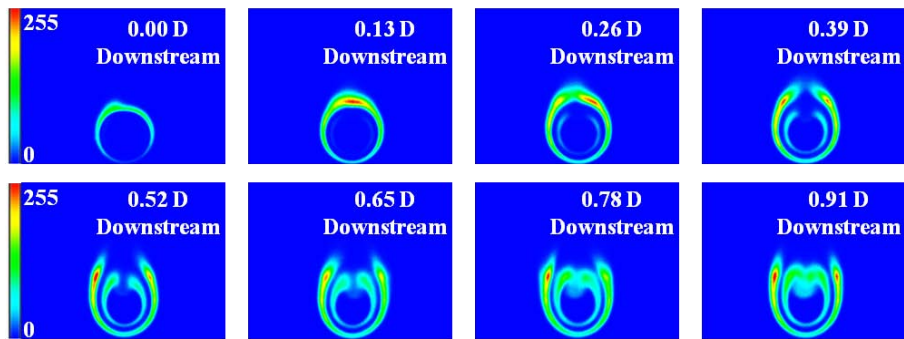
Figure 64. Case 8 Cross Sections, Cold Flow Comparison

The second similarity observed was the correlation between the inner core breakdown in the reacting jets and the areas where the strongest signals were observed in the cold flow data. In both cases, the top outer edges seem to extend upward. In the cold flow data, this area of higher intensity bifurcated into two spiked regions, growing upward, as seen in Figure 65. In the reacting jets, this area in the inner core was observed to have higher concentrations of OH production. It was hypothesized this area of the cold flow jet had the highest rates of change, or fluctuations in intensity; therefore, the corresponding location within the reacting jet experienced higher mixing, and thus more PAHs production. When the outer edges of the jet joined together at the top of the jet, a knife edge area of high OH production was created.
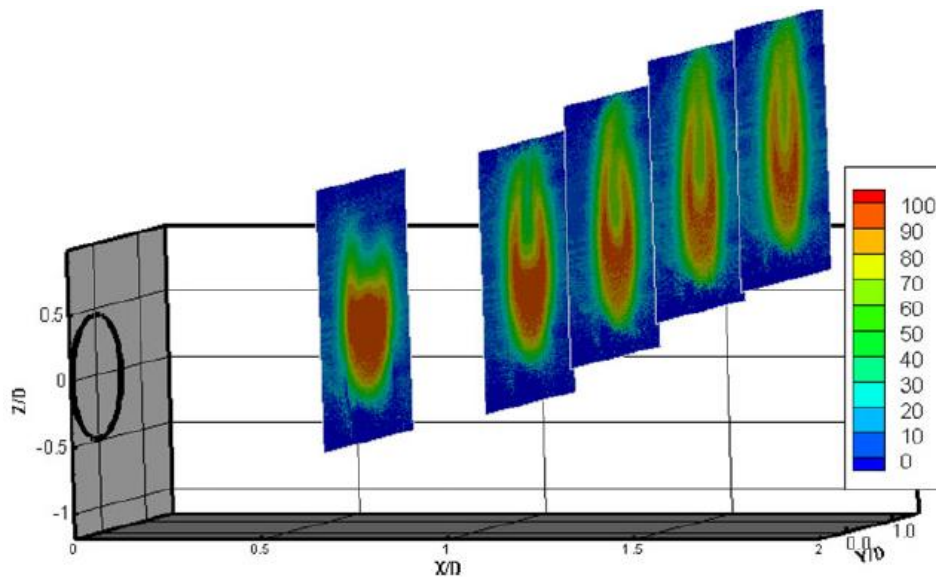
Figure 65. Helium Jet Cross-Sections, Re = 100, Fr = 0.71, 10.4 LPM (16)

In the cold flow experiments, bifurcation was more prominent in cases where the Froude number was less than 1.0 (16). Therefore, it was postulated the reacting jets investigated in this research all contained Froude numbers less than one, as the inner cores all appeared to experience bifurcation, as seen in Figure 66.
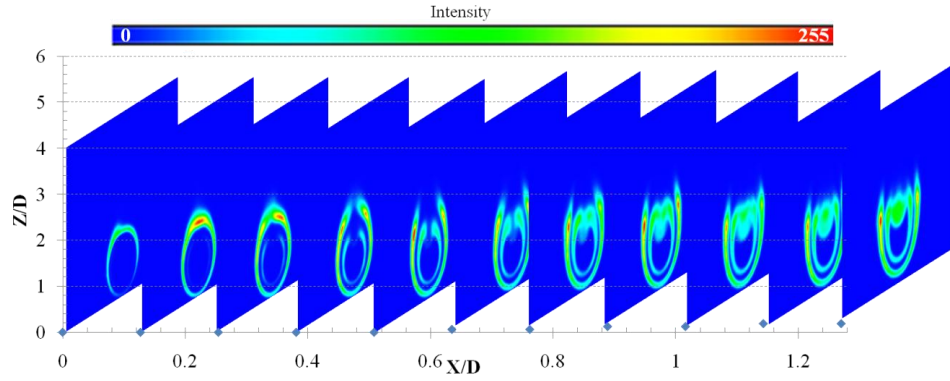
Figure 66. Case 6: Propane, Re = 1000, Fr = 1.19, ¾ in Tube

IV.2.9. Density Analysis

Both the PLIF trajectory results and the cold flow comparison indicated that the tube Froude number was not a good indicator of turning rate. Furthermore, it appeared the reacting Froude numbers were similar across fuel types, as seen in the PLIF trajectory results. The cold flow comparison analysis also indicated the reacting Froude numbers were less than 1.0, because bifurcation was observed within the inner core of all jets. In order to confirm these predictions, the reacting jet density would be needed for every case. Although this data was not experimentally captured, educated predictions were made in order to add merit to the results drawn from the PLIF trajectory results and the cold flow comparison.

Unreacted propane has a density of 1.83 kg/m^3 while unreacted ethylene has a density of 1.17 kg/m^3 at room temperature. Therefore, differences in trajectories were expected simply due to the fact that propane is approximately 1.5 times denser than ethylene. However, the PLIF trajectories indicated similar reacting densities. Using GasEq, densities of premixed flames were calculated for a range of equivalence ratios as well as their corresponding viscosities. Table 6 shows these densities and viscosities as well as the percent difference between the two fuels.

Table 6. Comparison of Density and Viscosity for Propane and Ethylene

Equivalence Ratio	Propane Density (kg/m³)	Ethylene Density (kg/m³)	Density Difference	Propane Viscosity (kg/m-s)	Ethylene Viscosity (kg/m-s)	Viscosity Difference
0.5	0.231	0.219	4.92%	5.5E-05	5.7E-05	4.17%
0.6	0.204	0.194	4.91%	6.0E-05	6.2E-05	4.03%
0.7	0.185	0.176	4.77%	6.4E-05	6.6E-05	4.09%
0.8	0.169	0.162	4.41%	6.7E-05	7.0E-05	3.73%
0.9	0.158	0.152	3.74%	7.0E-05	7.2E-05	3.29%
1	0.151	0.146	3.22%	7.2E-05	7.4E-05	2.93%
1.1	0.149	0.143	3.99%	7.2E-05	7.4E-05	3.50%
1.2	0.150	0.142	5.39%	7.0E-05	7.3E-05	4.86%
1.3	0.153	0.143	6.43%	6.8E-05	7.2E-05	5.71%
1.4	0.156	0.144	7.25%	6.7E-05	7.1E-05	6.47%
1.5	0.159	0.146	8.00%	6.5E-05	6.9E-05	7.10%

Interestingly, the reacting densities and viscosities of propane and ethylene are very similar. This is most likely because both are hydrocarbon fuels which produce the same types of products. Table 6 shows the difference in density and viscosity is less than 5% for the most part, while all differences were less than 8%. This information can be used to predict the reacting Reynolds and Froude numbers for the 27 cases investigated. However, it is important to note the density of the jet is constantly changing, and also varies with axial location; locations further downstream are expected to have higher densities because more of the fuel in the core will be reacted. In order to predict the reacting Reynolds and Froude numbers corresponding to the 27 test cases, an average equivalence ratio of 1.0 was chosen. Table 7 shows the predicted reacting Reynolds and Froude numbers based on an average phi of 1.0 and the corresponding densities and viscosities found in Table 6. In all cases the reacting Reynolds number is nearly 100 times smaller than the colder flow Froude number. This is due to the viscosity within the jet rising nearly two orders of magnitude as a result of combustion, as well as a reduction in density. Similarly the reacting Froude numbers are approximately 4 times smaller for

the propane and 15 times smaller for the ethylene. This is due to the density change

within the jet as a result of combustion.

Table 7. Estimated Reacting Reynolds and Froude Numbers

Case Number	Reacting Reynolds Number	Reacting Froude Number	Tube OD	Flow Rate (SLPM)
1	3	0.24	3/8 in	0.49
2	3	0.14	1/2 in	0.69
3	3	0.08	3/4 in	0.99
4	9	0.79	3/8 in	1.62
5	9	0.48	1/2 in	2.29
6	9	0.27	3/4 in	3.30
7	14	1.20	3/8 in	2.44
8	14	0.71	1/2 in	3.43
9	14	0.41	3/4 in	4.95
10	1	0.11	3/8 in	0.23
11	2	0.11	1/2 in	0.55
12	4	0.11	3/4 in	1.37
13	3	0.23	3/8 in	0.46
14	4	0.23	1/2 in	1.09
15	8	0.23	3/4 in	2.79
16	4	0.34	3/8 in	0.69
17	7	0.34	1/2 in	1.64
18	12	0.34	3/4 in	4.10
19	5	0.47	3/8 in	0.98
20	5	0.28	1/2 in	1.38
21	5	0.16	3/4 in	2.01
22	18	1.57	3/8 in	3.27
23	18	0.94	1/2 in	4.62
24	18	0.55	3/4 in	6.70
25	27	2.36	3/8 in	4.91
26	27	1.41	1/2 in	6.93
27	27	0.82	3/4 in	10.05

IV.3. High Speed Imaging Results

In addition to PLIF data, two different types of high speed images were captured –

unfiltered raw images, and CH[*] filtered images. In both cases, the respective images

captured were averaged together to produce figures resembling the general behavior of

111

the jets. Figure 67 shows an example side by side comparison of the filtered and unfiltered images produced. These images were subsequently used to track the bottom edge trajectories, as well as for qualitative analysis. Both unfiltered and filtered images were collected for all 27 cases; the resulting figures can be seen in Appendices B and C, respectively.
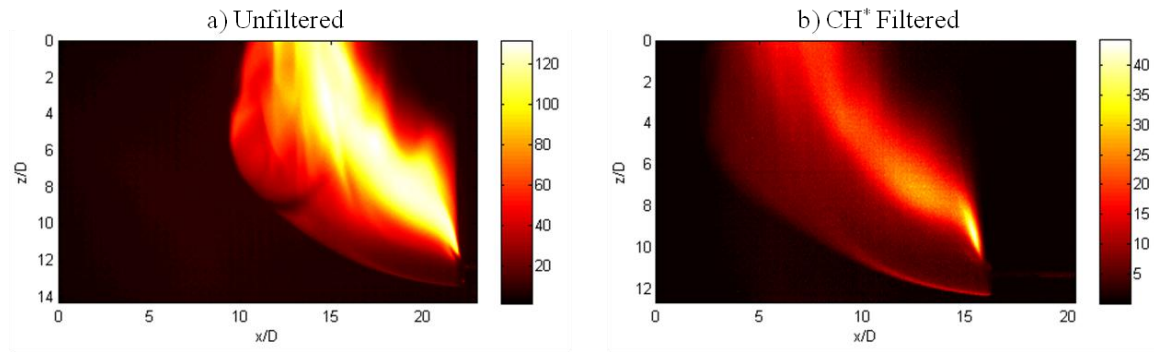
Figure 67. Case 26, Unfiltered and Filtered High Speed Images

IV.3.1. Trajectory Results

The first type of analysis conducted with these results was a comparison to the PLIF data. Figure 68 shows an example bottom edge trajectory plot created, comparing all three types of data collection – PLIF, unfiltered, and filtered. In Figure 68 each color represents a different test case, while the different types of lines correlate to the respective type of data collection. Overall, the high speed imaging results appeared to confirm the findings from the PLIF data. Therefore only two high speed trajectory figures were provided in this section. However, trajectory plots were calculated and created for all 27 cases and can be found in Appendix D. Although the general trends were maintained for most cases, there was no apparent correlation between the type of data collection method used and the predicted trajectory with respect to the other two types of

112

collection. For example, the PLIF data did not consistently under predict the trajectory.

Prior to testing it was hypothesized the CH[*] filtered trajectories would be contained

within (above) the unfiltered trajectory due to unfiltered collecting mostly blackbody soot

intensities; however, this was not the case, as seen in Figure 68 and Figure 69.
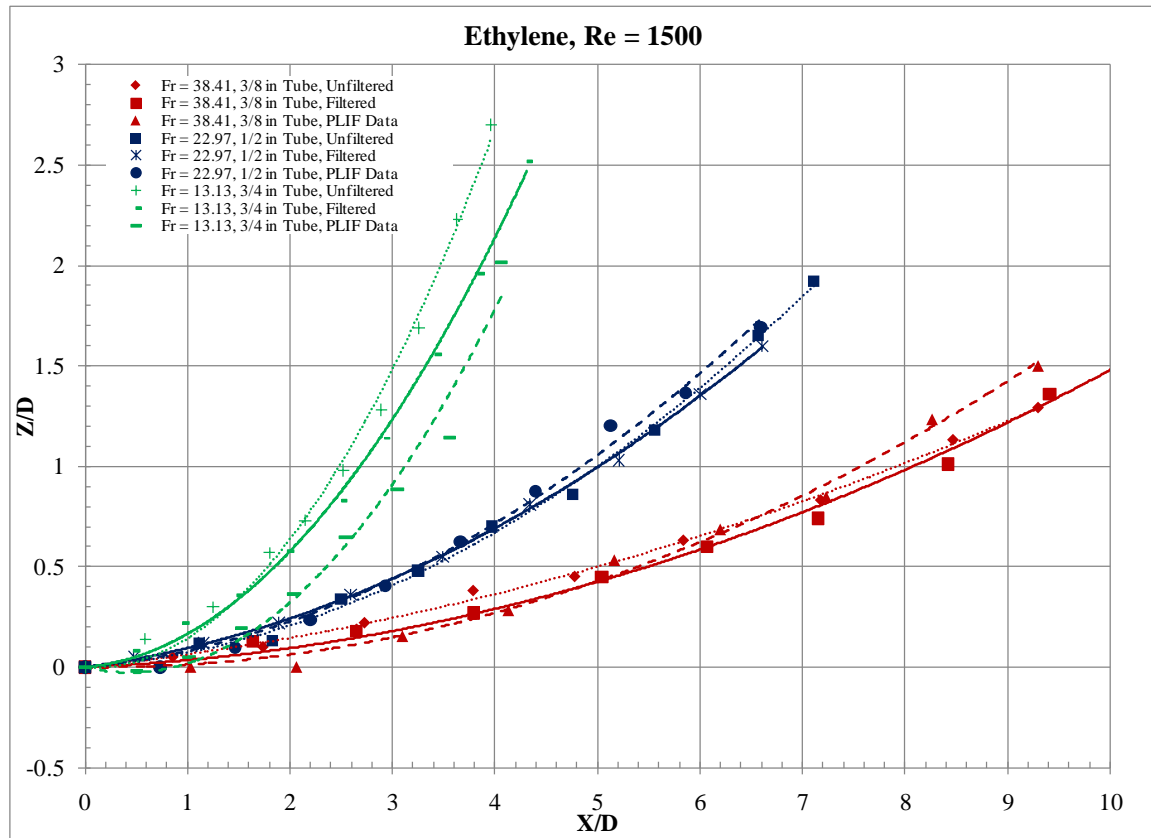
Figure 68. Ethylene, Re = 1500, Bottom Edge Trajectories, Cases 25, 26, and 27

Although the general trends were maintained across the different types of data

collection, differences were observed within the respective cases. These differences were

most likely due to the inconsistency of the flame. Although all images were time

averaged, the amount of time data was collected for each method was different. With the

PLIF, data was collected for 20 seconds, at 10 Hz per test location; therefore, the flame

had time to change between test points, but a good general trend was captured. With the

unfiltered high speed imaging, frames were captured at 6200 fps. Due to computing

constraints, approximately 600 images were averaged together to capture the general

behavior. These 600 images equate to a time span of approximately 1/10th of a second,

the temporal spacing between two consecutive PLIF images. Finally, the filtered images

were collected at 100 fps, and 200 images were then averaged to find the general

behavior. This corresponds to a 2 second interval. These differences in imaging time

were not a significant factor in the higher flow rate cases, like those seen in Figure 68.

However, when the flow rates were small, the flames were less consistent, and

consequently the trajectory results had a larger margin for error as seen in Figure 69.
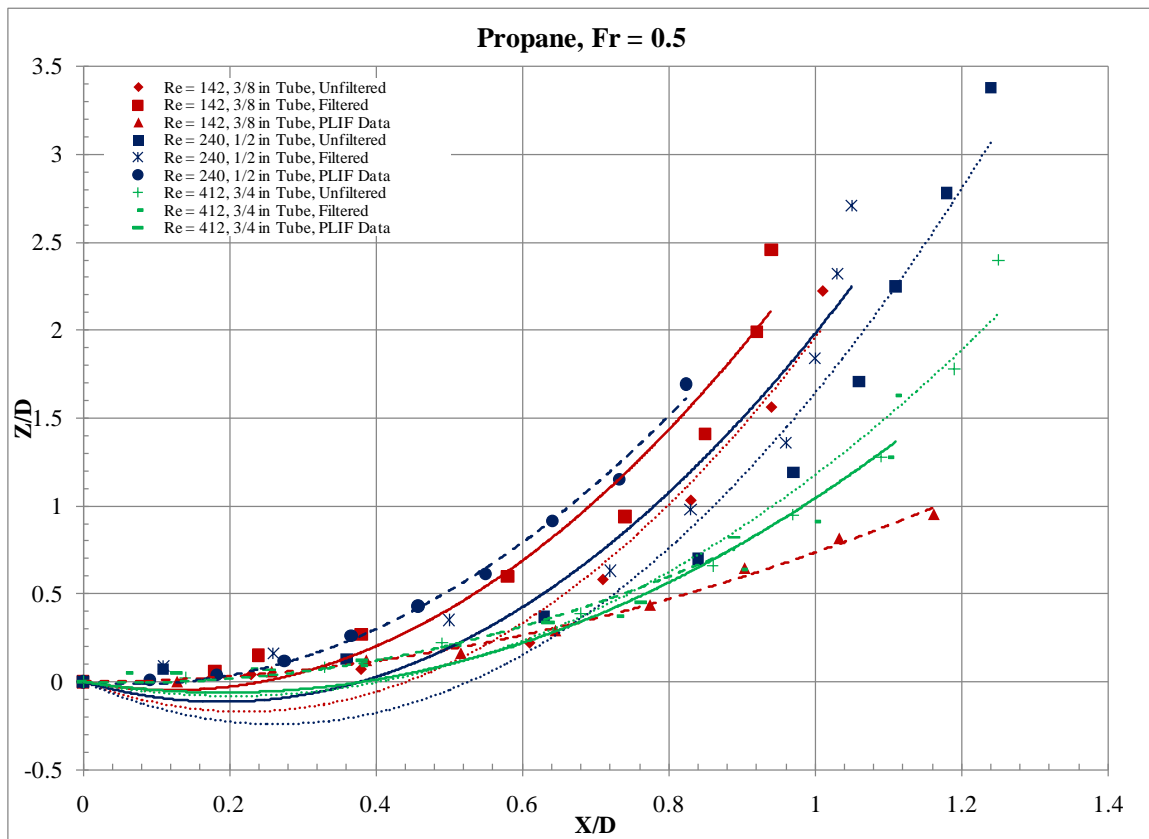
Figure 69. Propane, Fr = 0.5, Bottom Edge Trajectories, Cases 10, 11, and 12

Initially, the results presented in Figure 69 seem surprisingly inconsistent across test cases. However, it was important to remember the PLIF data for cases 10, 11, and 12 presented in Figure 60 were also found to be inconclusive. Thankfully, through the implementation of high speed imaging, further insights into these inconsistencies were drawn. Upon investigation of the corresponding high speed figures produced, seen in Figure 70, it was found these cases all turn vertically almost instantly. In fact, within 1 diameter downstream, all three test cases had turned completely vertical. This phenomenon was observed in both the unfiltered and the filtered test results.
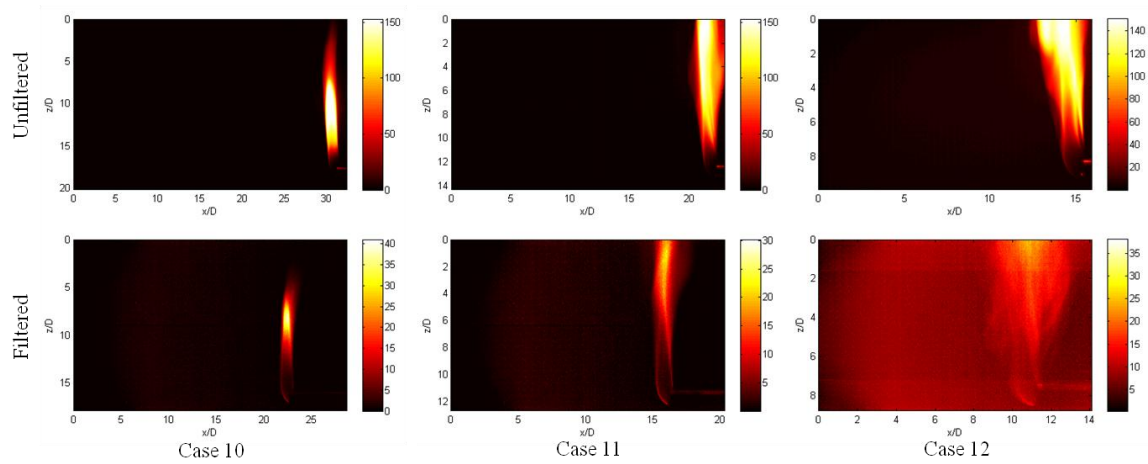
Figure 70. Reacting Propane Jets, Fr = 0.5

Because these jets had such low flow rates and turned vertically nearly immediately, it was difficult to find the trajectories. In essence these jets ceased to be horizontally issuing and became vertical flames and therefore did not provide significant insights into the characterization of horizontally issuing buoyant jets.

IV.3.2. Correlations to PLIF Data

The final type of analysis conducted was an effort to show how the planar interrogation regions from the PLIF data related to the corresponding high speed images.

Figure 71 shows how the interrogation planes of case 8 corresponded to the unfiltered figure. In this, and similar subsequent figures, the dashed vertical white lines represented the location and size of the PLIF interrogation regions. The solid white line represented the top of the laser sheet, thus the region below this line identified the actual region PLIF data was collected.
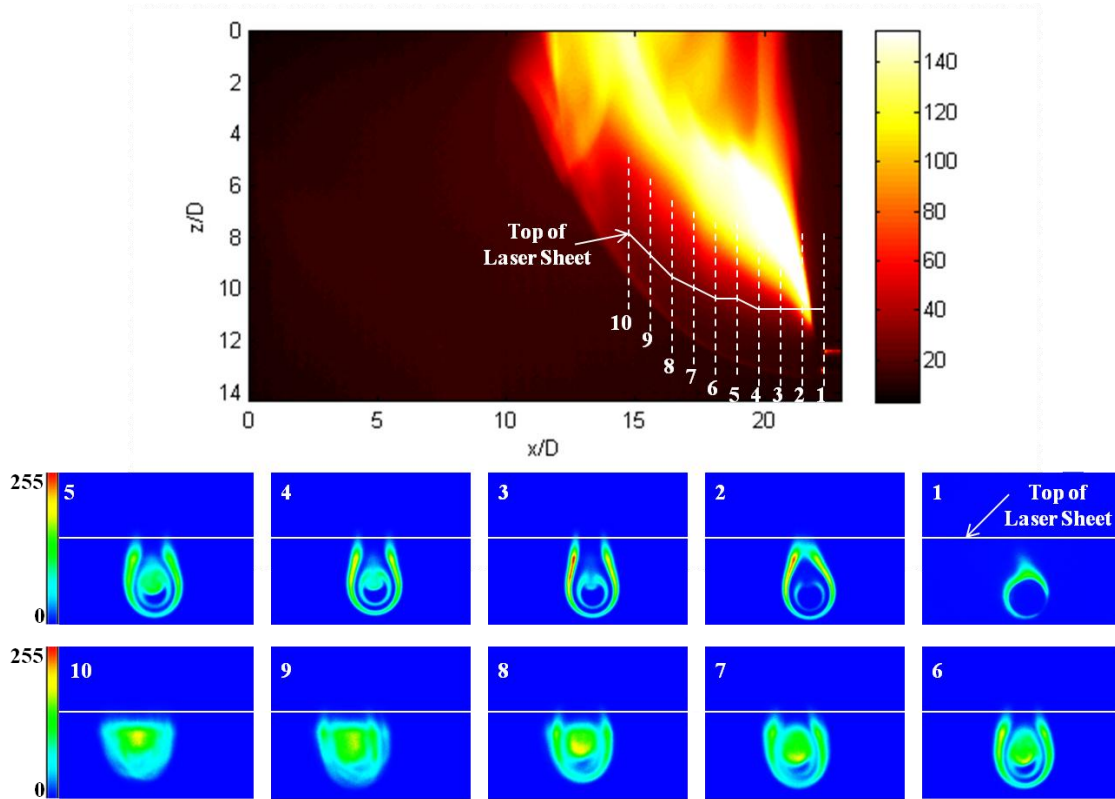
Figure 71. Unfiltered & PLIF Data, Case 8: Re = 1500, Fr = 3.13, ½ in Tube

In Figure 71 most of the signal strength of the high speed image was the result of soot emissions. Because most of the signal strength was the result of soot, regions of highest intensity in the high speed image did not necessarily directly relate to areas of high OH concentration, or combustion. One interesting observation was the strong signal at the top edge of the jet. Looking at the first three interrogation planes, this line of

116

intensity seemed to relate the area where the two sides of the flame came back together to form a sort of knife edge.

In order to gain a better understanding of how the high speed images related to the PLIF data, the filtered images were used. Prior to testing it was hypothesized CH^* and OH would exist in similar regions due to their short existence as intermediate products of combustion. When the PLIF data was compared with the filtered images, the results were similar to those observed in Figure 71. Figure 72 shows there was still an area of high intensity on the upper edge of the jet. From observations made on all three types of data collection, it was apparent a large majority of the combustion was occurring on the upper edges of the jets. However, these regions were outside the bounds of most interrogation planes.
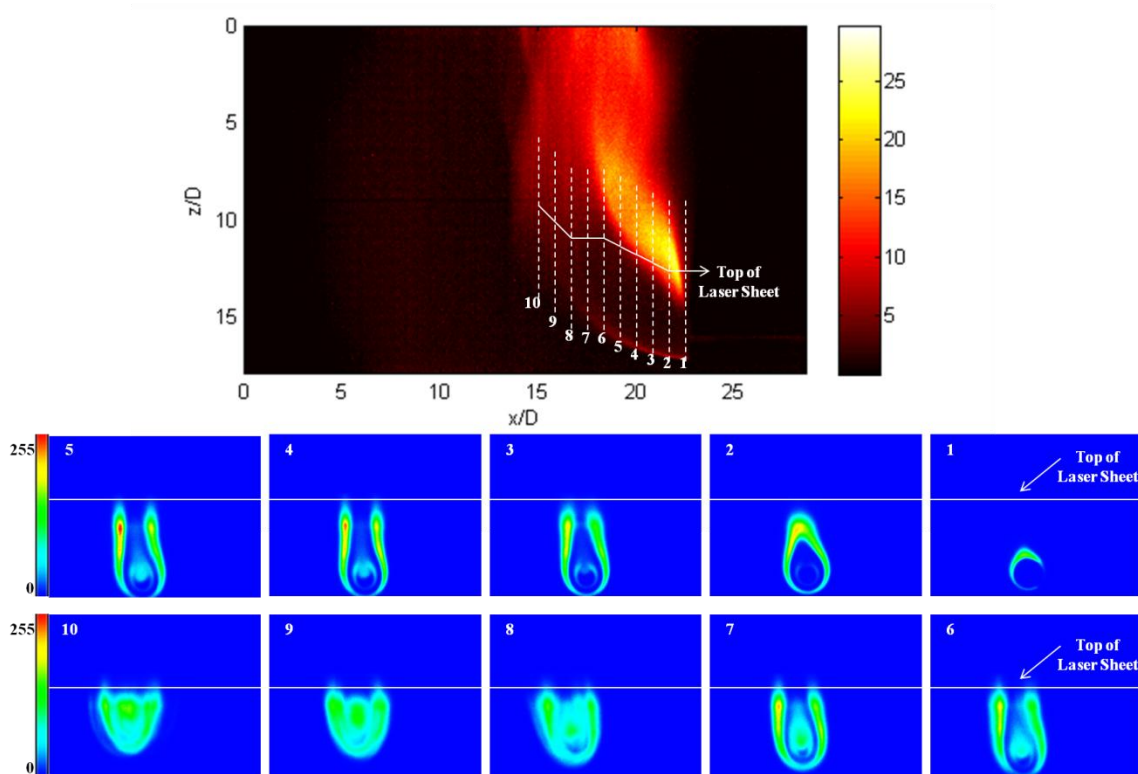
Figure 72. CH* Filtered & PLIF Data, Case 4, Propane

Similar results were observed for both the propane and the ethylene, as seen in Figure 72 and Figure 73. Again, a strong knife edge was observed almost immediately after the exit of the tube and continued nearly 5 diameters downstream. Similarly, this knife edge appeared to coincide with the merging of the outer edges of the combusting jet.
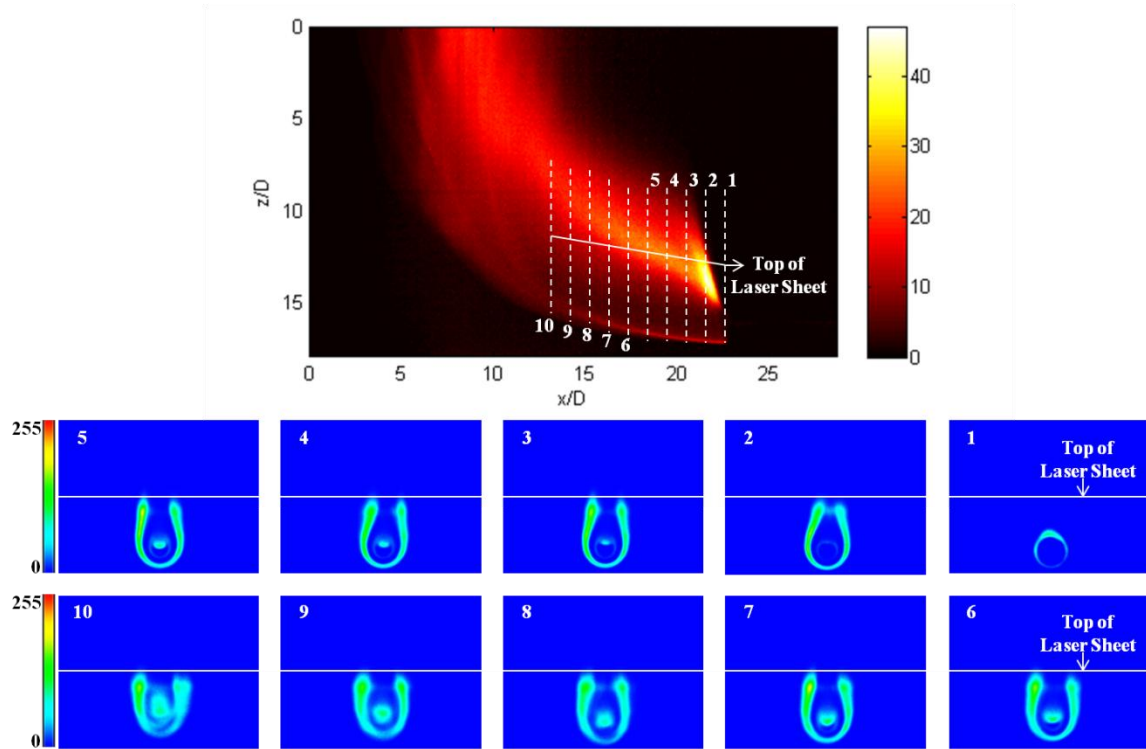
Figure 73. CH* Filtered & PLIF Data, Case 25, Ethylene

Based on observations drawn from all three types of data collection it was predicted that the areas of higher intensity of CH* are related to higher regions of OH production. Therefore, the knife edge was the result of two highly reacting jet edges reconnecting at the top of the jet. The dark regions below the areas of high intensity were predicted to contain higher concentrations of un-reacted fuel, which was consistent with

the PLIF results. This is why higher intensities were observed on both the upper and the lower surface of the jet. These regions contain the greatest amounts of mixing and thus highest OH productions. Although the edges in the middle region of the flame also experience higher mixing, as shown in the PLIF data, these areas do not appear as intense on the filtered and unfiltered high speed images because the presence of the un-reacted inner core impedes some intensity transmission. Additionally, the CH^* images were in essence representative of an integrated path thru the flame. As such, intensities were a function of path length and signal strength. Therefore, at the sides, the path length of the high signal area is short, thus limiting the intensity, as seen in. The region at the top of the jet is thicker and has stronger signal strength; therefore, this region had the highest intensities. The area at the bottom of the jet is also well defined because it has a larger path length than those regions in the middle of the jet.
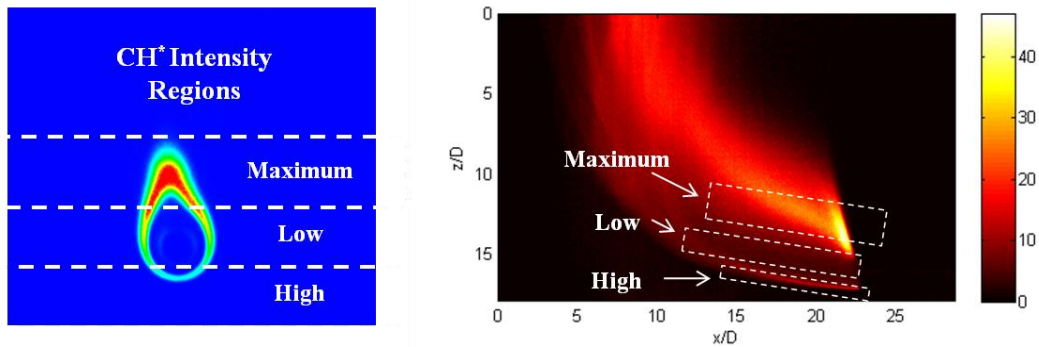
Figure 74. CH^* Intensity Regions

V.   Conclusion

V.1.   Main Takeaways

Characterization of combusting, horizontally issuing, buoyant jets was achieved through a series of OH PLIF, unfiltered, and CH^* imaging experiments. In total, 27 cases were investigated, encompassing two fuels, propane and ethylene. These cases had tube flows with Reynolds numbers ranging from 300 to 1500 and tube Froude numbers ranging from 0.5 to 36. All jets produced displayed characteristics indicative of positively buoyant jets. Even propane, which is denser than air turned vertical due to the effects of combustion. In all cases, increased mixing rates were also observed on the upper regions of the inner core due to instabilities resulting from density fluctuations. These results were consistent with past research suggesting higher mixing rates on the side of the jet with greater instabilities. Additionally, increased OH and CH^* production was observed on the upper edges of the jet.

Perhaps the most interesting discovery was the different regions observed within the horizontally issuing buoyant jet. Prior to experimentation it was expected the cross sectional PLIF images would portray a continuous range of intensities produced from very rich combustion near the core to very lean combustion at the outer edges of the jet; however, this was not the case. Although both combustion regimes were observed, there was an intermediate layer where there appeared to be no OH production. This region was hypothesized to be comprised of the air being entrained from the top of the jet, or possibly the byproducts of rich combustion occurring at the edges of the inner core, or some combination of the two scenarios. However, further analysis revealed this region was actually the result of PAH production.

Furthermore, numerous other similar phenomena were observed within the different jets. In all cases, the inner cores exhibited two traits. First, all of the inner cores seemed to experience some level of elongation as they propagated downstream. Additionally, the inner cores had a methodical breakdown, with axial distance. The rate of inner core breakdown was strongly related to the amount of initial momentum present in the tube flow. Jets with higher momentum rates required more axial distance to fully breakdown, while jets with lower momentum had almost immediate breakdown.

Although a more exact description of the phenomena surrounding the changes in jet cross section, especially the inner core, could not be provided, many similarities were found between different jets as well as past research. Additionally, the cross sectional PLIF images provided new insights into the progression of a horizontally issuing buoyant jet.

Implementing PLIF to capture OH intensities in a plane normal to the jet was necessary to determine how the jet cross section changed with axial distance. This was significant because most past studies analyzed data gathered only in the plane of symmetry, much like the high speed images captured in this research. Additionally, most of the past research identified the trajectory of the jet based on the centroid of the jet. Due to the limitation of a 40 mm laser sheet, this was not possible. Therefore, the bottom edge trajectories were calculated and compared across three different types of data collection. The data collected suggested the jet trajectory was mostly dependent upon the initial momentum of the fluid, which can be related to the tube Reynolds number and the exit velocity. Tube Froude number did not seem to be a significant factor influencing trajectory. It was hypothesized that the tube Froude number was insignificant because the

121

reacting Froude numbers in all the jets produced were similar. Naturally, this finding was quite different to the results found in past cold flow tests indicating a correlation between Froude number and trajectory. While cold flow Froude number may have impact on the trajectory, it was concluded to be significantly less than the effects resulting from the jets initial momentum.

Finally, and possibly most importantly, these results confirm the effectiveness and usefulness of performing cold flow experiments. Throughout the experimentation process, numerous similarities were observed between the reacting jets and the non-reacting cold flow jets. If parallels could be drawn between the reacting Froude numbers and the cold flow Froude numbers, it may be possible to use cold flow data to predict how a reacting jet will behave. This is important because cold flow experiments are less complex, thus offering a better first step into the analysis of possible combustion applications.

With respect to the UCC efforts being conducted at the AFIT, these findings provide merit to current investigations of cold flow testing in a new, up scaled, UCC. By knowing how the cold flow will react, inferences can be made into the behavior of a reacting jet.

V.2. Future Work

The results found in this experiment provided many insights into the structure of horizontally issuing buoyant jets. Moreover, they can be used as a stepping stone for further work and analysis.

With respect to the current experiment, more work could be done to expand the characterization of horizontal jets. Due to equipment failures, only the bottom edge of the

jets was tracked. Initially the bottom edge of the jet was tracked in order to provide trajectory data; however, before other regions could be tracked, the Nd:YAG laser stopped working. It would be interesting and beneficial to track the jet in the region where the peak CH^* intensities were observed in order to determine what is occurring within these regions. It would be noteworthy to determine if the jets continued to come to a sharp point as hypothesized, or if the jets opened up at the top allowing for air to be better entrained and mixed.

One of the major limiting factors in this research was the 40 mm laser sheet height. This restricted height limited the size of the interrogation plane. One suggested solution to this problem was to use a mirror to turn the laser sheet such that it intersects the jet from the bottom and then moves in a vertical direction, instead of the horizontal intersection indicative to this research. Because all of the jets were less than 40 mm wide, the vertical laser sheet could effectively traverse the height of the flame and reveal how the combustion is progressing with axial distance.

One potential problem with this approach would be laser absorption from the bottom of the jet to the top. Because the region of OH production the laser sheet will have to progress thru would increase, the effects of absorption would be more severe than in this research, but the side to side intensities should be similar. In order to combat these effects, more laser energy would be required. Ideally, the laser sheet would contain sufficient amounts of energy such that the OH absorption is basically saturated from the bottom of the flame to the top. In theory, if this threshold were achievable the effects of absorption could be negated because the ensuing laser sheet would still contain enough energy by the time it reached the top of the jet to effectively saturate the OH. In other

words, every OH molecule would be excited. Another solution to this problem would be the implementation of two beams intersecting the jets from opposite directions. If the absorption effects were assumed to be similar from both directions, then the resulting image captured by the camera would depict consistent OH intensities. In order successfully implement this solution, the beam would either have to be split, or another laser would be needed.

The current PLIF setup could also be used to analyze the cross sections of other combustion applications such as the up scaled UCC test section currently being produced by students in AFIT's COAL lab. Even thought the current setup is for horizontally issuing jets, the experimental setup could be easily changed to accommodate for a wide range of both vertical and horizontally issuing applications.

The final suggestion for future work would be the simple analysis of vertically issuing jets. Compared to horizontally issuing jets, these are less complicated and would be easily integrated into the current lab setup. Capturing cross sectional images, similar to those collected in this research, and drawing similarities would be interesting. It is expected the vertical flames would display the same types of regions within the cross sections, but it is possible, the peculiar combustions regions observed in this research were the result of buoyancy effects.

Appendix A: Three-Dimensional OH PLIF Plots
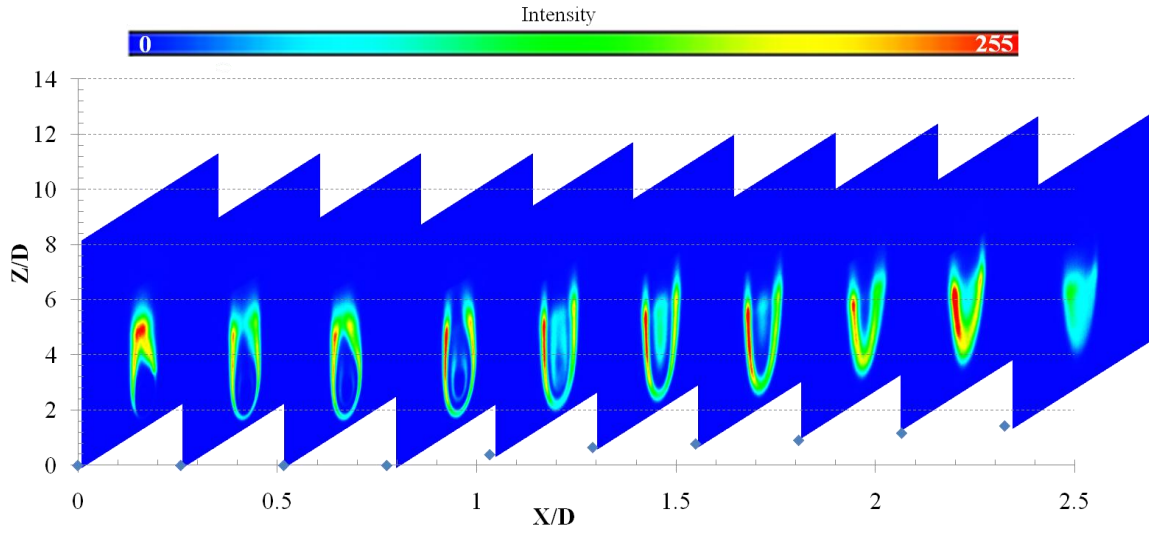
A. 1. Case1: Propane, Re = 300, Fr = 1.06, $^3/_8$ in Tube
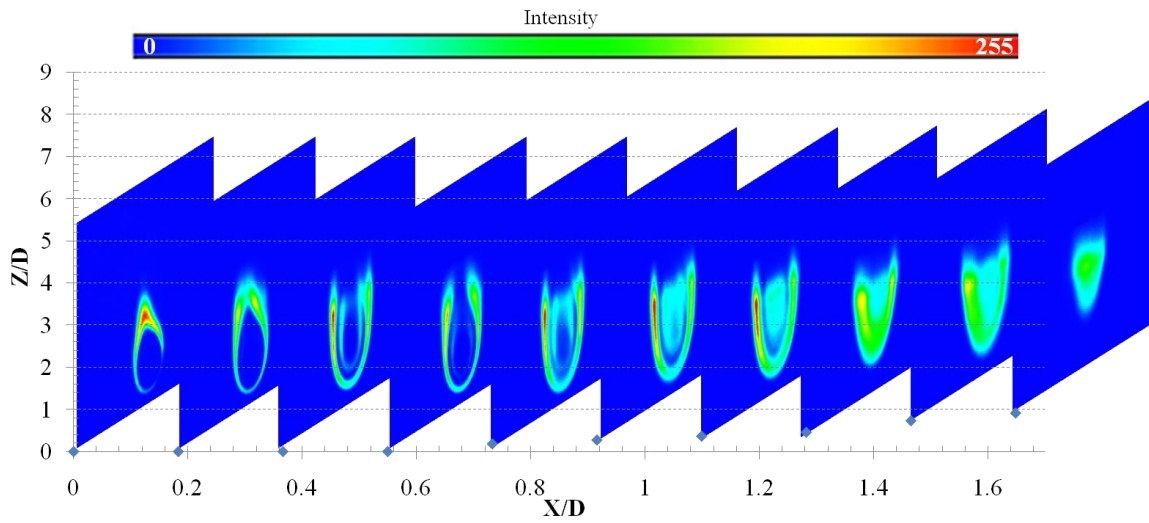
A. 2. Case 2: Propane, Re = 300, Fr = 0.63, ½ in Tube
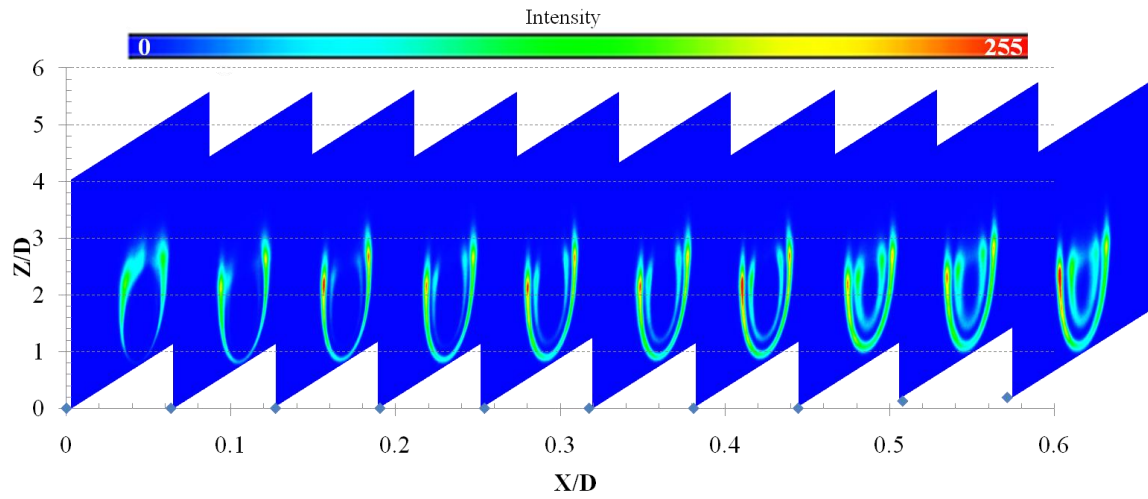
A. 3. Case 3: Propane, Re = 300, Fr = 0.36, ¾ in Tube
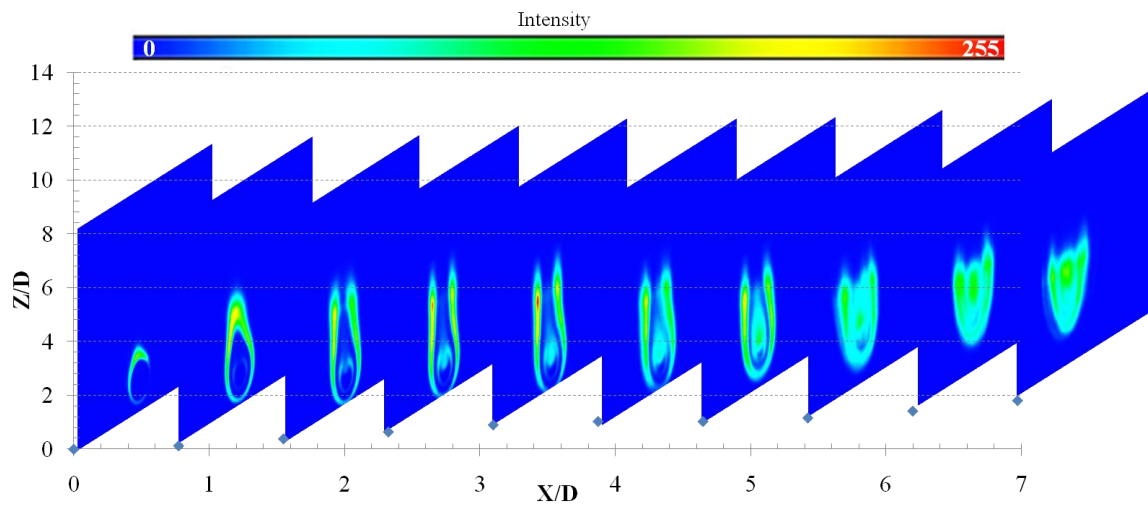
A. 4. Case 4: Propane, Re = 1000, Fr = 3.49, $^3/_8$ in Tube
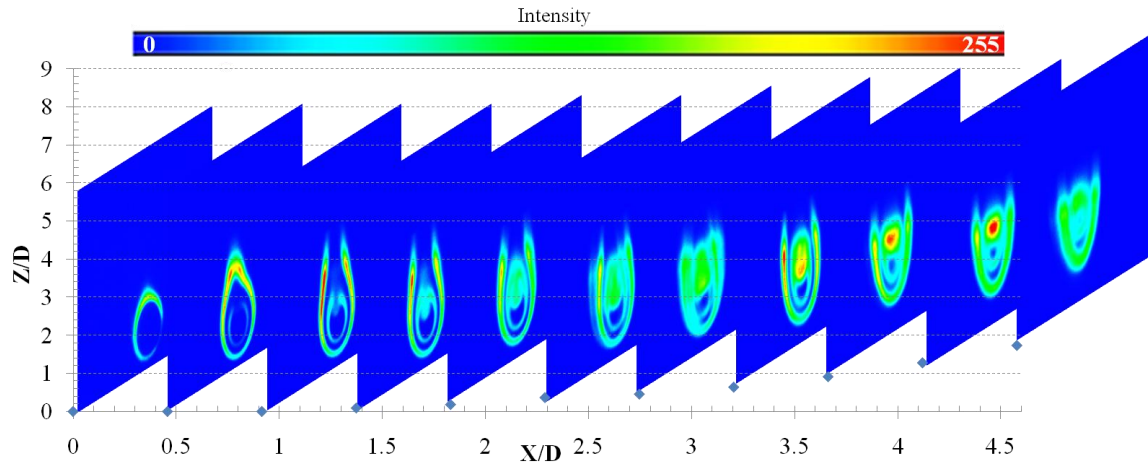
A. 5. Case 5: Propane, Re = 1000, Fr = 2.09, ½ in Tube
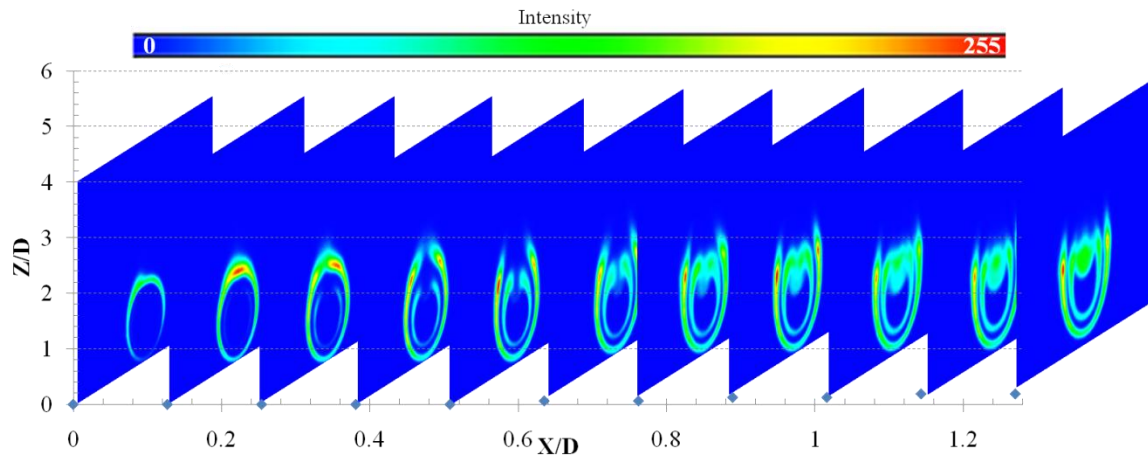
A. 6. Case 6: Propane, Re = 1000, Fr = 1.19, ¾ in Tube

127
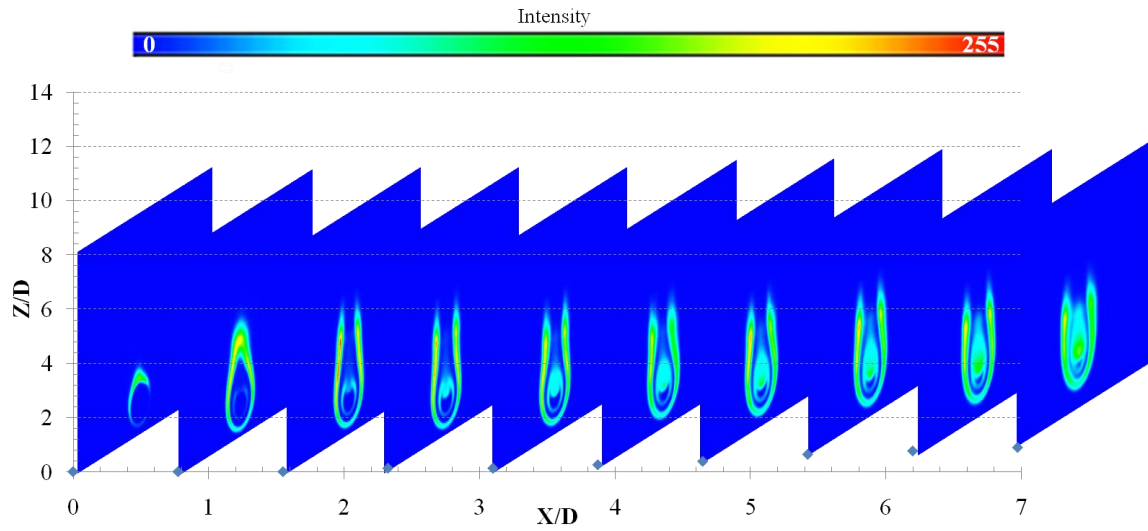
A. 7. Case 7: Propane, Re = 1500, Fr = 5.26, $^3/_8$ in Tube
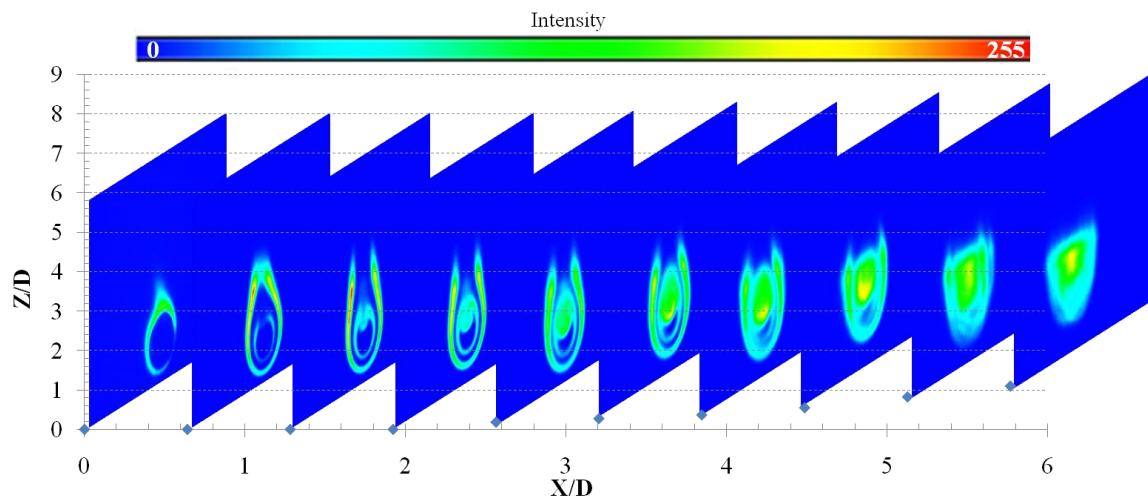
A. 8. Case 8: Propane, Re = 1500, Fr = 3.13, ½ in Tube
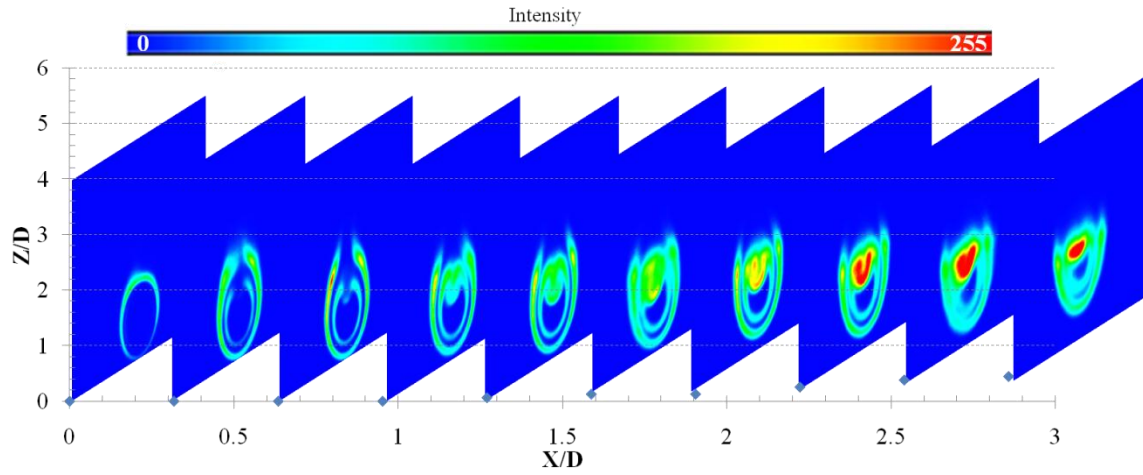
A. 9. Case 9: Propane, Re = 1500, Fr = 1.78, ¾ in Tube
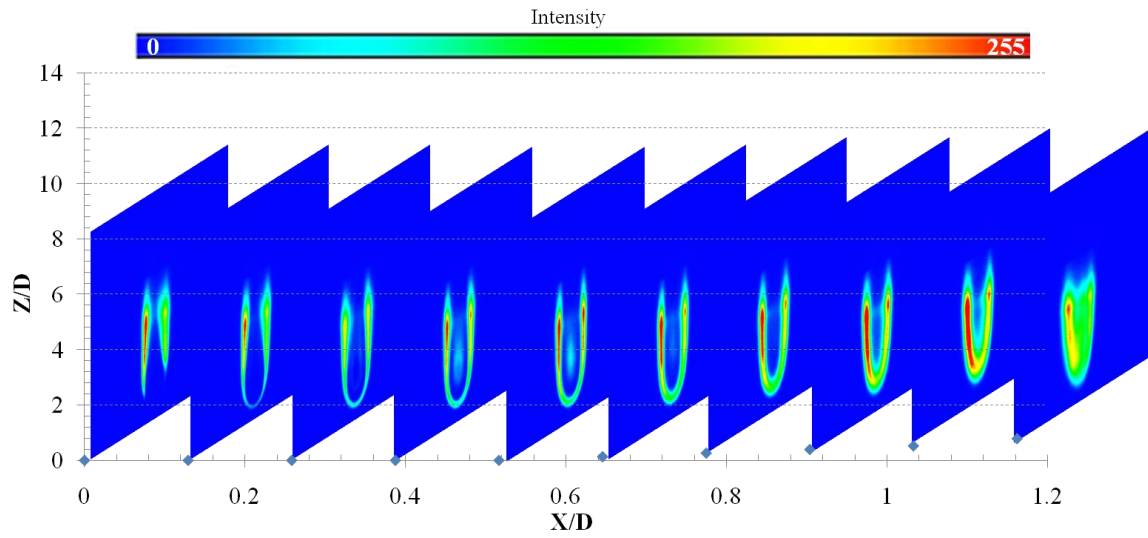
A. 10. Case 10: Propane, Re = 142, Fr = 0.5, $^{3}/_{8}$ in Tube

129
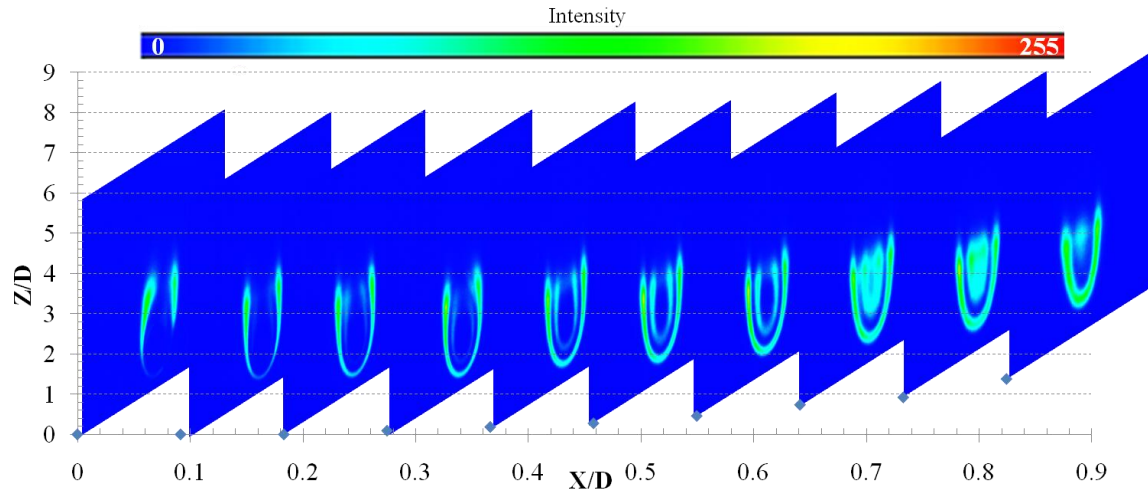
A. 11. Case 11: Propane, Re = 240, Fr = 0.5, ½ in Tube
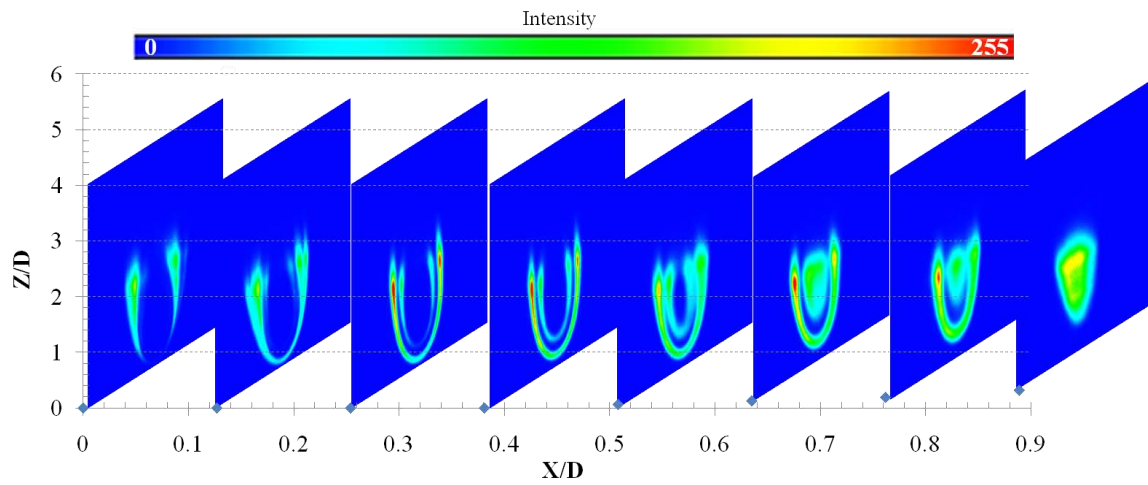
A. 12. Case 12: Propane, Re = 412, Fr = 0.5, ¾ in Tube
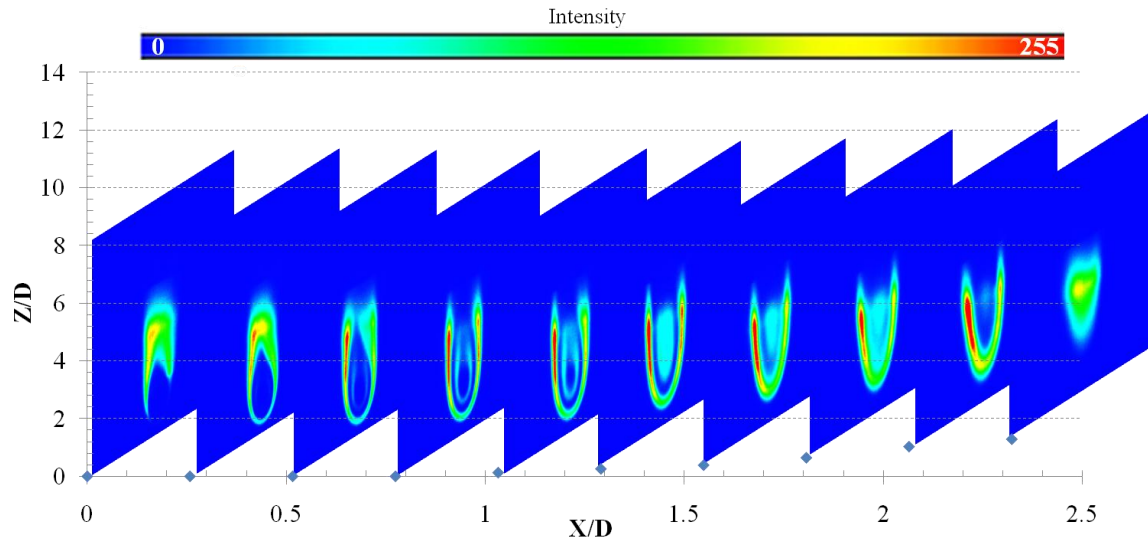
A. 13. Case 13: Propane, Re = 283, Fr = 1.0, $^3/_8$ in Tube
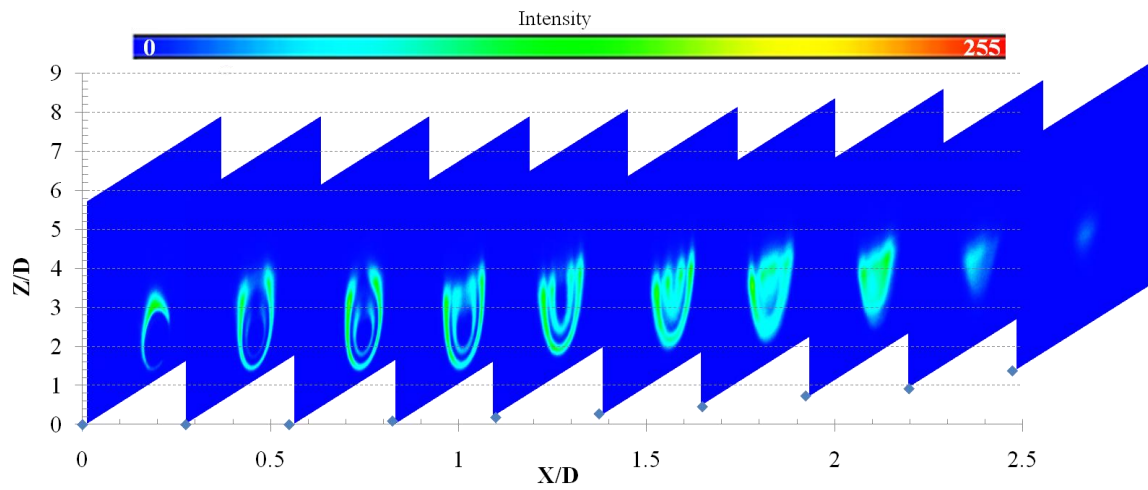
A. 14. Case 14, Propane, Re = 476, Fr = 1.0, ½ in Tube
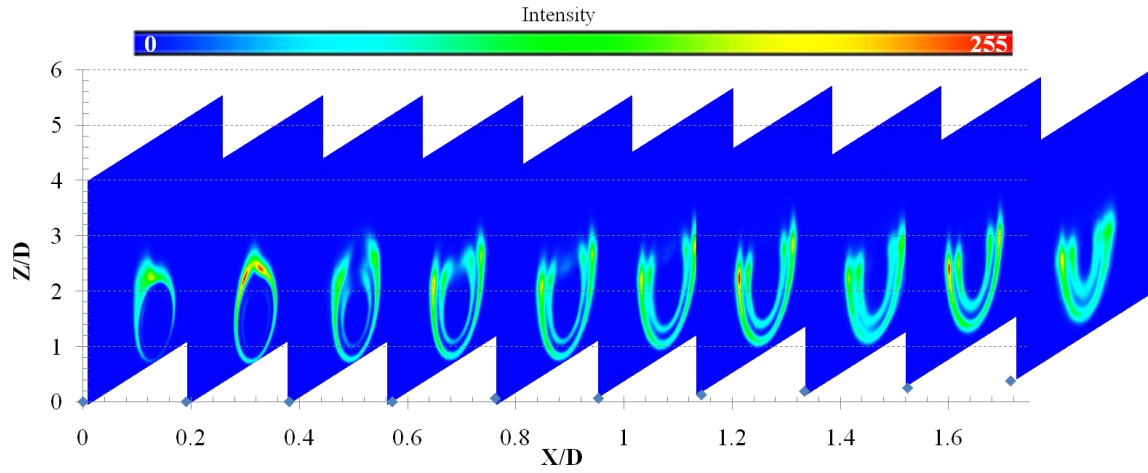
A. 15. Case 15: Propane, Re = 840, Fr = 1.0, ¾ in Tube
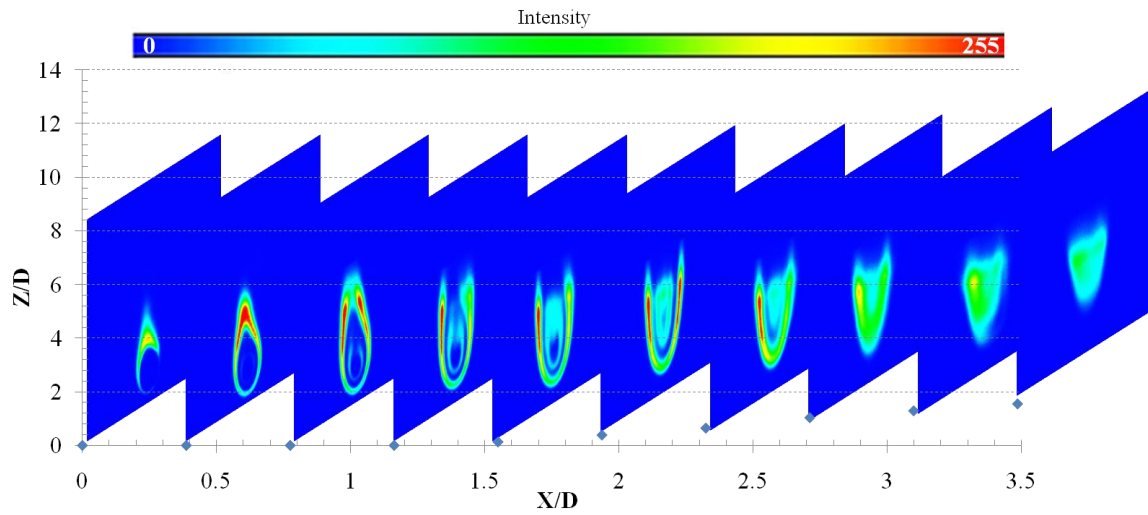
A. 16. Case 16: Propane, Re = 425, Fr = 1.5, $^3/_8$ in Tube
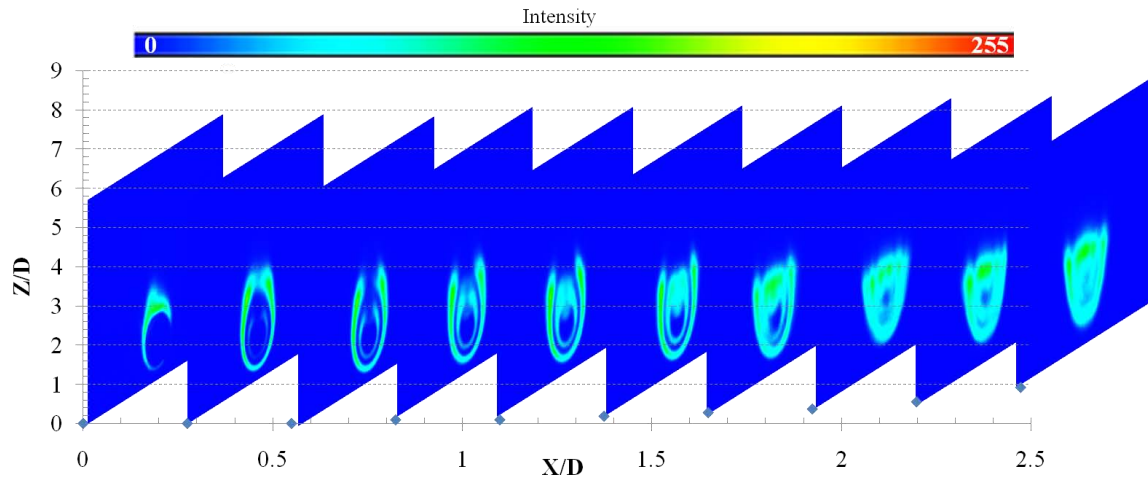
A. 17. Case 17: Propane, Re = 716, Fr = 1.5, ½ in Tube
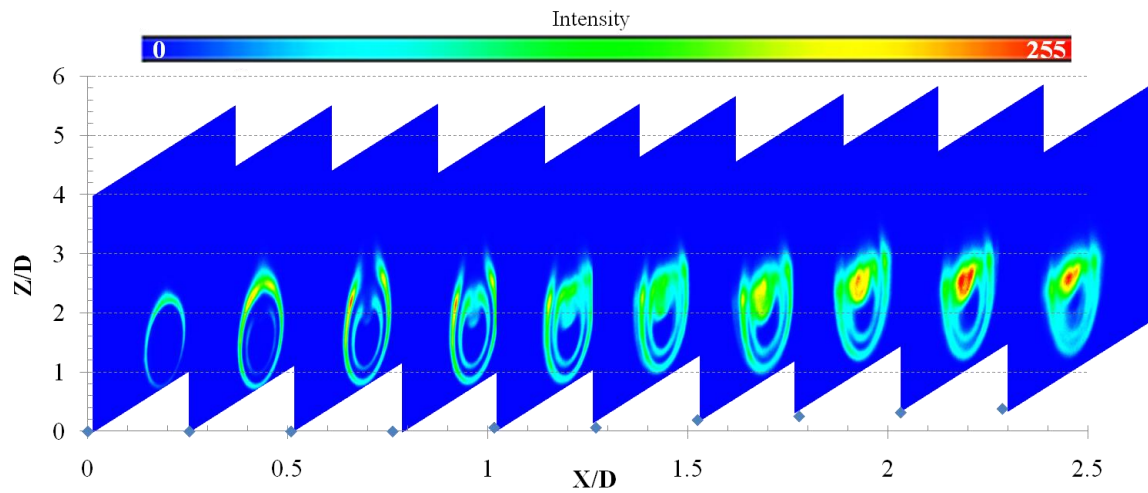
A. 18. Case 18: Propane, Re = 1234, Fr = 1.5, ¾ in Tube
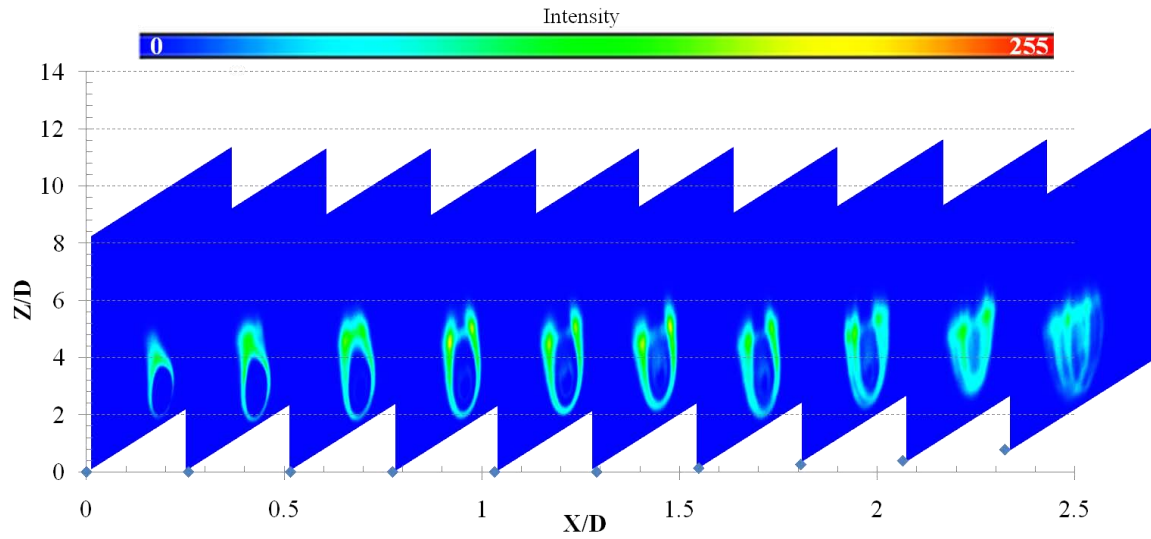
A. 19. Case 19: Ethylene, Re = 300, Fr = 7.67, $^3/_8$ in Tube
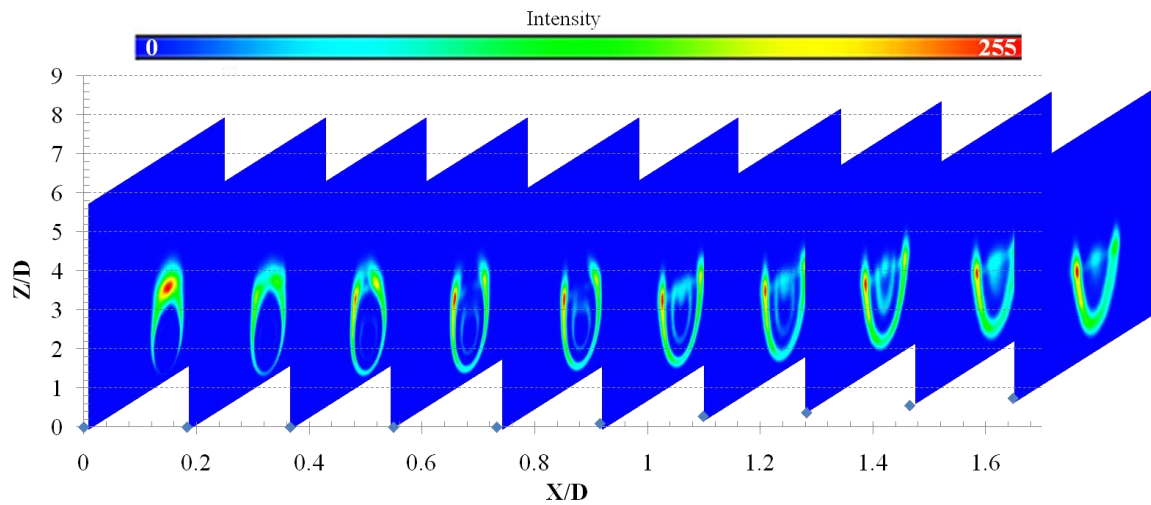
A. 20. Case 20: Ethylene, Re = 300, Fr = 4.57, ½ in Tube
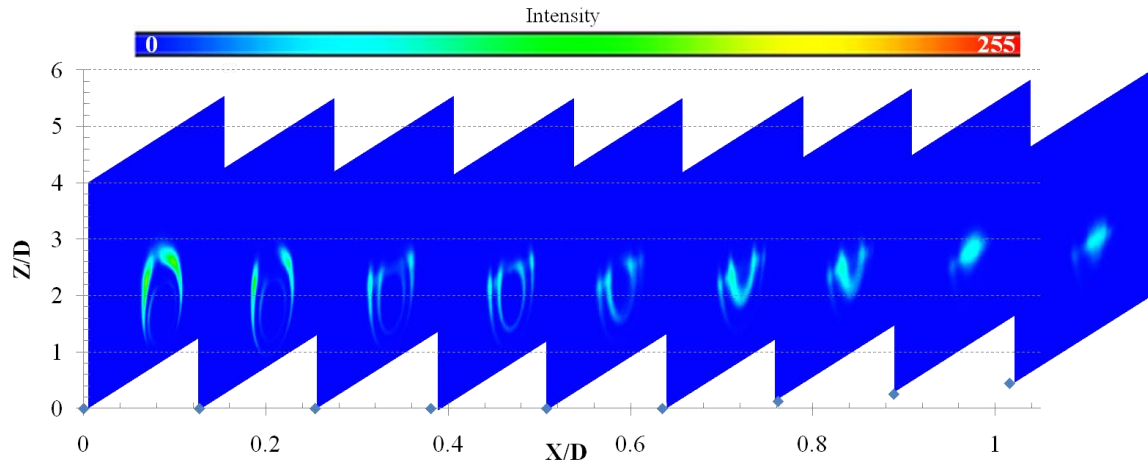
A. 21. Case 21: Ethylene, Re = 300, Fr = 2.63, ¾ in Tube
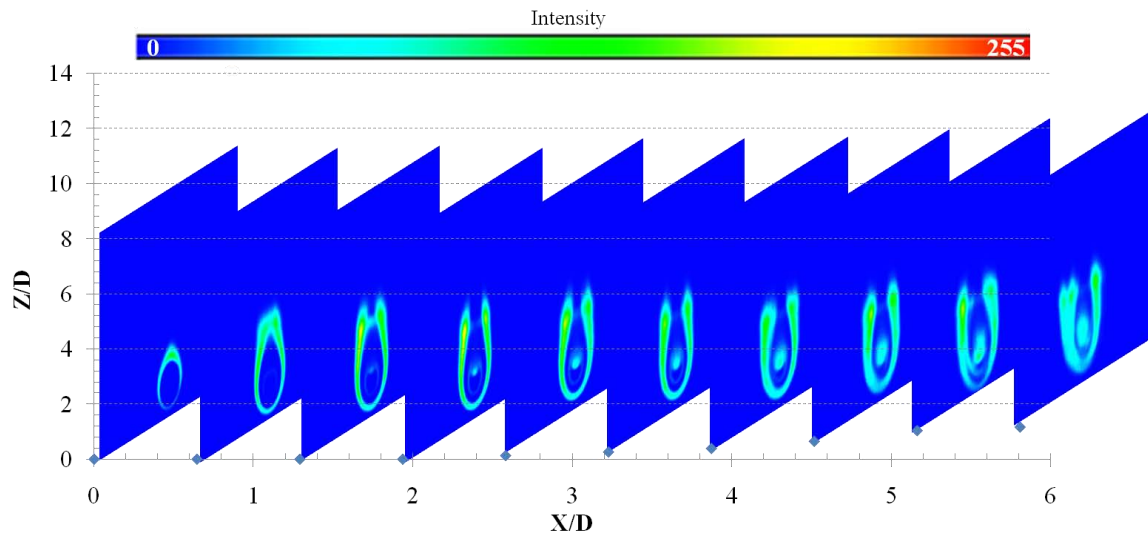
A. 22. Case 22: Ethylene, Re = 1000, Fr = 25.58, $^{3}/_{8}$ in Tube

135
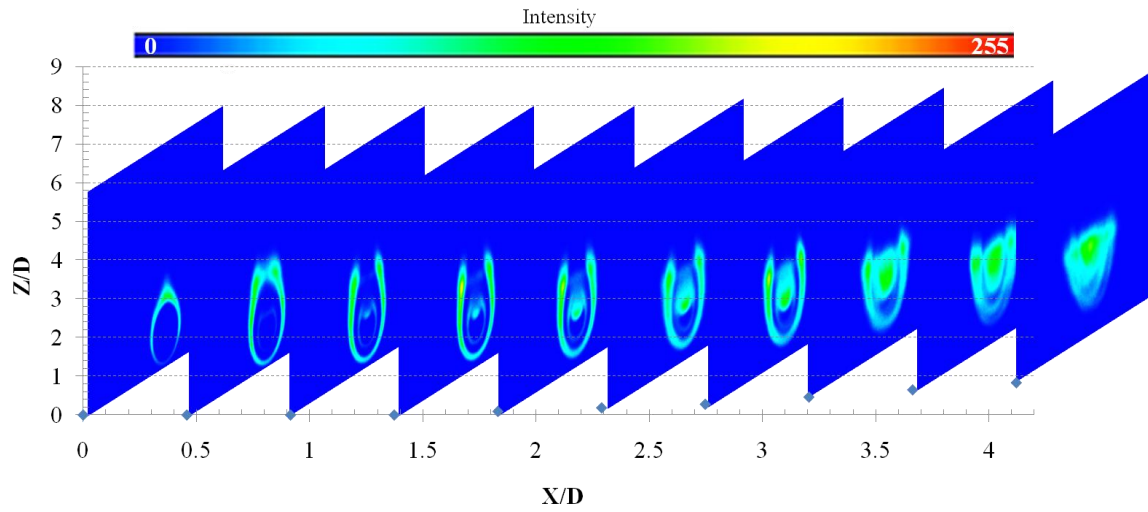
A. 23. Case 23: Ethylene, Re = 1000, Fr = 15.31, ½ in Tube
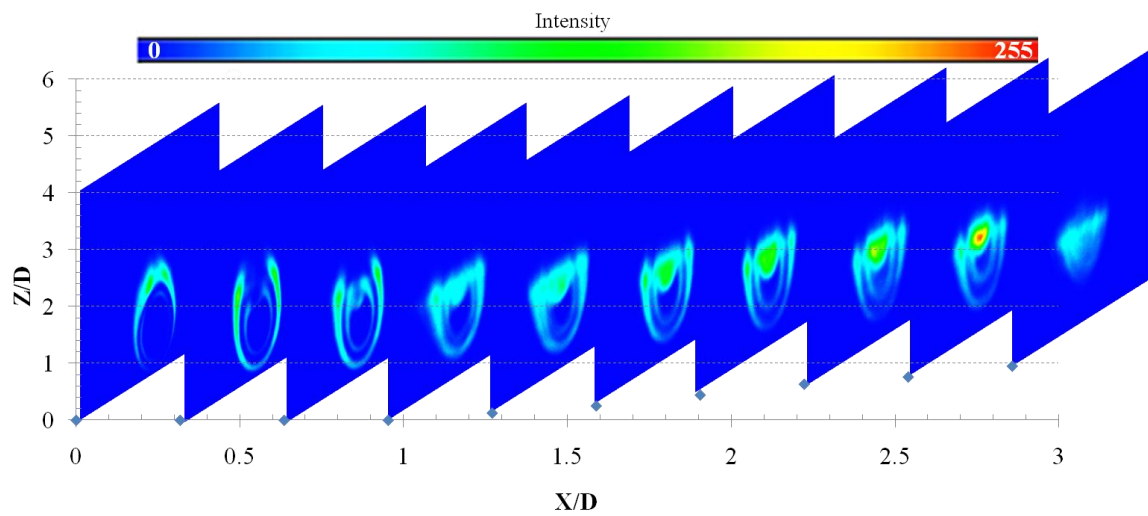
A. 24. Case 24: Ethylene, Re = 1000, Fr = 8.75, ¾ in Tube
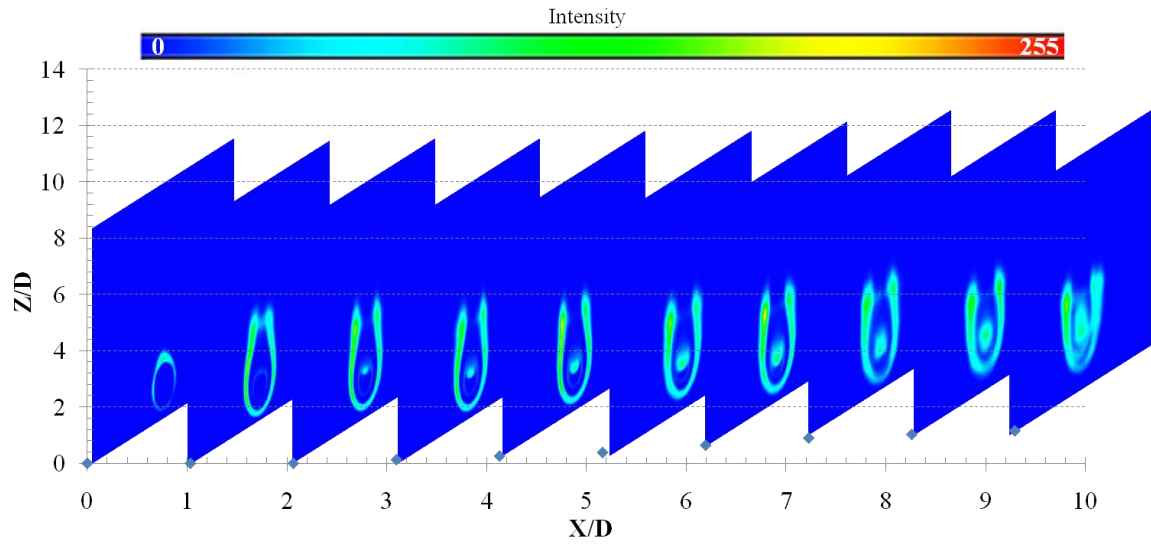
A. 25. Case 25: Ethylene, Re = 1500, Fr = 38.41, $^{3}/_{8}$ in Tube
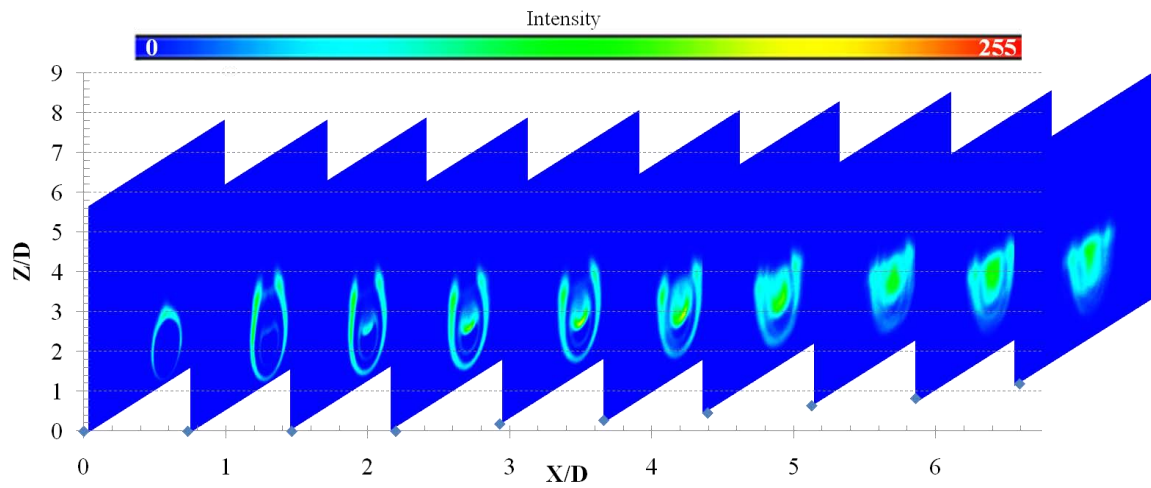
A. 26. Case 26: Ethylene, Re = 1500, Fr = 22.97, ½ in Tube
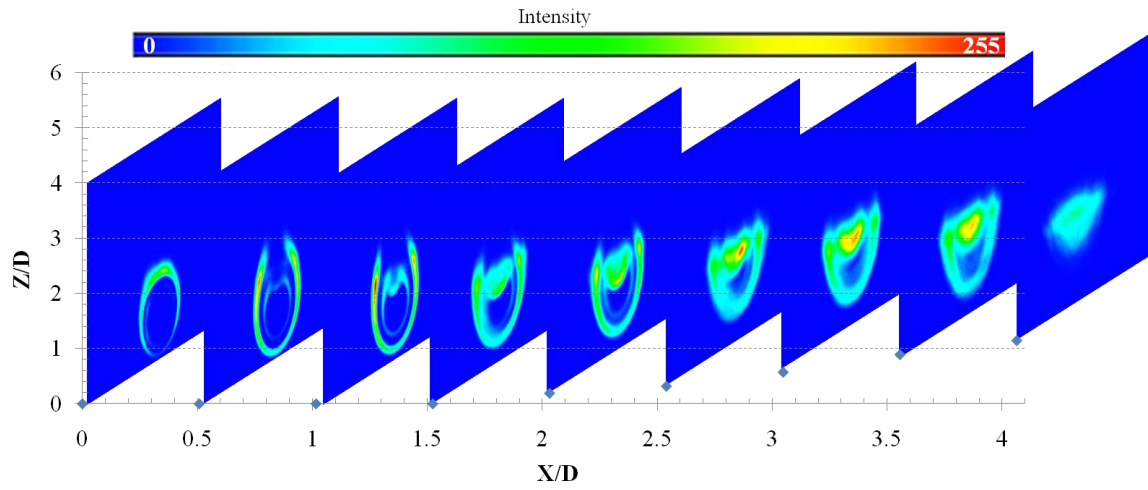
A. 27. Case 27: Ethylene, Re = 1500, Fr = 13.13, ¾ in Tube
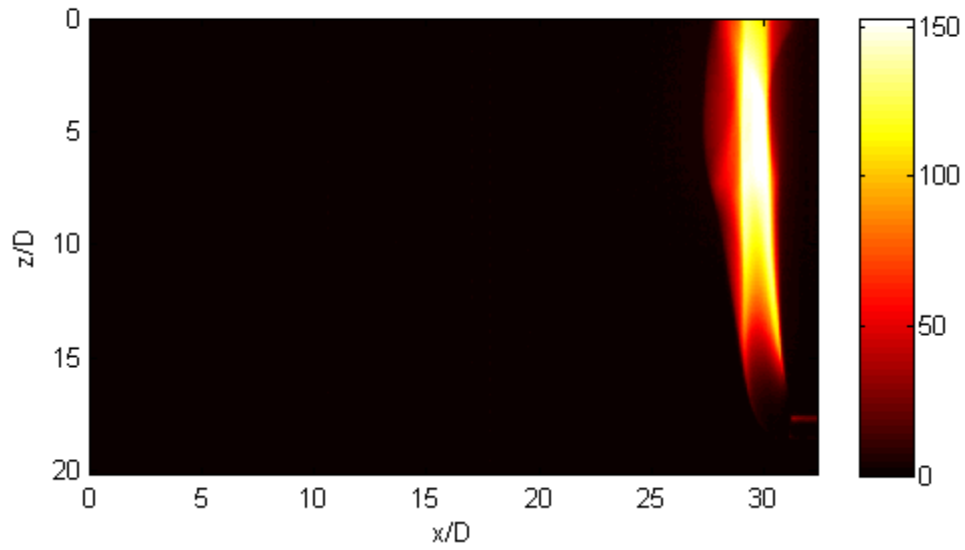
B. 1. Case1: Propane, Re = 300, Fr = 1.06, $^3/_8$ in Tube
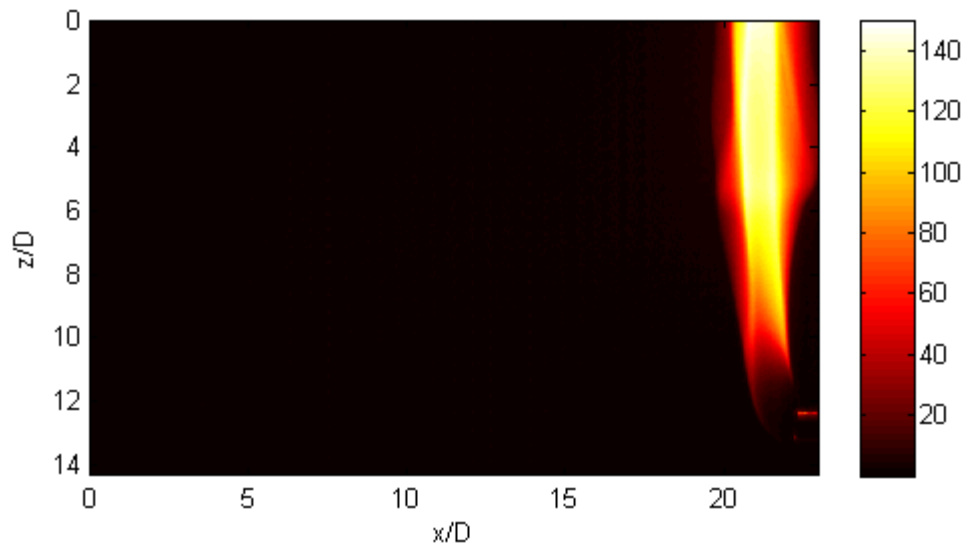
B. 2 Case 2: Propane, Re = 300, Fr = 0.63, ½ in Tube
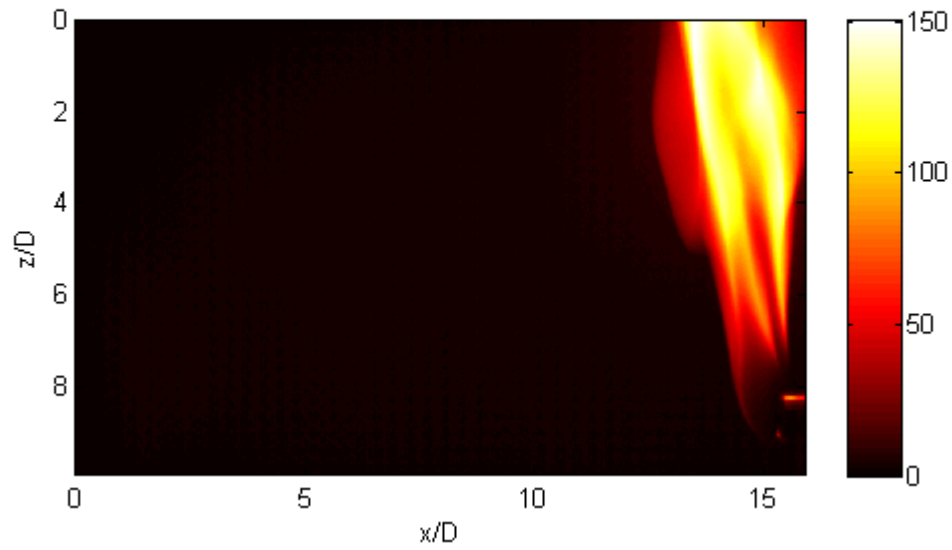
B. 3. Case 3: Propane, Re = 300, Fr = 0.36, ¾ in Tube
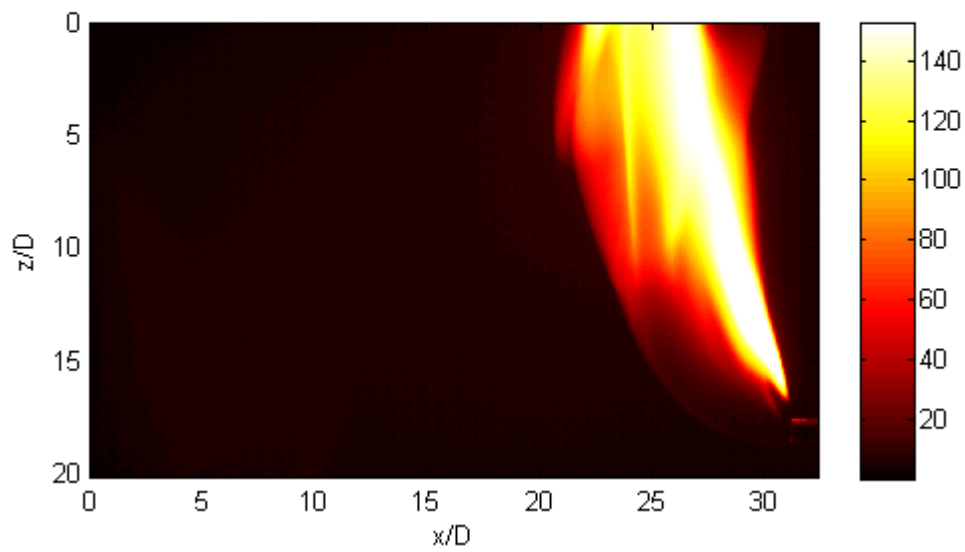
B. 4. Case 4: Propane, Re = 1000, Fr = 3.49, $^{3}/_{8}$ in Tube
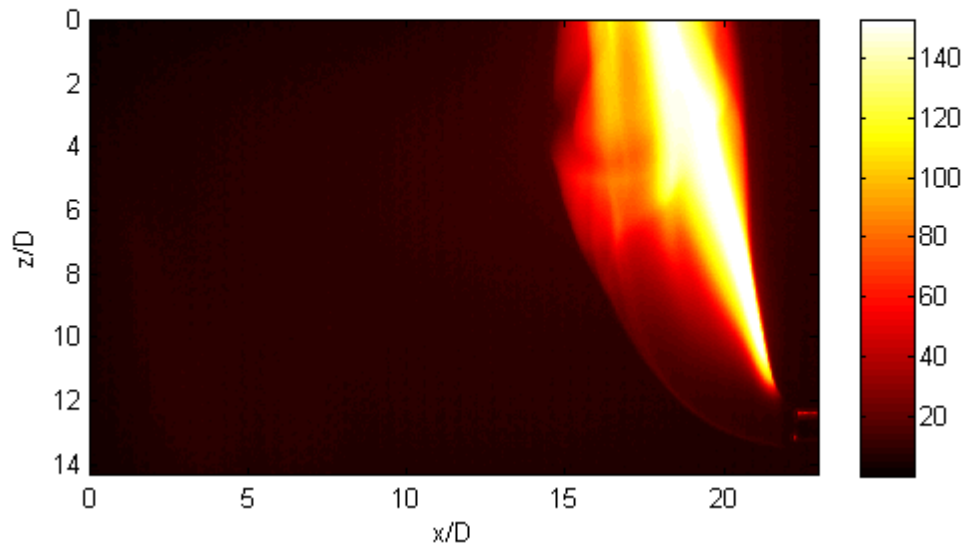
B. 5. Case 5: Propane, Re = 1000, Fr = 2.09, ½ in Tube
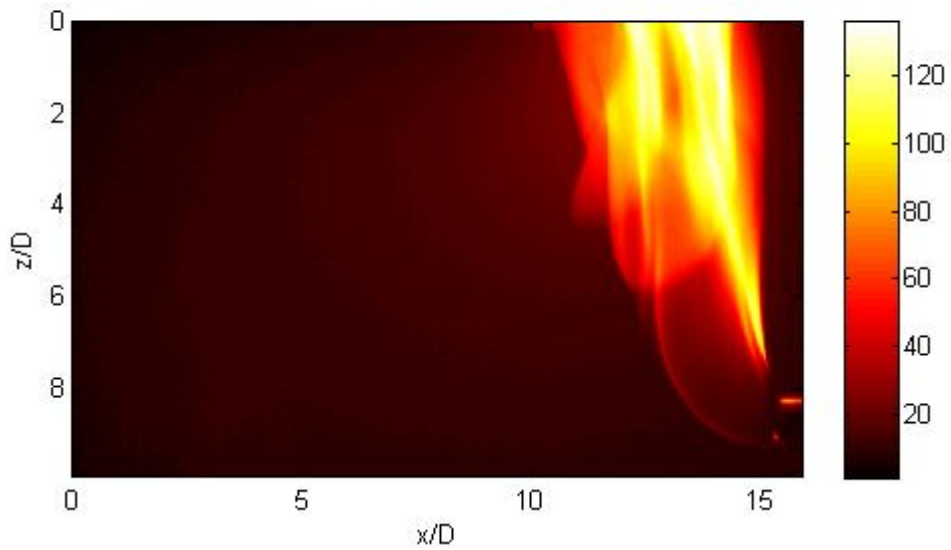
**B. 6. Case 6: Propane, Re = 1000, Fr = 1.19, ¾ in Tube**
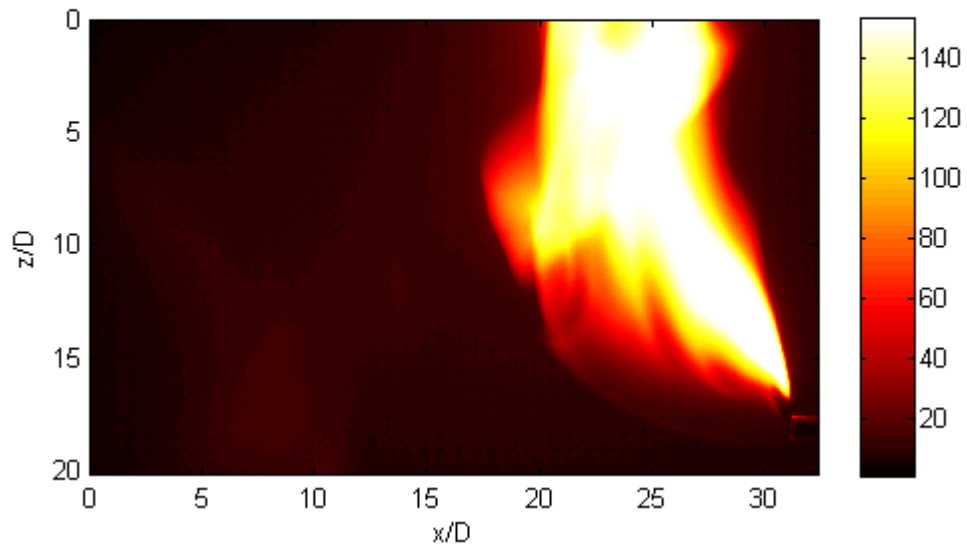
B. 7. Case 7: Propane, Re = 1500, Fr = 5.26, $^3/_8$ in Tube
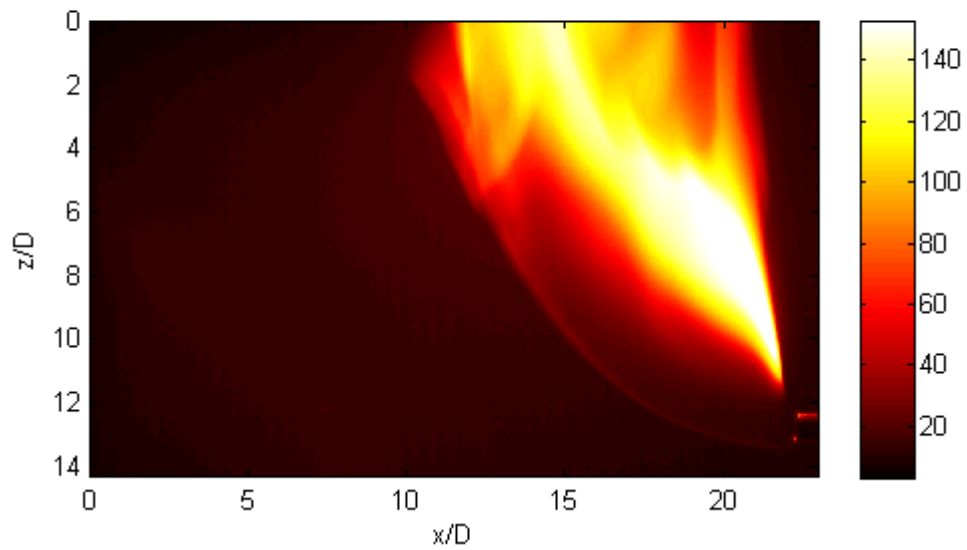
B. 8. Case 8: Propane, Re = 1500, Fr = 3.13, ½ in Tube
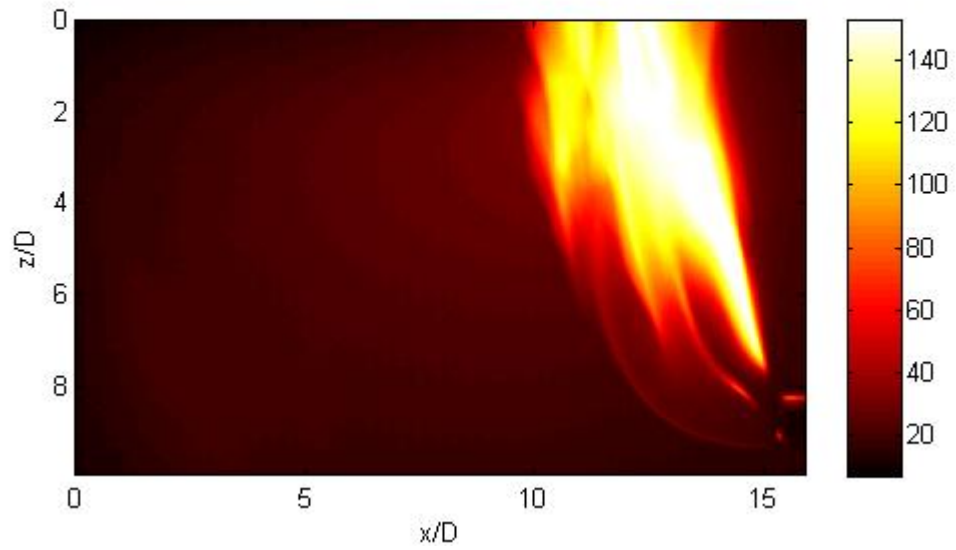
B. 9. Case 9: Propane, Re = 1500, Fr = 1.78, ¾ in Tube
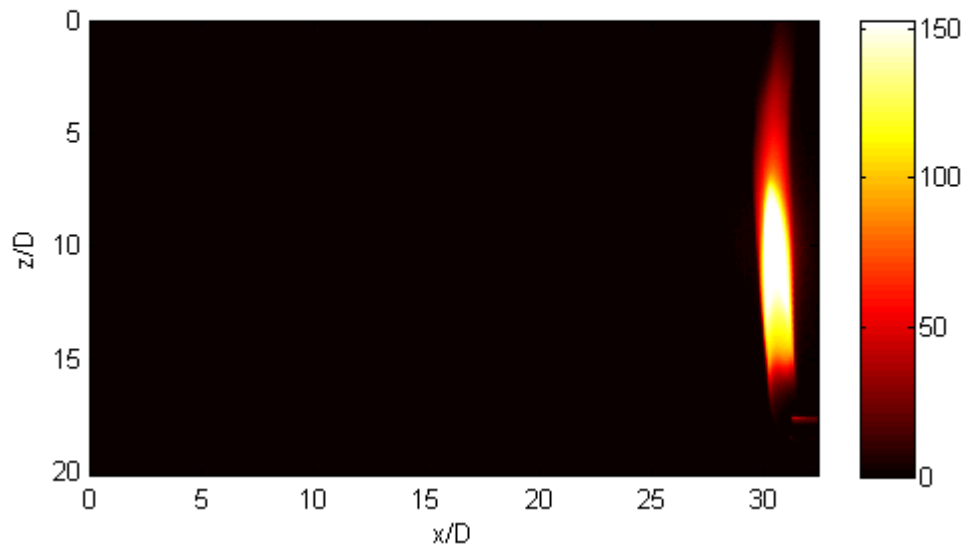
B. 10. Case 10: Propane, Re = 142, Fr = 0.5, $^3/_8$ in Tube
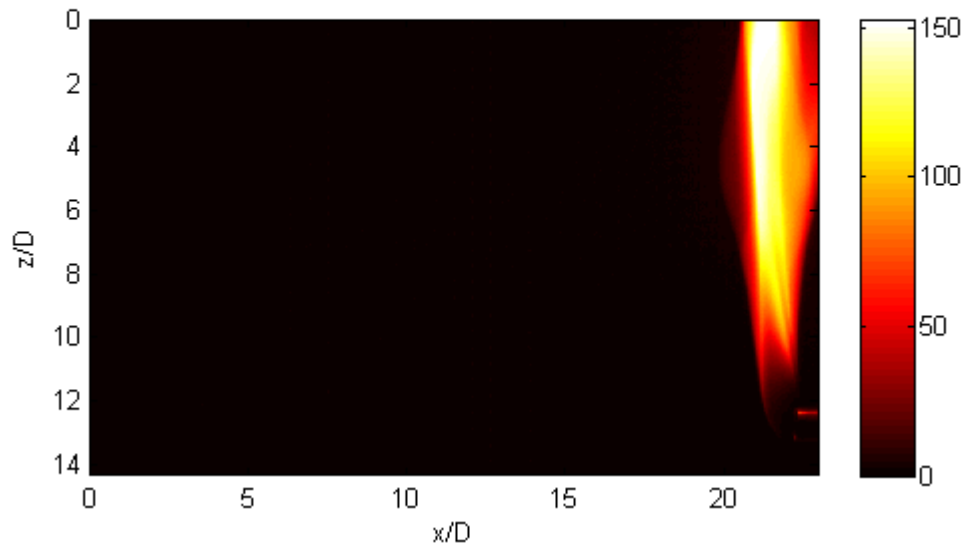
B. 11. Case 11: Propane, Re = 240, Fr = 0.5, ½ in Tube
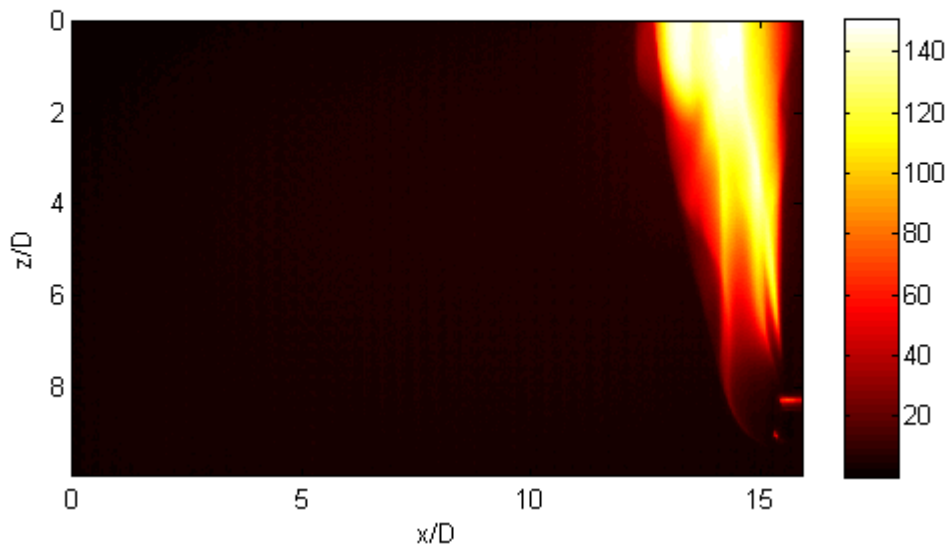
B. 12. Case 12: Propane, Re = 412, Fr = 0.5, ¾ in Tube
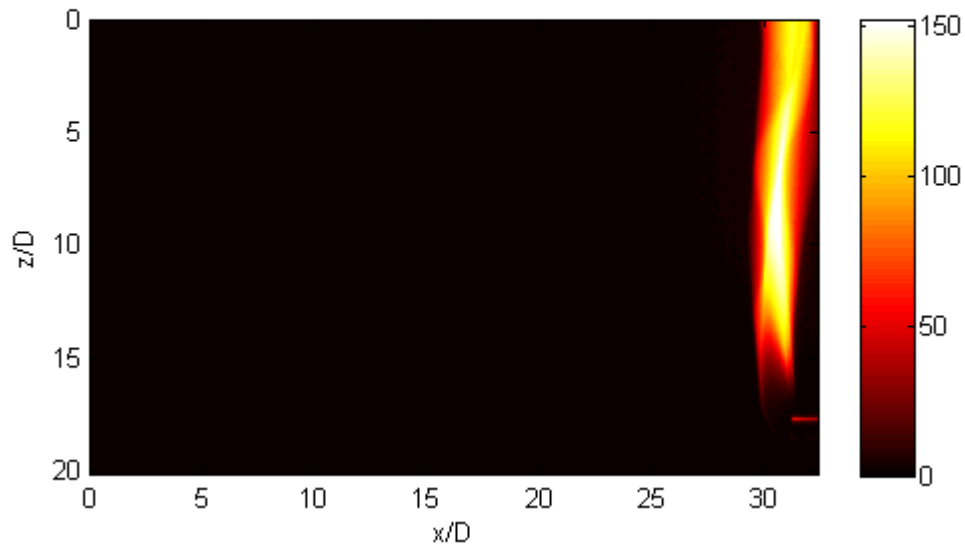
B. 13. Case 13: Propane, Re = 283, Fr = 1.0, $^3/_8$ in Tube
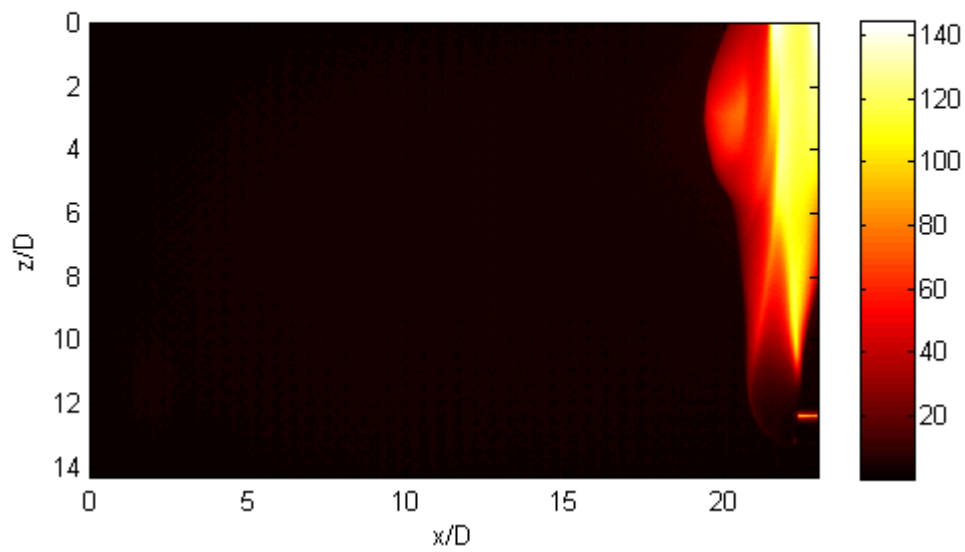
B. 14. Case 14, Propane, Re = 476, Fr = 1.0, ½ in Tube
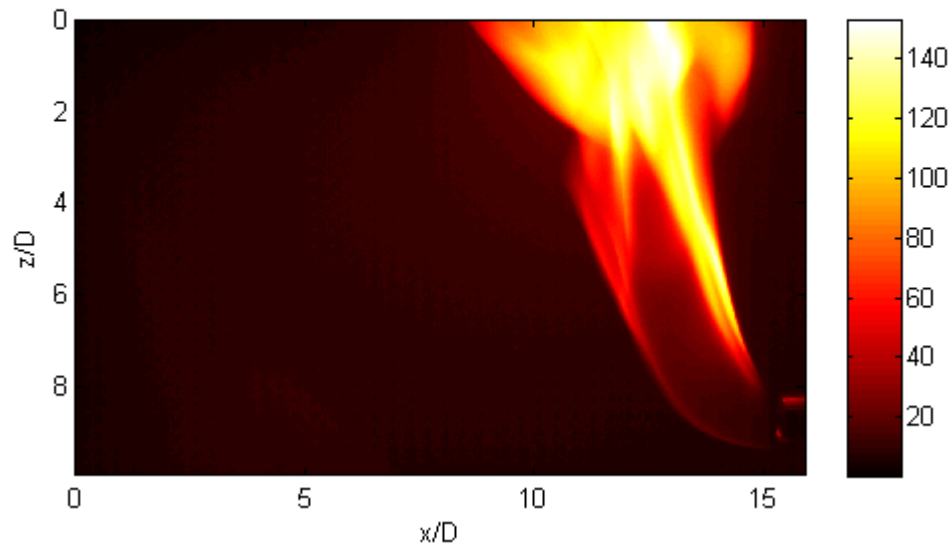
B. 15. Case 15: Propane, Re = 840, Fr = 1.0, ¾ in Tube
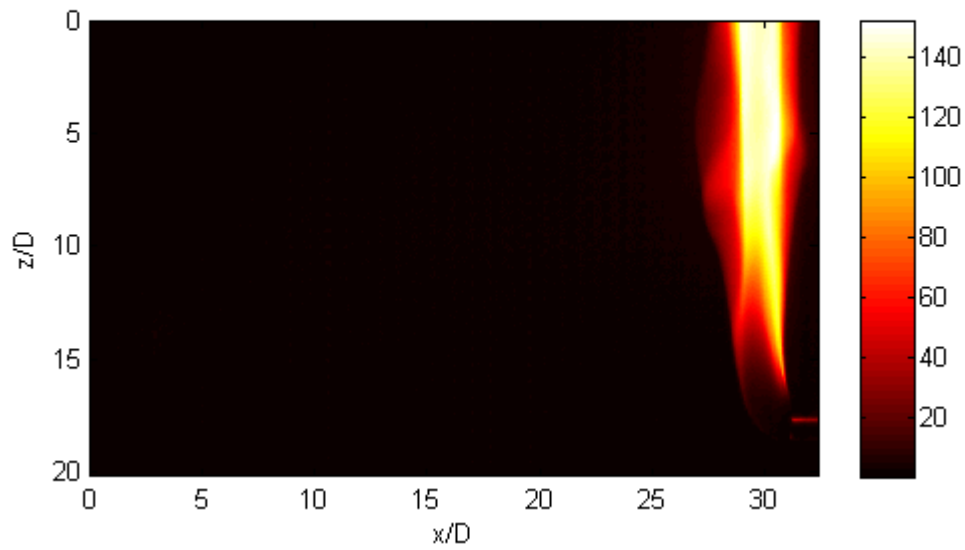
B. 16. Case 16: Propane, Re = 425, Fr = 1.5, $^{3}/_{8}$ in Tube

146
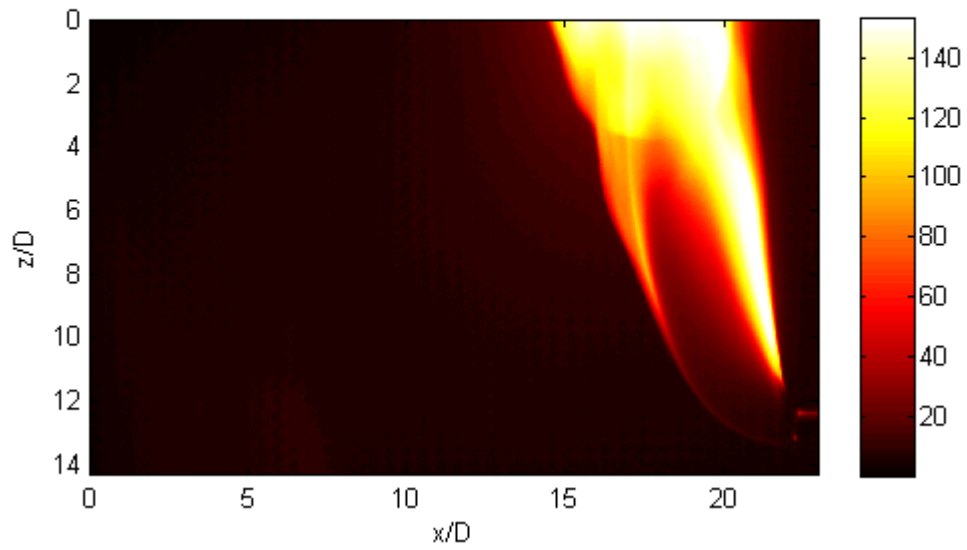
B. 17. Case 17: Propane, Re = 716, Fr = 1.5, ½ in Tube
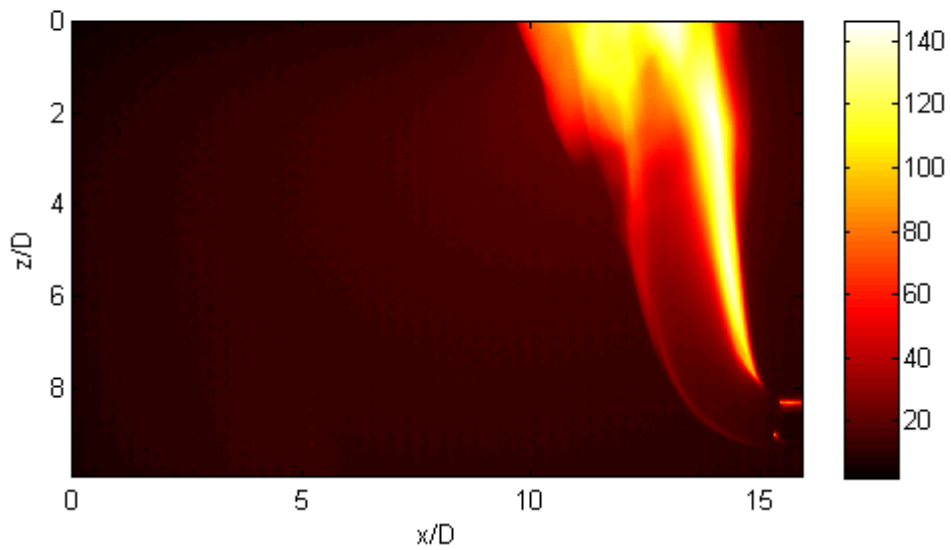
B. 18. Case 18: Propane, Re = 1234, Fr = 1.5, ¾ in Tube
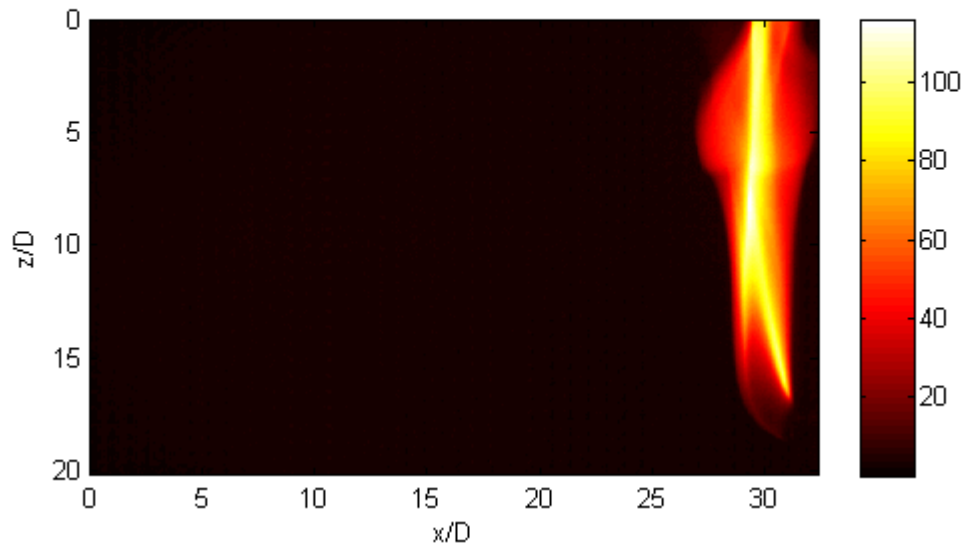
B. 19. Case 19: Ethylene, Re = 300, Fr = 7.67, $^3/_8$ in Tube
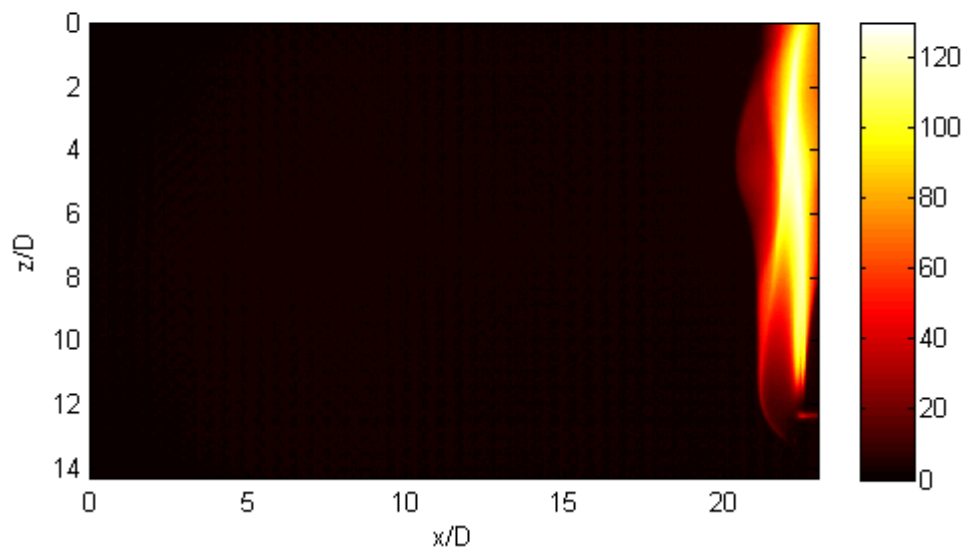
B. 20. Case 20: Ethylene, Re = 300, Fr = 4.57, ½ in Tube
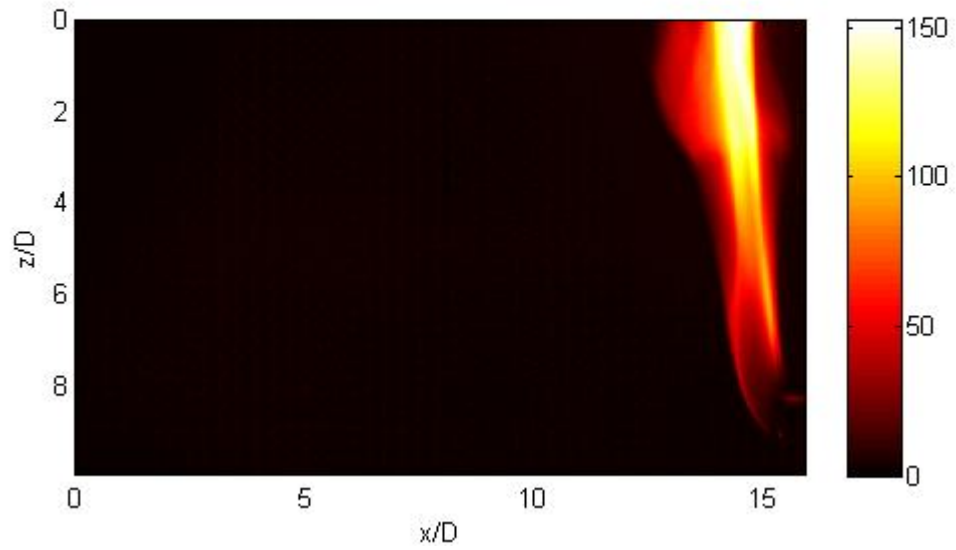
B. 21. Case 21: Ethylene, Re = 300, Fr = 2.63, ¾ in Tube
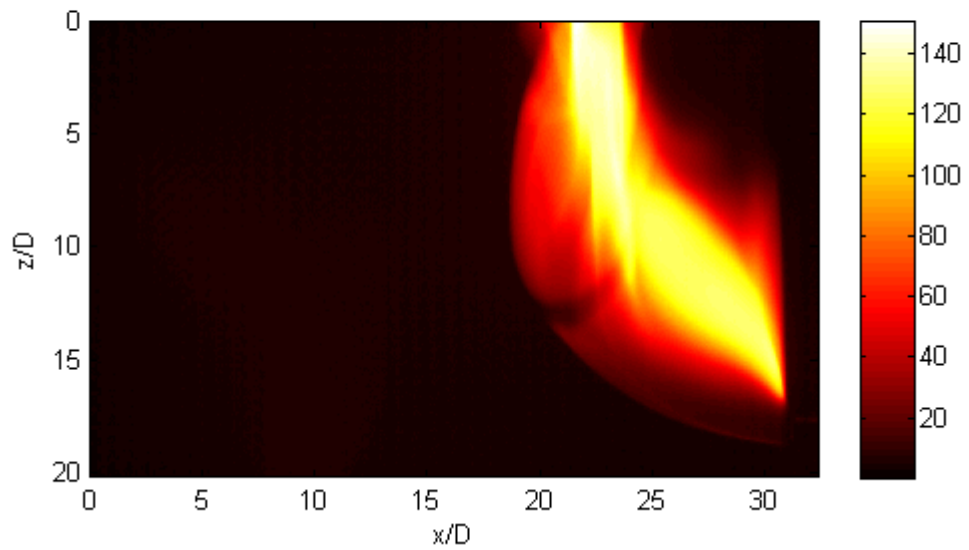
B. 22. Case 22: Ethylene, Re = 1000, Fr = 25.58, $^3/_8$ in Tube
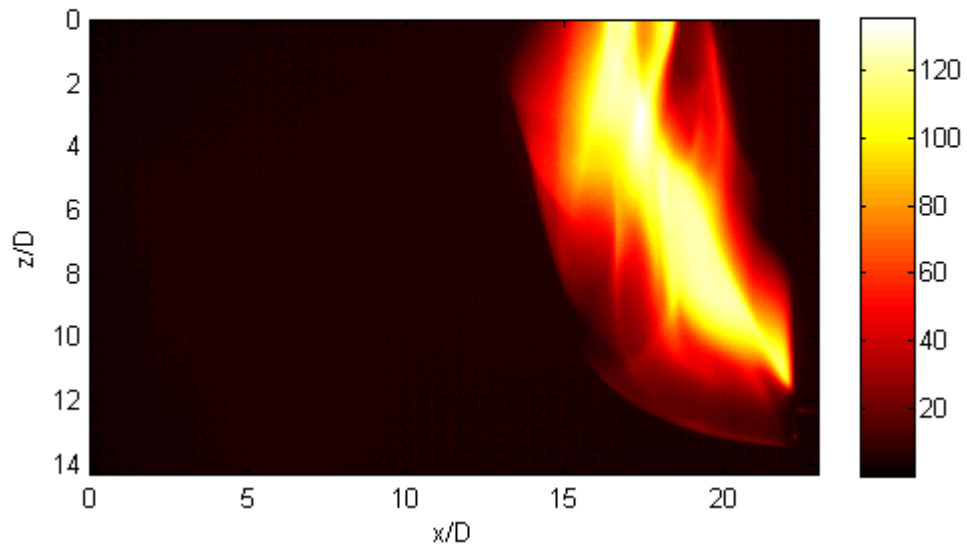
B. 23. Case 23: Ethylene, Re = 1000, Fr = 15.31, ½ in Tube
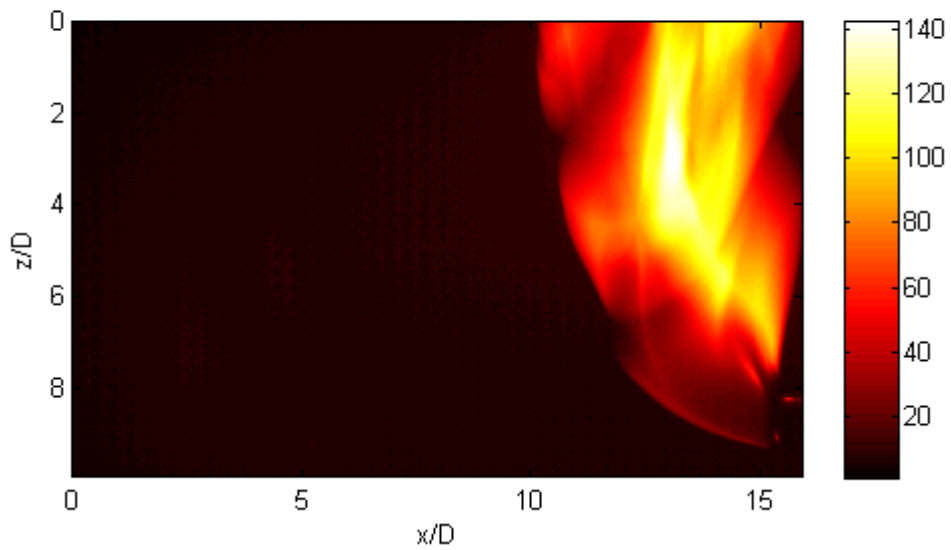
B. 24. Case 24: Ethylene, Re = 1000, Fr = 8.75, ¾ in Tube
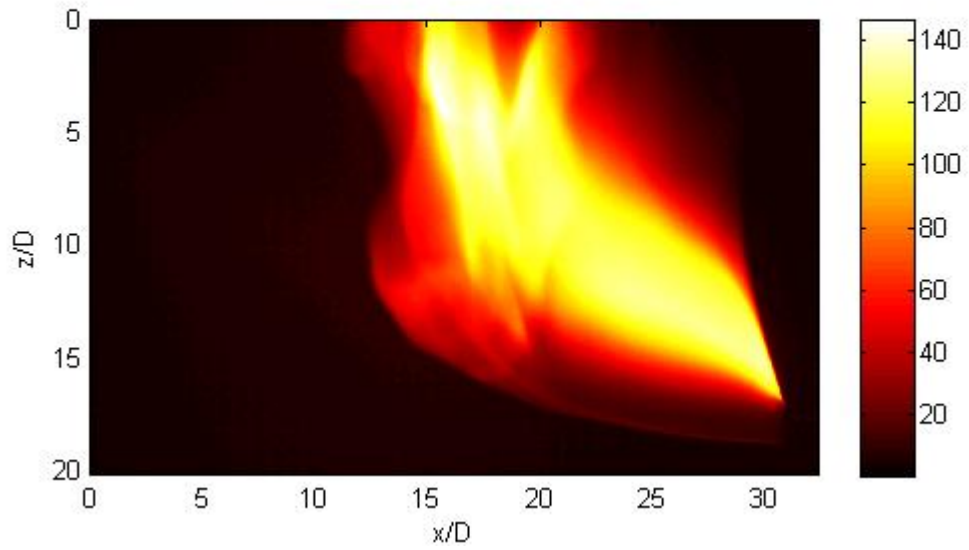
B. 25. Case 25: Ethylene, Re = 1500, Fr = 38.41, $^3/_8$ in Tube
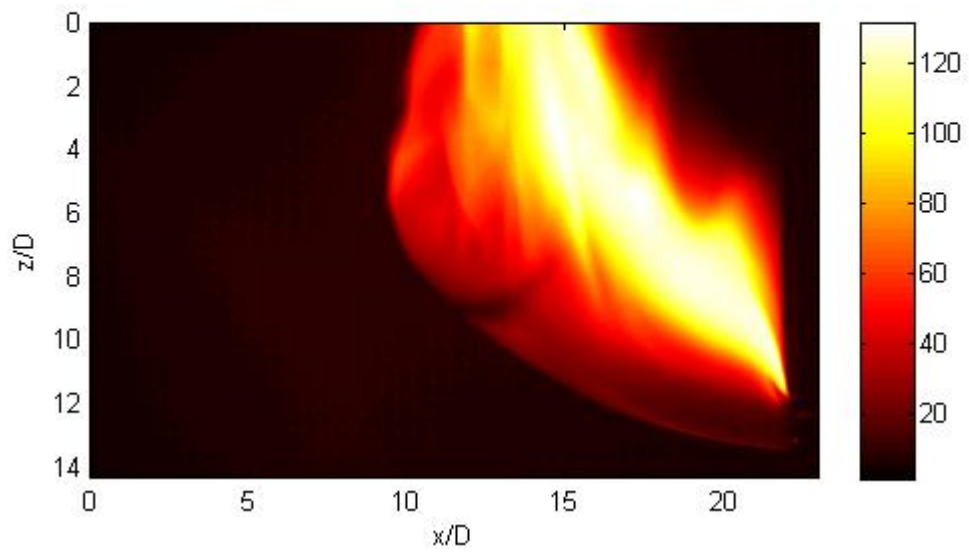
B. 26. Case 26: Ethylene, Re = 1500, Fr = 22.97, ½ in Tube
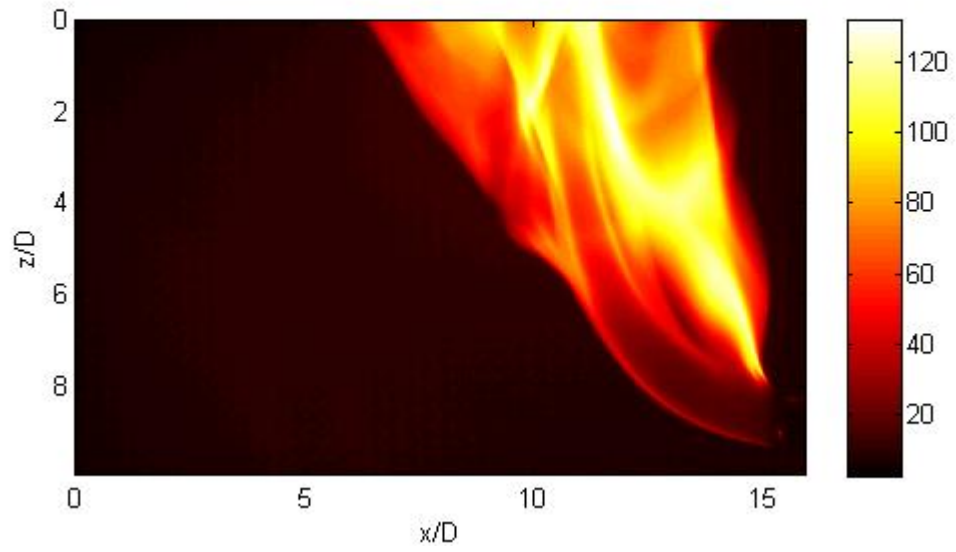
B. 27. Case 27: Ethylene, Re = 1500, Fr = 13.13, ¾ in Tube

Appendix C: CH* Filtered High Speed Imaging Results
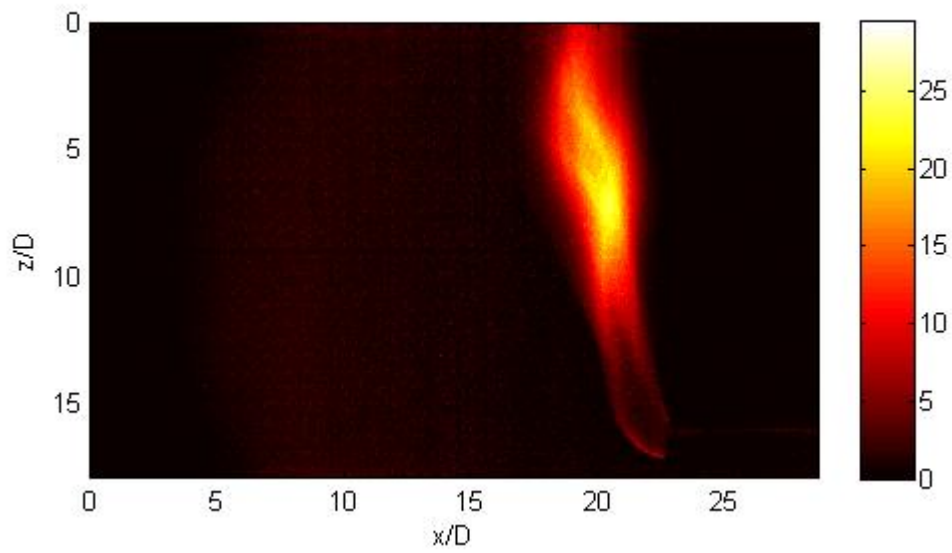
C. 1. Case 1: Propane, Re = 300, Fr = 1.06, $^3/_8$ in Tube
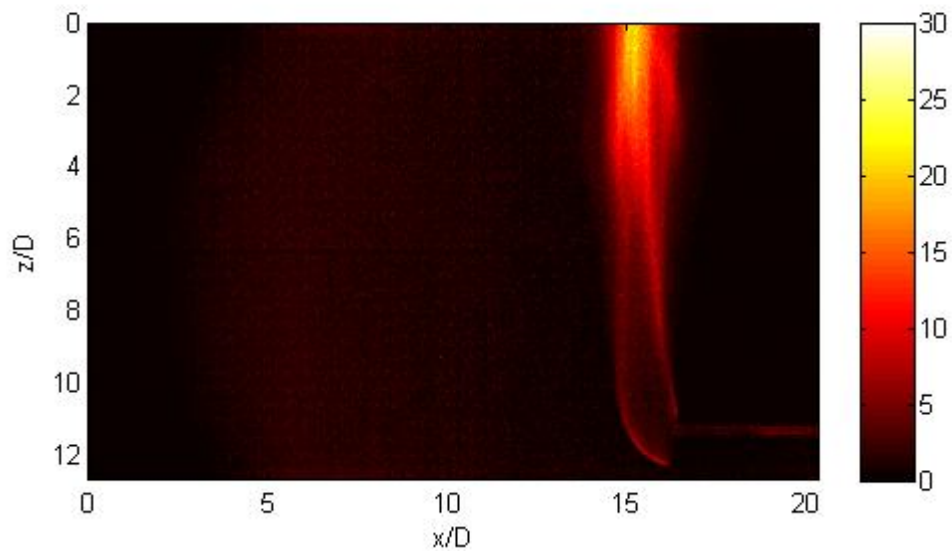
C. 2. Case 2: Propane, Re = 300, Fr = 0.63, ½ in Tube
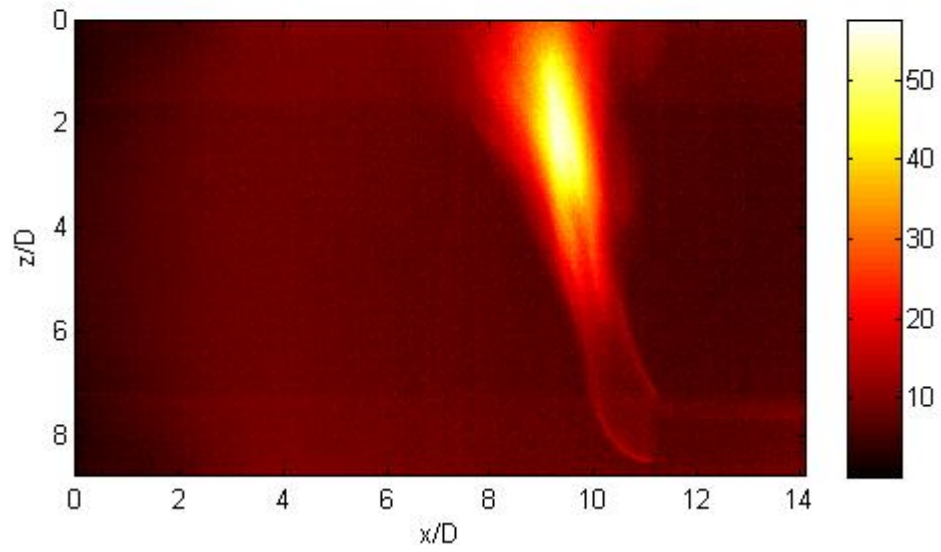
C. 3. Case 3: Propane, Re = 300, Fr = 0.36, ¾ in Tube
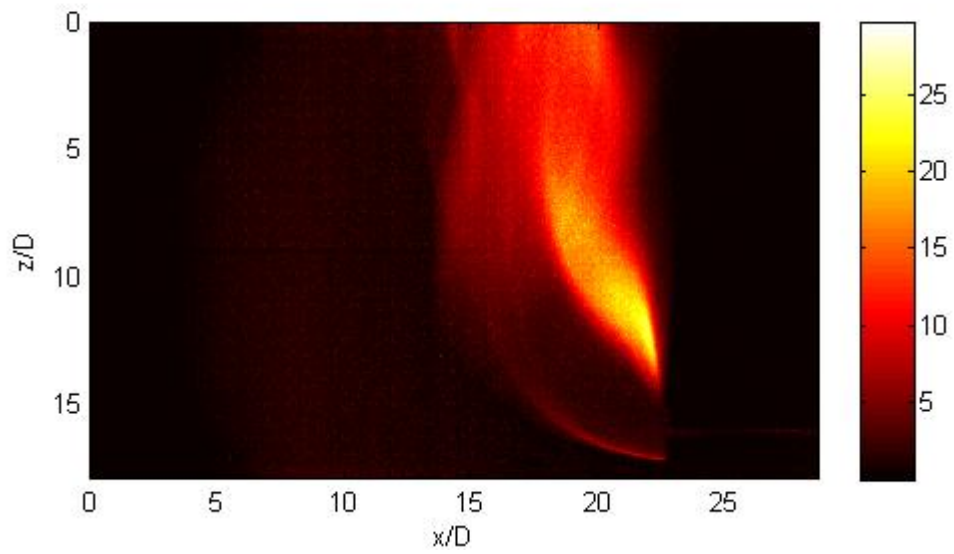
C. 4. Case 4: Propane, Re = 1000, Fr = 3.49, $^3/_8$ in Tube
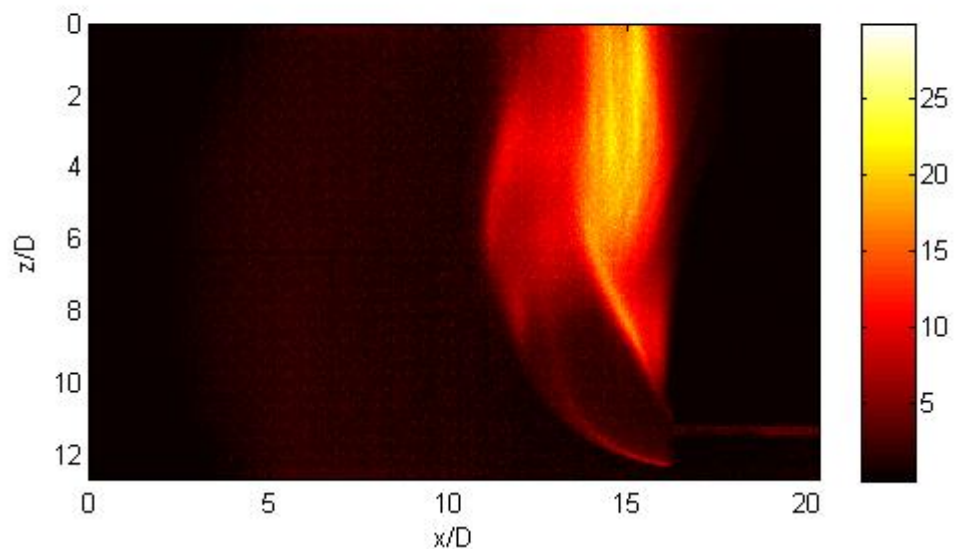
C. 5. Case 5: Propane, Re = 1000, Fr = 2.09, ½ in Tube
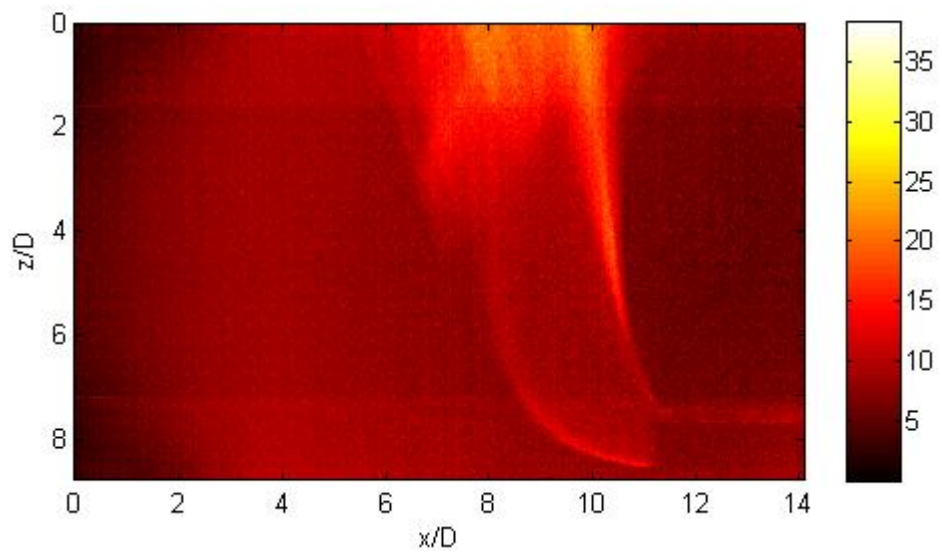
C. 6. Case 6: Propane, Re = 1000, Fr = 1.19, ¾ in Tube
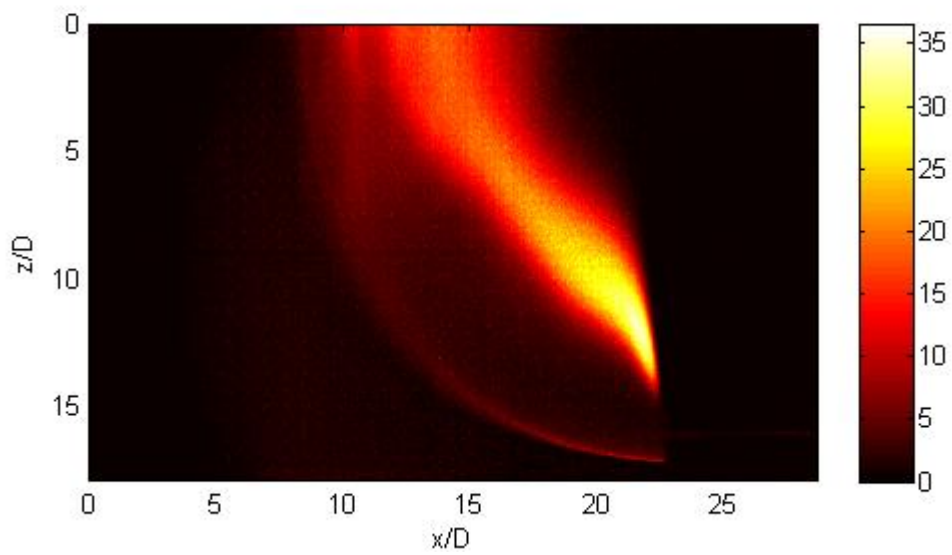
C. 7. Case 7: Propane, Re = 1500, Fr = 5.26, $^3/_8$ in Tube
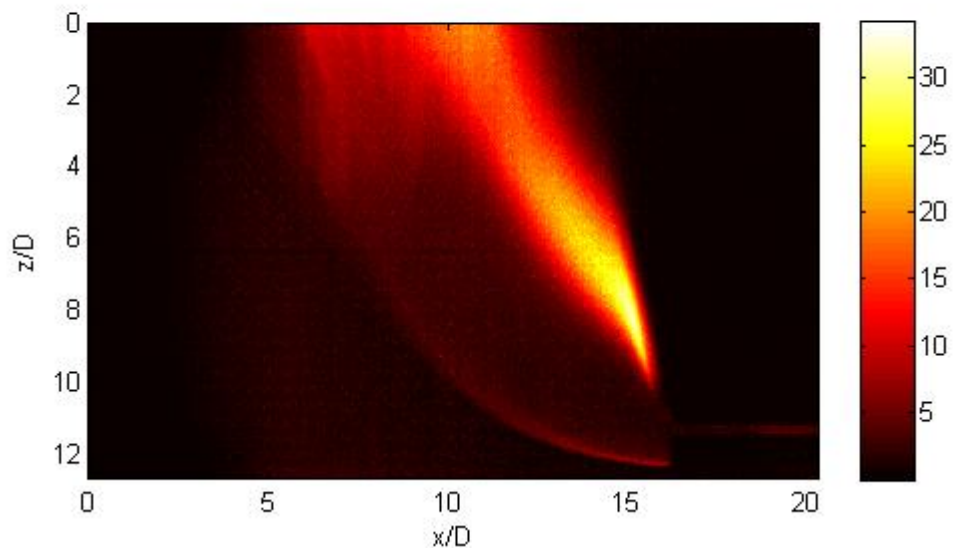
C. 8. Case 8: Propane, Re = 1500, Fr = 3.13, ½ in Tube
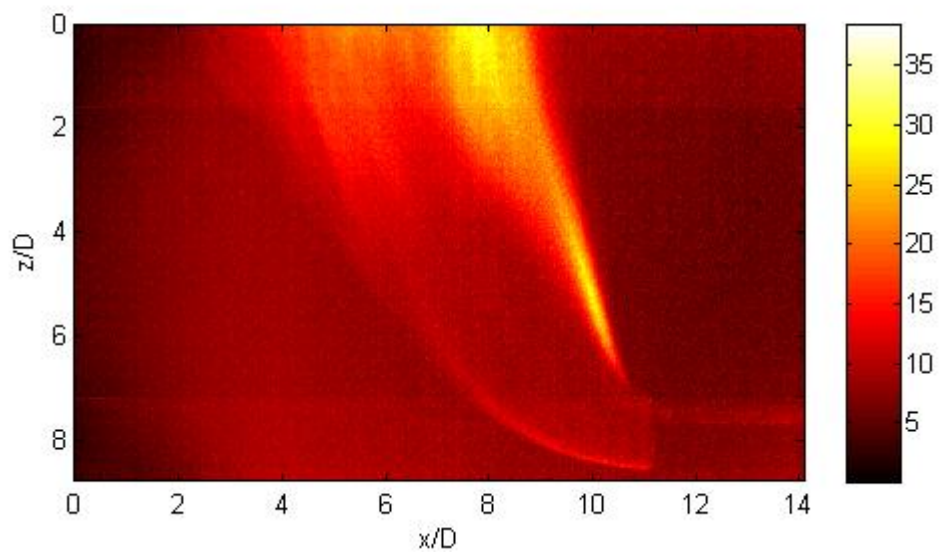
C. 9. Case 9: Propane, Re = 1500, Fr = 1.78, ¾ in Tube
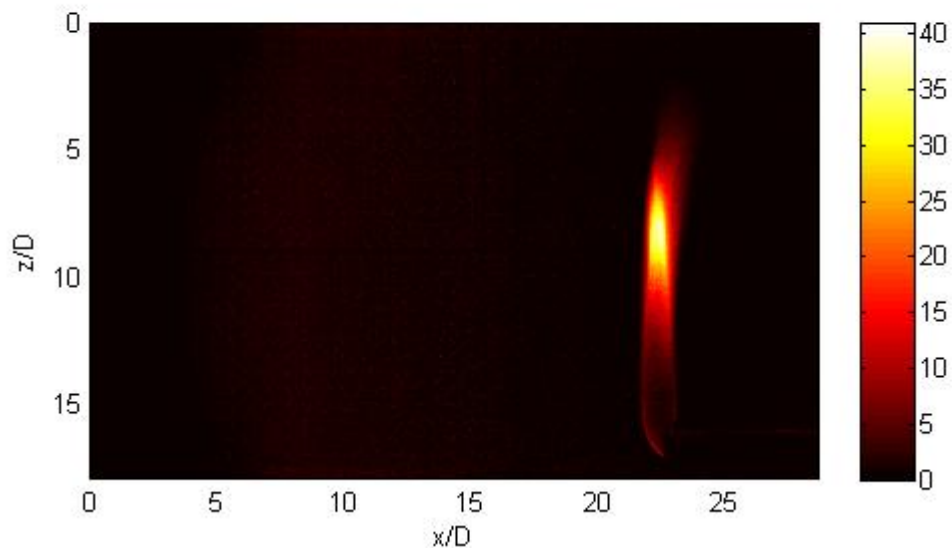
C. 10. Case 10: Propane, Re = 142, Fr = 0.5, $^{3}/_{8}$ in Tube
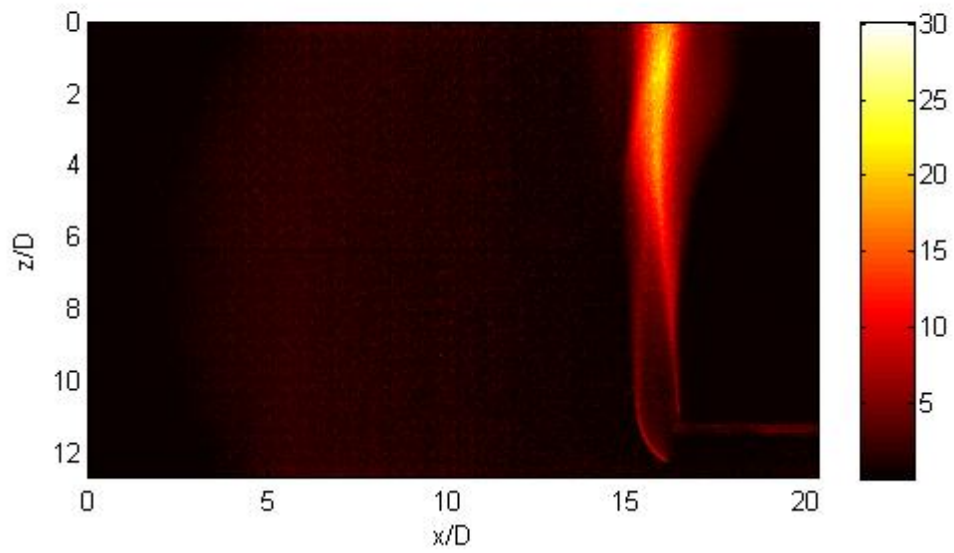
C. 11. Case 11: Propane, Re = 240, Fr = 0.5, ½ in Tube
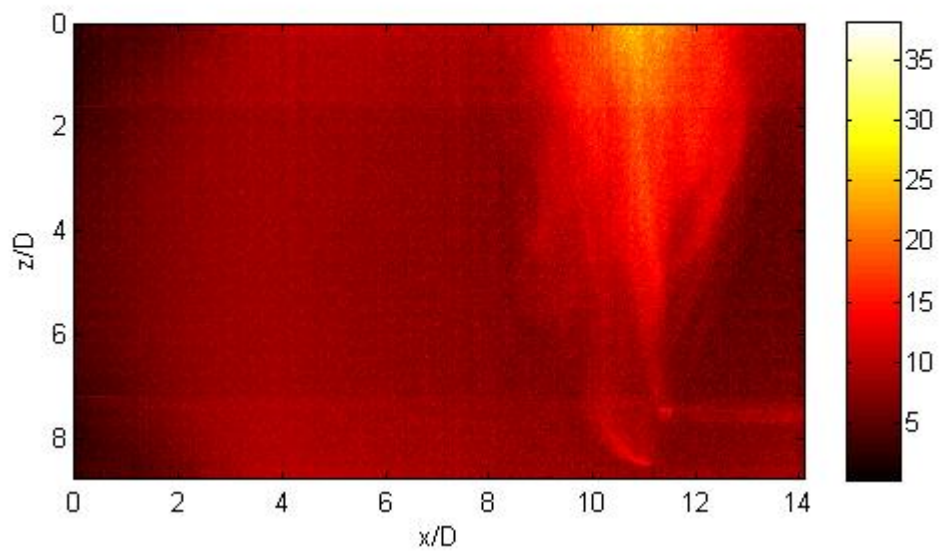
C. 12. Case 12: Propane, Re = 412, Fr = 0.5, ¾ in Tube
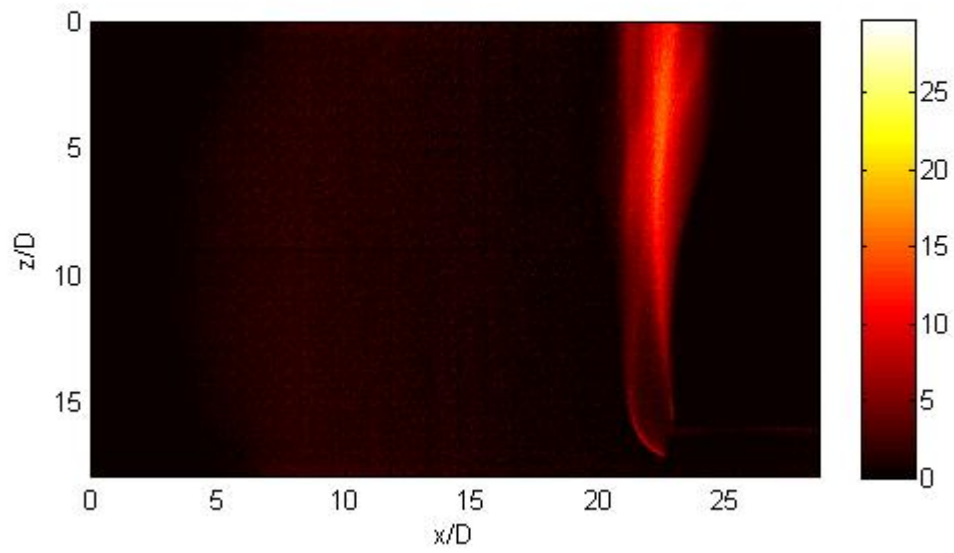
C. 13. Case 13: Propane, Re = 283, Fr = 1.0, $^{3}/_{8}$ in Tube
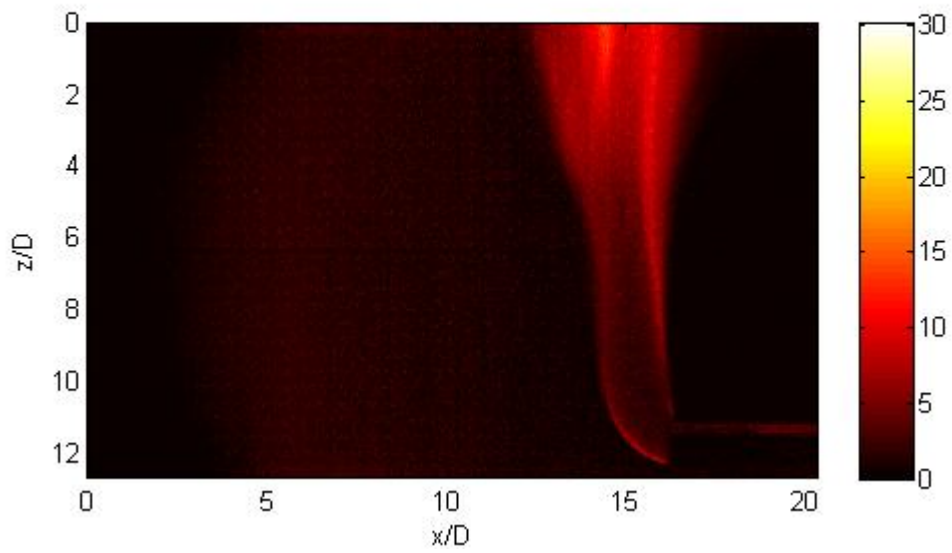
C. 14. Case 14, Propane, Re = 476, Fr = 1.0, ½ in Tube
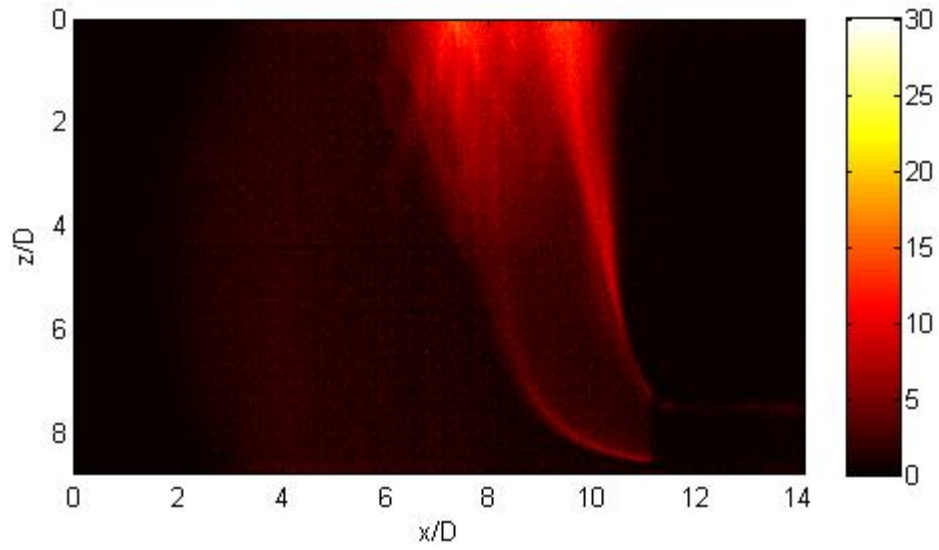
C. 15. Case 15: Propane, Re = 840, Fr = 1.0, ¾ in Tube
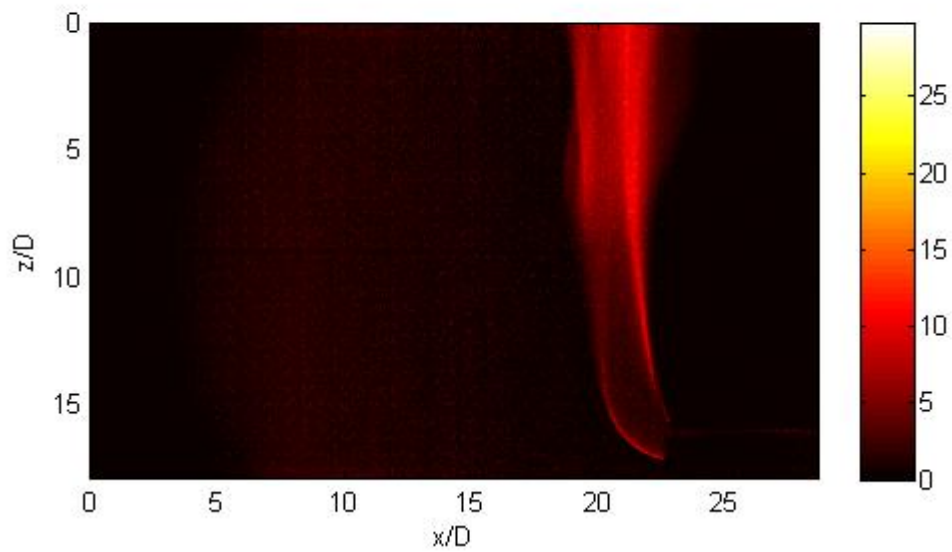
C. 16. Case 16: Propane, Re = 425, Fr = 1.5, $^3/_8$ in Tube
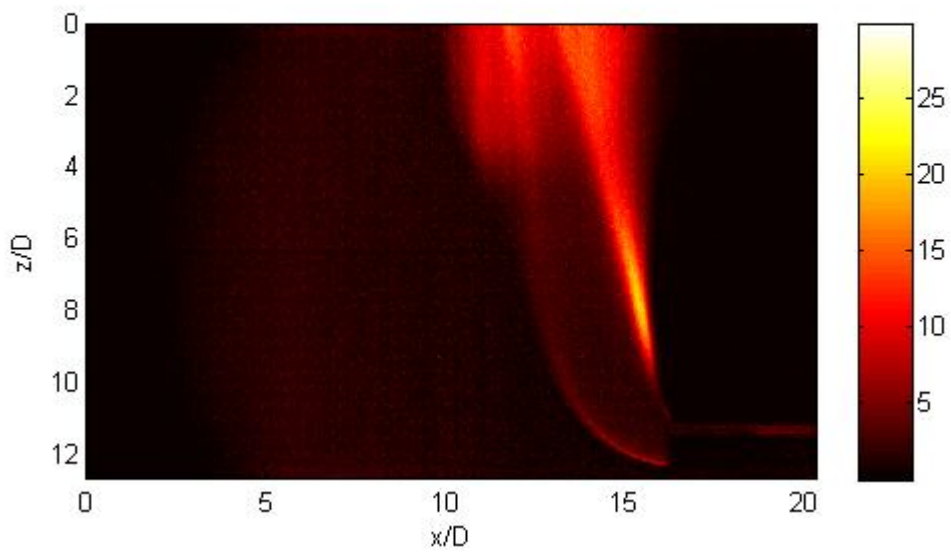
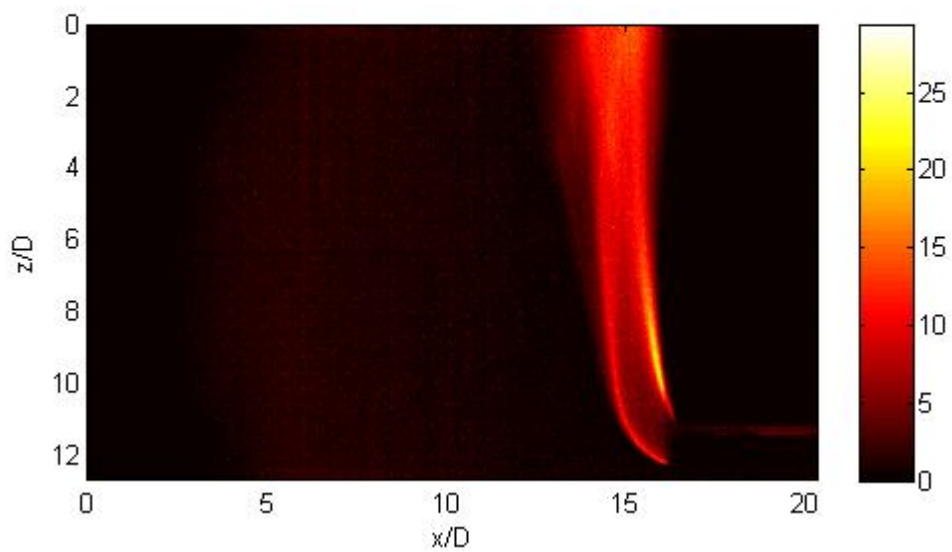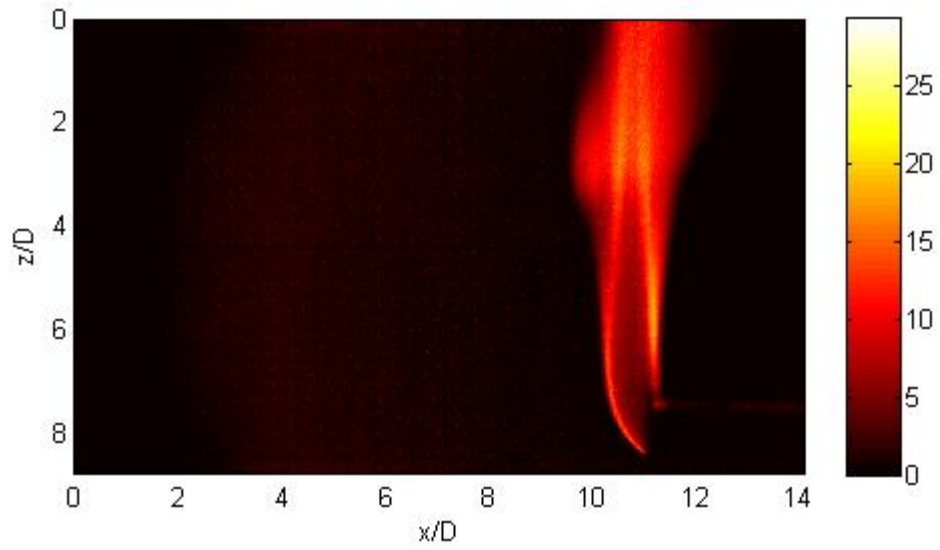**C. 17. Case 17: Propane, Re = 716, Fr = 1.5, ½ in Tube**
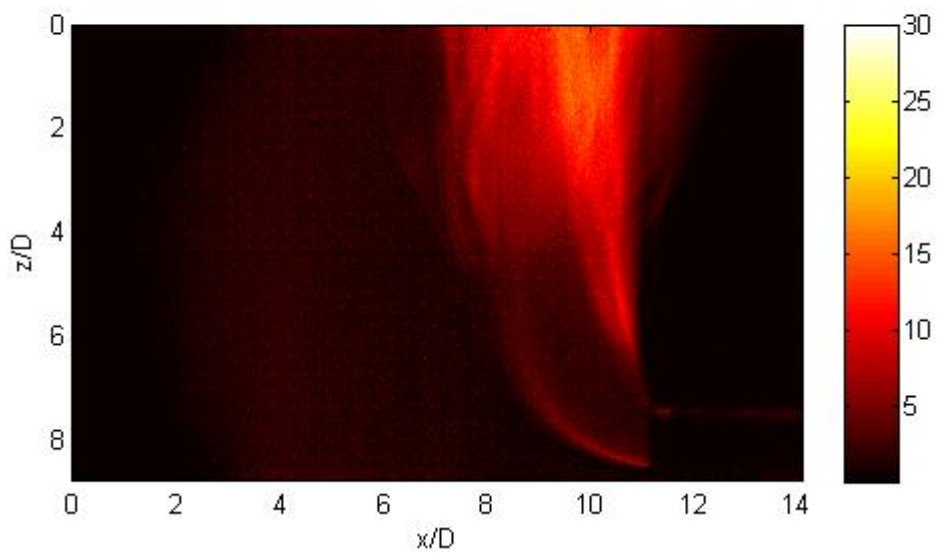
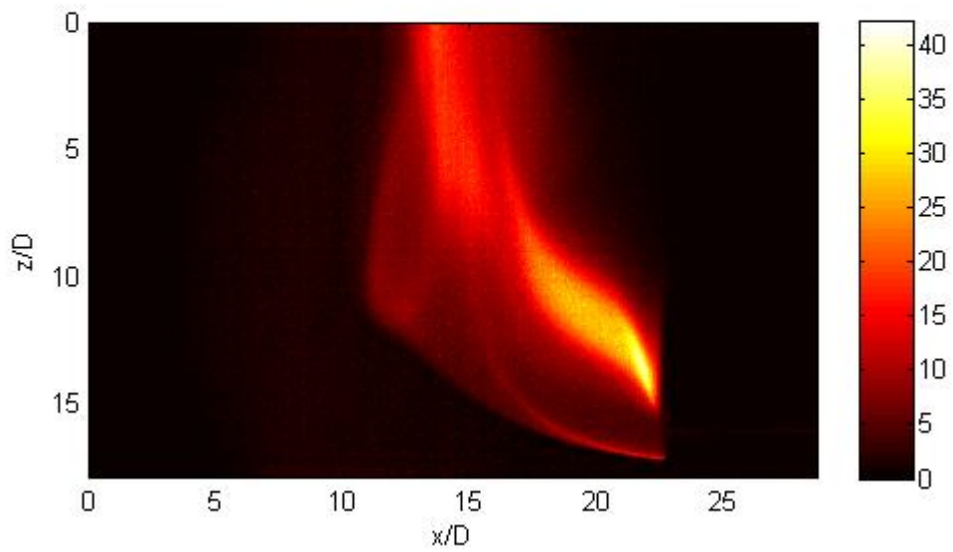**C. 18. Case 18: Propane, Re = 1234, Fr = 1.5, ¾ in Tube**
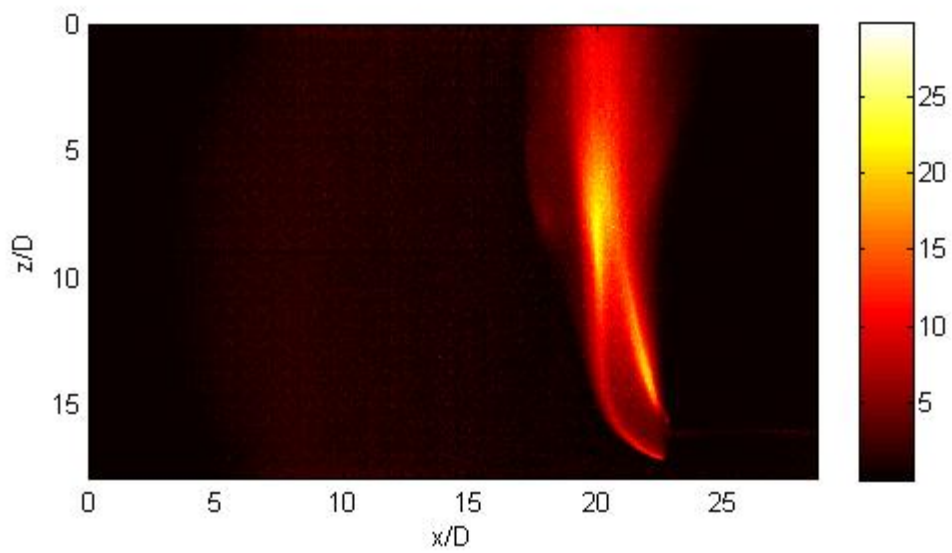
C. 19. Case 19: Ethylene, Re = 300, Fr = 7.67, $^3/_8$ in Tube

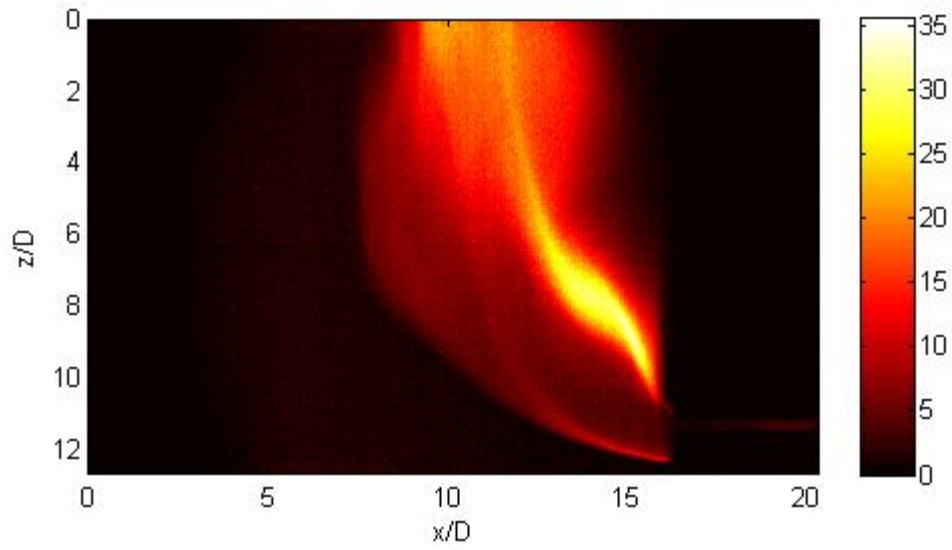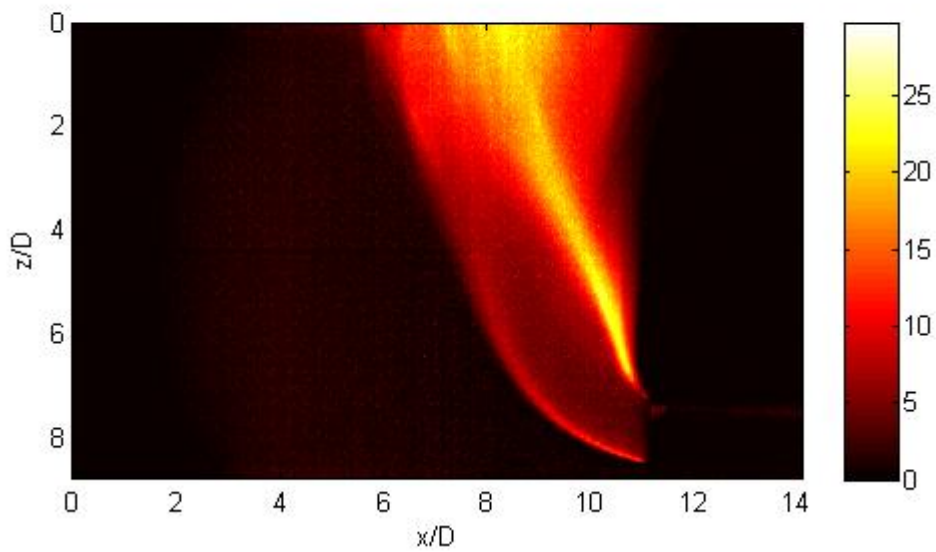**C. 20. Case 20: Ethylene, Re = 300, Fr = 4.57, ½ in Tube**

C. 21. Case 21: Ethylene, Re = 300, Fr = 2.63, ¾ in Tube

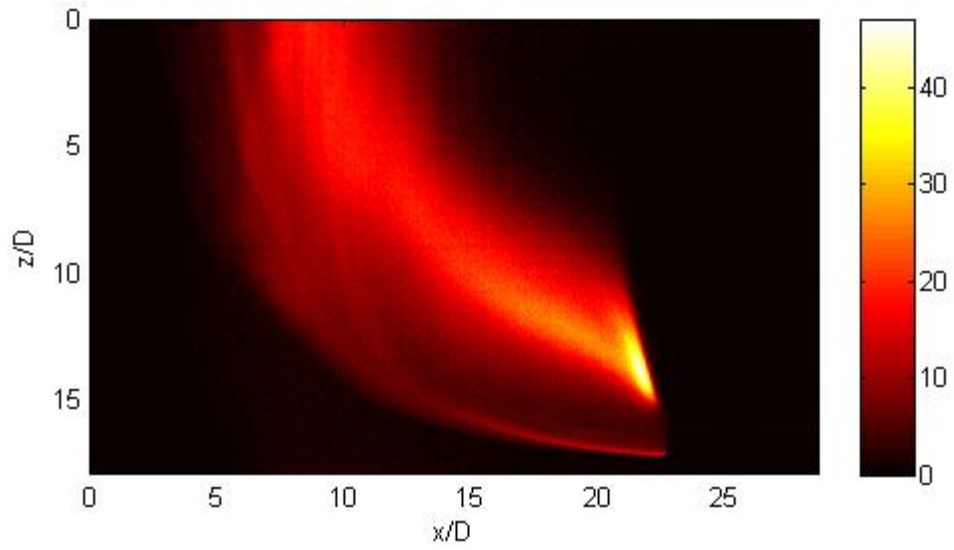**C. 22. Case 22: Ethylene, Re = 1000, Fr = 25.58, $^3/_8$ in Tube**

C. 23. Case 23: Ethylene, Re = 1000, Fr = 15.31, ½ in Tube

C. 24. Case 24: Ethylene, Re = 1000, Fr = 8.75, ¾ in Tube

C. 25. Case 25: Ethylene, Re = 1500, Fr = 38.41, $^3/_8$ in Tube
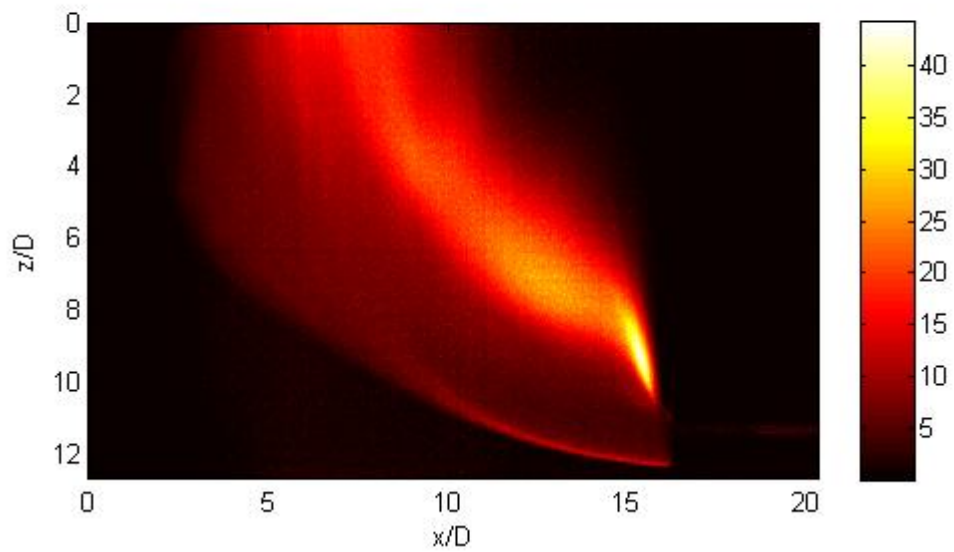
C. 26. Case 26: Ethylene, Re = 1500, Fr = 22.97, ½ in Tube
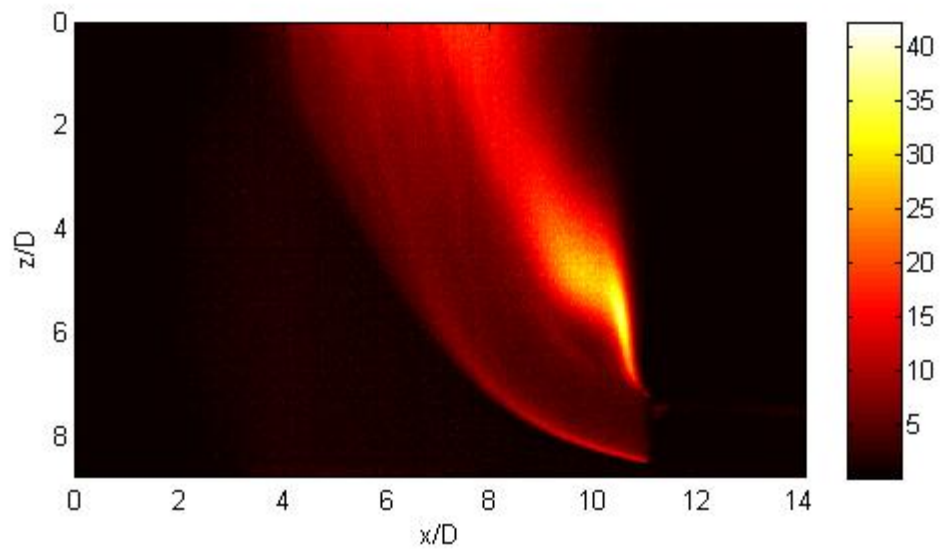
C. 27. Case 27: Ethylene, Re = 1500, Fr = 13.13, ¾ in Tube

Appendix D: Trajectory Plots
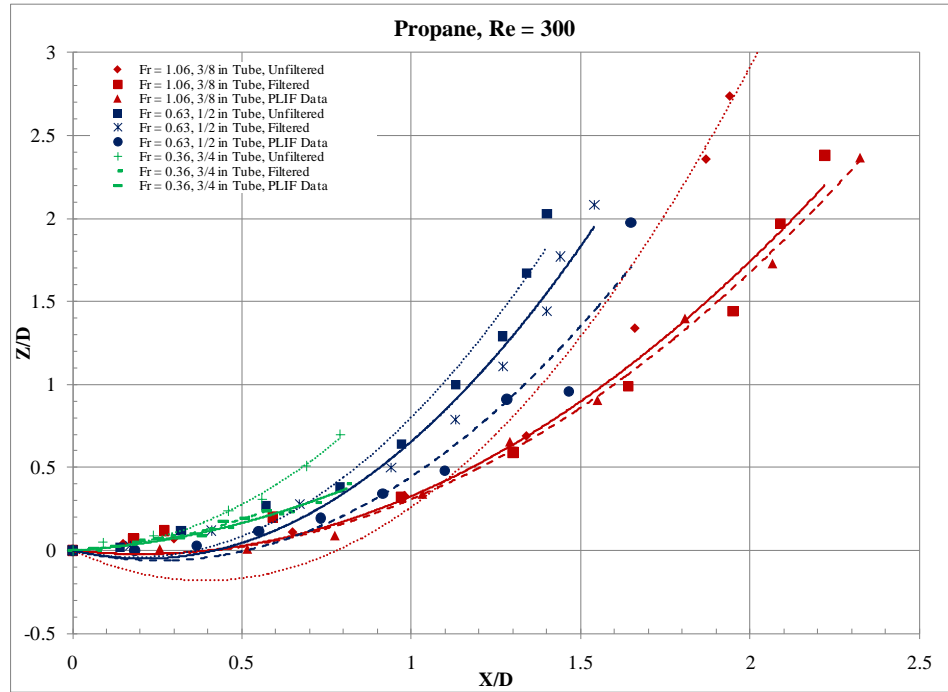
D. 1. Propane, Re = 300, Bottom Edge Trajectories, Cases 1, 2, and 3
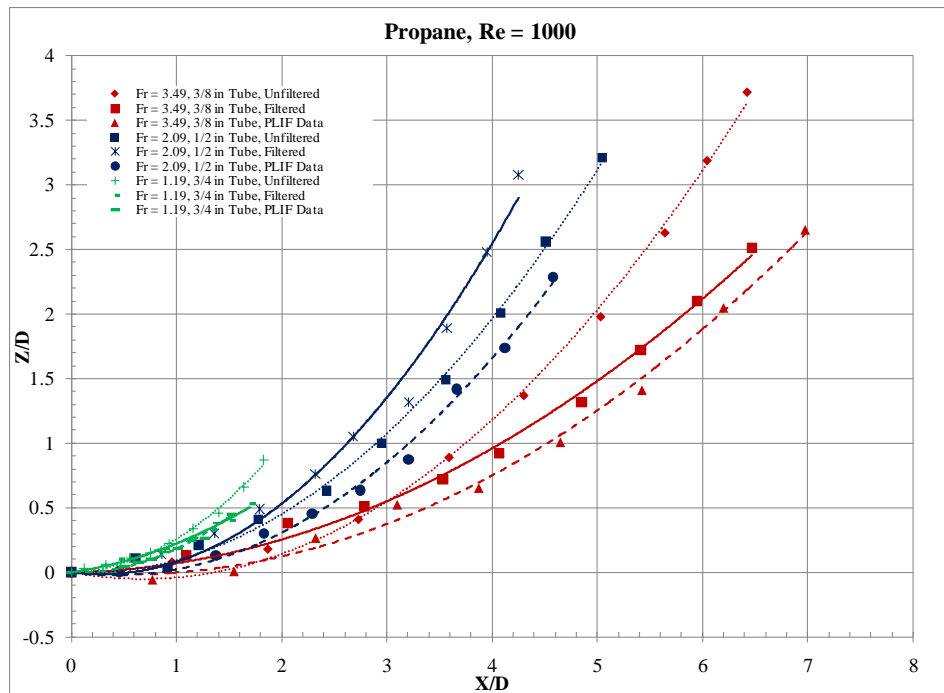
D. 2. Propane, Re = 1000, Bottom Edge Trajectories, Cases 4, 5, and 6
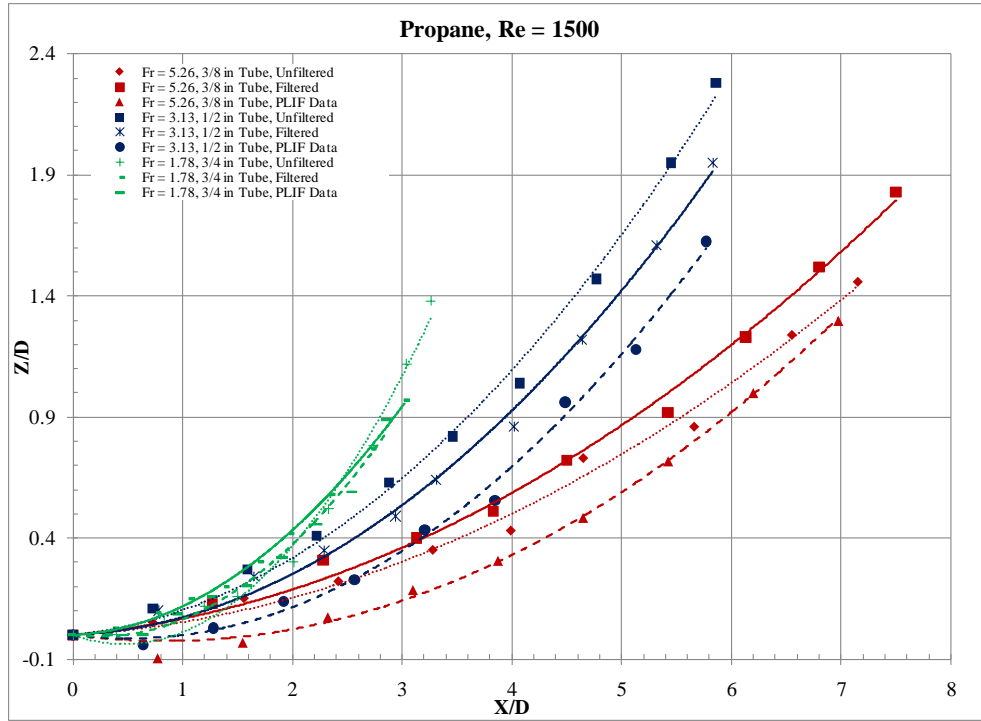
D. 3. Propane, Re = 1500, Bottom Edge Trajectories, Cases 7, 8, and 9
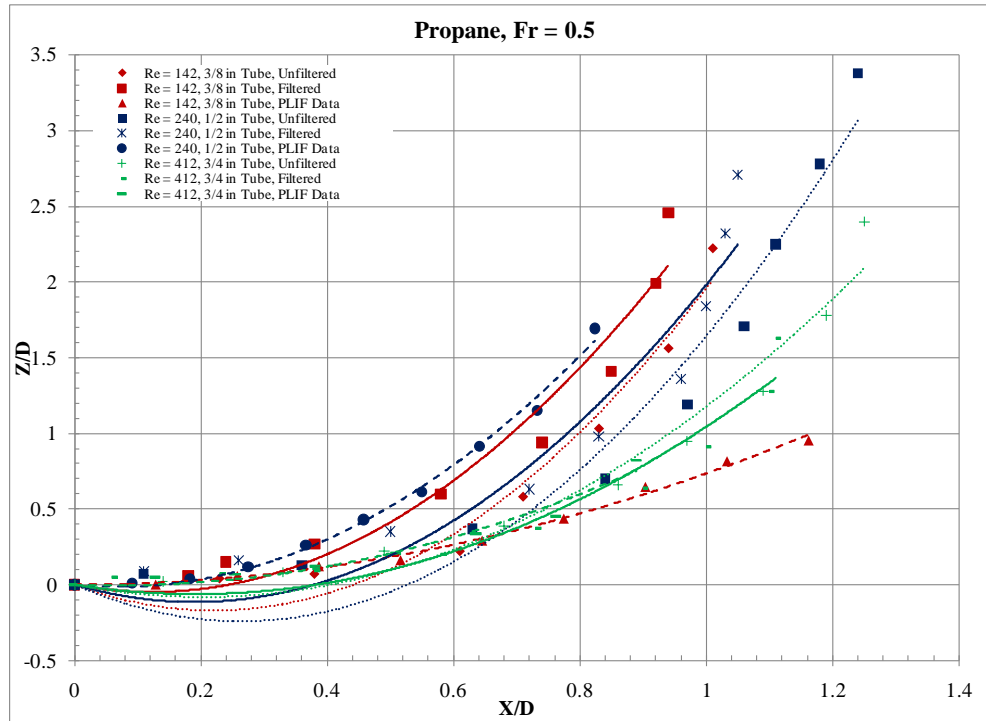
D. 4. Propane, Fr = 0.5, Bottom Edge Trajectories, Cases 10, 11, and 12
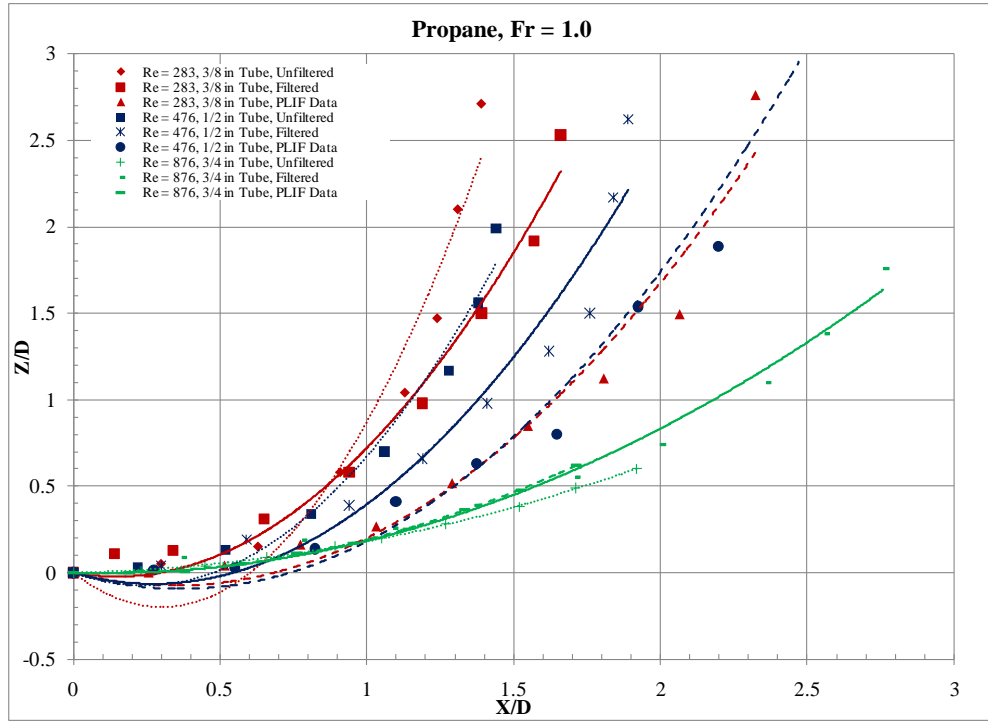
D. 5. Propane, Fr = 1.0, Bottom Edge Trajectories, Cases 13, 14, and 15

D. 6. Propane, Fr = 1.5, Bottom Edge Trajectories, Cases 16, 17, and 18
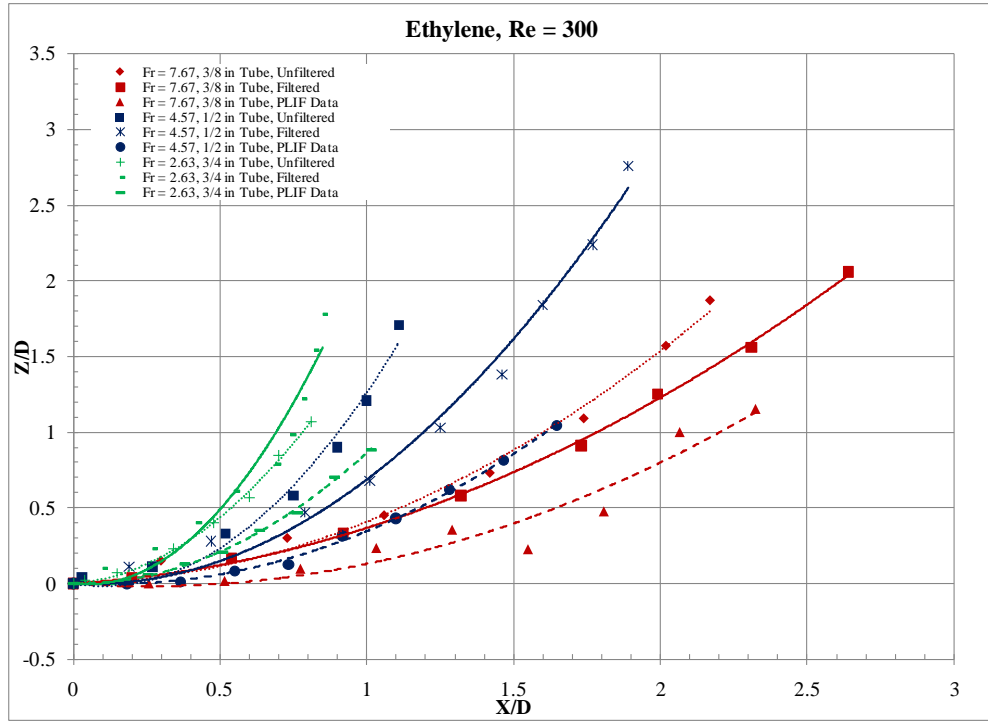
D. 7. Ethylene, Re = 300, Bottom Edge Trajectories, Cases 19, 20, and 21
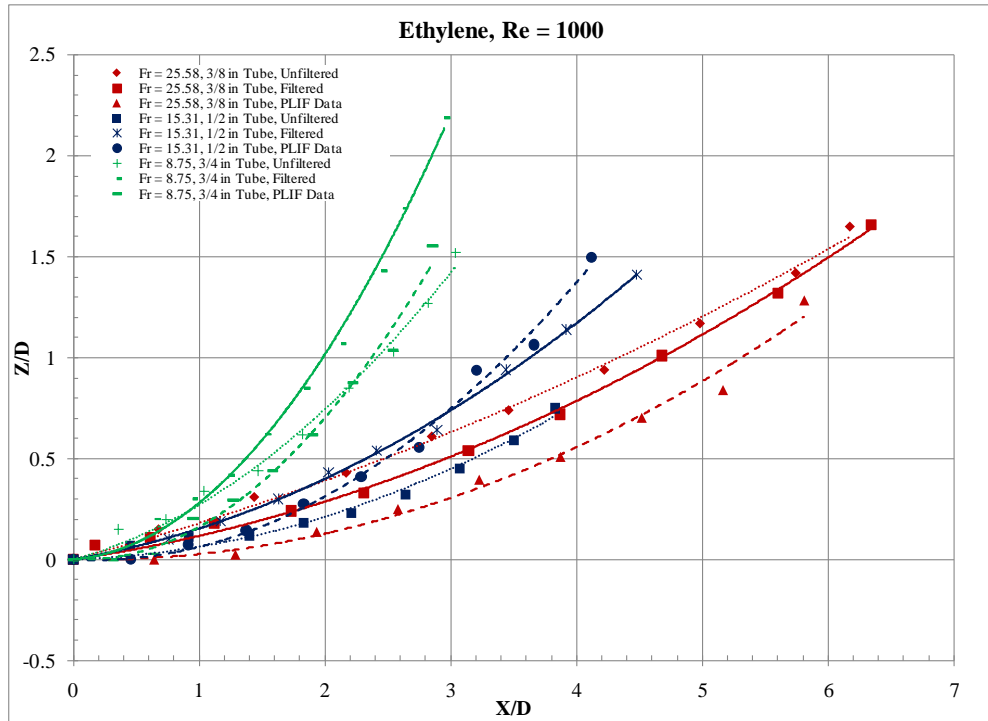
D. 8. Ethylene, Re = 1000, Bottom Edge Trajectories, Cases 22, 23, and 24

170
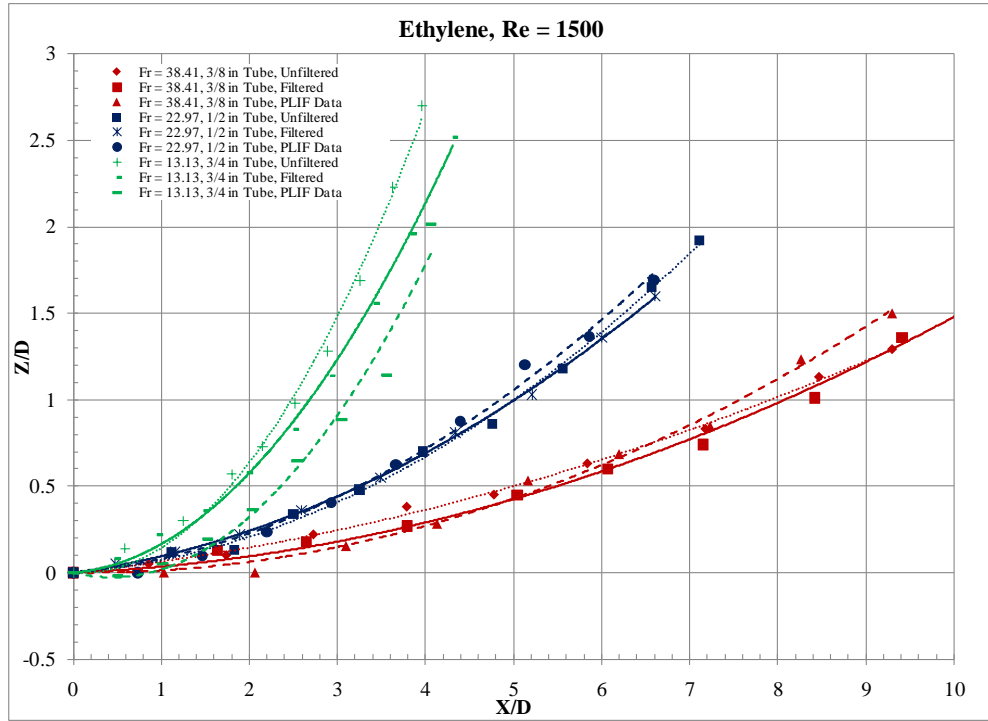
D. 9. Ethylene, Re = 1500, Bottom Edge Trajectories, Cases 25, 26, and 27

Appendix E: MATLAB Code
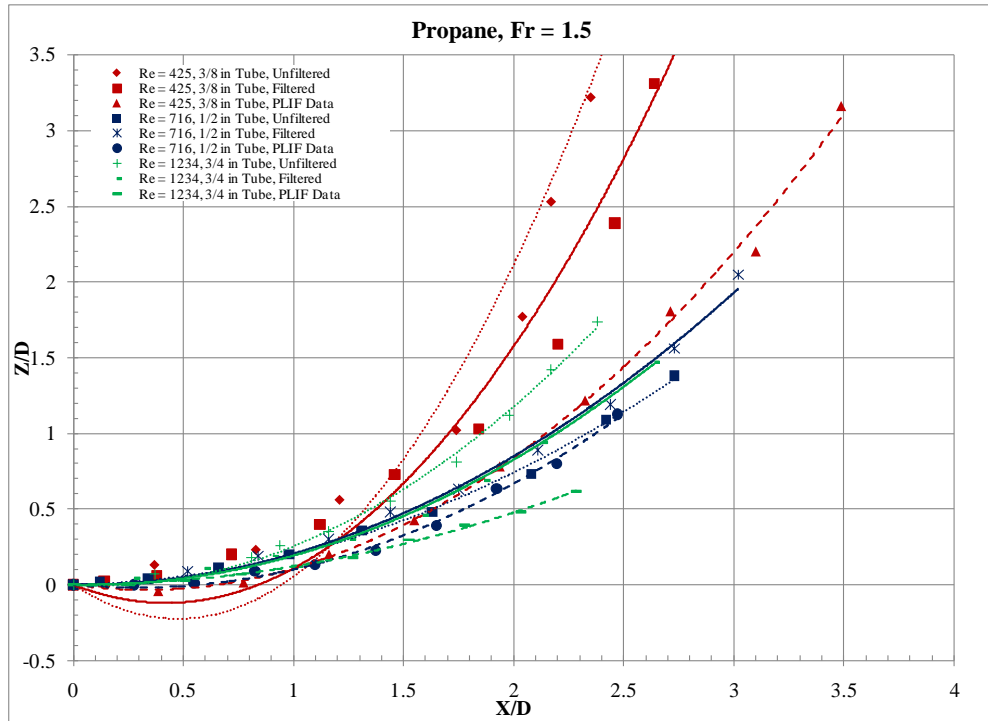
```matlab
clear
clc
%*%*%*%*%*UNFILTERED%*%*%*%*%*%*%*

%% Averaging High Speed Images
%% Joshua Heffernen
%% February 2011

%filenames
FN_Input='Case 27.tif';
D = 15.748; %TUBE DIAMETER 3/8 = 7.747; 1/2 = 10.922; 3/4 = 15.748
% D = 7.747;
% D = 10.922;

%set image size
num_columns=1280;
num_rows=800;

%set conversion from pixels to mm w/ mm/px value
dx=0.1959375/D;  %252mm/1280 pixels
dy=0.1959375/D;  %156mm/800 pixels

%% convert from pixels to length
x=zeros(1,num_columns);y=zeros(1,num_rows);
for i=1:num_columns
    x(i)=(i-1)*dx;
end

for j=1:num_rows
    y(1)=(j-1)*dx;

end

new_y=fliplr(y);

%import images
FN=FN_Input;
info=imfinfo(FN);
num_images=numel(info);
% num_images = 200;
z=zeros(num_rows,num_columns);
images=zeros(num_rows,num_columns,200);

for k=1:200
    z=imread(FN,k);
    images(:,:,k)=mean(z,3);
end
averaged = mean(images,3);

for k=201:400
    z=imread(FN,k);
    images(:,:,(k-200))=mean(z,3);
```

```matlab
end
averaged1 = mean(images,3);


for k=401:600
    z=imread(FN,k);
    images(:,:,(k-400))=mean(z,3);
end
averaged2 = mean(images,3);


Final = zeros(num_rows, num_columns, 5);
Final(:,:,1)=averaged;
Final(:,:,2)=averaged1;
Final(:,:,3)=averaged2;

% Final = averaged*3/0.4; % correct for 40% transmisivity and averaging
% BW = edge(averaged);
AFinal = mean(Final,3);


figure
imagesc(x,new_y,AFinal);
axis equal;
axis([0 max(x) 0 max(y)]);
xlabel('x/D');
ylabel('z/D');
colormap(hot)
colorbar;
```

Appendix F: PAHs Frequency Sweep

* All images are from Case 4 at 3D downstream
** All images are presented using the same intensity scale which ranges from 0 to 100

282.89662 nm	282.89935 nm	282.90146 nm
282.90295 nm	282.90531 nm	282.90693 nm
282.90916 nm	282.91139 nm	282.91301 nm
282.91499 nm	282.91723 nm	
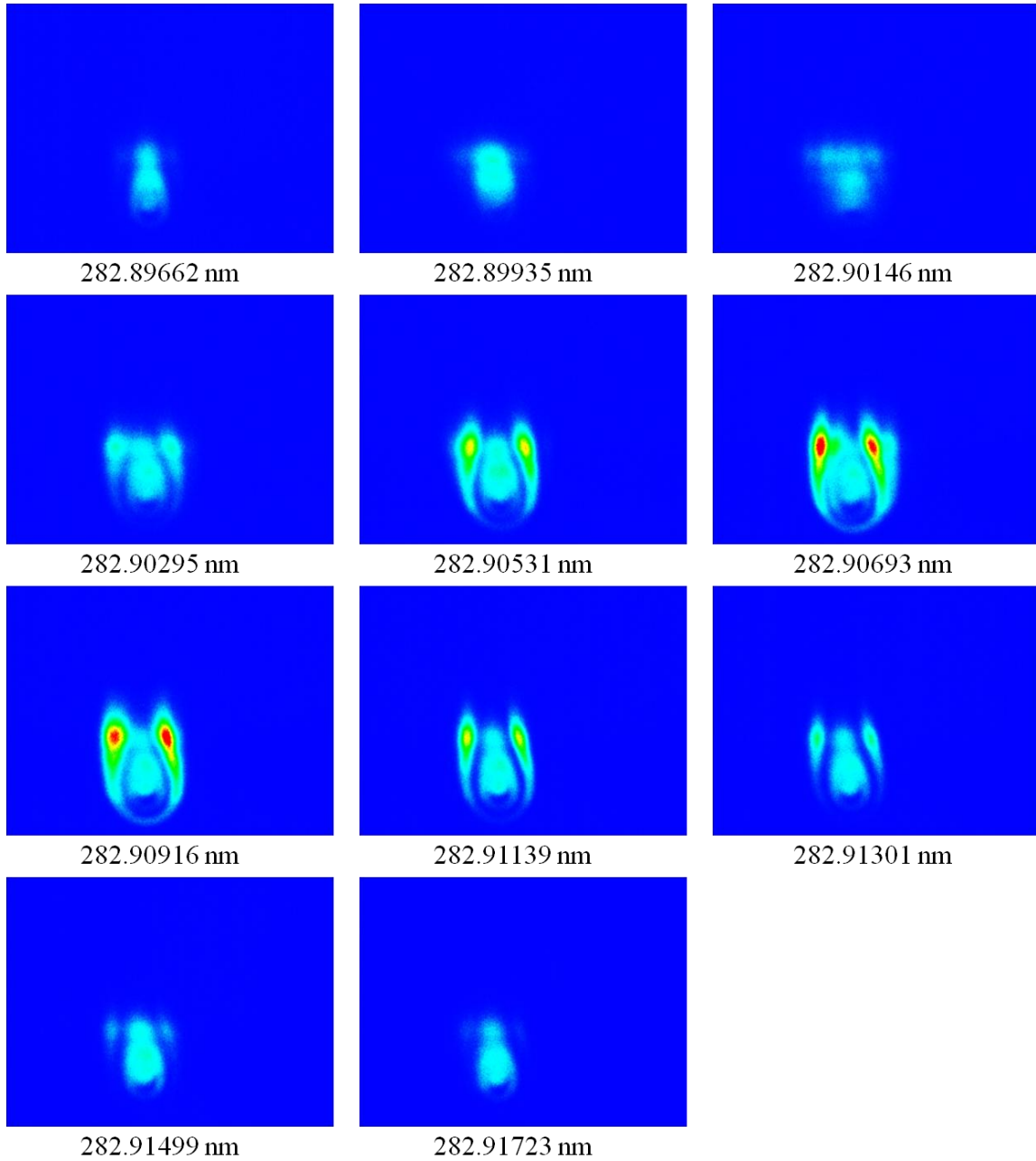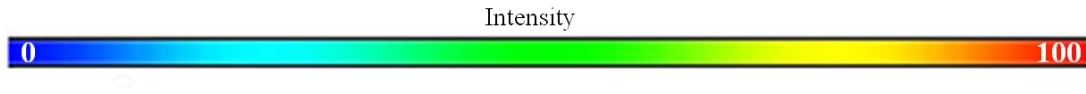
Bibliography

1. **BP.** *BP Statistical Review of World Energy.* 2009.

2. **Karbuz, S.** *U.S. Military Energy Consumption - Facts and Figures.* May 2007. Energy Bulletin.

3. **AIAA Air Breathing Propulsion Technical Committee.** *Versatile Affordable Advanced Turbine Engines (VAATE) Initiative.* Reston, VA : s.n., January 2006. AIAA Position Paper.

4. **Anthenien, R. A., Mantz, R. A., Roquemore, W. M., & Sturgess, G.** *Experimental Results for a Novel, High Swirl, Ultra Compact Combustor for Gas Turbine Engines.* 2nd Joint Meeting of the United States Section of the Combustion Institute. Oakland, CA : s.n., 2001.

5. **Drenth, A. C.** *Laser-Induced Fluorescence and Synthetic Jet Fuel Analysis in the Ultra Compact Combustor.* s.l. : MS thesis, AFIT/GAE/ENY/09-D03. Graduate School of Engineering and Management, Air Force Institute of Technology (AU), Wright-Patterson AFB OH, December 2009.

6. **Xiao J, Travis JR, Breitung, W.** Non-Boussinesq Integral Model for Horizontal Turbulent Buoyant Round Jets. 2009, Vols. 2009, Articel ID 862934, p. 7.

7. **Mattingly, J. D.** *Elements of Gas Turbine Propulsion .* New York : McGraw-Hill, Inc., 1996.

8. **El-Sayed, Ahmed F.** *Aircraft Propulsion and Gas Turbine Engines.* Boca Raton, FL : Taylor & Francis Group, 2008.

9. **Quaale, R. J.** *Experimental Results for a High Swirl, Ultra Compact Combustor for Gas Turbine Engines.* s.l. : MS thesis, AFIT/GAE/ENY/03-5. Graduate School of

Engineering and Management, Air Force Institute of Technology (AU), Wright-Patterson AFB OH, 2003.

10. **Hsu, K. Y., and Goss, L. P.** Characteristics of a Trapped-Vortex Combustor. *Journal of Propulsion and Power.* 1998, Vol. 14, 1.

11. **Roquemore, W. M., Shouse, D., Burrus, D., Johnson, A., Cooper, C., & Duncan, B., et al.** *Trapped Vortex Combustor Concept for Gas Turbine Engines.* Reno, NV : 39th AIAA Aerospace Sciences Meeting & Exhibit, July 2006.

12. **Koether, S. J.** *Validation of the AFIT Small Scale Combustion Facility and OH Laser-Induced Fluorescence of an Atmospheric Laminar Premixed Flame.* s.l. : MS thesis, AFIT/GAE/ENY/07-S03. Graduate School of Engineering and Management, Air Force Institute of Technology (AU), Wright-Patterson AFB OH, September 2007.

13. **Lewis, George D.** *Swirling Flow Combustion - Fundamentals and Application.* Las Vegas, NV : s.n., 1973.

14. —. *Centrifigual-Force Effects on Combustion.* Pittsburgh, PA : s.n., 1972. pp. 413-419.

15. **Young, A. D.** *Boundary Layers.* London : Blackwell Scientific Publications Ltd, 1989.

16. **Reeder, M. F., Huffman, R. E., Branam, R. D., Lebay, K. D., Meents, S. M.** *Mixing of Gas-Phase Horizontal Laminar Jets with Positive and Negative Buoyancy Measured with Filtered Rayleigh Scattering.* Air Force Institute of Technology, WPAFB, OH (USA) : s.n., 2010.

17. **Batchelor, G. K., Canuto, V. M., Chasnov. J. R.** Homogeneous Buoyancy-Generated Turbulence. *Journal of Fluid Mechanics.* 225: 349-378, 1992.

18. **Livescu, D., Ristorcelli, J. R.** Variable-Density Mixing in Buoyancy Driven Turbulence. . *Journal of Fluid Mechanics.* 605:145-180, 2008.

19. **Papantniou, D., List, E. J.** Large-Scale Structure in the Far-Field of Buoyant Jets. *Journal of Fluid Mechanics.* 209: 151-190, 1989.

20. **Monkewitz, P. A., Pfizenmair, E.** Mixing by Side Jets in Strongly Forced and Self-Excited Round Jets. *Physics of Fluids.* A 3:1356-1361, 1991.

21. **Subbaro, E. R., Cantwell, B. J.** Investigation of a Co-Flowing Buoyant Jet: Experiments on the Effect of Reynolds Number and Richardson Number. *Journal of Fluid Mechanics.* 245:69-90, 1992.

22. **Jirka, G.** Integral Model for Turbulent Buoyant Jets in Unbounded Stratified Flows. Part I: Single Round Jet. *Environmental Fluid Mechanics.* 4:1-56, 2004.

23. **Satyanarayana, S., Jaluria, A.** A Study of Laminar Buoyant Jets Discharged at an Inclination to the Vertical Buoyancy Force. *International Journal of Heat and Mass Transfer.* 25:1569-1576, 1982.

24. **Arakeri, J. H., Das, D., Srinivasan, J.** Bifurcation in a Buoyant Horizontal Laminar Jet. *Journal of Fluid Mechanics.* 412:61-73, 2000.

25. **Querzoli, G., Cenedese, A.** On the Structure of a Laminar Buoyant Jet Released Horizontally. *Journal of Hydraulic Research.* 43:71-85, 2005.

26. **Turns, Stephen R.** *An Introduction to Combustion - Concepts and Applications.* Boston : McGraw-Hill Companies, Inc., 2000.

27. **Kolhe, P. S., Agrawal, A. K.** Role of Buoyancy on Instabilities and Structure of Transitional Gas Jet Diffusion Flames. *Flow, Turbulence and Combustion.* 79:343-360, 2007.

28. **Escudier, M. P.** Analysis and Observations of Inclined Turbulent Flame Plumes. *Combustion Science and Technology.* 10:163-171, 1975.

29. **Eckbreth, A. C., In Gupta, A. K., Lilley, D. G. (Eds.).** *Laser Diagnostics for Combustion Temperature and Species.* Tunbridge Wells, Kentucky : Abacus Press, 1998.

30. **Eckbreth, A. C., Bonczyk, P. A., & Verdieck, J. F.** Combustion Diagnostics by Laser Raman and Fluorescence Techniques. *Progress in Energy and Combustion Science.* 5:253-322, 1979.

31. **Hankins, T. B.** *Laser Diagnositc System Validation and Ultra Compact Combustor.* s.l. : MS thesis, AFIT/GAE/ENY/08-M14. Graduate School of Engineering and Management, Air Force Institute of Technology (AU), Wright-Patterson AFB OH, March 2008.

32. **Seitzman, J. M., Hanson, R. K., Debarber, P. A., & Hess, C. F.** Application of Quantitative Two-Line OH Planar Laser-Induced Fluorescence for Temporally Resolved Planar Thermometry in Reacting Flows. *Applied Optics.* June 1994, Vol. 33, 18.

33. **Tamura, Masayuki, Berg, P. A., Harrington, J. E., Luque, J., Jefferies, J. B., Smith, G. P., Crosley, D. R.** Collisional Quenching of CH(A), OH(A), and NO(A) in Low Pressure Hydrocarbon Flames. *Combustion and Flame.* 114:502-114, 1998.

34. **Quantel.** *Brilliant/Brilliant B Instruction Manual.* Issue # 5.1, October 2005.

35. —. *TDL 90 Instruction Manual.* Issue 1 : s.n.

REPORT DOCUMENTATION PAGE			*Form Approved* *OMB No. 0704–0188*		
The public reporting burden for this collection of information is estimated to average 1 hour per response, including the time for reviewing instructions, searching existing data sources, gathering and maintaining the data needed, and completing and reviewing the collection of information. Send comments regarding this burden estimate or any other aspect of this collection of information, including suggestions for reducing this burden to Department of Defense, Washington Headquarters Services, Directorate for Information Operations and Reports (0704–0188), 1215 Jefferson Davis Highway, Suite 1204, Arlington, VA 22202–4302. Respondents should be aware that notwithstanding any other provision of law, no person shall be subject to any penalty for failing to comply with a collection of information if it does not display a currently valid OMB control number. PLEASE DO NOT RETURN YOUR FORM TO THE ABOVE ADDRESS.					
1. REPORT DATE (DD–MM–YYYY) 24-03-2011		2. REPORT TYPE Master's Thesis		3. DATES COVERED (From — To) Sept 09 – Mar 11	
4. TITLE AND SUBTITLE Characterization of Horizontally-Issuing Reacting Buoyant Jets			5a. CONTRACT NUMBER		
			5b. GRANT NUMBER		
			5c. PROGRAM ELEMENT NUMBER		
6. AUTHOR(S) 2Lt Joshua J. Heffernen			5d. PROJECT NUMBER		
			5e. TASK NUMBER		
			5f. WORK UNIT NUMBER		
7. PERFORMING ORGANIZATION NAME(S) AND ADDRESS(ES) Air Force Institute of Technology Graduate School of Engineering and Management (AFIT/ENY) 2950 Hobson Way WPAFB OH 45433-7765			8. PERFORMING ORGANIZATION REPORT NUMBER AFIT/GAE/ENY/11-M12		
9. SPONSORING / MONITORING AGENCY NAME(S) AND ADDRESS(ES) Dr. Joseph Zelina Air Force Research Laboratory/ Propulsion Directorate Building 490, Room 116, WPAFB 45433 DSN 785-7487 Joseph.Zelina@wpafb.af.mil			10. SPONSOR/MONITOR'S ACRONYM(S) AFRL/RZ		
			11. SPONSOR/MONITOR'S REPORT NUMBER(S)		
12. DISTRIBUTION / AVAILABILITY STATEMENT APPROVED FOR PUBLIC RELEASE; DISTRIBUTION UNLIMITED					
13. SUPPLEMENTARY NOTES The views expressed in this thesis are those of the author and do not reflect the official policy or position of the United States Air Force, Department of Defense, or the U.S. Government. This material is declared a work of the U.S. Government and is not subject to copyright protection in the United States					
14. ABSTRACT This research studied the mixing and combustion behavior of low Reynolds number, horizontally-issuing gaseous fuel jets with ambient air. The study focused on the mixing characteristics of propane and ethylene. These fuels are, respectively, heavy and neutral with respect to air, and were tested at various Froude numbers and laminar tube Reynolds numbers. Using low Froude and Reynolds number flows allowed for isolation of the buoyant jet effects. The process was characterized through the use of a non-invasive, OH Planar Laser-Induced Fluorescence (PLIF) technique, and supplemented with filtered (CH*) and unfiltered high speed imaging. The resulting cross sectional PLIF images were used to produce a three-dimensional mapping of the jet spreading, jet path, and combustion progress through OH concentrations up to $x/D = 9$, for both fuels. Combustion locations were further visualized and confirmed through CH* high speed imaging.					
15. SUBJECT TERMS ultra compact combustor, buoyancy, horizontally-issuing jets					
16. SECURITY CLASSIFICATION OF:			17. LIMITATION OF ABSTRACT	18. NUMBER OF PAGES	19a. NAME OF RESPONSIBLE PERSON Lt Col Carl R. Hartsfield
a. REPORT U	b. ABSTRACT U	c. THIS PAGE U	UU	193	19b. TELEPHONE NUMBER (Include Area Code) 937-255-3636 ext. 7472 Email: Carl.Hartsfield@afit.edu